



Université
de Toulouse

THÈSE

En vue de l'obtention du

DOCTORAT DE L'UNIVERSITÉ DE TOULOUSE

Délivré par : *l'Université Toulouse III – Paul Sabatier*

Discipline ou spécialité : *Génie Mécanique*

Présentée et soutenue par **Farid MIAH**

Sur

Numerical and Experimental Analysis of CFRP Machining Process in Orthogonal Cutting

Soutenu le 17 janvier 2020 devant le JURY composé de :

Olivier CAHUC	Professeur des Universités, Universités de Bordeaux	(Examinateur)
Mohamed EL-MANSORI	Professeur des Universités, ENSAM Aix-en Provence	(Rapporteur)
Mohammed NOUARI	Professeur des Universités, Universités de Lorraine	(Rapporteur)
Xiaojing GONG	Professeure des Universités, IUT de Tarbes	(Examinatrice)
Yann LANDON	Maitre de Conférences, HDR, Universités de TOULOUSE	(Invité)
Frederic LACHAUD	Professeur, ISAE-SUPAERO	(Directeur de thèse)
Emmanuel DE LUYCKER	Maitre de Conférences, ENIT de Tarbes	(Co-directeur de thèse)

Ecole doctorale : *Mécanique, Energétique, Génie Civil & Procédés (MEGeP)*

Unité de recherche : Institut Clément Ader

To my parents...

Acknowledgment

Sometimes I look back at these last three years of my doctoral school and I wonder while I feel that these three years have passed by as like three days. I become ravenously hungry to discover more knowledge while I ask myself if I could bring to light a drop amount of information in machining from within oceanic scale of machining knowledge. My experience at Institut Clement Ader (ICA) laboratory has been nothing short of amazing. I have been given unique research opportunities... and taken advantage of them. I am indebted to many people for making the time for working my PhD an unforgettable experience.

I am very grateful to my advisors Frederic LACHAUD and Emmanuel DE LUYCKER, two incredible persons, who have supported me patiently not only by providing the research assistance and planning, but also the freedom I needed to move on through the rough road to finish this thesis. Frederic's remarkable supports in numerical modelling, which include incredible new ideas to find out solutions, played a significant role in the advancement of my PhD. I sincerely acknowledge the patience of Emmanuel he showed to align my research work with research goals, to guide me on scientific analysis, scientific report writing, presentation making and so on. To work with both of them has been a real pleasure to me. Besides, I am grateful to my external supervisors, Yann LANDON and Robert PIQUET, for their support and discussions in this thesis.

I would like to thank Abdallah BOUZID, engineer at ICA, for his generous assistances during the machining experiments at the workshop. I remember while we encountered any problem during the tests he used to tell me "there is no problem but only solutions, because problem does not exist". I am also thankful to Olivier CHERRIER and Alexandre CHARDONNEAU, two engineers of ICA, who always lent their helpful hands for the installation and operation of high speed cameras. Furthermore, I have been very privileged to work with my colleagues at the laboratory; notably, Benoit MONTAGNE who was my officemate, Jean-Emmanuel CHAMBE, Agathe JAILLON, Akshay HEJJAJI, Malek BENAÏSSA and many other. There is no way I can ever list all of the amazing people who got me this far. They are truly amazing people. I learned a lot from them about research, how to tackle new problems and develop techniques to solve them.

The work on this thesis was financed by French government. I hereby show my humble gratitude to the French government for the finance which permitted me to have this extraordinary PhD research experience.

Finally, I think of my late father who, if were alive today, would be highly delighted by my today's acquirement. I specially thank my mother, my brothers and sisters and all other family members for their infinite support in all my pursuits. I exceptionally thank my brother Mustofa SARWAR and his spouse Shanta AKTER who have given unconditional care and support in every way throughout my whole study life. I would not have made it this far without their supports.

Outline

The Composite materials, including CFRP (Carbon Fiber Reinforced Polymer), are increasingly used in aeronautics and automotive as these materials are capable of playing a unique role in industrial applications by their outstanding lightweight properties. In the latest model of Airbus, A350-900, the CFRP content is more than 50% in weight. This extensive use of composite structures is currently raising many complications in the machining processes as those materials are made with multiple phase microstructures which are accountable for poor machining quality and undesired damages, e.g. delamination, crack generation. Along with some other machining operations, drilling is the most common machining operation for CFRP processing; for example, around 1.2 million bores are required in one Airbus A350 for rivet joining which primarily needs drilling operation. Therefore, it is believed that the fundamental analysis of cutting mechanism and chip formations process of CFRP can help to increase the process effectiveness, which will result reduced defects in the machined parts.

On that account, a thesis was already done by [Blanchet, 2015] at Institut Clement Ader which focused to a simplified cutting technique called orthogonal process. Nevertheless, many particular questions remained unanswered in this process as there are many process parameters which play distinct significant role on the quality of manufactured parts. The present thesis is thematically connected to the work of [Blanchet, 2015]. It seeks to better understand the fundamental physical technique involved in the process by combined numerical and experimental study, and how certain cutting parameters affect the machining quality. To this aim, initially the focus was made to the strain field generation in the workpiece while the tool cuts the materials. At the same time, an in-depth observation was made on how chips are formed at 0° , 45° , 90° and 135° fiber orientations. For that study, a micro-mechanical model was developed distinguishing the properties of fiber and matrix separately. A cohesive interface property (zero volume) was introduced in fiber-matrix interface. Both the experimental and numerical observations clearly showed the physics of chip formation mechanism.

Following that, the influences of cutting depth, which is an important process variable, to (i) cutting and thrust forces, (ii) surface roughness, (iii) subsurface damage and, (iv) chip shape and size were studied. The studies were carried out by experimental tests as well as by a macro-mechanical model which was developed with equivalent homogeneous material (EHM). Besides, the X-ray tomography tests revealed the machining induced interply delaminations and inner crack generation in the workpiece.

The definition of a minimum cuttable depth, classical for metal cutting, still does not exist for CFRP in literature. Therefore, an experimental observation was made to find out the minimum cuttable depth below which the material does not get cut smoothly over the whole surface. At the end, this research work has been finished by a preliminary study on cutting tool wear mechanism.

Content

Context of the Research	11
I.I. Introduction.....	11
I.II. Defects in CFRP Machining in Orthogonal Cutting.....	14
I.III. Goals of the Research.....	15
Chapter 1: State of the Art.....	19
1.1. Literature Review	21
1.1.1. Orthogonal Cutting in Machining	21
1.1.1.1. Mechanics of Orthogonal Cutting	22
1.1.2. Findings on Cutting Parameters and Generated Defects.....	25
1.1.2.1. Cutting Operation and Variables	25
1.1.2.2. Machining Induced Defects.....	41
1.1.3. Various Developed Models in CFRP Machining.....	47
1.1.3.1. Micro-mechanic Models.....	47
1.1.3.2. Macro-mechanic Models.....	59
1.1.3.3. Analytical Models	66
1.1.4. Summary of Literature Study	72
1.2. Conclusion	73
Chapter 2: Developed Models, Strain Field Analysis and Chip Formation Mechanisms.....	75
2.1. Experimental Process	77
2.1.1 Machine Setup.....	77
2.1.1.1. Machine Operation and Its connections	78
2.1.1.2. Cutting Parameters and Related Configurations.....	79
2.1.2. Cutting Tool Selection	80
2.1.3. Workpiece Preparation	81
2.2. Developed Models.....	83
2.2.1. Micro-mechanical Model	83
2.2.1.1. Boundary Conditions and Meshes.....	85
2.2.1.2. Interaction Properties	86
2.2.1.3. Material's Property and Failure Criteria.....	91
2.2.2. Macro Model	93

2.2.2.1. Geometry and Boundary Conditions	93
2.2.2.2. Contact Modeling	94
2.2.2.3. Meshing, Adaptive Meshing and Distortion Control.....	94
2.2.2.4. Failure Criteria	96
2.3. Strain Measurement Process	100
2.3.1. Experimental Strain Measurement Process	100
2.3.2. Numerical Strain Measurement Process.....	104
2.4. Strain Field Analysis.....	106
2.4.1. Experimental Results	106
2.4.2. Comparison of Numerical and Experimental Results.....	110
2.5. Chip Formation Mechanism in Orthogonal Cutting of CFRP	113
2.5.1. The Course of Chip Formation.....	114
2.6. Conclusion	124
Chapter 3: Effects of Cutting Depths.....	125
3.1. Configurations of Analysis	127
3.1.1 Machine Setup.....	127
3.1.2. Materials and Cutting Conditions.....	127
3.1.3. Measurement Techniques.....	128
3.1.3.1. Force Measuring Procedure	128
3.1.3.2. Roughness Measuring Technique	130
3.1.3.3. Chip's Dimensions Measuring Technique	131
3.2. Effects to Machining Forces	132
3.2.1. Results and Discussion	133
3.2.1.1 Cutting Force	133
3.2.1.2. Thrust Force.....	135
3.2.2. Force When the Tool Touches the Workpiece	137
3.3. Effects to Surface Roughness	139
3.3.1. Results and Discussions.....	139
3.4. Effect to Subsurface Damage	144
3.4.1. Crack Generation and Propagation	144
3.4.2. Subsurface Damage Analysis by X-ray Tomography	149
3.5. Effects to Chip's Shape and Size	156

3.5.1. Chip's Length	157
3.5.2. Chip's Height and Width.....	159
3.6. Conclusion	161
Chapter 4: Tool Wear and Minimum Cutting Depth for Continuous Cut.....	163
4.1. Minimum Cutting Depth for Continuous Cut	165
4.1.1. Experimental Procedure.....	165
4.1.2. Result Analysis.....	168
4.1.3. Conclusion, Difficulties and Perspectives.....	175
4.2. Tool Wear Mechanism	176
4.2.1. The Tool and the Wear Measuring Procedure	177
First Test	177
Second Test	180
4.2.2. Results Analysis	181
4.2.2.1. First Test	181
4.2.2.2. Second Test	184
4.2.3. Conclusion and Perspectives	186
Global Conclusion and perspectives	187
References	189
Appendixes	203

Glossary

- τ : Equivalent shear stress
- τ_{lim} : Limiting shear stress
- ε : Lagrange strain
- $\dot{\varepsilon}$: Strain rate
- $\bar{\varepsilon}$: strain vector
- δ : Displacement in cohesive interface
- α : Rake angle
- γ : Clearance angle
- μ : Friction coefficient
- σ : Cauchy stress
- σ_y : Yield stress
- σ_0 : Initial yield stress
- σ_n : In-plane normal stress
- σ_f : In-plane normal strength
- η : Cohesive property parameter
- ϕ : Shear angle
- \varnothing_i : Damage evolution variable
- \bar{p} : Stiffness matrix
- Δ_n : Normal displacement
- b : Cohesive sliding resistance
- B : Hardening modulus
- C : Strain rate sensitivity coefficient
- CFRP : Carbon Fiber Reinforced Polymer
- D : Damage variable
- EHM : Equivalent Homogeneous Material
- $\dot{\varepsilon}_p$: Plastic strain rate (s⁻¹)
- $\dot{\varepsilon}_0$: Reference plastic strain rate (s⁻¹)

E : Modulus of elasticity
E_p : Plastic hardening modulus
E_{tan} : Tangent modulus
F : Force
FEM : Finite Element Analysis
G_r/E_p : Graphite/Epoxy
G_n^C : Critical fracture energy in normal direction
G_s^C : Critical fracture energy in first shear direction
G_t^C : Critical fracture energy in second shear direction
ICA : Institut Clement Ader
K_n : Normal stiffness component
K_s & K_t : Shear stiffness components
m : Thermal softening coefficient
n : Hardening coefficient
P : Contact pressure / the effective plastic strain
T : Temperature of the work material (K)
T_{eff}⁰ : Effective traction at damage initiation
t_n : Normal contact stress
t_s & t_t : Shear contact stresses
T₀ : Room temperature (K)
X₂ : Angle between fiber orientation and cutting direction
X_t : Longitudinal tensile strength
Y_t : Transverse tensile strength

Context of the Research

I.I. Introduction

Since the industrial revolution the manufacturing technologies have been the driving force behind modern economies. The machineries and structures which we need at every aspect of our life are created by these technologies. Today the technologies have become more sophisticated by the advances of computer and material sciences which increased our ability to develop predictive capability and optimization for various applications. Metal cutting processes are some of the oldest widely used methods which are used to give a particular shape to a metal piece and these processes are involved in manufacturing process, whether directly or indirectly, of most of the items we use today [Altintas, 2012] [Limido et al., 2011]. In machining, to understand the mechanics of chip formation of metal machining much work has been done over the past century, and the same techniques have been used to study the composites machining but no much success was found [Ahmad, 2009]. Moreover, the numerical modeling of composites cutting is still poorly developed [Cantero et al. 2012].

The necessity of good understanding of composites machining is becoming highly important as the composite materials, including CFRP (Carbon Fiber Reinforced Polymer), are increasingly used in aeronautics and automotives because of their high mechanical strength with respect to the density, good resistance to corrosion and to fatigue. During the last decade the demand for composite materials has increased significantly. In 2010 the global carbon fiber demand was 33 thousand tons, and it is estimated at 89 thousand tons for 2020, which is mostly for aerospace & defense (30%), and then automotive, molding & compound and wind turbines, Fig. I.I, [Mark H., 2014]. In addition, the European regulations to reduce the CO₂ consumption and pushing for lightweight manufacturing are playing a significant role on the growth demand these days. The Airbus model A350 XWB already used a CFRP content of 50% [Altaire, 2012], Boeing 787 Dreamliner used 53% for outer skin [Fay B., 2012] [Boeing AEOR]; similarly, the fighter jet Eurofighter used 40% composite in weight [Smith and al., 2013], Fig. I.II.

This extensive use of composite structures is presently raising a lot of complications in their machining processes. Along with some other machining operations, drilling is the most common machining operation for CFRP processing; for example, around 1.2 million bores are required in one Airbus A350 for rivet joining which primarily needs drilling operation. But composite materials are not homogeneous, and the chip formation process in machining composite laminates is significantly different from that in machining of metals, e.g. milling, turning and drilling. According to [Lasri et al., 2009] the machining of fiber reinforced polymer (FRP) materials differs from machining conventional metals and their alloys due to the heterogeneity and anisotropy of FRP materials. [Liu et al., 2012] noted composite laminates are regarded as hard-to-machine materials, which results in low machining efficiency and undesirable

machining-induced delamination. Moreover, in cutting mechanism of composites, fiber orientation, cutting depth, rake and clearance angles play significant role on the cutting forces. The surface roughness of the newly generated surface varies depending on the process variables. The shape and size of the chip depends not only on depth of cut but also on the fiber orientation and rake angle. Overall, composite machining draws many questions to be solved in order to increase the quality of machining.

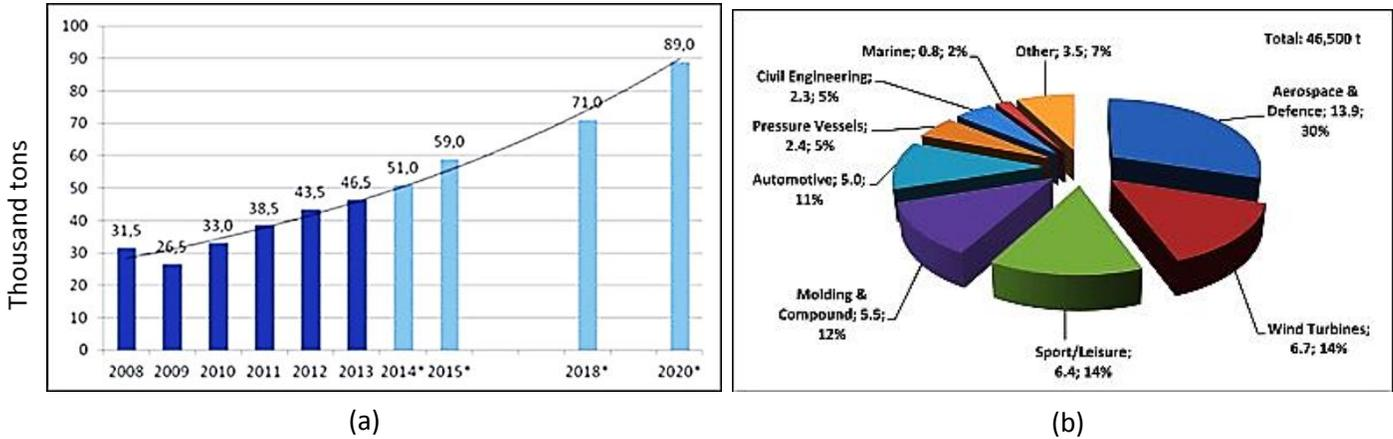


Fig. 1.1: Global demand for carbon fiber (a) trend of demand (in thousand tons), (b) demand by application (in 2010), [Mark H., 2014].

It is believed that the fundamental analysis of cutting mechanism and chip formations process of CFRP material can help increasing the machining efficacy. Orthogonal cutting is a type of material cutting technique in which the cutting edge of a wedge shape cutting tool is perpendicular to the direction of the tool motion. This cutting process involves the systematic removal of layers of material in the form of chips from a workpiece by the action of a wedge shaped cutting tool. This process directly refers to Turning, External Threading, Grinding and Filing, and can be used indirectly to make reference to Milling and Drilling (a chart of most common machining processes has been shown in Diag.1.1.1). Milling and Drilling are considered as oblique processes of which the tool has minimum 3 angles, and that is why analyzing the machining phenomenon, machining quality and more especially the machining induced defects in manufactured part is difficult. In drilling, visual inspection inside of hole is very complex; as a result it becomes difficult to identify the machining induced defects inside a hole. Moreover, for numerical analysis, the 3 angles of cutting tool obliges to make model in 3D which also amplify the complexity of the model.

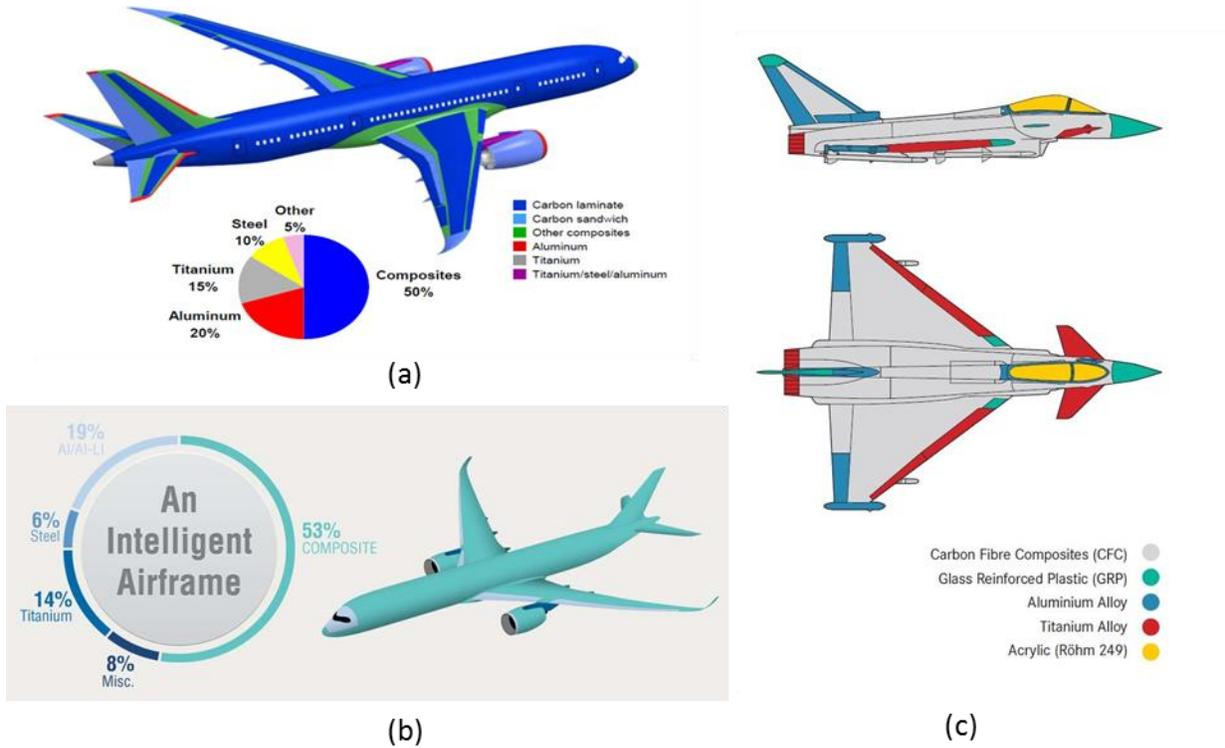


Fig. 1.II: Materials used in the outer body of (a) Airbus A350 XWB [Altaire, 2012], (b) Boeing 787 Dreamliner [Fay B., 2012] [Boeing AEOR], (c) Eurofighter [Cephas and Luling, 2017].

Recently the research activities in orthogonal cutting of composite laminates have been increased since it has been recognized that fundamental knowledge of orthogonal machining process can help in the solution of many particular production problems of composite parts. The simpler conditions of orthogonal machining in studying chip formation permits to gather knowledge about different components like chip shape and size, shear stress and strain in chip, friction conditions, cutting forces, cutting temperatures etc. [Klinkova et al., 2011].

In this context, a PhD research was done by Blanchet [Blanchet, 2015] in the same laboratory and defended in 2015. His PhD disclosed some process parameter's influences to machining quality in orthogonal cutting of CFRP along with defining cutting tool geometry and test bench for experimentation. However, many physical phenomenon remains unrevealed, especially the mechanics of chip formation, cutting depth influence, machining induced damages, tool sharpness loss etc. which deserves inclusive research. Aiming at those problematics this present research has been carried out. The physical phenomena have been analyzed experimentally along with numerical simulation. For the experimentations an existing experimental bench developed by [Blanchet, 2015] has been used. Concerning numerical analysis there are some methods exists to simulate the cutting process. FEM method is well-known for cutting

simulations, and so FEM is chosen for current analysis. Some researchers (found in literature) have used SPH method too and argued that this method gives better result compare to FEM as it is a meshless method.

Regarding the microstructure development for CFRP in FEM machining two approaches have been implemented which are micro-mechanical and macro-mechanical approaches. The micro-mechanical describes the local material microstructure by two separate phases, fiber and epoxy, and introduces distinctive material properties. This approach gives better understanding of micro mechanics for fiber damage, failure, surface roughness, chip formation and separation etc. On the other hand, the macro-mechanical approach provides larger scale informations using homogenized microstructure with equivalent anisotropic properties. This approach has the limitations of homogenized methods in the case of CFRP machining but is capable of evaluating macroscopic data such as the cutting forces.

Having said that, this research in orthogonal technique not only will help to well understand the cutting physics in turning, external threading, grinding and filling but also bring up the phenomenon and physics of drilling and milling of CFRP.

I.II. Defects in CFRP Machining in Orthogonal Cutting

Composite laminates are regarded as hard-to-machine materials, which results in low cutting efficiency and undesirable delamination [Liu et al., 2012]. Most of the defects in CFRP machining are arising due to the multiple phase characteristics of this material. The high abrasive behavior of this material is mostly responsible for tool wear which not only affects the quality of the machined parts but also increases the manufacturing time and cost (cutting tools are expensive and changing tool because of wear is time consuming).

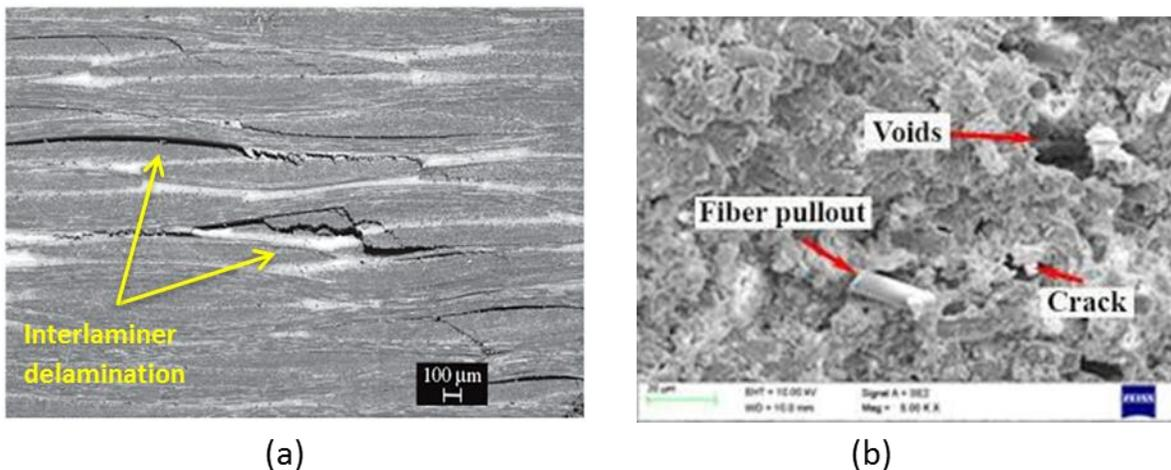


Fig. I.III: Generated defects in CFRP machining; (a) interlaminar delamination [Paiva et al., 2005] and (b) crack and voids [Vijayan et al., 2018]

According to [Haitao L. et al., 2019], machining damage occurs on the surface of CFRP composites during the processing. Some defects, mentioned in literatures, are: delamination, surface roughness, spring back, tool wear, crack generation and propagation, deformation of material, fiber crushing, surface burning, and scratching [Dref, 2014], [Guegan, 1994], [Konig and Gr ab, 1989], [Ghidossi, 2003], [Rahme, 2008], [Lazar and Xirouchakis, 2011], [Gaitonde et al. 2008], [Liu et al., 2008].

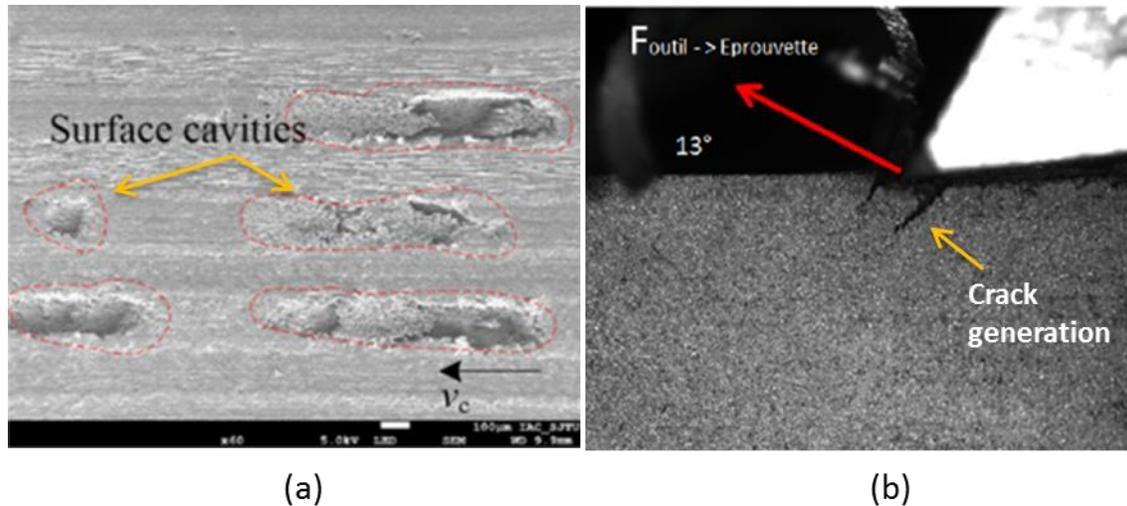


Fig. I.IV: Machining induced defects; (a) Surface cavities [Changying et al., 2016], (b) Crack generation [Blanchet, 2015]

Delamination can be of many types like pill up, push down, interlaminar etc. One of the most critical defects in CFRP machining is interlaminar delamination which is very difficult to identify. The main reason for interlaminar debonding between fiber and matrix is the high strength of fibers in comparison to the matrix one [Shchurov et al., 2016]. It may be possible to minimize the scale of most of the defects but might not be possible to resolve all absolutely.

I.III. Goals of the Research

In order to control the quality of machining in composite laminates and determine its influence on the mechanical behavior, it's necessary to better understand the cutting processes for these materials. The importance of these materials brought its cutting processes in the shade of research which is being focused more and more with time. Some remarkable research work on orthogonal cutting have been found through the literature study but many physical phenomenon, responsible for poor quality of machining, have remained unanswered.

[Blanchet, 2015] carried out a numerical and experimental study at the present laboratory focusing to the effect of different cutting speeds and positive and negative rake angles to the cutting efforts and surface roughness of machined parts. Nevertheless, a fundamental understanding of chip formation mechanism and the influences of some cutting variables are still untouched. The importance of understanding the influences of cutting variables in orthogonal cutting of CFRP is crucial because of their significant influences to the machining quality.

For this purpose in this research we will firstly analyze the strain field generation in the workpiece during cutting. Then we will focus on the stress-strain propagation and the fiber-matrix debonding phenomenon of the process. This analysis will give a fundamental understanding of the chip formation mechanism as well as a broad overview of the reason of surface roughness on newly generated cut surface.

[Nayak et al. 2005] and [Zitoune et al. 2005] mentioned that cutting depth affects the morphology of chip. If the morphology of chip is changed then the surface state of the newly generated surface as well as other relevant phenomenon will be affected too. So it is necessary to understand the influence of cutting depths. For this reason the effects of different cutting depths (from very low to high) to the cutting efforts, surface roughness, crack generation and propagation will be analyzed. Additionally, the generated chips' size and shape at different depths will be studied.

When the concern is cutting depth, a question becomes apparent which is: what is the minimum cuttable depth? The minimum cuttable depth in CFRP machining is more complex than metallic materials as CFRP are made with multiple phases and fiber orientation. Regarding this fact, an experimental study will be carried out in order to see what is the minimum depth a tool can cut at different fiber orientations of CFRP.

The issue of subsurface damage in the workpiece is an important concern. As the subsurface damages are not openly visible, it is difficult to identify those defects inside, including inter-laminar delamination. So in order to study the subsurface damages the test specimens will be brought under X-ray tomography. It is expected that tomography tests will reveal the potential subsurface damages which are generated during cut.

CFRP are highly abrasive which results in high tool wear. Tool wear affects the quality of the machined parts. On the other hand, changing tool counts high costs as cutting tools are expensive. In the literature no much research has been found on the mechanism of tool wear and how it can be minimized in CFRP machining. We will make a preliminary study on the tool wear phenomenon with respect to the length of cut with different fiber orientations, which will permit us to apprehend and predict the tool wear mechanism in CFRP machining.

In this research, both a model based on experimental observation and a unique approach to finite element machining model will be implemented to help interpreting of cutting mechanisms.

Chapter 1: State of the Art

The first chapter exposes the literature study in general. In favor of the discussions, this chapter has been organized in two parts. The first part talks about the research relevant technology, and the second part discusses the relevant literature findings which includes each cutting parameter, their influences on the cutting process, on the generated defects and the interrelation among themselves. At the end of the chapter, different numerical models for Carbon Fiber Reinforced Polymer (CFRP) machining have been shown.

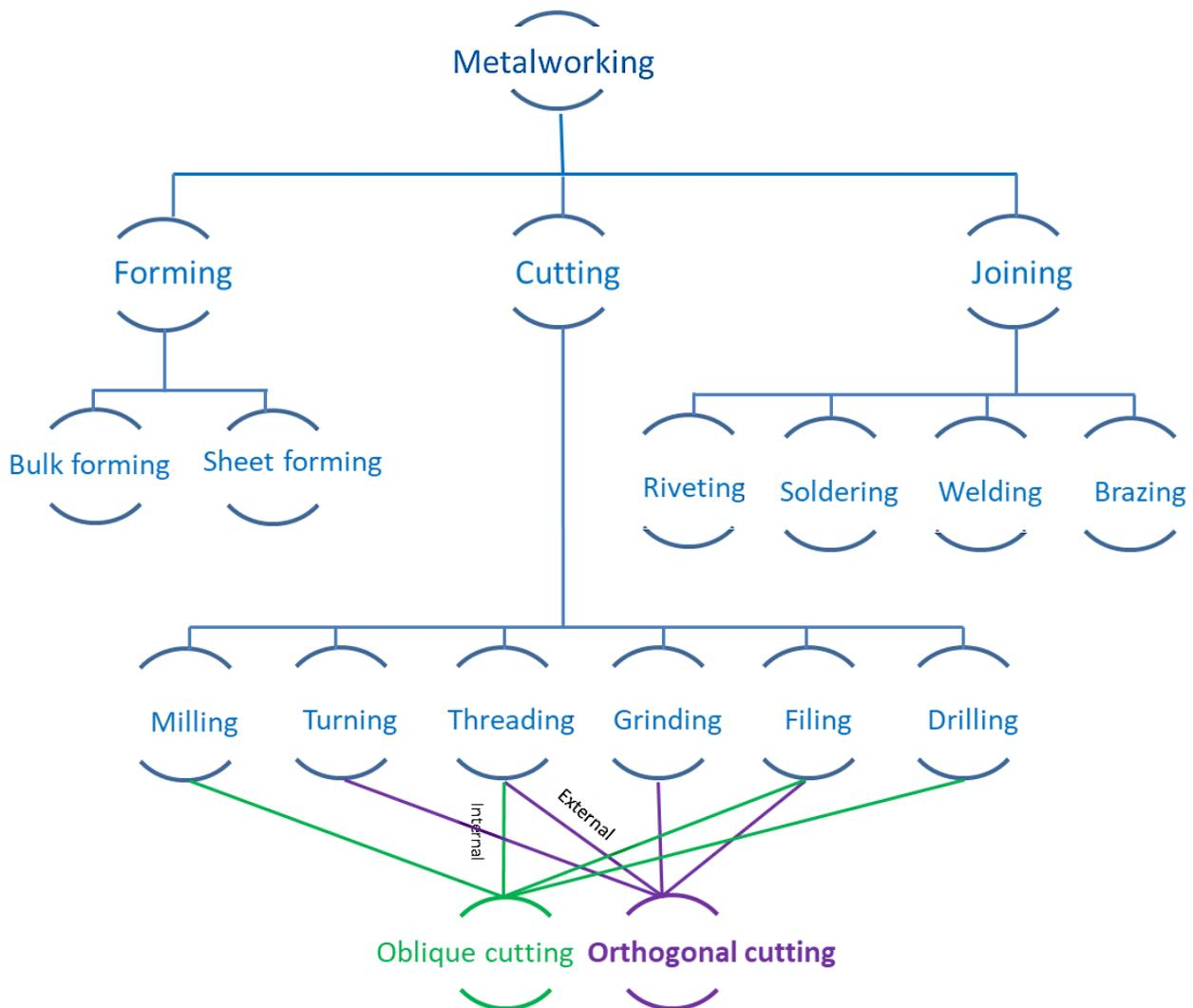
Content

1.1. Literature Review	21
1.1.1. Orthogonal Cutting in Machining	21
1.1.1.1. Mechanics of Orthogonal Cutting	22
1.1.2. Findings on Cutting Parameters and Generated Defects	25
1.1.2.1. Cutting Operation and Variables	25
1.1.2.2. Machining Induced Defects	41
1.1.3. Various Developed Models in CFRP Machining	47
1.1.3.1. Micro-mechanic Models	47
1.1.3.2. Macro-mechanic Models	59
1.1.3.3. Analytical Models	66
1.1.4. Summary of Literature Study	72
1.2. Conclusion	73

1.1. Literature Review

1.1.1. Orthogonal Cutting in Machining

Metal cutting processes are the essential processes throughout engineering design and manufacturing industries [Edward M. and Paul K., 2000]. In these processes a hard and sharp wedge-shaped cutting tool removes unwanted material from the surface of a softer workpiece by relative motion under interference. According to [Mahadevan, 2005], the tool causes a large strain in the work piece ($\epsilon > 1$) over a thin zone called the primary shear zone and results in the formation of a chip. The large deformation within the thin primary zone results high strain rates in between $10^3/s$ to $10^6/s$. The most common metalworking processes are shown in the Diag. 1.1.1.



Diag. 1.1.1: Most common metalworking processes

The major metalworking processes are forming, cutting and joining. Each of these types has subtypes; for example, cutting processes are milling, turning, threading, grinding, filing and drilling. According to the orientation of the tool edge, these processes lie in orthogonal or oblique technique.

1.1.1.1. Mechanics of Orthogonal Cutting

[Merchant, 1945a] defines the orthogonal cut as: "where the cutting tool generates a plane surface and parallel to the original planar surface of the machined material. This surface is machined with a cutting edge perpendicular to the direction of the relative displacement between the tool and the workpiece". A simplified geometrical representation of orthogonal cutting from [Zadshakoyan and Pourmostaghimi, 2013] has been shown in Fig. 1.1.1.

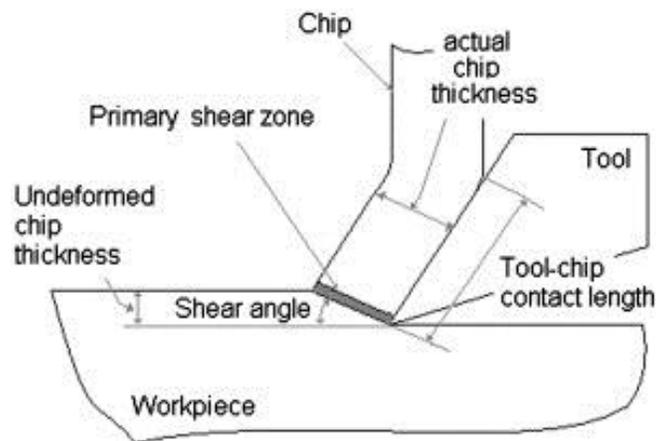


Fig. 1.1.1: Representation of orthogonal cutting [Zadshakoyan and Pourmostaghimi, 2013]

In orthogonal cutting the cutting edge and the fibers form an angle X_1 , whereas the angle between the cutting direction and the fibers form an angle X_2 ; defined by [Mckenzie, 1960], Fig. 1.1.2.

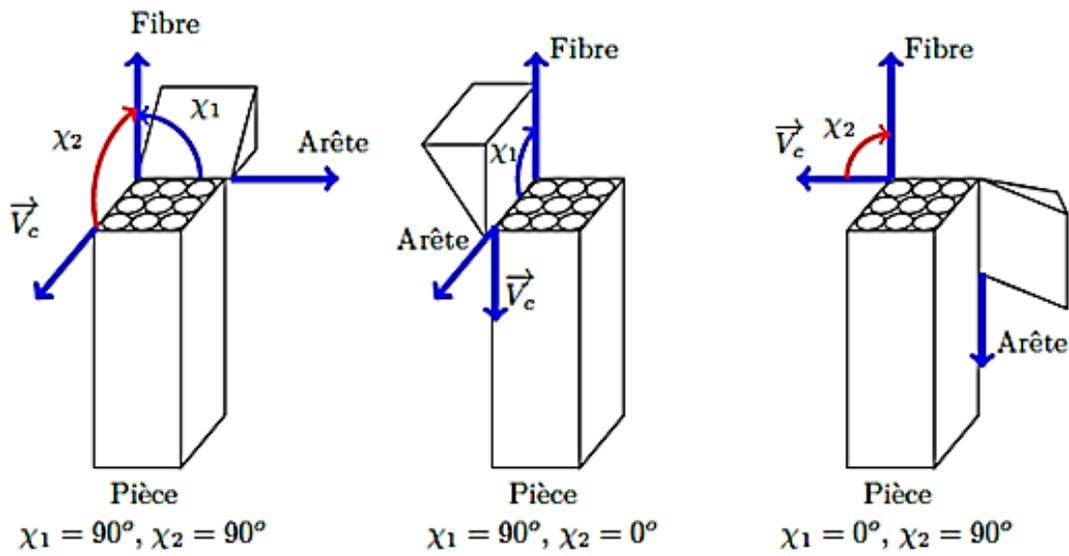


Fig. 1.1.2: Angles drawn by McKenzie [Mckenzie, 1960].

To facilitate the explanation of the cutting mechanisms, [Arola and Ramulu, 1997] defines two rupture paths presented in Fig. 1.1.3. A primary break occurs at the tip of the tool along the direction of the cutting speed. The stress distribution on the primary rupture zone is composed of compression and shear. A secondary rupture then occurs along the fiber / matrix interface from the primary crack to the free edge. It joins the primary break and the free edge.

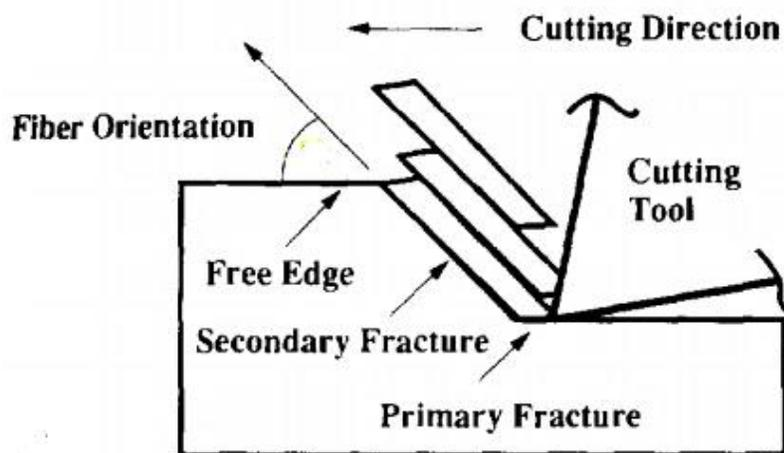


Fig. 1.1.3: Primary and secondary failure [Arola and Ramulu 1997].

Because of the two-dimensional configuration, orthogonal process is easier to model numerically than a three-dimensional (oblique) process. The different models that result from it allows for a better understanding of the phenomena present and give the possibility to simulate the mechanisms of formation of the chip, the induced forces and the surface states generated. In orthogonal cutting, all forces, motions, and deformations are in the plane formed by the cutting velocity vector and the direction normal to it [Ahmad, 2009]. To relate the forces encountered during cutting with the identified mechanisms, [Wang et al, 1995] defines them in a fiber-related reference frame where F_s is the component of the cutting forces in the direction of the fibers and N_s is the component of orthogonal cutting forces perpendicular to the fibers (Equ. 1.1.1 and 1.1.2). χ_2 denotes the angle between the fiber orientation and the cutting plane.

$$N_s = F_c \sin \chi_2 + F_p \cos \chi_2 \quad 1.1.1$$

$$F_s = F_c \cos \chi_2 - F_p \sin \chi_2 \quad 1.1.2$$

1.1.2. Findings on Cutting Parameters and Generated Defects

1.1.2.1. Cutting Operation and Variables

Chip Formation

Understanding the chip formation mechanism of composite materials is remained a vital part in research. There are some remarkable differences of mechanics of chip formation between metallic materials and composite materials whereas the case of composite materials remained left behind. The chip formation process of composite materials is affected by many process parameters. [Koplev et al., 1983] and [Blanchet, 2015] mentioned that chip formation process in machining FRPs is critically controlled by the fiber orientation and the cutting edge rake angle. [Alaiji et al., 2015] supported the theory of Koplev and added that it is a series of fractures observed in the fibers. Similar observations were later made by several authors [Rao et al., 2008] [Zitoune et al. 2005] [Blanchet, 2015]. There are four basic modes of failure that occur in a composite structure which are matrix cracking, fiber-matrix shearing, fiber failure, and delamination [Ilyas, 2010]. The damage of different components like fiber, matrix, and fiber matrix interface, simultaneously progresses until the complete chip formation process [Blanchet, 2015].

According to [Liu et al., 2012], bending-induced fracture occurs ahead of the cutting edge and perpendicular to the fiber direction. A small distinct chip segment is thus formed and the process repeats itself again. [Pramanik et al., 2007] said, numerically chip separation occurs when the strain value of the leading node is greater than or equal to a limiting value, noting that during the process of chip formation some reinforcements in the cutting region will go into the chip, some will be debonded or fractured and the rest will be on the machined surface. But contrary to the previous findings [Lasri et al., 2009] noted one recent finding that chip formation strongly depends on the microstructure in regard to the local damage caused by the tool cutting edge. They explained the whole process saying fiber–matrix deboning is the first failure developed in composite structure during the cutting process. It initiates near the cutting tool edge and is accompanied with the matrix cracking at different stage of chip formation progression whereas the fiber breaking is the last failure mode occurs in the chip formation process. [Arola et al., 2002] did post-process visual observations of macrochips during the edge trimming process and found that unlike metals, material removal in the machining of FRPs consists of a series of brittle fractures, each resulting in a discrete chip. The process is comprised of “primary fracture”, consisting predominantly of fiber failure, and “secondary fracture,” that occurs through matrix failure which is clearly agree with [Alaiji et al., 2015].

At the same time they made a table of the required displacement of tool to form chip with different fiber orientation which has been shown on the Table 1.1.1.

Orientation	0°	15°	30°	45°	60°	75°	90°
δ (μm)	n/a	3.5	4.2	4.3	6.7	7.7	20.2
δ (μm)	n/a	85	60	55	40	30	25

Table 1.1.1: Tool displacement required for chip formation [Arola et al., 2002].

One interesting finding by [Lasri et al., 2009] is that they compared the chip thickness with fiber orientation and then compared the results with the experimental measurements with [Nayak et al. 2005], (Fig. 1.1.4). The chip thickness decreases with increasing the fiber orientation which means there is a strong correlation between the chip formation process and the fiber orientation.

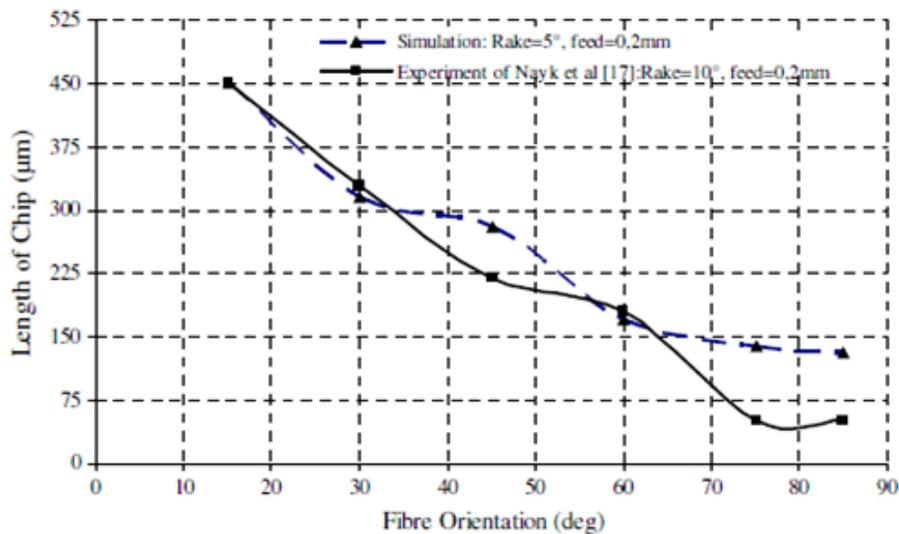


Fig. 1.1.4: Chip thickness with respect to the fiber orientation and comparison with the measured values which obtained by [Nayak et al. 2005].

This research was carried out with 5° rake angle and 0.2 mm/s feed rate. The Experimental results of [Nayak et al. 2005] were almost similar indeed a little difference towards 70° to 85° fiber orientation. Regardless of the fiber angle or tool angle there are four different types of chips that have been mentioned in the literatures namely continuous chip, discontinuous chip, continuous chip with build-up edge and serrated chips.

Cutting and Thrust Force

In orthogonal cutting, the total force F is conveniently resolved into two components, the horizontal direction and the vertical direction. The cutting force takes place in the direction of primary motion (motion of the tool) and the thrust force takes place in the direction of feed motion (vertical). The forces have been shown in the Fig. 1.1.5.

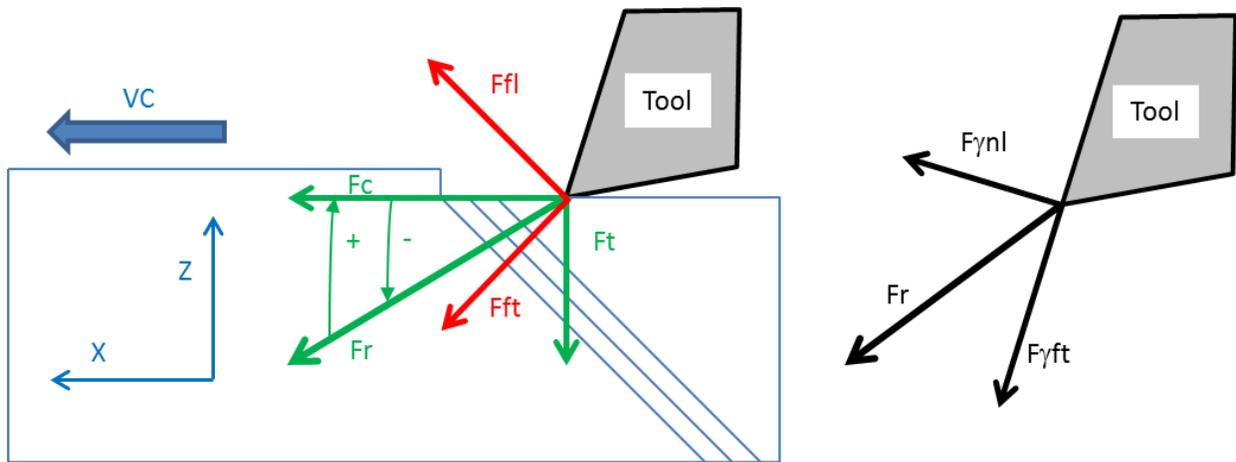


Fig. 1.1.5: Determination of cutting and thrust forces [Blanchet, 2015].

In case of polymers and composites cutting, elastic deformation plays a significant role in determining the cutting force, especially in the tertiary deformation zone. A high degree of fluctuation in the cutting forces is exhibited when machining FRP. Several analytical models [Zhang et al., 2001] [Jahromi and Bahr, 2010] [Bhatnagar et al., 1995] have been found for predicting the forces. [Blanchet, 2015] analyzed the resultant force of F_c and F_t along the fiber direction with respect to the fiber orientations.

There are many parameters which affect these forces. [Wang and Zhang, 2003] and [Alaiji et al., 2015] both mentioned that the machining forces are strongly dependent on the angle X_2 , which influences the component of the normal force but Alaiji added it is less influenced by the rake angle. The edge acute radius plays an important role on the efforts observed insofar as it is responsible for the elastic spring back, which, according to [Caprino et al., 1998] and [Caprino and Santo, 1998], generates a non-negligible effort with respect to the cutting and thrust forces. The fluctuation of cutting and thrust forces according to fiber orientation has been shown in Fig. 1.1.6.

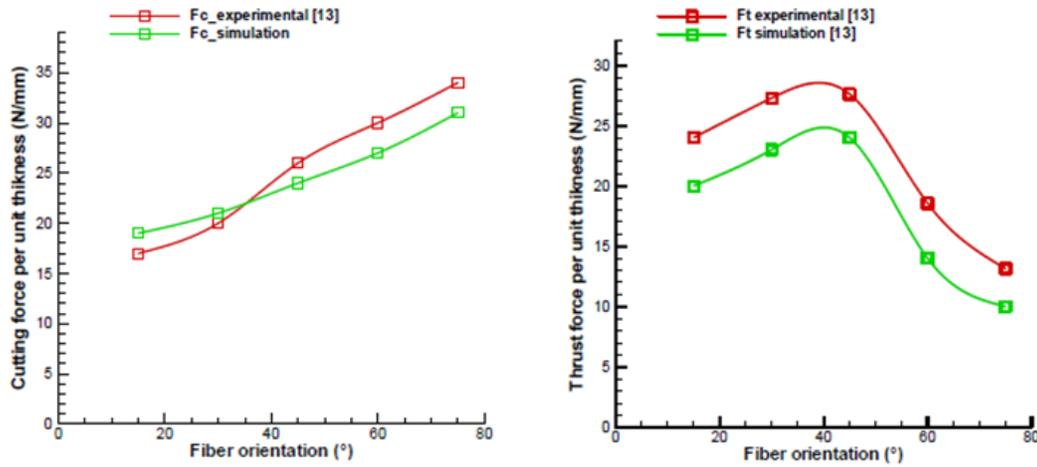


Fig. 1.1.6: Variation of machining forces with respect to the fiber orientation (a) cutting force, (b) thrust force. The cutting conditions are $\alpha=10^\circ$, $\gamma=6^\circ$, $a_p=200\ \mu\text{m}$, $r_\epsilon=50\ \mu\text{m}$ [Alaiji et al., 2015].

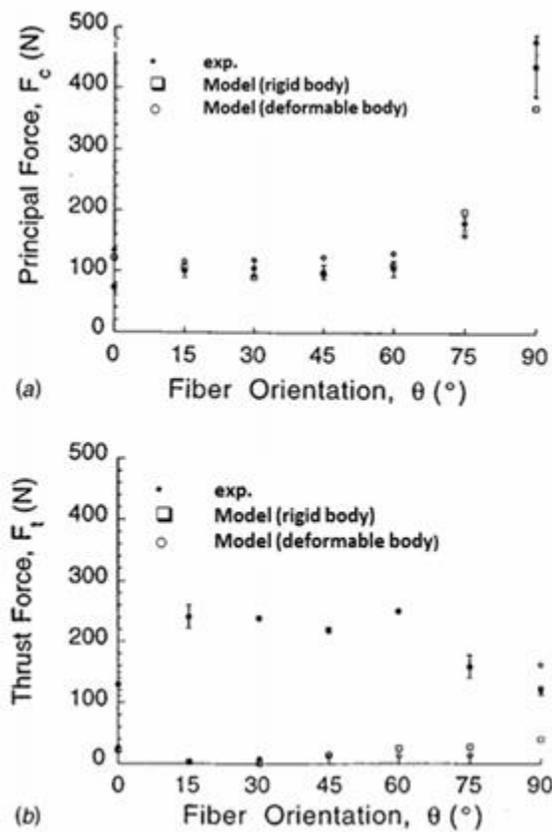


Fig. 1.1.7: Cutting force history resulting from trimming of unidirectional Gr/Ep with a $10^\circ \alpha / 17^\circ \gamma$ cutting tool (a) 60° unidirectional Gr/Ep (b) 90° unidirectional Gr/Ep [Arola et al., 2002].

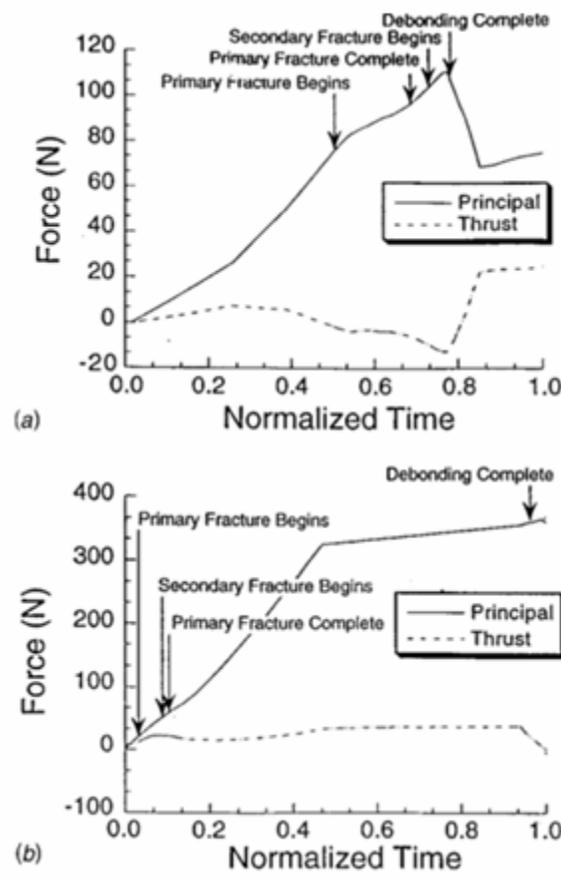


Fig. 1.1.8: Verification of the numerical model with experimental results for orthogonal cutting of Gr/Ep ($\alpha=10^\circ$, $\gamma=17^\circ$) (a) principal cutting force (b) thrust force [Arola et al., 2002].

In Fig. 1.1.6, it is clear that the cutting force increases with increasing the fiber orientation both numerically and experimentally whereas the thrust force increases up to around 45° and then decreases ([Calzada et al. 2012] found the forces are highest at $X_2=45^\circ$ and [S. Zenia et al. 2015] found at 90°). But [Arola et al., 2002] found, in Figs. 1.1.7. and 1.1.8, the cutting force does not increase remarkably until 60° fiber orientation which is not akin with the previous authors. On the other hand, the thrust force remains almost the same until 60° fiber angle and decreases subsequently. [Wang and Zhang, 2003] performs orthogonal cutting tests where he varies the angle of cut from -20° to $+40^\circ$ and the angle X_2 from 0° to 150° with 30° increment. Fig. 1.1.9, illustrates the collinear forces at different rake angles; (Fig 1.1.9-a) cutting force and (Fig 1.1.9-b) thrust force.

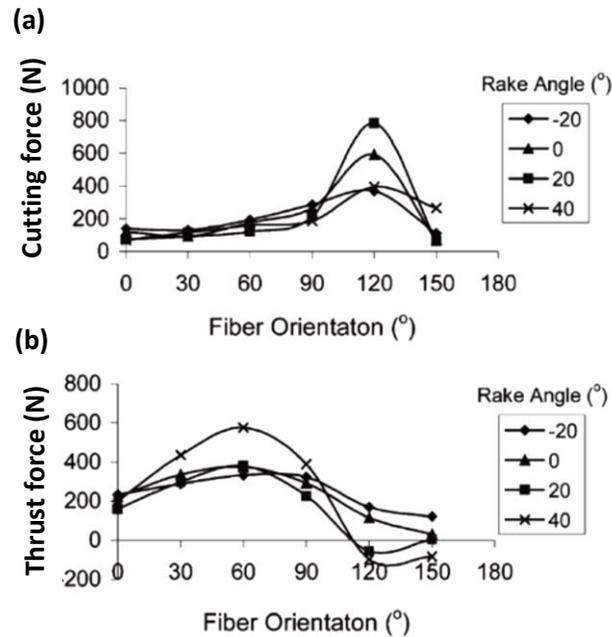


Fig. 1.1.9: Cutting forces as a function of X_2 : (a) Cutting force (b) Thrust force [Wang and Zhang, 2003].

A strong increase in cutting force is observed between 90° and 150°. For a cutting angle greater than 20° the diving force becomes negative from 120° which means that the tool pulls the chip towards outside of the specimen. On the other hand, [Lasri et al., 2009] and [Ghidossi et al., 2003] are not agree totally with Alaiji and Arola. They said that the minimum cutting force occurs in the fiber orientation at 30° for the three criteria and they continued that the thrust force strongly depends on the bouncing back (spring back) phenomenon. Due to this phenomenon, the real and nominal depths of cut are very different. This situation happens when a part of the material in the cutting direction is pushed down during cutting but elastic spring back (partially) happens after the tool passed away. Consequently, the spring back contributes to the generation of the cutting forces [Caprino et al., 1998]. The direct dependence of principal cutting force on the spring back is not important. However, this effect strongly influences the experienced thrust force.

Different angles of cutting tool position play role to the cutting force. [Arola et al., (2002)] mentioned some values of the angles for some definite parameters:

- The best tool geometry for minimizing cutting forces has been found to consist of a 15° rake angle.
- To minimize subsurface damage, a 10° rake angle tool was found to be optimum.
- The minimum stress in the tool nose has been achieved with a 5° rake angle.
- The minimum cutting force occurred in the trimming of 30° unidirectional materials.

- The largest deviation between the numerical cutting force and experimental values occurred in simulations for edge trimming at 0° fiber orientation.

Cutting Tool

Cutting tool plays an important role in all metal cutting processes. Proper materials for tool and an optimum tool design should not only provide a high surface quality, but also minimize tool wear. (Abrão et al., 2008) and [Iliescu et al., 2010] reported that the material of the tool plays an important role in its life duration, such as extending tool life and delamination reduction. Most common materials for tools are: high speed steel, cemented carbide and diamond coated carbides. [Lazar and Xirouchakis, 2011] used solid carbide steels with small grain size (micro-grain) while [Arola et al., 2002] emphasized on Polycrystalline diamond (PCD) and Tungsten Carbide (WC).

Regarding the tool rake angle [Arola et al., 2002] mentioned that the tool rake angle has limited influence on cutting forces for all orientations other than $\alpha=50^\circ$ and 90° . But the tool geometry does affect the degree of subsurface damage resulting from interlaminar shear failure as well as the cutting tool stress distribution. In the same literature, the stress distribution on the cutting tool is shown which gives a comprehensive understanding of stress intensified areas as in Fig. 1.1.10.

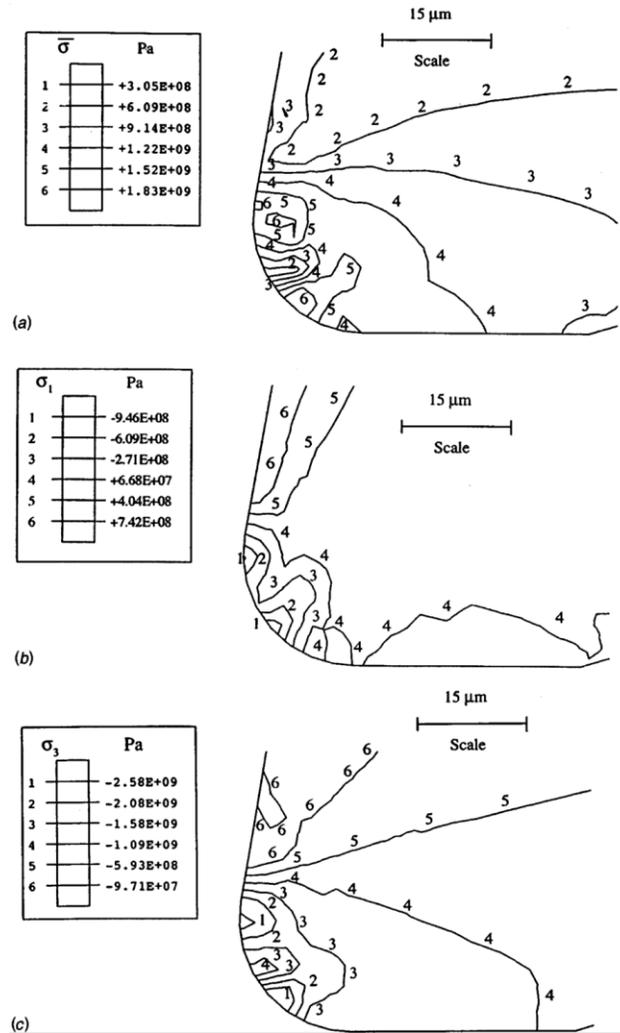


Fig. 1.1.10: The stress distribution at the nose of a $\alpha = 17^\circ$ cutting tool resulting from trimming 75° unidirectional Gr/Ep. (a) effective stress distribution (b) maximum principal stress distribution (c) maximum compressive stress distribution [Arola et al., 2002].

In figure (Fig. 1.1.10) it is clear that the location of maximum principal stress is always found to be near the tool rake face region (Fig. 1.1.10-a). The maximum effective stress is identified in the region as in (Fig. 1.1.10-b) and the maximum normal compressive stress is found to occur in the region (Fig. 1.1.10-c).

Cutting Speed

In orthogonal cutting a diverse range of cutting speed has been tested in research. [Abena et al., 2017] used 0.5 m/min in his numerical and experimental work. [Blanchet, 2015] used 0.5 m/min to 120 m/min to analyzed the surface quality of machined surface. [Klinkova et al. 2011]

reported a range of speed mentioning that usually 10 m/min to 40 m/min speed is applied during machining of CFRP. The influence of cutting speed to other parameters have been studied by [Soussia, 2014] and [Iliescu, 2008], (Fig. 1.1.11).

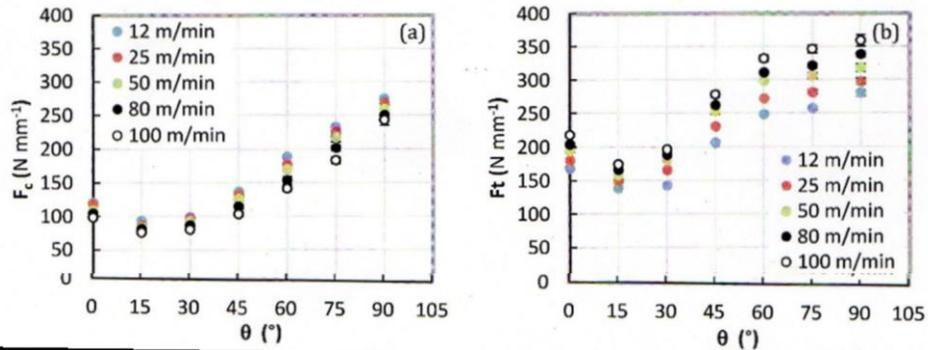


Fig. 1.1.11: Influence of cutting speed on (a) cutting force, (b) thrust forces [Soussia, 2014].

Soussia observed that for the values of X_2 between 0° and 90° , the cutting speed tends to increase the thrust force and reduce the cutting force. The values concern cutting speeds between $V_c = 12$ m/min to 100 m/min. However, since these variations are relatively small and the objective of their work is not to study the effect of speed, it would be reasonable to ignore these effects. On the other hand, from a trimming arrangement [Turki et al. 2011] analyzed the cutting forces as a function of cutting speed (Fig. 1.1.12).

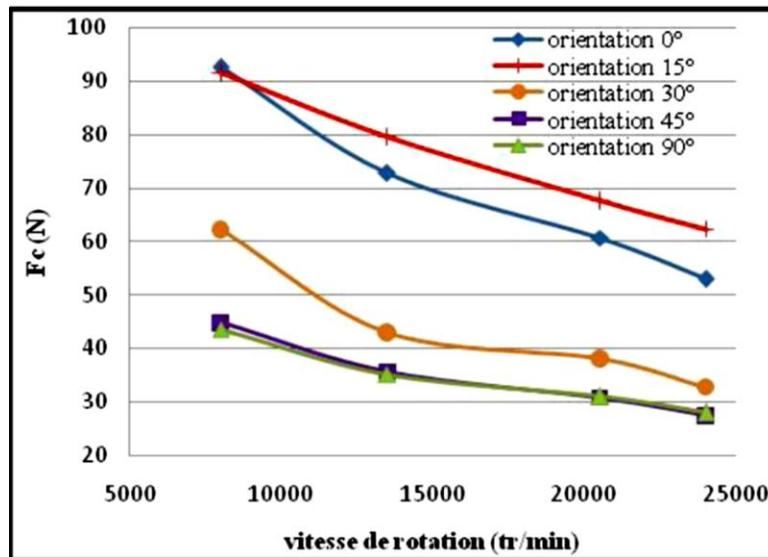


Fig. 1.1.12: Variation of cutting forces as a function of cutting speed in trimming tests [Turki et al. 2011].

They found that an increase in the cutting speed tends to reduce the cutting forces. So it can be noted that the cutting speed has a significant influence on the forces.

Depth of Cut

Cutting depth is an important parameter in machining. Many researchers mentioned its importance but any specific quantitative proposition regarding the cutting depth has not been found. [Blanchet, 2015] used 0.1 mm cutting depth in his experimentation. [Nayak et al. 2005] used 0.2 mm in his model to compare the chip thickness with respect to the fiber orientation, whereas [Zitoune et al. 2005] varied the depth of cut during orthogonal cutting considering 0.05 mm as representative cutting depth for drilling. They observe that the depth of cut affects the morphology of the chip and further added that for a depth of cut $a_p = 0.07$ mm, a continuous chip is formed and the chip is ejected at the end of the pass; for $a_p = 0.125$ mm, a very friable chip is formed which breaks before the end of cut; and for $a_p > 2$ mm, no chip is observed but fine particles are projected. In orthogonal cutting of CFRP it is not possible to conclude any unique cutting depth for the best quality as other parameters, eg: fiber orientation, cutting speed etc., play important role too. However, cutting depth influence is still a subject of interest for future research.

Feed Rate (associate with drilling)

Feed rate is seen to make the largest contribution to delamination, thrust force and tool wear during machining of composite laminate. According to [Rahman et al., 1999] feed rate combined with depth of cut and cutting speed influence to the fluctuation of tool wear, the surface finish and the cutting force. Generally, the use of low feed rate and high cutting speed favor minimum reduction of the machining-induced delamination, more specially interface delamination [Xu et al., 2016], and extend tool life [Liu et al., 2012]. At low feed rates, the load concentration seems to occur on the chisel edge [Lazar and Xirouchakis, 2011]. However, as the feed rate increases, the loads on the first part of the cutting lip increase more rapidly, becoming the critical area. It should be noted that feed is referred to drilling and it is not a parameter of orthogonal cutting. However, the greater study of machining induced defects draws the drilling parameters into discussion.

Rake and Clearance Angle

In orthogonal cutting the rake angle refers to the rake surface inclined angle from the vertical line and the clearance angle refers to the angle between the bottom surface of the tool and the generated surface of the workpiece. Rake angle determines the direction that the chip follows and the clearance angle provides a small clearance between tool flank and newly generated work surface [Khuzdar, 2013]. A positive rake angle will tend to propagate a crack along the fiber/matrix interface upstream of the tool, while a negative cutting angle will tend to make the

chip flame as said by [Wang et al., 1995] and [Arola et al., 1996]. Cutting parallel to the fibers with a high positive rake angle produces chips by delamination and brittle fracture (peel fracture) but in this condition the continuous chip is formed; the transition to smaller positive rake angles favors the formation of discontinuous chips while cutting with zero and negative rake tools produce chips by buckling of fibers perpendicular to fiber orientation by compression. A wide range of qualitative findings regarding these two angles have been found. A few particular rake angles 0° , 5° , 10° and 15° with clearance angles 7° and 17° were used by [Arola et al., 2000] for a factorial analysis. They have found that an increasing rake angle decreases the effective cross sectional area of the tool and results in higher contact stress due to a reduction in contact area. An increase in rake angle also causes a decrease in the cutting force. A 5° rake angle has been suggested by them to minimize the tool wear.

Fiber Orientation

In orthogonal cutting of fiber composite laminates, the angle X_2 between the cutting direction and the direction of the fibers is an additional parameter which can be referred to the orientation of fibers. Different work from the literature focused on the influence of this angle on cut in terms of phenomenology, surface damage and stresses generated during cutting. Elementary cutting tests were conducted with remarkable values of angle X_2 ; the latter being constant during an orthogonal cutting test. Most authors considered the angles for X_2 are 0° , 45° , 90° and 135° (-45°). The first orthogonal sectional CFRP study dates back to [Koplev et al., 1983] which carried out orthogonal cutting tests for an angle $X_2 = 0^\circ$. The CFRP cutting mechanism consists in a series of shavings that create chips. These chips are rarely continuous. In order to observe their shape, Koplev places a thin layer of rubber-based adhesive on the original surface, which allows the chips to be bonded together to form a macro chip. Fiber orientations play an important role on the degree of plastic deformation of the matrix [Pramanik et al., 2007] and may influence friction at the tool / CFRP interface [Klinkova et al. 2011].

[Arola et al., 1996] and [Wang et al., 1995] explained that the cutting angle affects the cutting mechanisms when $\theta (X_2) = 0^\circ$ (Fig. 1.1.13). If the cutting angle is negative, the chip will be formed by buckling; if it is positive the chip will be formed by bending and crack propagation along the fiber-matrix interface. With the displacement of the tool this crack propagates. The chip is then subjected to a bending load. Wang also performs abruptly interrupted tests with $X_2 = 45^\circ$. The author observes that in the area in contact with the edge, the fibers are crushed in compression by the tool. In addition, the flow plane of the oriented chip along the matrix fiber interface is observed. This surface is highly grooved, which, according to the author, is characteristic of a fragile fracture.

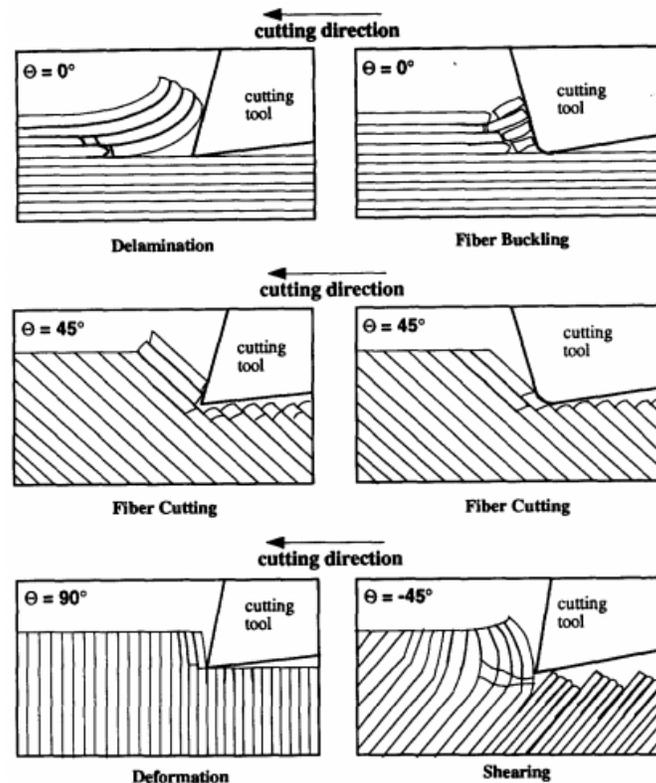


Fig. 1.1.13: Formation of chip with respect to different fiber orientations [Wang et al., 1995].

In the case where $\theta (X_2) = 45^\circ$ (Fig. 1.1.13) the chip is formed by shearing in the fiber-matrix interface, fiber breakage is consecutive and this angle gives rough surface together with crack propagation along the fiber-matrix interface. At the angle $X_2 = 45^\circ$ [Zitouné et al. 2005] varies the depth of cut and found that it affects the morphology of the chip. Note that the tool displacement, required for chip formation in the numerical simulations, increases with increasing fiber orientation. Changes in the tool rake or clearance angles do not influence the required displacement [Arola et al., 2002]. Differently, [Koplev and Bunsell, 1980] observed the fracture of laminates and the surface generated at $X_2=90^\circ$ and concluded that the tool presses the CFRP until a crack appears along the fiber / matrix interface and creates a chip. At the same time, cracks propagate obliquely to a depth of 0.1 to 0.3 mm. The surface quality is poor compared to that obtained for $X_2 = 0^\circ$. But according to [Wang et al., 1995], at $X_2 = 90^\circ$, fractures occur at the fiber / matrix interface by shear in the plane but also out of plane. The fibers are then sheared perpendicularly to their direction. Fig. 1.1.14, shows the plate of the orthogonal cutting of a test piece with $X_2 = 90^\circ$. Macro-cracks generated by machining are easily observed.

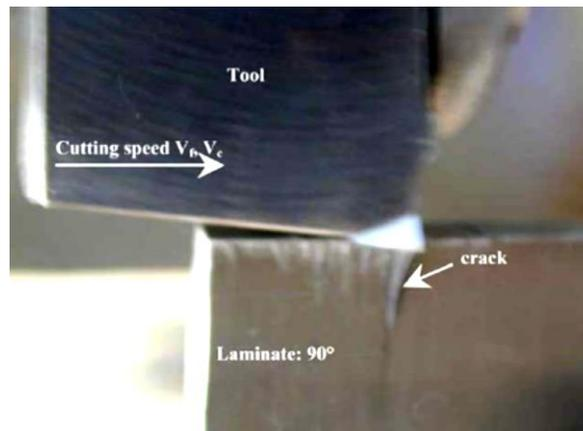


Fig. 1.1.14: Cutting mechanisms for $X_2 = 90^\circ$ [Zitoun et al. 2005].

The cracks along the fiber / matrix interface are longer at $X_2 = 135^\circ$ than $X_2 = 90^\circ$ (Fig. 1.1.14). The process is more difficult to observe in this configuration since the specimen is quickly destroyed by the planing operation [Zitoun et al. 2005]. Cracks are easily observed along the fiber / matrix interface. In the same way as for $X_2 = 90^\circ$, very little literature study the influence of the cutting angle on the cutting mechanisms in the case where $X_2 = 135^\circ$. Some findings about the influence of fiber orientation to subsurface damage have been shown in Fig. 1.1.15 & 1.1.16 [Alajji et al., 2015] [Lasri et al., 2009].

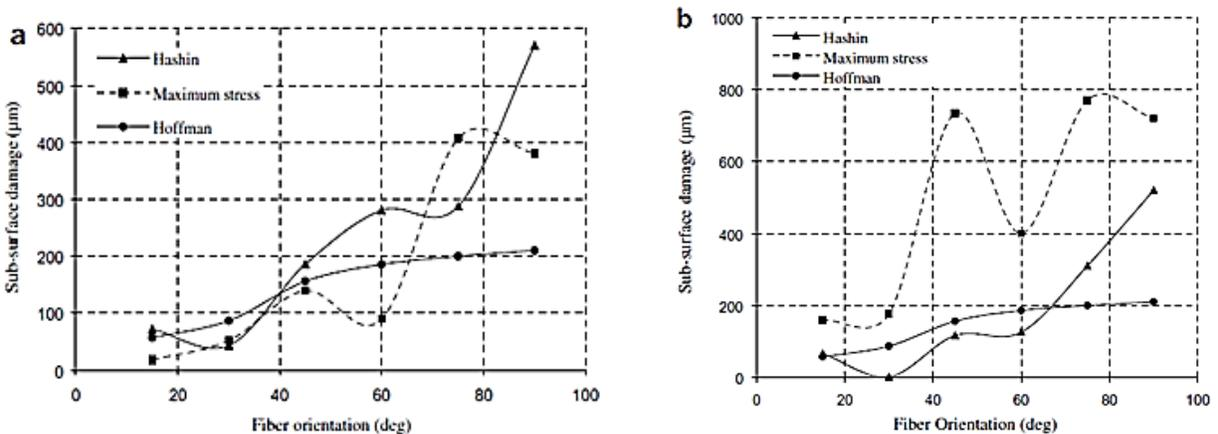


Fig. 1.1.15: Variation of sub-surface damage with respect to the fiber orientation (a) damage in matrix, (b) fiber-matrix debonding; comparison between values calculated with different criteria: Hashin, Maximum Stress and Hoffman [Lasri et al., 2009].

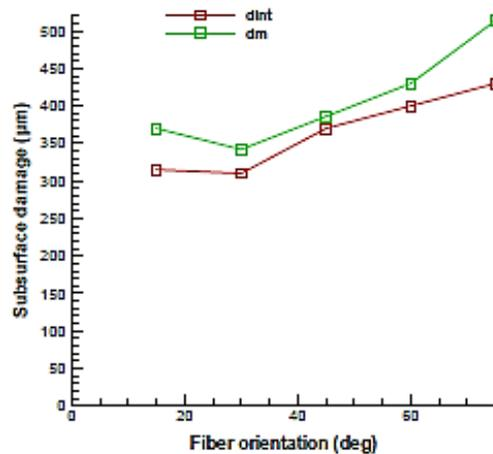


Fig. 1.1.16: Variation of subsurface damage with respect to the fiber orientation. ***Dint*** and ***dm*** indicate damage in matrix and damage in interface, respectively. The cutting conditions are $\alpha=10^\circ$, $\gamma=6^\circ$, $\alpha_p=200\ \mu\text{m}$, $r\epsilon=50\ \mu\text{m}$ with Hashin failure criterion [Alajji et al., 2015]

Fig. 1.1.15 shows a comparison of subsurface damage with different models, e.g.: Hashin, Maximum stress and Hoffman whereas Fig. 1.1.16 shows the results by Hashin failure criterion. It is clearly visible in both of the Fig. 1.1.15 & 1.1.16 that the subsurface damage increases with increasing the fiber orientation. It seems that the Hashin's model gives high surface damage values than other two models. According to the Fig. 1.1.15 and 1.1.16 it is possible to come to some points that:

- Whatever the model is, the subsurface damage increases if the degree of fiber orientation increases.
- The results which are found by different authors are not the same even though the models' criteria are same. On the other hand, different models give dissimilar results.

The cutting forces vary with fiber orientation. [Lasri et al., 2009] compared the cutting force result with fiber orientation using different failure models, Fig. 1.1.17.

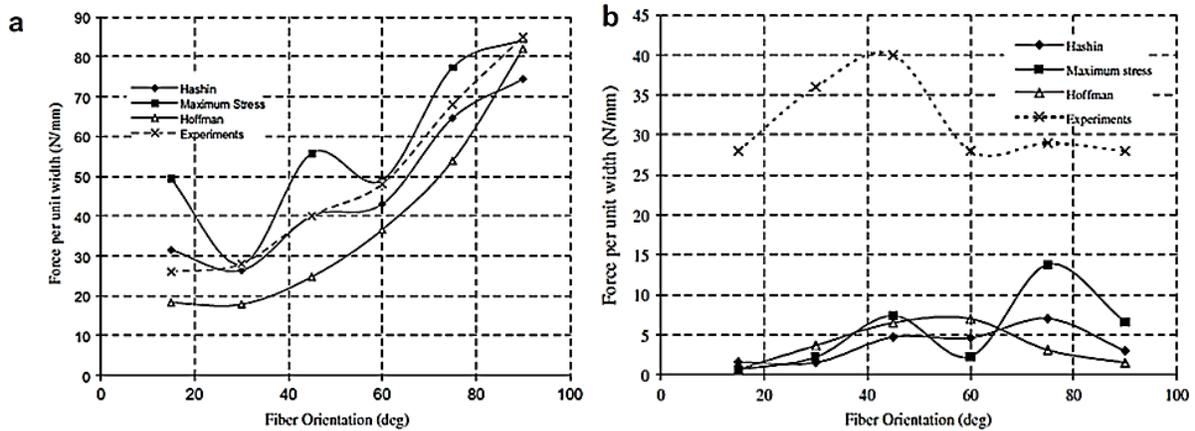


Fig. 1.1.17: Evolution of cutting forces with respect to the fiber orientation θ (X_2) (comparison between experimental and simulated values), (a) principal cutting force (b) thrust cutting force. The experimental results are provided from the work of [Bhatnagar et al. 1995].

The principal cutting force increases with increasing the fiber orientation for all of the models (Fig. 1.1.17 (a)) and it seems that the experimental values confirm the numerical values of the models. The thrust force and its evolution is low compare to principal cutting force but the experimental values do not support the numerical values (the experimental values were extracted from [Bhatnagar et al. 1995]).

Multidirectional Laminates Cutting

[Arola et al., 1996] carried out tests on stratified specimens having layer of 0° , 90° , 45° , and 135° . They explain that during cutting these types of laminates, each ply behaves independently. However, the off-plane bending generally present for orientations $X_2 > 90^\circ$ is suppressed by the adjacent plies. The (Fig. 1.1.18) from [Iliescu, 2008] shows visually the machined surfaces of multidirectional specimens.

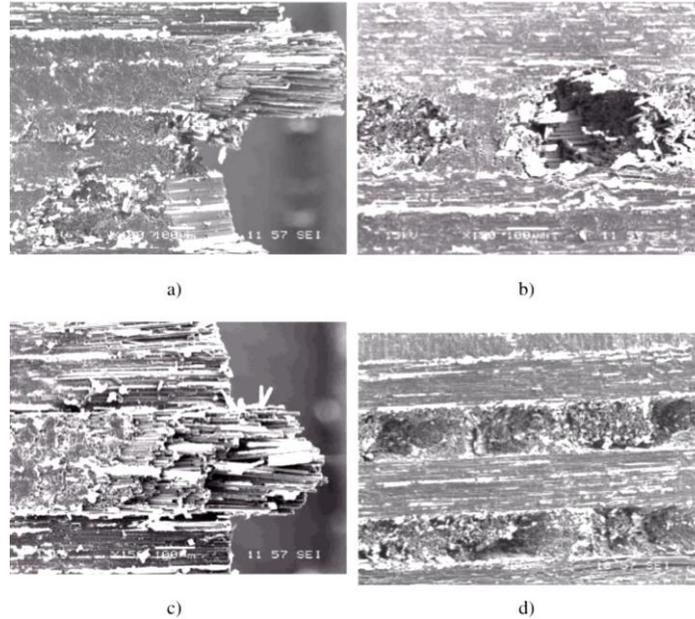


Fig. 1.1.18: Damage of multi-directional specimen with H13A tool for $V_c = 60$ m/min, $f = 0.2$ mm: a) interface $45^\circ/90^\circ/135^\circ$ for $\gamma = 15^\circ$; b) interface $0^\circ/135^\circ/0^\circ$ for $\gamma = 15^\circ$; c) interface $0^\circ/45^\circ/0^\circ$ for $\gamma = 15^\circ$; d) interface $0^\circ/135^\circ/0^\circ/135^\circ$ for $\gamma = 30^\circ$ [Iliescu, 2008].

There is clear difference on the surfaces among the different folds having distinct fiber orientation values. It also appears that the surface state of the folds at 135° fiber orientation is improved with respect to the surface condition of an unidirectional specimen at $X_2 = 135^\circ$ machined under the same conditions (Fig. 1.1.19).



Fig. 1.1.19: Damage to specimens with tool H13A ($X_2 = 1350$) [Iliescu, 2008].

It is thus observed that the folds at $X_2 = 135^\circ$ have a behavior during cutting which is influenced by the adjacent plies.

1.1.2.2. Machining Induced Defects

Crack Generation and Propagation

A strong influence of fiber orientation to the direction of crack generation and propagation in composite laminates has been found by [Blanchet, 2015], indeed cutting tool angle also plays role behind it. [Pramanik et al., 2007] reported that cracks are generated due to debonding of particles (case of glass-fiber and matrix debonding) in front of tool whereas [Shchurova et al., 2016] said the main reason for this fact is the high strength of fibers in comparison with the matrix one. These are the general reasons. To understand this physics in details, it can be reasoning to focus more on the damage mechanism of composite laminates. According to [Lasri et al., 2009], damage mechanisms in composite laminates include four types of failure modes: transverse matrix cracking, fiber– matrix interface debonding, fiber rupture and inter-ply delamination. They carried out simulations with different stress criteria and found that in cases of Hashin and Maximum stress criteria (Fig. 1.1.20-a and 1.1.20-b), fiber–matrix interface debonding is the first damage developed in the composite structure during the chip formation process. Matrix failure starts and progress in the same way as fiber–matrix interface failure before complete debonding, then continue to propagate in depth until completion of the chip formation. But in case of Maximum stress criterion, (Fig. 1.1.20-b), matrix failure initiates late and then gradually progresses in the vicinity of the cutting tool edge. The fiber breaking is the last failure occurring during the chip formation process in both Hashin and Maximum stress criteria.

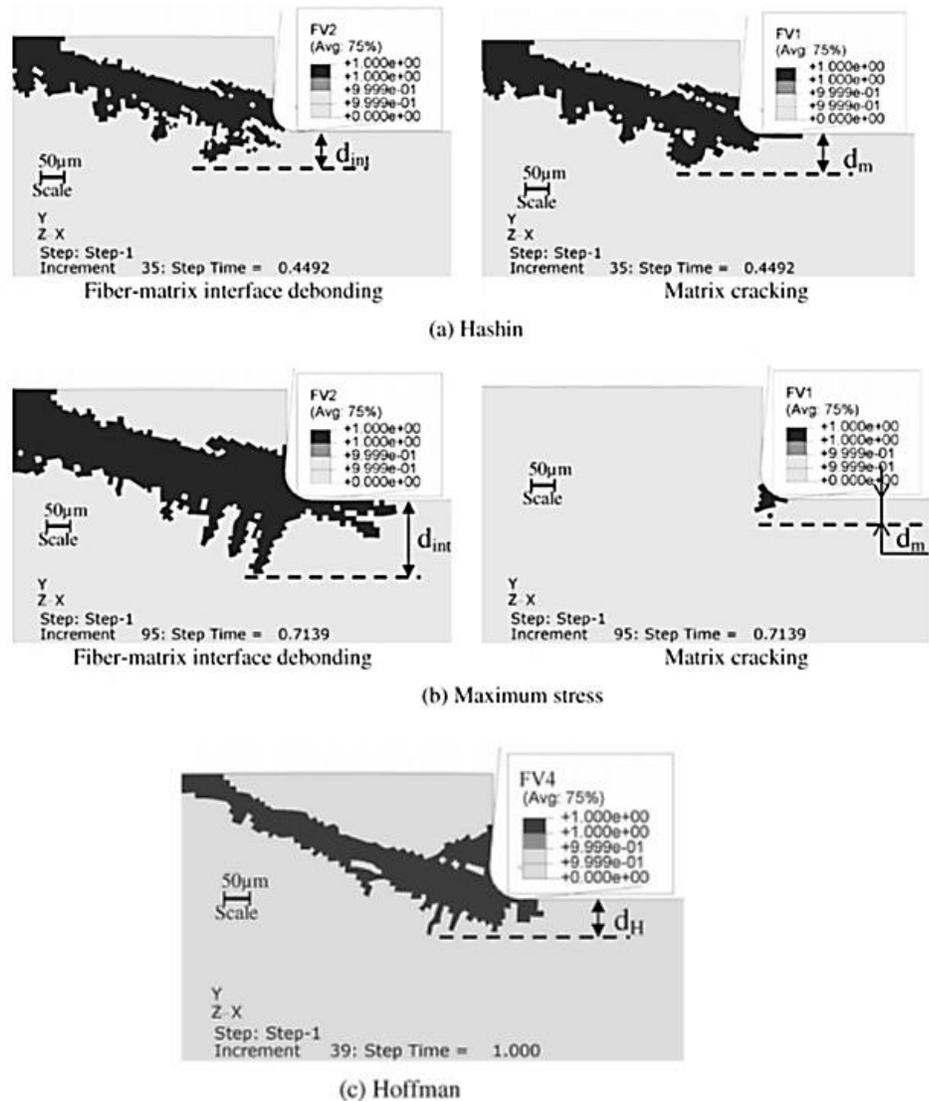


Fig. 1.1.20: Crack generation and propagation with different stress models [Lasri et al., 2009].

According to these findings it can be said that transverse failure can occur without breaking the longitudinal fibers. Such failures, occurring parallel to the fibers may take place during machining and leads to the stiffness degradation.

Delamination

Delamination is an inter-ply failure phenomenon which is a highly undesirable problem and has been recognized as a major damage encountered when machining composite laminates [Liu et al., 2012]. In laminated materials, repeated cyclic stresses, impact, and so on can cause layers

to separate, forming a mica-like structure of separate layers, with significant loss of mechanical toughness which can lead to failure in use [Lazar and Xirouchakis, 2011]. [Lachaud et al., 2001] and [Piquet et al., 2000] discussed delamination in terms of drilling and found that the major delamination is generated during the entrance and exit of the tool into the workpiece which can be the same case for orthogonal cutting. The initial delamination is propagated with the advance of the tool [Rahme, 2008]. Delamination is not usually visually detectable and a special inspection process is necessary. There are some instruments which can be used to observe the delamination which are: optical microscope, stereomicroscope, ultrasonic C-scan, digital photography technique, shadow moiré laser based imaging technique and X-ray computerized tomography (CT).

It was reported that, in aircraft industry, the rejection of parts consist of composite laminates due to drilling- induced delamination damages during final assembly was as high as 60% [Liu et al., 2012]. Throughout the literature study there are many theoretical suggestions found on how to reduce the delamination indeed the experimental validations were limited. High speed cutting is one of the promising technologies for reducing delamination which is mentioned by [Gaitonde et al. 2008] and they further explained that the delamination tendency decrease with increase in cutting speed and the combination of low feed rate and point angle are also essential in minimizing delamination during high speed cutting of composite laminates. It is believed that there is a critical thrust force below which no delamination appears [Hocheng and Tsao, 2005] and to avoid this delamination the thrust force applied to work-piece should not exceed the critical thrust force [Liu et al., 2012].

Spring Back

The edge radius of cutting tool plays an important role on the spring back phenomenon. Spring back generates a significant proportion of the diving effort which is supported by [Arola et al., 2002] and they added that it contributes to the thrust force component of cutting. An extended explanation for this phenomenon has been given by [Wang and Zhang, 2003] which explains that when the tool cuts the material, a part of the cut material is elastically deformed when pressed under the tool. When the cutting operation is completed, a bouncing-back of the uncut material is observed. The actual feed depth is thus different (lower) from the nominal pass depth. (Fig. 1.1.21) illustrates this phenomenon.

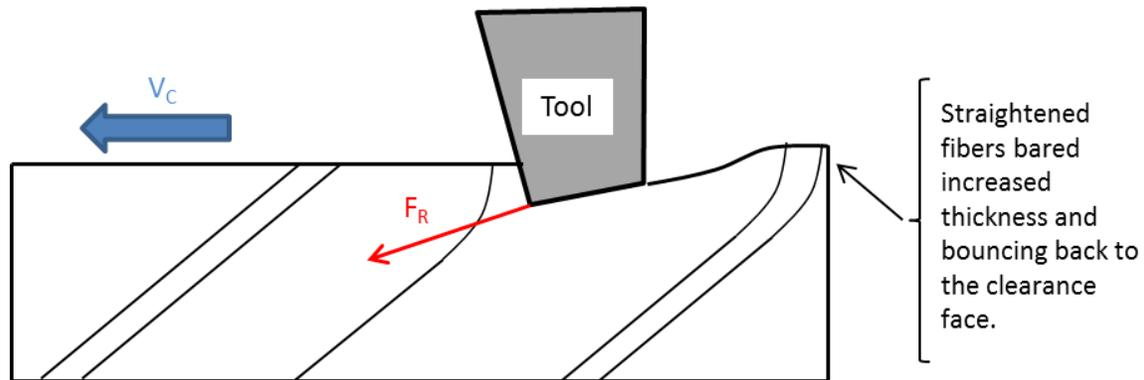


Fig. 1.1.21: Bouncing back phenomenon [Wang and Zhang, 2003].

[Blanchet, 2015] analyzed the spring back phenomenon with negative and positive rack angle and found that it varies with varying rack angle. An addition by [Wang and Zhang, 2003] is that in the case where $X_2 < 90^\circ$, the elastic spring back is equal to or slightly greater than the radius of acuity. In the case where $X_2 > 90^\circ$, the elastic spring back can go up to 2 times the radius of acuity.

Surface Damage

The surface condition of a machined CFRP part in an orthogonal section is sensitive to a large number of parameters. [Pramanik et al., 2007] found that the newly generated surfaces remain under compressive residual stress and these surfaces are damaged due to cavities left by the pull-out of fibers whereas [Shchurov et al., 2016] said it is the interfacial debonding between fibers and matrix in the area under machined surface which is responsible and the values cohesive bonding strength increases with increased separation, reaches a maximum value before causing permanent debonding [Nayak et al. 2004]. According to [Wang and Zhang, 2003], [Koplev, 1983] and [Iliescu, 2008], the larger the cutting angle the higher the roughness. Wang indicate that the sub-surface damage is linked to the orientation of the fibers, the feed depth and to the cutting angle. Fig. 1.1.22-a shows the surface condition following an orthogonal cut-out for $X_2 = 0^\circ$ in which [Koplev et al., 1983] said the surface state is "relatively good", the cracks do not exceed a depth of 2 times the diameter of the fibers. In Fig. 1.1.22-b the surface condition for $X_2 = 90^\circ$ is of "poor quality". Sub-surface cracks with a depth from 0.1 mm to 0.3 mm are observed inside the composite (more than fifteen times the diameter of the fibers).

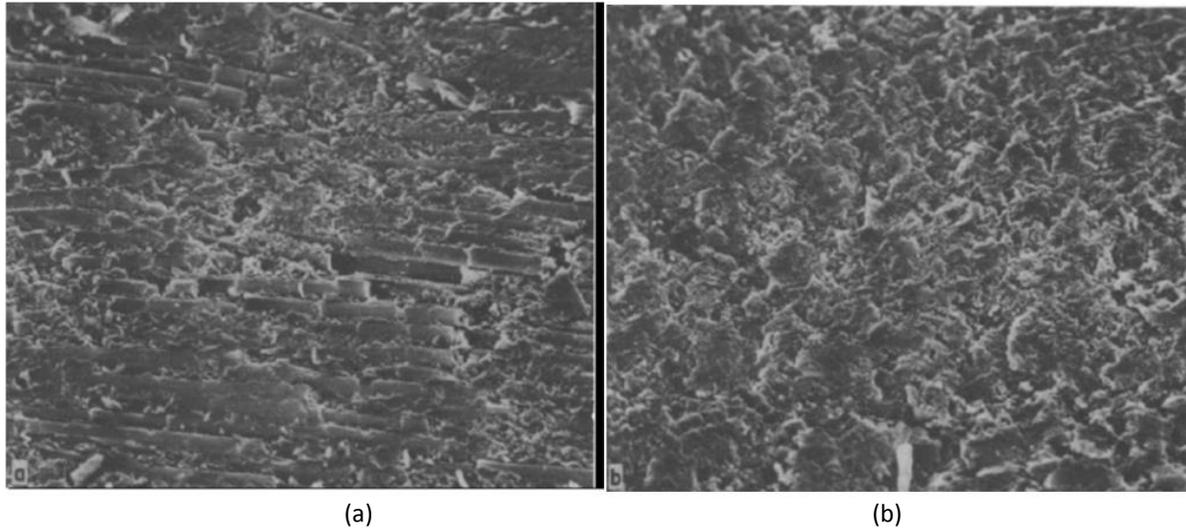


Fig. 1.1.22: (a) Surface condition following an orthogonal section planing for $X_2 = 0^\circ$. (b) $X_2 = 90^\circ$ [Koplev et al., 1983].

Fig. 1.1.23 shows the roughness induced using four different rake angles with different fiber orientations where the roughness increases only after 90° fiber orientation (the other criterions of roughness are not indicated) [Wang and Zhang, 2003]. Wang further noted that the extent of this damage varies as a function of the cutting angle.

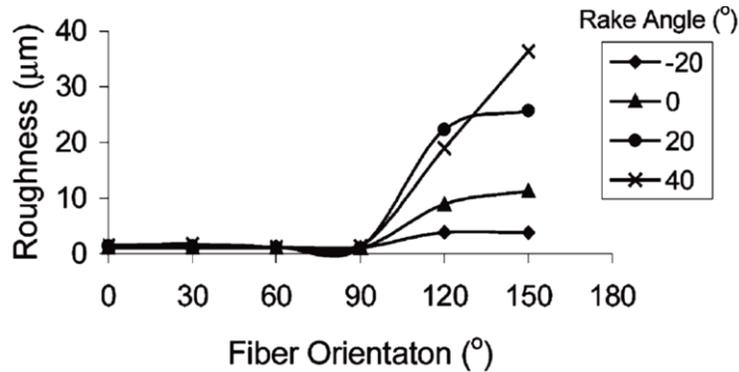


Fig. 1.1.23: Roughness versus X_2 for multiple cutting angles. The depth of cut is 0.05 mm [Wang and Zhang, 2003]

The best surface condition according to [Zitoune et al. 2005] is obtained for $X_2 = 45^\circ$ indeed [Arola et al., 2002] [El Alaiji et al., 2015] found at 90° trimming at 0° rake angle and [Lasri, 2009] found at 30° fiber orientation. The worst being obtained at $X_2 = 135^\circ$ by Zitoune whereas Lasri

said the worse starts beyond 45° fiber angle. Zitoune clarified that when $X_2 = 45^\circ$, the fibers and the matrix are sheared cleanly with good surface condition. At the contact between the test piece and the tool, the plane of sliding of the chip is observed (Fig. 1.1.24-a and 1.1.24-b). The author also explains that at $X_2 = 0^\circ$, bending induced chip breaking leaves fibers raised. This phenomenon is illustrated by photographs Fig. 1.1.24-c and 1.1.24-d.

The subsurface damage varies with different failure models. [Lasri et al., 2009] carried out research with three different models and saw that in case of Hashin criterion, the sub-surface damage in the matrix and the extent fiber–matrix debonding are close each other, while in the case of Maximum stress criterion, the predicted sub-surface damage in the matrix below the flank plane is lower than the extent of fiber–matrix debonding and localized around the cutting tool edge. However, the Maximum stress criterion predicts fiber–matrix debonding deeper than what predicts Hashin criterion. [Arola et al., 1996] found that the extent of damage to plies can be limited if the surrounding plies are oriented in different direction. For all fiber orientations, the subsurface damage, such as matrix cracking, fiber–matrix debonding and predicted Hoffman damage starts near the cutting tool edge and propagates in directions parallel and perpendicular to the fiber inside the workpiece [Lasri, 2009].

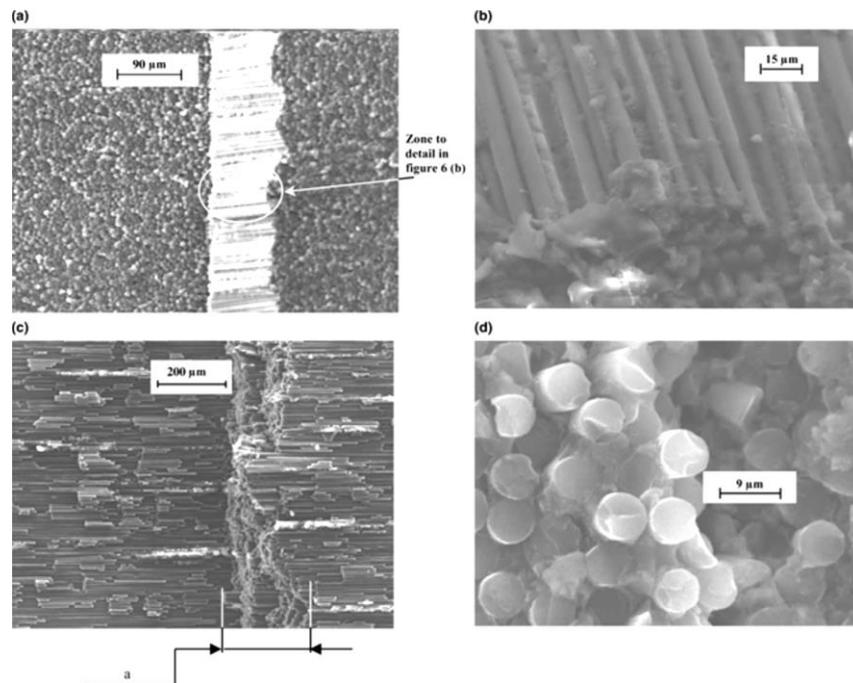


Fig. 1.1.24: Enlargements of a machined surface with cutting depth $a_p = 0.25 \text{ mm}$: (a) $X_2 = 45^\circ$; (b) enlargement of (a); (c) $X_2 = 0^\circ$; (d) enlargement of (c) [Zitoune, 2004].

To reduce surface damage [Shchurov et al., 2016] said one of the ways to reduce such damage is special deformation redistribution, such that fibers have to be lesser stretched after the cutting wedge indeed [Arola et al., 2002] emphasized on tool angle, saying a tool with 10° rake angle would minimize damage.

Tool Wear

Abrasive wear, chipping, and adhesion are attributed to the tool wear mechanisms during machining of composite laminates. Although existing models can provide estimates for the principal cutting forces resulting from orthogonal cutting, tool wear is often overlooked [Arola et al., 2002]. A lot of research work identified abrasive wear as dominant tool wear mechanisms in composite laminates cutting due to the highly abrasive nature of the carbon and glass fibers [Liu et al., 2012]. Abrasive wear mechanism is a mechanical wear that is caused by scratching action of hard fibers inside the soft polymer matrix [Pramanik et al., 2007].

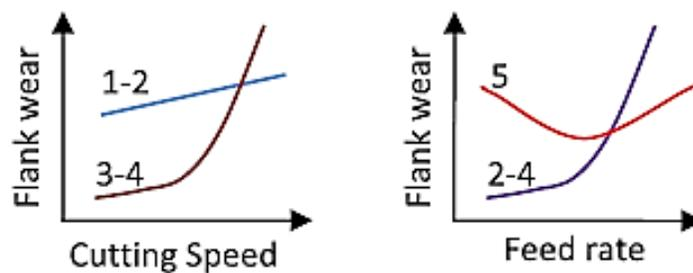


Fig. 1.1.25: Flank wear with respect to the cutting speed and feed rate in drilling [Liu et al., 2012].

The Fig. 1.1.25 shows the flank wear during drilling which can be taken into consideration to analyze orthogonal cutting. On the figure the numbers are the references mentioned at [Liu et al., 2012]. It can be seen that the flank wear increases with increasing the cutting speed but in case of feed rate it remains controversial among different authors. In order to reduce the tool wear Liu said that carbide tools, coated carbide tools and PCD tools yield good results in terms of tool wear and tool life.

1.1.3. Various Developed Models in CFRP Machining

Different kinds of models have been developed by researchers depending on their objectives. Here, a few Micro, Macro and Analytical models have been presented.

1.1.3.1. Micro-mechanic Models

Model of [Abena et al., 2017]

Abena has proposed a new approach for the cohesive interface. The model employs zero thickness of the cohesive elements following the traction-separation law. The simulations have been carried out with 0° , 45° , 90° and 135° fiber orientation. The authors emphasize that the model can represent very thin interface behavior. It showed good agreement regarding the cutting and thrust forces with respect to different fiber orientations against the published literature findings. Fig. 1.1.26, shows the traction separation law for the cohesive model.

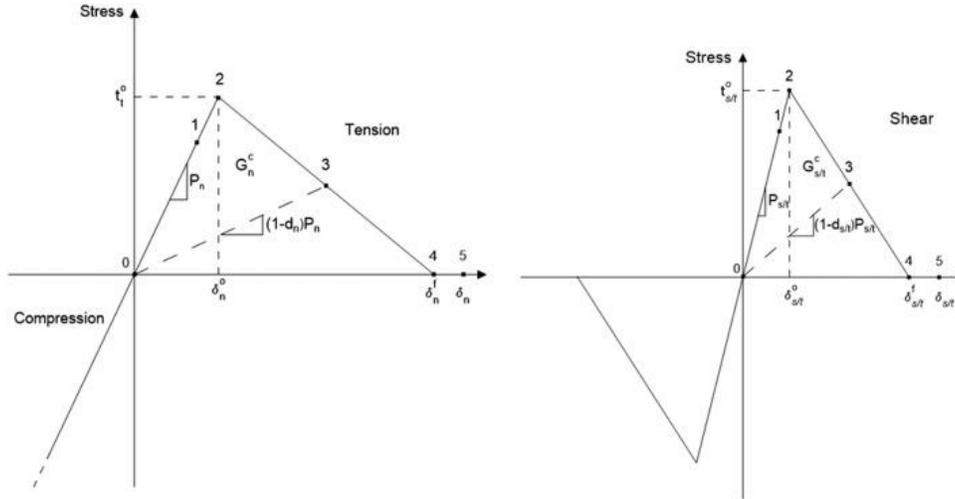


Fig. 1.1.26: Cohesive model based on traction–separation law and mechanical response for (left) normal and (right) tangential behavior [Abena et al., 2017].

The linear elastic response in this model is composed by normal and shear behavior. The strains ϵ are displaced by δ by means of the Eq. 1.1.3.

$$\epsilon_n = \frac{\delta_n}{T_0}, \quad \epsilon_s = \frac{\delta_s}{T_0}, \quad \epsilon_t = \frac{\delta_t}{T_0} \quad 1.1.3$$

Here the T_0 represents the constitutive thickness and the n , s , and t indicate the normal and the two shear directions respectively. The linear elastic behavior until the damage is initiated according to the Eq. 1.1.4.

$$\bar{t} = \begin{Bmatrix} t_n \\ t_s \\ t_t \end{Bmatrix} = \begin{bmatrix} P_n & 0 & 0 \\ 0 & P_s & 0 \\ 0 & 0 & P_t \end{bmatrix} \begin{Bmatrix} \epsilon_n \\ \epsilon_s \\ \epsilon_t \end{Bmatrix} = \bar{P}\bar{\epsilon} \quad 1.1.4$$

Here, \bar{t} , \bar{P} , and $\bar{\epsilon}$ represent the stress vector, the stiffness matrix and the strain vector respectively. Once the stress and displace reach point 2 (Fig. 1.1.26) the interface reaches its

yield point and crossing this point initiates the damage. The damage initiation in this model has been chosen based on quadratic nominal stress criterion, coupling traction and shear behavior as Eq. 1.1.5.

$$\left\langle \frac{t_n}{t_0} \right\rangle^2 + \left\langle \frac{t_s}{t_0} \right\rangle^2 + \left\langle \frac{t_t}{t_0} \right\rangle^2 = 1 \quad 1.1.5$$

Here the Macaulay brackets $\langle \rangle$ mean that no damage initiation is possible under compressive behavior. The degradation of adhesive phase has been expressed in Eq. 1.1.6.

$$P_{n/s/t}^d = P_{n/s/t}(1 - d_{n/s/t}) \quad 1.1.6$$

Here

$$d_{n/s/t} = \frac{\delta^f d_{n/s/t} (\delta_{n/s/t}^{\max} - \delta_{n/s/t}^0)}{\delta_{n/s/t}^{\max} (\delta_{n/s/t}^f - \delta_{n/s/t}^0)}, \quad d_{n/s/t} \in [0, 1] \quad 1.1.7$$

In the Eq. 1.1.6, $d_{n/s/t}$ represents the damage variable introduced for each failure mode, $\delta_{n/s/t}^0$, $\delta_{n/s/t}^f$, $\delta_{n/s/t}^{\max}$ represent the displacement at the damage initiation, the displacement at failure and the maximum displacement reached during the analysis until the time considered respectively. They found that for 0° fiber orientation the cohesive element's shear and tensile stress both together are responsible for damage initiation and evolutions until failure with bigger contribute of the shear for damage initiation. On the other hand, for 45° , 90° and 135° fiber orientation the shear stress is mainly responsible for damage initiation and failure.

Model of [Alaiji et al., 2015]

The authors have developed a three-dimensional (3D) finite element (FE) model to study the machining of unidirectional (UD) carbon fiber reinforced polymer composite (CFRP). The objectives of this study were to analyze the physical mechanisms responsible in the chip formation process, to predict the cutting forces and to simulate the cutting induced damage.

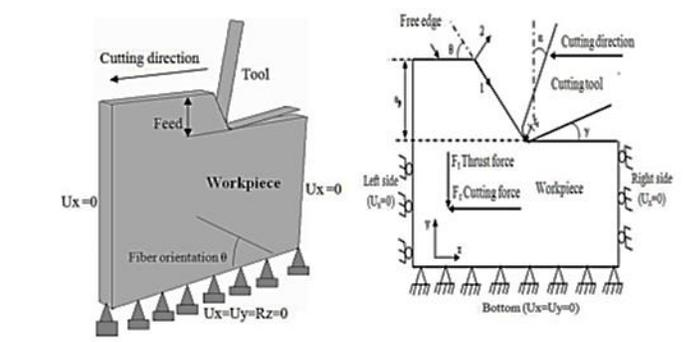


Fig. 1.1.27: Geometry and boundary conditions of [Alaiji et al., 2015].

In the model the cutting tool is a rigid body with a geometry defined by the rake and clearance angles (α and γ) and tool nose radius r_ϵ . The elements employed are eight-node brick elements (C3D8R). The element size employed in fine mesh domain is around $5\mu\text{m} \times 5\mu\text{m} \times 5\mu\text{m}$ and $30\mu\text{m} \times 30\mu\text{m} \times 30\mu\text{m}$ in the extreme sides and bottom of the workpiece. The Coulomb friction law (with constant values 0.3) and Tresca shear stress limit to model the sticking and sliding conditions at the tool–chip interface are used (Eq. 1.1.8).

$$\tau = \mu \sigma_n \quad 1.1.8$$

$$|\tau| \leq \tau_{\text{lim}} \quad 1.1.9$$

Hashin 3d failure criteria is used in which four failure modes (matrix cracking, fiber-matrix shearing, fiber failure, and delamination) are taken into account.

Matrix tensile cracking

$$e_m^2 = \left(\frac{\sigma_{yy}}{Y_t} \right)^2 + \left(\frac{\sigma_{xy}}{S_{xy}} \right)^2 + \left(\frac{\sigma_{yz}}{S_{yz}} \right)^2 \quad \text{for } \sigma_{yy} \geq 0 \quad 1.1.10$$

Matrix compressive failure

$$e_m^2 = \left(\frac{\sigma_{yy}}{Y_c} \right)^2 + \left(\frac{\sigma_{xy}}{S_{xy}} \right)^2 + \left(\frac{\sigma_{yz}}{S_{yz}} \right)^2 \quad \text{for } \sigma_{yy} < 0 \quad 1.1.11$$

Fiber matrix shearing failure

$$e_{fs}^2 = \left(\frac{\sigma_{xx}}{X_c} \right)^2 + \left(\frac{\sigma_{xy}}{S_{xy}} \right)^2 + \left(\frac{\sigma_{xz}}{S_{xz}} \right)^2 \quad \text{for } \sigma_{xx} < 0 \quad 1.1.12$$

Fiber tensile failure

$$e_f^2 = \left(\frac{\sigma_{xx}}{X_t} \right)^2 + \left(\frac{\sigma_{xy}}{S_{xy}} \right)^2 + \left(\frac{\sigma_{xz}}{S_{xz}} \right)^2 \quad \text{for } \sigma_{xx} \geq 0 \quad 1.1.13$$

Fiber compressive failure

$$e_f^2 = \left(\frac{\sigma_{xx}}{X_c} \right)^2 \quad \text{for } \sigma_{xx} < 0 \quad 1.1.14$$

The authors used Hashin criteria in progressive failure and material degradation process. Progressive failure is based on two main ingredients: failure criteria to be checked locally, i.e., at each gauss point of the FE mesh and a degradation rule to be applied once the failure criterion is satisfied in some points. The degradation rules are shown in Table 1.1.2.

Failure modes	Associated solution defined variable	Reduced material properties
Matrix tensile failure ($\sigma_{22} \geq 0$)	SDV1	$E_2, \nu_{12} \rightarrow 0$
Matrix compressive failure ($\sigma_{22} < 0$)	SDV1	$E_2, \nu_{12} \rightarrow 0$
Fiber matrix shearing failure ($\sigma_{11} < 0$)	SDV2	$\nu_{12}, G_{12}, G_{13} \rightarrow 0$
Fiber tensile failure ($\sigma_{11} \geq 0$)	SDV3	$E_1, E_2, E_3, \nu_{12}, \nu_{23}, \nu_{13}, G_{12}, G_{23}, G_{13} \rightarrow 0$
Fiber compressive failure ($\sigma_{11} < 0$)	SDV3	$E_1, E_2, E_3, \nu_{12}, \nu_{23}, \nu_{13}, G_{12}, G_{23}, G_{13} \rightarrow 0$

Table. 1.1.2: Hashin criterion with five failure modes and associated degradation rules [Alajji et al., 2015].

They found that the chip formation mechanism is a series of fractures in the fibers and a rougher surface is observed for 90° fiber orientation samples as compared to 0° fiber orientation.

Model of [Lasri et al., 2009]

The primary objective of this article was to develop a new approach for modelling chip formation and induced damage over a range of fiber orientations. It focuses on progressive failure of unidirectional glass fiber-reinforced polymer composites (FRP) using three sets of failure criteria: Hashin, Maximum stress and Hoffman.

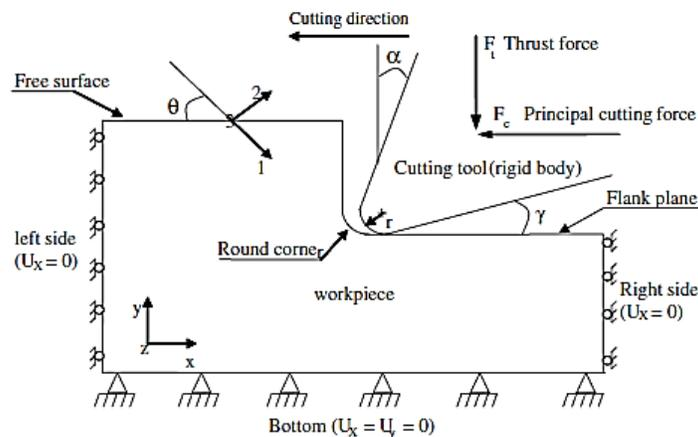


Fig. 1.1.28: Schematic view of orthogonal cutting model showing the tool geometry, composite workpiece and boundary conditions [Lasri et al., 2009].

In the physical model the displacements of the workpiece bottom in both cutting and perpendicular direction are restrained. The displacements of extreme sides (left and right) are also restrained in the cutting direction. Orthogonal cutting tool was modelled as a rigid body, and a reference point controls the movement of the cutting tool. A tool edge radius of 50 μm , a depth of a cut of 0.2 mm, a rake angle of 5° and flank angle of 6° are used throughout the numerical analysis. The reinforced laminate is modelled as a homogeneous orthotropic material using four nodes, quadrilateral, isoparametric and plane stress elements. The mesh size is about 10 μm which is approximately equal to the fiber diameter. Coulomb friction law is used in which a constant friction coefficient of 0.5 is considered.

Hashin and Maximum stress failure criteria offer advantages of considering each failure mode separately. Table 1.1.3 specifies the criterion for each failure mode.

<u>Failure mode</u>	<u>Failure index for Hashin failure criteria</u>	<u>Failure index for maximum stress criteria</u>
Matrix <u>tensile failure</u> ($\sigma_{22} \geq 0$)	$e_{m,Hashin}^2 = \left(\frac{\sigma_{22}}{Y_t}\right)^2 + \left(\frac{\sigma_{12}}{S_c}\right)^2 \geq 1$	$e_{m,Maximum\ stress}^2 = \left(\frac{\sigma_{22}}{Y_t}\right)^2 \geq 1$
Matrix <u>compressive failure</u> ($\sigma_{22} < 0$)	$e_{m,Hashin}^2 = \left(\frac{\sigma_{22}}{Y_c}\right)^2 + \left(\frac{\sigma_{12}}{S_c}\right)^2 \geq 1$	$e_{m,Maximum\ stress}^2 = \left(\frac{\sigma_{22}}{Y_c}\right)^2 \geq 1$
<u>Fiber-matrix interface shear failure</u>	$e_{m,Hashin}^2 = \left(\frac{\sigma_{22}}{X_c}\right)^2 + \left(\frac{\sigma_{12}}{S_c}\right)^2 \geq 1$ if $\sigma_{11} \geq 0$	$e_{s,Maximum\ stress}^2 = \left(\frac{\sigma_{12}}{S_c}\right)^2 \geq 1$
<u>Fiber tensile failure</u> ($\sigma_{11} \geq 0$)	$e_{f,Hashin}^2 = \left(\frac{\sigma_{11}}{X_t}\right)^2 \geq 1$	$e_{f,Maximum\ stress}^2 = \left(\frac{\sigma_{11}}{X_t}\right)^2 \geq 1$
<u>Fiber compression failure</u> ($\sigma_{11} < 0$)	$e_{f,Hashin}^2 = \left(\frac{\sigma_{11}}{X_c}\right)^2 \geq 1$	$e_{f,Maximum\ stress}^2 = \left(\frac{\sigma_{11}}{X_c}\right)^2 \geq 1$

Table. 1.1.3: Hashin and Maximum stress failure criteria for each failure mode [Lasri et al., 2009].

Here on the table the $e_{i,Maximum\ stress}$ and $e_{i,Hashin}$ are the failure index of Maximum stress and Hashin failure criteria, where i indicates the failure mode. Specifically, $i = m$ indicates matrix failure, $i = s$ indicates fiber–matrix interface shear failure and $i = f$ indicates fiber failure.

<u>No Failure</u>	Matrix cracking	<u>Fiber-matrix interface failure</u>	<u>Fiber failure</u>
E_{11}	E_{11}	E_{11}	$E_{11} \rightarrow \delta E_{11}$
E_{22}	$E_{22} \rightarrow \delta E_{22}$	E_{22}	$E_{22} \rightarrow \delta E_{22}$
v_{12}	$v_{12} \rightarrow \delta v_{12}$	$v_{12} \rightarrow \delta v_{12}$	$v_{12} \rightarrow \delta v_{12}$
G_{12}	G_{12}	$G_{12} \rightarrow \delta G_{12}$	$G_{12} \rightarrow \delta G_{12}$
FV1=0	FV1=1	FV1=0	FV1=0
FV2=0	FV2=0	FV2=1	FV2=0
FV3=0	FV3=0	FV3=0	FV3=1

Table. 1.1.4: Dependence of material elastic properties on the field variables and stiffness degradation scheme used with Hashin and Maximum stress.

At the beginning of the simulation, all material properties are equal to their initial values. The continuous tool advance generates an increased loading. At the end of each increment, stresses and failure indices are computed at the integration points of each element. If the failure index exceeds 1 the material properties are automatically reduced to zero according to the implemented stiffness degradation scheme, (Table 1.1.4). The procedure is repeated until the chip formation is complete.

$$e_{Hoffman} = -\frac{\sigma_{11}^2}{X_t X_c} + \frac{\sigma_{11} \sigma_{22}}{X_t X_c} - \frac{\sigma_{22}^2}{Y_t Y_c} + \frac{X_t + X_c}{X_t X_c \sigma_{11}} + \frac{Y_t + Y_c}{Y_t Y_c \sigma_{22}} + \frac{\sigma_{12}^2}{S_c^2} \geq 1 \quad 1.1.15$$

Eq. 1.1.15 shows the Hoffman failure criterion and the table 1.1.5 shows the stiffness degradation scheme used with this criterion.

No failure	E_{11}	E_{22}	V_{12}	G_{12}	FV4=0
Hoffman failure	$E_{11} \rightarrow \delta E_{11}$	$E_{22} \rightarrow \delta E_{22}$	$V_{12} \rightarrow \delta V_{12}$	$G_{12} \rightarrow \delta G_{12}$	FV4=1

Table. 1.1.5: Dependence of material elastic properties on the field variables and stiffness degradation scheme used with Hoffman failure criterion.

In Hashin, Hoffman and Maximum stress equations, σ_{ij} , X_t , $-Y_t$, X_c , $-Y_c$ and S_c are the principal stress (expressed in the principal material coordinate system (1, 2, 3), longitudinal–transverse

tensile strength, longitudinal transverse compressive strength and shear strength, respectively. They found that the trend of predicted principal cutting forces with Hashin, Maximum stress and Hoffman criteria agreed well with the experimental data. The values predicted with Hashin criterion were closer to experiments.

Model of [Pramanik et al., 2007]

The paper discusses the fiber-matrix deformation and tool–particle interactions phenomenon during orthogonal machining. The authors analyzed the development of stress-strain fields in the MMC (metal matrix composites) material and explored the physical phenomena such as tool wear, particle debonding, displacements and inhomogeneous deformation of matrix. In the model the Lagrangian formulation for material continuum is used to develop a plane-stress model. A temperature independent plastic kinematic material model (from ANSYS/LS-DYNA) and associated flow rule are used for the matrix. According to LS DYNA, yield stress (Eq. 1.1.16) in the plastic kinematic material is used.

$$\sigma_y = \left[1 + \left(\frac{\dot{\epsilon}}{C} \right)^{1/P} \right] (\sigma_0 + \beta E_p \epsilon_p^{\text{eff}}) \quad 1.1.16$$

Where

$$E_p = \frac{E_{\text{tan}} E}{E - E_{\text{tan}}} \quad 1.1.17$$

Here, σ_y is the yield stress, σ_0 is the initial yield stress, $\dot{\epsilon}$ is the strain rate, C and P are the Cowper-Symonds strain rate parameters and the effective plastic strain, E_p is the plastic hardening modulus, E_{tan} , the tangent modulus, E, the modulus of elasticity. The Coulomb friction model is used as defined in Eq. 1.1.18.

$$\tau_{\text{lim}} = \mu P + b \quad 1.1.18$$

$$|\tau| \leq \tau_{\text{lim}} \quad 1.1.19$$

Here τ_{lim} is limiting shear stress, τ is equivalent shear stress, P is contact pressure, μ is friction coefficient and b is cohesion sliding resistance (sliding resistance with zero normal pressure). They found that the magnitude and distribution of stresses/strains in the MMC material and interaction of particles with the cutting tool are the main reasons for particle fracture (fiber fracture) and debonding during machining of MMC. The interfaces of particles in the workpiece far below the cutting edge do not experience any plasticity during machining. But those situated immediately below the cutting edge are subjected to plastic deformation when the tool passes over them.

Model of [Gopala et al., 2007]

[Gopala et al., 2007] proposes a micro-mechanical model for orthogonal cutting of composite materials. In the model the angle X_2 between the cutting direction and the fiber varies in steps by 15° in a range from 15° to 90° . A distinction is made between the different elements. The elements representing the fibers are linked to the elements representing the matrix by cohesive elements. In order to save computing time, the elements remote from the area of interest represent the equivalent homogeneous material. In order to model the behavior of the fiber / matrix interface, a potential separation function is defined (Eq. 1.1.20) as a function of the normal displacement Δ_n , tangential displacement Δ_t and normal and tangential characteristic lengths δ_n and δ_t . When this potential is derived from the displacement in one direction (in the normal or tangential case), the component of the stress in this direction is obtained (Eq. 1.1.21).

$$\phi(\vec{\Delta}) = \phi_n(1 - e^{-\frac{\Delta_n}{\delta_n}})(1 + \frac{\Delta_n}{\delta_n})e^{-\frac{\Delta_t^2}{\delta_t^2}} \quad 1.1.20$$

$$\vec{T} = \frac{\partial \phi}{\partial \vec{\Delta}} \quad 1.1.21$$

This means that if the potential ϕ is derived with respect to the normal displacement Δ_n , it is possible to obtain the value of the normal stress T_n (Eq. 1.1.22). In the same way, deriving ϕ with respect to the tangential displacement Δ_t , the value of the tangential stress T_t (Eq. 1.1.23) is obtained.

$$T_n = \left(\frac{\phi_n}{\delta_n} e^{-\frac{\Delta_n}{\delta_n}}\right) \left(\frac{\Delta_n}{\delta_n} e^{-\frac{\Delta_t^2}{\delta_t^2}}\right) \quad 1.1.22$$

$$T_t = \left(2\frac{\delta_n}{\delta_t}\right) \frac{\phi_n}{\delta_n} \frac{\Delta_t}{\delta_t} \left(1 + \frac{\Delta_n}{\delta_n}\right) e^{\frac{\Delta_n}{\delta_n}} e^{-\frac{\Delta_t^2}{\delta_t^2}} \quad 1.1.23$$

The Fig. 1.1.29-a represents the normal stress at the interface as a function of the normal displacement in the case where the tangential displacement is zero. The Fig. 1.1.29-b represents the tangential stress as a function of the tangential displacement in the case where the normal displacement is zero.

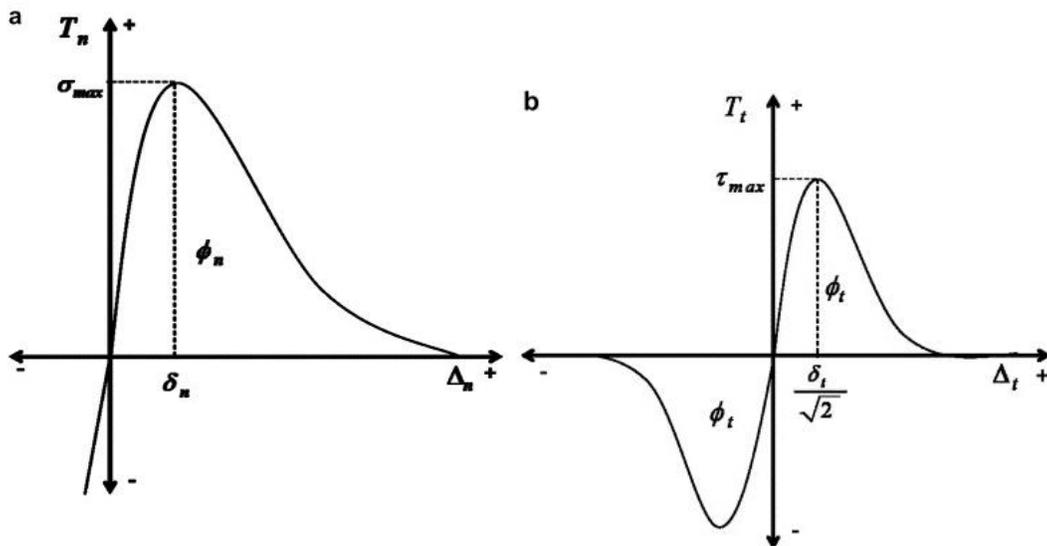


Fig. 1.1.29: Behavior of the cohesive interface: (a) Normal force as a function of the normal displacement in the case where the tangential displacement is negligible; (b) Tangential force as a function of tangential displacement in the case where the normal displacement is negligible [Gopala et al., 2007].

Model of [Nayak et al. 2005]

The first micro-mechanical model of cutting was proposed by [Nayak et al. 2005]. Nayak put a single fiber, and the rest of the specimen is modeled with the properties of the matrix. The decohesion of the fiber/matrix interface is modeled by a nodal separation based on a criterion of maximum stresses, the same is true for the rupture of the fiber.

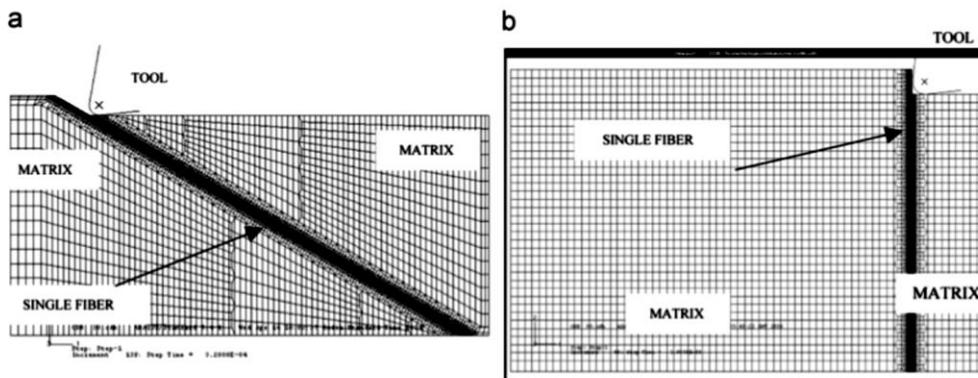


Fig. 1.1.30: Model of Nayak: $X_2 = 30^\circ$; (b) $X_2 = 90^\circ$ [Nayak et al. 2005].

The calculated cutting forces have a relatively low error compared to GFRP test specimens, up to 17 %. The model can also predict sub-surface damage.

Model of [Blanchet, 2015]

Blanchet proposed a micro-mechanical model making two distinct phases of materials (fiber and cohesive elements) in the workpiece. The aims of the model was to study the cutting mechanism including elastic return phenomenon, and the effect of cutting speed together with rake angle in orthogonal cutting. The model was created by a Matlab code in “.inp” format instead of graphical interface system. Later he used the “.inp” file in Abaqus for simulation.

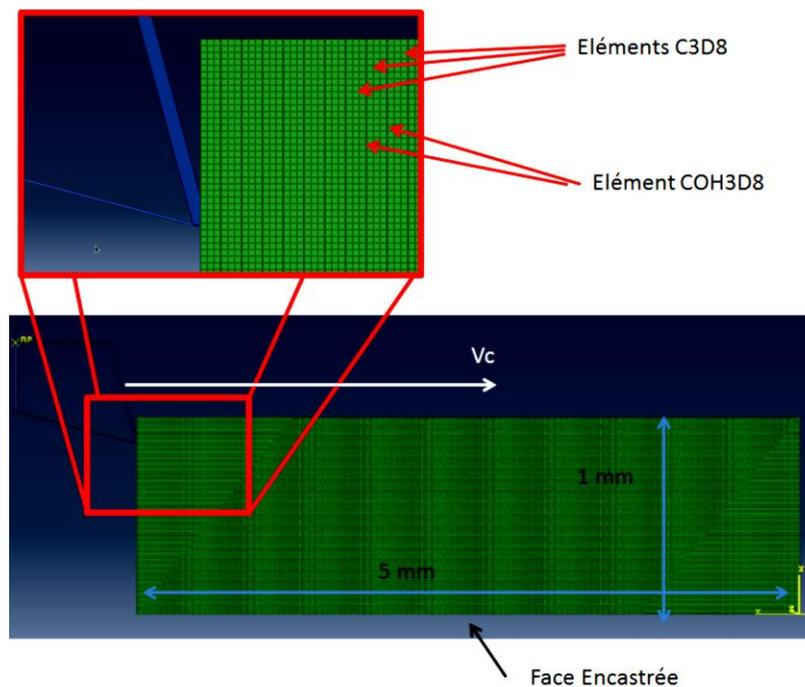


Fig. 1.1.31: Micro-mechanical model of [Blanchet, 2015]

The fibers have been considered as linear orthotropic until failure. The failure of the fibers is obtained with a local criterion for deletion of element. The criterion of material failure was introduced by a VUSDFLD subroutine. The maximum stress criterion was used which means if the failure stress reaches to the maximum defined value then the corresponding element will be deleted from calculation. The failure conditions are as follow:

Tensile failure in fiber direction

$$\left(\frac{\langle \sigma_{11} \rangle^+}{X_{RT}}\right)^2 \geq 1$$

1.1.24

$$\text{Compressive failure in fiber direction} \quad \left(\frac{\langle \sigma_{11} \rangle^-}{X_{RC}}\right)^2 \geq 1 \quad 1.1.25$$

$$\text{Compressive failure in transverse direction} \quad \left(\frac{\langle \sigma_{22} \rangle^-}{Y_{RC}}\right)^2 \geq 1 \quad 1.1.26$$

$$\text{Shear failure} \quad \left(\frac{\sigma_{12}}{S}\right)^2 \geq 1 \quad 1.1.27$$

To represent decohesion of fiber matrix interface, he introduced volumetric cohesive elements in between fibers. The elements for cohesive are COH3D8 and for fiber are C3D8R as in the Fig. 1.1.31. The elements have elastic damageable behavior, shown in Fig. 1.1.26.

The cutting tool was modeled as an analytical rigid tool in which he applied displacement which corresponds to cutting speed.

General contact with Coulomb friction 0.3 is used for the friction between cutting tool and workpiece which correspond to quasi-static friction coefficient.

Model of [Iliescu 2008] and [Iliescu et al. 2010]

Iliescu proposes a discrete element method to cut composite materials. This method, different from finite element method, is based on the principle that the material is decomposed into a set of particles. For a given time step, each particle is defined by its mass, radius, position, speed and its acceleration. The interpenetrations between the spheres are calculated; each interpenetration allows the calculation of the forces of interactions between the particles. The dynamics of Newton is applied to determine the acceleration. An explicit integration algorithm is used to calculate the velocities and positions at the next time step.

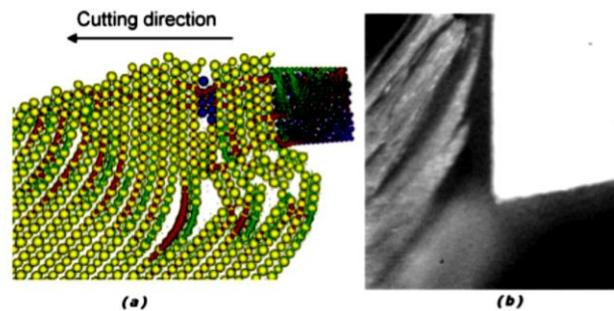


Fig. 1.1.35: Cutting mechanisms at $X_2 = 135^\circ$ and the cutting angle 0° .

This method also shows good results from the point of view of the mean predicted forces, although their value shows great variations during a test. Despite the promising results observed by Iliescu, the discrete element method remains little used for the simulation of the orthogonal cut of CFRP.

1.1.3.2. Macro-mechanic Models

Model of [Arola et al., 2000]

Arola compared the cutting and thrust force history resulting from numerical simulations of orthogonal cutting to those obtained from edge trimming of unidirectional Graphite/Epoxy (Gr/Ep) using polycrystalline diamond tools.

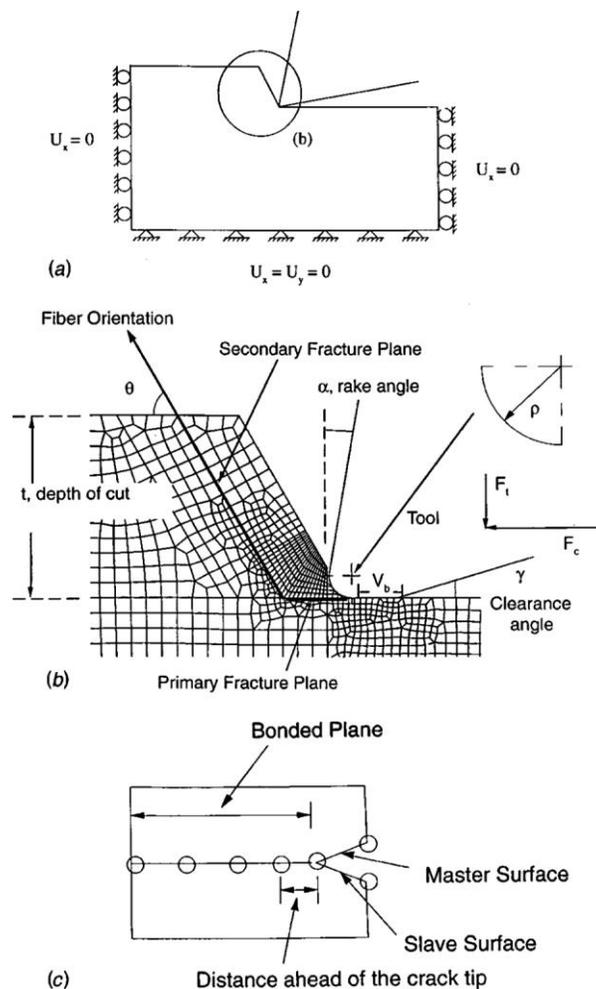


Fig. 1.1.32: Schematic diagrams and terminology associated with a discrete chip: (a) workpiece and boundary conditions, (b) primary and secondary fracture planes and (c) fracture criterion [Arola et al., 2000].

To simulate the cutting process an arbitrary forced displacement is assigned to the cutting tool towards the workpiece and Coloumb friction model with friction coefficient 0.4 is used. Debonding of node pairs on both fracture planes that occurs during chip formation is governed by a critical nodal stress criterion according to the Eq. 1.1.28.

$$f = \sqrt{\left(\frac{\sigma'_n}{\sigma^f}\right)^2 + \left(\frac{\tau_1}{\tau_1^f}\right)^2 + \left(\frac{\tau_2}{\tau_2^f}\right)^2}; \quad \sigma'_n = \max(\sigma_n, 0) \quad 1.1.28$$

Here σ'_n and τ_1 are the in-plane normal and shear stress across the interface and τ_2 is the transverse shear stress, respectively. Similarly σ^f and τ_1^f are the in-plane normal and shear strength and τ_2^f is the transverse shear strength of the material.

$$1 - f_{\text{tol}} \leq f \leq 1 + f_{\text{tol}} \quad 1.1.29$$

The crack tip nodes on each fracture plane debonded according to the Eq. 1.1.28 when the failure criterion ratio (f) reaches 1 within a given tolerance of 10 percent according to the Eq. 1.1.29.

Model of [Mahdi and Zhang, 2001]

Mahdi investigated the variation of cutting force against both the cutting conditions and the anisotropy of the material with the following development: (a) a constitutive model of the homogeneous anisotropic elastic material under plane deformation (b) a failure model of the work-material based on the Tsai-Hill criterion and (c) a contact model of the mechanisms of the cutting process. An equivalent homogeneous anisotropic material (EHAM) has been used to predict the cutting force. Both the fiber and matrix materials are assumed to be isotropic. By using an homogenization procedure and the FEM, the global constitutive behavior of the corresponding orthotropic material can be expressed by symmetric stiffness matrix D as Eq. 1.1.30.

$$D = \begin{bmatrix} \frac{E_{11}}{1 - \nu_{12}\nu_{21}} & \frac{\nu_{12}E_{22}}{1 - \nu_{12}\nu_{21}} & 0 & \frac{\nu_{13}E_{33}}{1 - \nu_{13}\nu_{31}} \\ \frac{E_{22}}{1 - \nu_{12}\nu_{21}} & \frac{\nu_{23}E_{33}}{1 - \nu_{23}\nu_{32}} & 0 & \frac{\nu_{23}E_{33}}{1 - \nu_{23}\nu_{32}} \\ \text{Sym.} & & \frac{1}{G} & 0 \\ & & & \frac{E_{33}}{1 - \nu_{13}\nu_{32}} \end{bmatrix} \quad 1.1.30$$

The Tsai-Hill failure criterion is applied to simulate the formation of chips and thereby the material separation during cutting. For an orthotropic lamina under plane-stress conditions the failure or separation occurs when the Eq. 1.1.31 is satisfied.

$$\frac{\sigma_1^2}{X_1^2} - \frac{\sigma_1\sigma_2}{X_1^2} + \frac{\sigma_2^2}{X_2^2} + \frac{\sigma_{12}^2}{S^2} \geq 1 \quad 1.1.31$$

Here, X_1 and X_2 are the tensile (or compressive) failure strength in the 1 and 2 directions and S is the shear failure strength.

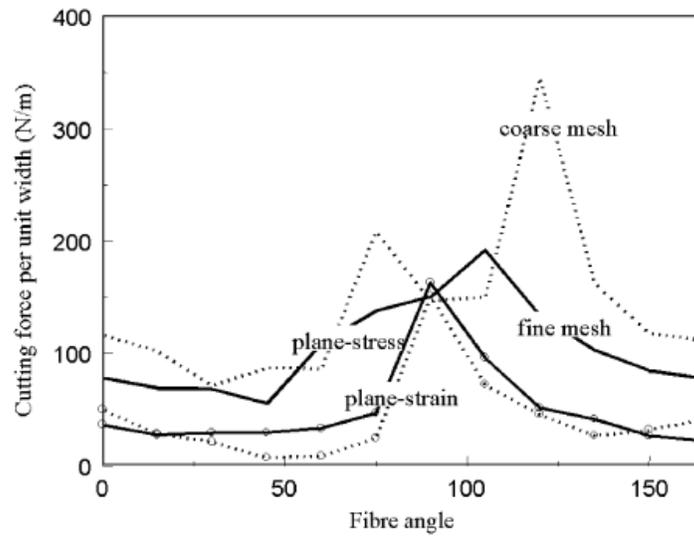


Fig. 1.1.33: Mesh refining effect of an anisotropic material cutting force [Mahdi and Zhang, 2001].

Fig. 1.1.33, shows the effect of mesh density and element type on the predicted cutting force. It is observed that for the plane stress case, the finer mesh reduces the variation of cutting force with respect to fiber orientation, while in the plane strain case the mesh dependence is negligible.

Model of [Ramesha et al. 1998]

Ramesha introduces a model with an elasto-plastic behavior with linear hardening. The crack propagates when the criterion of [Vaziri et al., 1992] is reached, which means the effective constraint (Eq. 1.1.32) reaches a threshold value.

$$\bar{\sigma}_u = \sqrt{\frac{1}{2}[\alpha_{12}(\sigma_x - \sigma_y)^2 + \alpha_{23}(\sigma_y - \sigma_z)^2 + \alpha_{31}(\sigma_x - \sigma_z)^2] + 3\alpha_{44}\tau_{xy}^2} \quad 1.1.32$$

With α_{12} , α_{23} , α_{31} , α_{44} , normalized anisotropic rupture coefficients. The interest of this model is to introduce an elastoplastic behavior.

Model of [Zitoune, 2004] and [Zitoune et al. 2005]

Zitoune proposes an orthogonal cutting model to predict the cutting forces. A crack is pre-existed and an effort is applied to the tool. By the VCE (Virtual Crack Extension) method, the energy recovery rate G is calculated. This method consists in calculating the elastic energy difference stored ΔE between a given load and the same load in a case where the crack would have increased by one surface ΔA (Eq. 1.1.33).

$$G = \frac{\Delta E}{\Delta A} \quad 1.1.33$$

This model also allows predicting the stress field (Fig. 1.1.34). The cutting force is calculated with 7 % error compared to the tests. The thrust effort is not calculated.

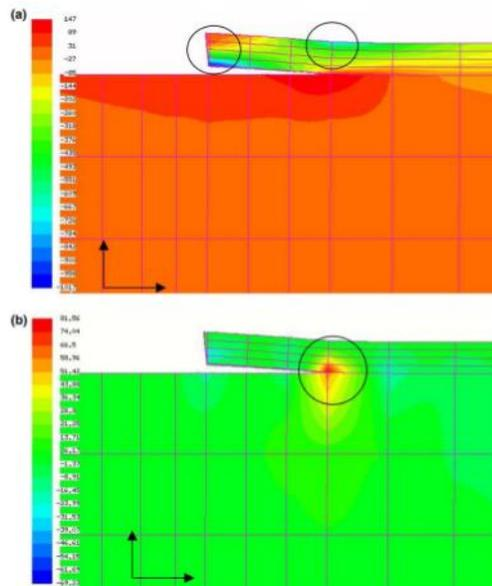


Fig. 1.1.34: Stress field prediction for $X_2 = 0^\circ$, $\gamma = 7^\circ$: (a) fiber direction; (b) cross direction [Zitoune et al. 2005].

Model of [Larbi, 2009]

Larbi proposes a macro-mechanical model of composite materials cutting in implicit schemes. He defines 4 variables under ABAQUS: FV_1 which corresponds to a matrix break, FV_2 which

corresponds to a rupture of the fiber / matrix interface, FV_3 which correspond to a fiber break, FV_4 which corresponds to a global break following the Hoffman criterion (Eq. 1.1.34).

$$\frac{X_c - X_t}{X_t X_c} \sigma_{11} + \frac{Y_c - Y_t}{Y_c Y_t} \sigma_{22} + \frac{\sigma_{11}^2}{X_t X_c} + \frac{\sigma_{22}^2}{Y_t Y_c} + \frac{\sigma_{12}^2}{S^2} - \frac{\sigma_{11} \sigma_{22}}{X_t X_c} \geq 1 \quad 1.1.34$$

FV_1 , FV_2 and FV_3 are defined by Maximum stress and Hashin criteria (Table 1.1.6).

<u>Failure mode</u>	<u>maximum stress criteria</u>	<u>Hashin failure criteria</u>	<u>Variable</u>
<u>Matrix tensile</u>	$(\frac{\sigma_{22}}{Y_t})^2 \geq 1$	$(\frac{\sigma_{22}}{Y_t})^2 + (\frac{\sigma_{12}}{S_{\square}})^2 \geq 1$	$FV_1=1$
<u>Matrix compressive</u>	$(\frac{\sigma_{22}}{Y_c})^2 \geq 1$	$(\frac{\sigma_{22}}{Y_c})^2 + (\frac{\sigma_{12}}{S_{\square}})^2 \geq 1$	$FV_1=1$
<u>Fiber-matrix interface shear</u>	$(\frac{\sigma_{12}}{S_{\square}})^2 \geq 1$	$(\frac{\sigma_{12}}{S_{\square}})^2 + (\frac{\sigma_{11}}{X_c})^2 \geq 1$	$FV_2=1$
<u>Fiber tensile</u>	$(\frac{\sigma_{11}}{X_t})^2 \geq 1$	$(\frac{\sigma_{11}}{X_t})^2 \geq 1$	$FV_3=1$
<u>Fiber compression</u>	$(\frac{\sigma_{11}}{X_c})^2 \geq 1$	$(\frac{\sigma_{11}}{X_c})^2 \geq 1$	$FV_3=1$

Table. 1.1.6: Rupture criteria associated with variables FV_1 , FV_2 and FV_3 [Larbi, 2009].

Lasri reports the values of the variables FV_1 , FV_2 , FV_3 and FV_4 . In the case where the criterion of maximum stress or Hashin is used, the chip is considered formed once the interface damage ($FV_2 = 1$) reaches the free edge. If Hoffman's criterion is used, the chip is considered formed once the Hoffman criterion ($FV_4 = 1$) is reached at the free edge. When one of the failure criteria is reached, a drop in rigidity is induced. Table 1.1.7 describes the falls of rigidity corresponding to the types of damage considered.

Rupture mode	Concerning variable	E_{11}	E_{22}	ν_{12}	G_{12}
Matrix	$FV_1=1$	E_{11}°	δE_{22}°	$\delta \nu_{12}^{\circ}$	G_{12}°
Interface	$FV_2=1$	E_{11}°	E_{22}°	$\delta \nu_{12}^{\circ}$	δG_{12}°
Fiber	$FV_3=1$	δE_{11}°	δE_{22}°	$\delta \nu_{12}^{\circ}$	δG_{12}°
Rupture globale	$FV_4=1$	δE_{11}°	δE_{22}°	$\delta \nu_{12}^{\circ}$	δG_{12}°

Table. 1.1.7: Rigidity drops depending on the type of damage [Larbi, 2009].

Model of [Mkaddem et al., 2008]

Mkaddem proposes a micro/macro-mechanical orthogonal cutting model. The micro/macro-mechanical terminology refers to remeshing operations (micro) and the choice to use an anisotropic homogeneous behavior for the material. Thus, only one type of element is used for the mesh. The criterion of rupture is the criterion of Tsai-Hill. The stress-based criterion of Tsai-Hill is retained for simulating the failure (Eq. 1.1.35).

$$I_F = \frac{\sigma_{11}^2}{X^2} - \frac{\sigma_{11}\sigma_{22}}{X^2} + \frac{\sigma_{22}^2}{Y^2} + \frac{\sigma_{12}^2}{S^2} < 1 \quad 1.1.35$$

Here X is the stress limit in the 1st-direction, Y is the stress limits in the 2nd-direction, and S is the in-plane shear strength in the X - Y plane. The author introduces the notion of cutting ratio R_c , It is the ratio between the length of the chip l_c and the distance d_c traveled by the tool to form it (Eq. 1.1.36).

$$R_c = \frac{l_c}{d_c} \quad 1.1.36$$

Here l_c and d_c are, respectively, the chip length and the cut distance covered by the tool. The work material is composed of UD-GFRP composite. The elastic properties of the material in tension are assumed different to the properties in compression. Linear elasticity in an orthotropic material is easily defined by 9 constants; giving the properties associated with the three material's principal directions: the modulus of elasticity E_1 , E_2 , E_3 ; the shear modulus G_{12} , G_{13} , G_{23} ; and the Poisson ratio ν_{12} , ν_{13} , ν_{23} . Thus, the stress-strain stiffness is given by the Eq. 1.1.37.

$$\begin{Bmatrix} \sigma_{11} \\ \sigma_{22} \\ \sigma_{33} \\ \sigma_{12} \\ \sigma_{13} \\ \sigma_{23} \end{Bmatrix} = \begin{bmatrix} D_{1111} & D_{1122} & D_{1133} & 0 & 0 & 0 \\ D_{1122} & D_{2222} & D_{2233} & 0 & 0 & 0 \\ D_{1133} & D_{2233} & D_{3333} & 0 & 0 & 0 \\ 0 & 0 & 0 & D_{1212} & 0 & 0 \\ 0 & 0 & 0 & 0 & D_{1313} & 0 \\ 0 & 0 & 0 & 0 & 0 & D_{2323} \end{bmatrix} \begin{Bmatrix} \epsilon_{11} \\ \epsilon_{22} \\ \epsilon_{33} \\ \epsilon_{12} \\ \epsilon_{13} \\ \epsilon_{23} \end{Bmatrix} \quad 1.1.37$$

For the orthotropic material, the D_{ijkl} components of the above matrix are given as the Eq. 1.1.38.

$$\begin{aligned} D_{kkkk(k=1,2,3)} &= E_k(1 - \nu_{ij}\nu_{ji})_{(i \neq j \neq k)} \psi \\ D_{kkll(k=1,2;l=2,3;k < l)} &= E_k(\nu_{lk} + \nu_{ik}\nu_{lk})_{(i \neq j \neq k)} \psi \\ D_{klkl(k=1,2;l=2,3;k < l)} &= G_{kl} \end{aligned} \quad 1.1.38$$

Here $\psi = 1/(1 - \nu_{12}\nu_{21} - \nu_{23}\nu_{32} - \nu_{31}\nu_{13} - 2\nu_{21}\nu_{32}\nu_{13})$ is a constant. The plane stress state imposes $\sigma_{33} = 0$ which reduces the materials stiffness matrix in the analysis as required.

Model of [Zenia S. et al., 2015]

[Zenia S. et al., 2015] proposed a macro-mechanical model which focused on understanding the interactions between fiber orientation and the physical phenomenon of orthogonal cutting, as well as drilling process. The workpiece was modeled as a homogeneous equivalent material (HEM) following the properties of T300/914 composite. They combined an elastoplastic damage behavior law for failure mechanism in a user routine VUMAT in Abaqus/Explicit. For the interply interface, they used cohesive elements (COH3D8) with a thickness of 5 μm . The cohesive elements permit them to take into account the delamination in the interply interface.

Regarding the damage model, they considered the fiber breaking in traction and in compression, matrix crushing and fiber-matrix debonding. The strain energy density of ply damage was defined by the Eq. 1.1.39.

$$e_D = \frac{1}{2} \left(\frac{1}{(1-D_{11})} \left[\frac{(\sigma_{11})^2}{E_{11}^0} - \left(\frac{\nu_{12}^0}{E_{11}^0} + \frac{\nu_{21}^0}{E_{22}^0} \right) \sigma_{11} \sigma_{22} - \left(\frac{\nu_{13}^0}{E_{11}^0} + \frac{\nu_{31}^0}{E_{33}^0} \right) \sigma_{11} \sigma_{33} - \left(\frac{\nu_{23}^0}{E_{22}^0} + \frac{\nu_{32}^0}{E_{33}^0} \right) \sigma_{22} \sigma_{33} \right] + \frac{\langle -\sigma_{22} \rangle_-^2}{E_{22}^0} + \frac{\langle -\sigma_{33} \rangle_-^2}{E_{33}^0} + \frac{1}{(1-D_{22})} \left[\frac{\langle \sigma_{22} \rangle_+^2}{E_{22}^0} + \frac{\langle \sigma_{33} \rangle_+^2}{E_{33}^0} \right] + \frac{1}{(1-D_{12})} \left[\frac{(\sigma_{12})^2}{G_{12}^0} + \frac{(\sigma_{23})^2}{G_{23}^0} + \frac{(\sigma_{31})^2}{G_{31}^0} \right] \right) \quad 1.1.39$$

Here

$$E_{22}^0 = E_{33}^0, G_{12}^0 = G_{13}^0, \nu_{12}^0 = \nu_{13}^0, G_{23}^0 = \frac{E_{33}^0}{2(1 + \nu_{23})} \quad 1.1.40$$

The damage activation and evolution are controlled by a square root of a linear combination of two thermodynamic forces Y_{22} and Y_{12} as in the Eq. 1.1.41.

$$Y = \sup_{\tau \leq t} (\sqrt{Y_{12} + b_1 Y_{22}}) \quad 1.1.41$$

Here, b_1 is a coupling term between the transverse and shear damage.

Fiber damage is introduced by considering E_{11} Young modulus as nonlinear which depends on stress σ_{11} . The fiber behavior was assumed as elastic brittle under tension and compression, Eq. 1.1.42, so the plastic potential function does not depend on the stresses of σ_{11} in the fiber direction.

$$F(\tilde{\sigma}, \sigma_y) = \sqrt{\tilde{\sigma}_{12}^2 + \tilde{\sigma}_{23}^2 + \tilde{\sigma}_{13}^2 + c^2[\tilde{\sigma}_{22}^2 + \tilde{\sigma}_{33}^2]} - R_0 + \beta p^\alpha \quad 1.1.42$$

Here the effective stresses are

$$\begin{aligned}\tilde{\sigma}_{12} &= \frac{\sigma_{12}}{(1 - D_{12})}; \tilde{\sigma}_{23} = \frac{\sigma_{23}}{(1 - D_{12})}; \tilde{\sigma}_{13} = \frac{\sigma_{13}}{(1 - D_{12})}; \tilde{\sigma}_{22} = \frac{(\sigma_{22})_+}{(1 - D_{22})} + (\sigma_{22})_-; \\ \tilde{\sigma}_{33} &= \frac{(\sigma_{33})_+}{(1 - D_{22})} + (\sigma_{33})\end{aligned}\quad 1.1.43$$

Here, β and α are the hardening parameters, R_0 is the initial yield stress and c is a coupling parameter.

They described the chip formation process by primary and secondary rupture. Moreover, they found a good matching of their cutting forces with the results which are found in the literature.

Model of (Blanchet 2015)

Blanchet used macro-mechanical model mainly to calculate the cutting efforts and to understand the different types of damage and rupture. The type of elements he used was C3D8R.

The macro-mechanical model (ply model) he used was first developed by [Matzenmiller, 1995] and later modified by [Ilyas, 2010]. In the model, for different modes of rupture, 5 criteria of damage r_i were defined. An equivalent homogeneous orthotropic material was used. The symmetric stiffness matrix of the material is shown in Eq. 2.2.18.

This macro-mechanical model has been used in this research which has been explained in chapter 2 (section 2.2.2). The modes of ruptures are the equations from Eq. 2.2.19 to Eq. 2.2.23. The evolution of damage and its related parameters are mentioned in the equations from Eq. 2.2.24 to Eq. 2.2.28.

1.1.3.3. Analytical Models

Model of [Merchant 1945a] and [Merchant 1945b]

Among the first analytical models proposed, some are based on the work of [Merchant 1945a] and [Merchant 1945b]. From visual observations during metals cutting Merchant observes an intense shear zone during chip formation. The author writes the components of the tool effort on the test piece in three references: a reference point related to the cutting speed, a reference point linked to the cutting face of the tool oriented by the cutting angle γ , and a reference point linked to the primary shearing zone of orientation ϕ comprising a representative tangential

force of the plastic flow stress of the machined material and a normal force. Fig. 1.1.36 illustrates these different efforts.

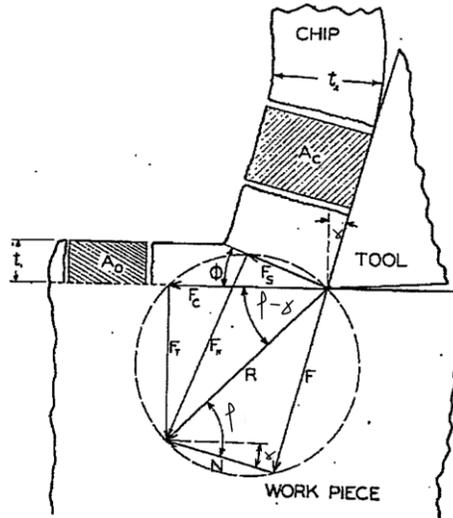


Fig. 1.1.36: Relationship between forces during orthogonal cutting [Merchant 1945a].

From the various relations between these efforts, the author formulates the power supplied by the tool as a function of the angles. From the hypothesis that the chip is formed for a minimum energy, it derives the work with respect to the primary shear angle. This leads to Eq. 1.1.44.

$$\phi = 45 + \frac{\gamma}{2} - \frac{\varphi}{2} \quad 1.1.44$$

It is therefore possible to deduce the cutting force F_c (Eq. 1.1.45) and thrust force F_p (Eq. 1.1.46) as a function of thickness of the test piece b , the depth of cut a_p , the plastic flow stress σ_0 , the coefficient of friction ϕ and the cutting angle γ .

$$F_c = ba_p\sigma_0 \frac{\cos(\varphi - \gamma)}{\cos(\phi + \varphi - \gamma) \sin(\phi)} \quad 1.1.45$$

$$F_p = ba_p\sigma_0 \frac{\sin(\varphi - \gamma)}{\cos(\phi + \varphi - \gamma) \sin(\phi)} \quad 1.1.46$$

This method presupposes the existence of a shear zone at the origin of the formation of the chips. Moreover, the author predicts the shear angle from the thickness t_2 of the chip generated by the geometric relation of (Eq. 1.1.47).

$$\tan \phi = \frac{\frac{a_p}{t_2} \cos \gamma}{1 - \frac{a_p}{t_2} \sin \gamma} \quad 1.1.47$$

This measurement is only possible in the case of a continuous chip; it is not adapted to the cases of particles generated in some cases of orthogonal CFRP cutting.

Model of [Everstine and Rogers, 1971]

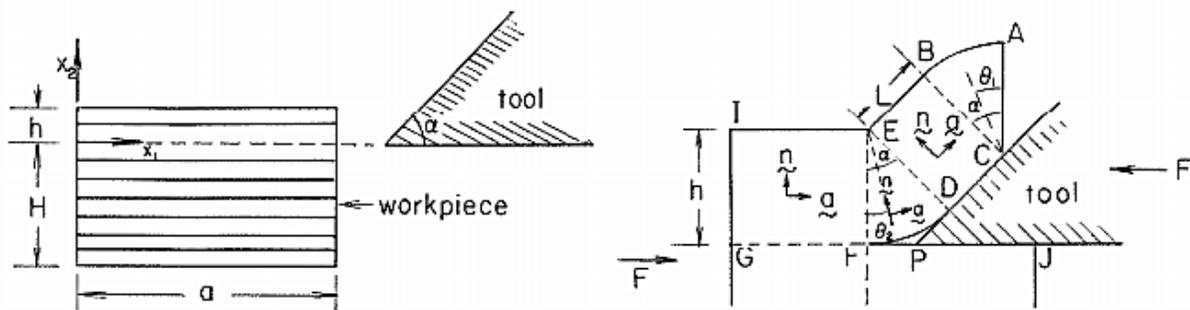


Fig. 1.1.37: Analytical model of [Everstine and Rogers., 1971].

Everstine and Rogers developed the first analytical model of orthogonal cutting at an angle $X_2 = 0^\circ$ with 0° edge radius and clearance angle. This model expresses the cutting force F_c as a function of the non-dimensional value η , the depth of cut a_p , the transverse tensile stress σ_{22} , the cutting angle γ and the orientation of the resultant δ (Eq. 1.1.48).

$$F_c = \eta \pi a_p \sigma_{22} (\tan(\frac{\pi}{2} - \gamma) + \tan(\delta)) \quad 1.1.48$$

Here,

$$\eta = \frac{2(1 - \nu_{12})G_{12}}{E_{22}} \quad 1.1.49$$

It is limited to the case where $X_2 = 0^\circ$ with a positive cutting angle. Moreover, it considers the crack along relatively weak fiber/matrix interface.

Model of [Takeyama and Lijima, 1998]

Takeyama and Lijima propose an analytical model to predict the cutting efforts based on the work of [Merchant 1945a]. The expressions of the cutting forces F_c (Eq. 1.1.50) and thrust forces F_p (Eq. 1.1.51) are very similar to those of [Merchant 1945a]; the difference lies in the shear failure stress σ_0 dependent on the angle X_2 .

$$F_c = ba_p \sigma_0(\phi) \frac{\cos(\varphi - \gamma)}{\cos(\chi_2 + \varphi - \gamma) \sin(\phi)} \quad 1.1.50$$

$$F_p = ba_p \sigma_0(\phi) \frac{\sin(\varphi - \gamma)}{\cos(\chi_2 + \varphi - \gamma) \sin(\phi)} \quad 1.1.51$$

Several limitations may be imposed on this model. Firstly the shear failure stress is a function of the shear angle ϕ ; a measurement of this rupture stress must be carried out for each value of ϕ . Then the shear angle ϕ remains difficult to evaluate in the same way as in case of metal chips (that is to say by the geometrical relationship between the thickness of the chip), the depth of cut and the angle of chopped off.

Model of [Pwu and Hocheng, 1998]

Pwu and Hocheng propose an orthogonal cutting model for angles $X_2 = 0^\circ$ (Fig. 1.1.38-a) and $X_2 = 90^\circ$ (Fig. 1.1.38-b). The model considers the chip to be a cantilever.

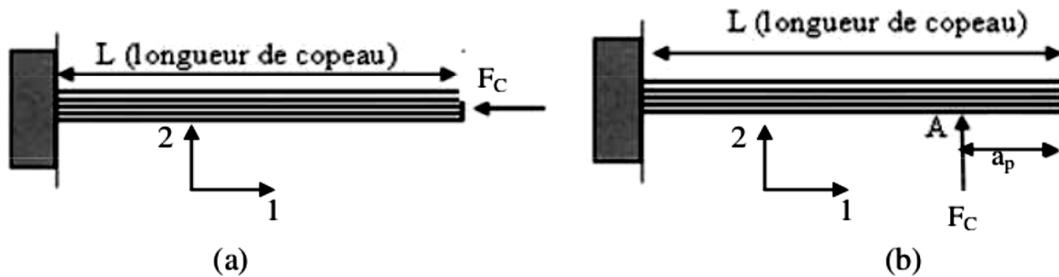


Fig. 1.1.38: Prediction model of the cutting force: (a) $X_2 = 0^\circ$; (b) $X_2 = 90^\circ$ [Pwu and Hocheng, 1998].

The authors consider two sub-cases in the case where $X_2 = 0^\circ$, namely a positive or negative cutting angle. In the case where the cutting angle is negative, the relationship between the length of the chip L and the cutting force F_c are calculated by considering the buckling of chip (Eq. 1.1.52).

$$L = \sqrt{\frac{\pi^2 E_{11} I}{4F_c (1 - \nu_{12} \nu_{21})}} \quad 1.1.52$$

Here I is the quadratic moment of the beam. In the case where $X_2 = 0^\circ$ and the cutting angle is positive, the relationship between the length L of the chip and the cutting force F_c is calculated

from the energy required to propagate a crack along the length of fiber/matrix Interface (Eq. 1.1.53).

$$IL = \sqrt{\frac{\sigma_{22RT}^2 b^2 a_p^4 \pi^2}{36F_c \left(\frac{\sigma_{22RT}^2 b^2 a_p^4}{9EI} + 16G_{IC}b \right)}} \quad 1.1.53$$

Here σ_{22RT} is the tensile rupture stress at transverse direction; G_{IC} is the energy release rate in mode I and b. Finally, in the case where $X_2 = 90^\circ$, the cutting force F_c is calculated by considering the deflection of the chip and the propagation of crack along the fiber/matrix interface according to the Eq. 1.1.54.

$$F_c = \frac{\sigma_{22RT} b a_{moy}^2}{6(L - a_p)} \quad 1.1.54$$

Here a_{moy} is the average thickness of the chip.

Model of [Zhang et al., 2001]

Zhang proposes a model to predict the cutting and thrust forces by considering 3 regions of distinct forces (Fig. 1.1.39-a).

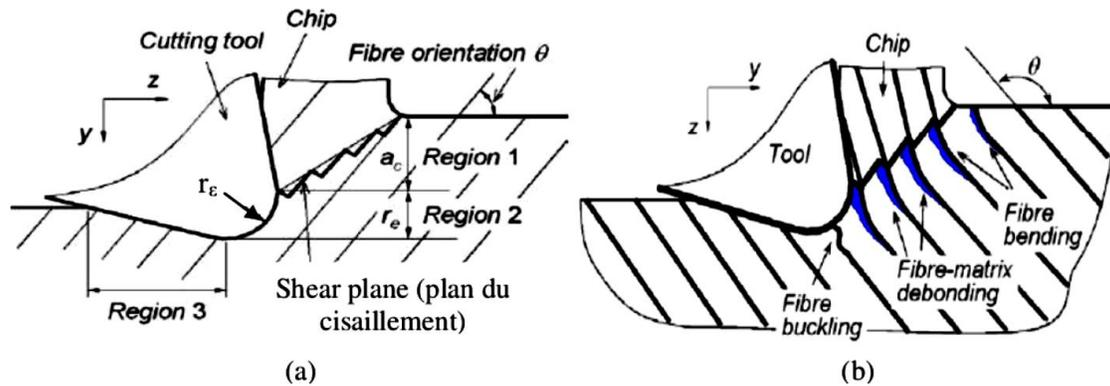


Fig. 1.1.39: Principle of the model of Zhang: (a) in case when $0^\circ \leq X_2 \leq 90^\circ$ (b) when $90^\circ \leq X_2 \leq 180^\circ$ [Zhang et al., 2001].

The cutting model concerns only the orientations $0^\circ \leq X_2 \leq 90^\circ$, the three chosen regions are: the chip forming zone (region 1), the pressure zone corresponding to the region in contact with the edge acuity (region 2) and the elastic return zone under the clearance face of the tool (region 3). In the chip formation zone, the expressions of the cutting forces F_{c1} and the thrust force F_{p1} are given respectively by the Eq. 1.1.55 and 1.1.56.

$$F_{c1} = \sigma_{12R} b a_p \frac{\cos \phi \tan(\phi + \varphi - \gamma) - \sin(\phi)}{\frac{\sigma_{12R}}{\sigma_{ZP}} \cos(\chi_2 - \phi) \sin(\chi_2) - \sin(\chi_2 - \phi) \cos(\chi_2)} \quad 1.1.55$$

$$F_{p1} = \sigma_{12R} b a_p \frac{\sin \phi \tan(\phi + \varphi - \gamma)}{\frac{\sigma_{12R}}{\sigma_{ZP}} \cos(\chi_2 - \phi) \sin(\chi_2) - \sin(\chi_2 - \phi) \cos(\chi_2)} \quad 1.1.56$$

Here the shear angle ϕ is estimated by $\tan(\phi) \simeq \frac{\cos(\gamma)}{1 - \sin(\gamma)}$, where σ_{12R} is the shear stress of the fiber/matrix interface, b is the width of the chip, φ is the coefficient of friction and σ_{zp} is the shear failure stress along the shear zone defined by the angle φ . In the pressure zone the expressions of the cutting forces F_{c2} and diving F_{p2} are given respectively by Eq. 1.1.57 and Eq. 1.1.58.

$$F_{c2} = \frac{K}{8} r_\varepsilon \pi \frac{E_{22}}{1 - \nu_{12}^2} h (\cos(\chi_2) - \mu \sin(\chi_2)) \quad 1.1.57$$

$$F_{p2} = \frac{K}{8} r_\varepsilon \pi \frac{E_{22}}{1 - \nu_{12}^2} h (\sin(\chi_2) + \mu \cos(\chi_2)) \quad 1.1.58$$

Here K is a correction factor and μ is the coefficient of friction. In the elastic return zone, the expressions of the cutting force F_{c3} and diving force F_{p3} are given respectively by the Eq. 1.1.59 and Eq. 1.1.60.

$$F_{c3} = \frac{1}{2} r_\varepsilon E_{zone3} h (1 - \mu \cos \gamma \sin \gamma) \quad 1.1.59$$

$$F_{p3} = \frac{1}{2} r_\varepsilon E_{zone3} h \cos^2(\gamma) \quad 1.1.60$$

Here E_{zone3} is the effective modulus in zone 3. The values of the cutting and feed forces are then determined by performing the sum of the forces in these three zones. The main contribution of this model is the consideration of the phenomena present under the edge and the flank face.

1.1.4. Summary of Literature Study

It has been found that the process variables have clear influence on defects generation. Similarly the generated defects are also interconnected among each other. Following the findings of different researchers we have made an inter-correlational chart, Fig. 1.1.40, which gives an overall view of the relations among different process variables and generated defects.

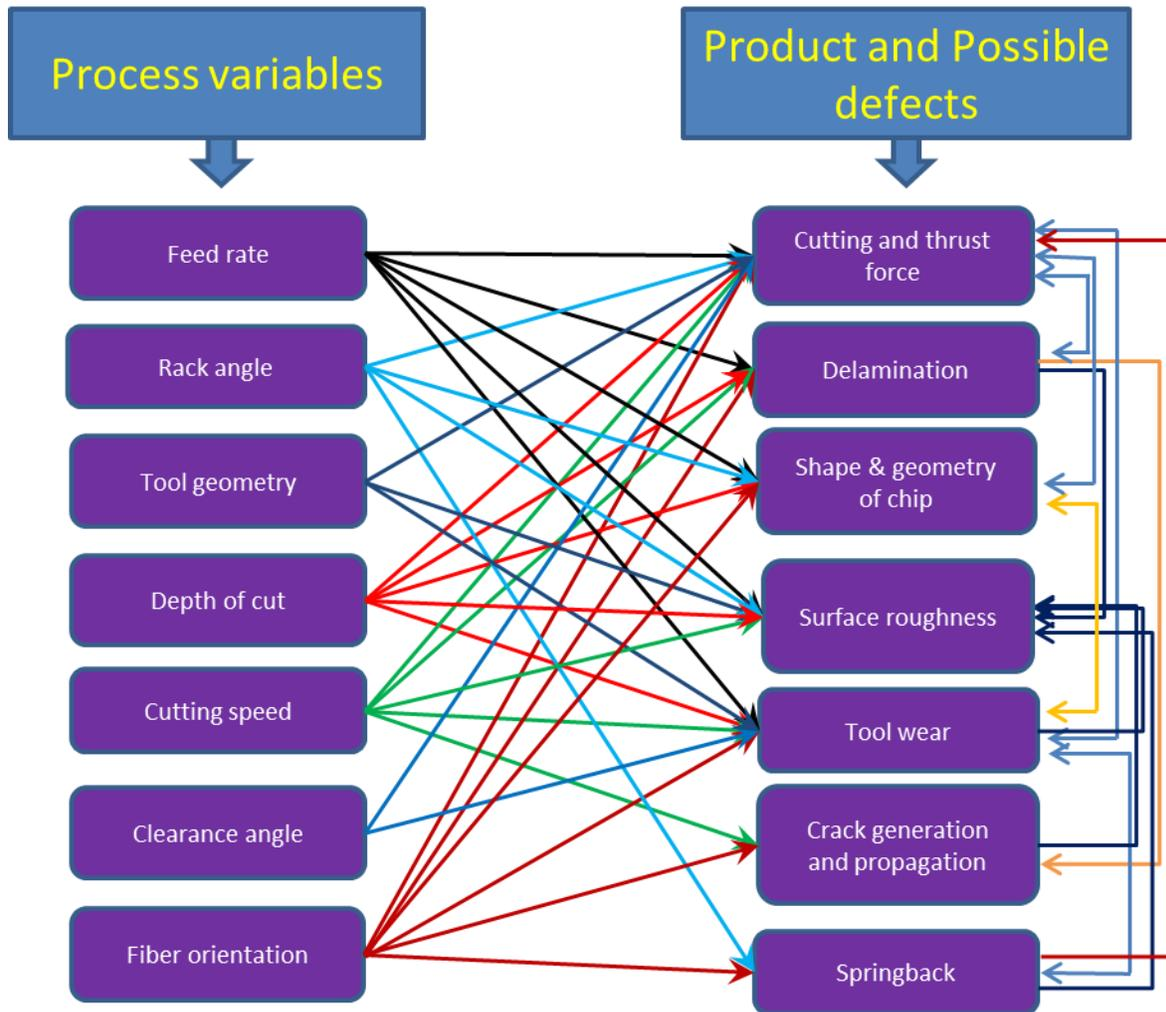


Fig. 1.1.40: Simplified intercorrelation among process parameters and generated defects

In Fig. 1.1.40, we can see the variables (feed rate, rack angle, tool geometry, depth of cut, cutting speed, clearance angle, and fiber orientation) which affect defects generation are input variables. On the other side, even though the generated defects (delamination, tool wear, crack generation and propagation and springback) are affected by the input variables but they also

have interdependence among each other; for example: if the tool wear increase, then the surface damage on the workpiece also increase.

As we discussed in the previous sections of the process parameters, there are some conflicts among the findings of different authors. For example; a few researchers found that delamination increases with increasing the cutting speed whereas some others researchers found it decreases with increasing the cutting speed. Nevertheless, it is sure that most of them have influence on others whether in positive or in negative way. However, no much research have been found regarding the influence of depth of cut and the mechanics of springback indeed these subjects are also important.

1.2. Conclusion

Machining domain is huge. Research, particularly, in orthogonal cutting of CFRP can reveal many mechanical phenomena which surely can help in understanding cutting mechanics of these materials. The goals of this present research are related to some principal mechanical behavior of cutting, so the outcome of this research will give a comprehensive understanding in orthogonal cutting of CFRP materials.

The literature study in this chapter discusses the corpus of orthogonal cutting of CFRP material. It covers the physics of orthogonal cutting, the influence of every cutting parameter on the machined parts, the reasons of defects generation and how they are related among each other.

A number of different models of micro, macro and analytic have been brought into discussions which were created by different researchers. Pointedly it should be noted that almost all of the macro-mechanical models were used to analyze the cutting and thrust force but no any micro-mechanical model was found which analyzes these forces. It is because a homogeneous anisotropic material in macro-mechanical model does not require very small element size; so the calculating machine needs less memory and less calculating time.

Chapter 2: Developed Models, Strain Field Analysis and Chip Formation Mechanisms

This chapter is divided in four sections. The experimental procedure is described in the first section. The type of cutting machine, its capacity and operating procedure are explained. Two different models are developed, one is micro-mechanical model and the other one is macro-mechanical model. In section-2, those models, their geometry, material properties, behavior, failure criteria and other related properties are explained.

The last two sections deal with discussion of results. In section-3, the strain field which is generated in the workpiece during cutting is discussed. A visual explanation on the strain field concentration area on the workpiece is made depending on the experimental results and then a comparison between numerical and experimental strains is shown. In section-4, a comprehensive explanation of chip formation process is made according to different fiber orientations. It describes the initiation of chip cut, the continuation of formation and the separation of chip from the main workpiece.

Content

2.1. Experimental Process	77
2.1.1 Machine Setup.....	77
2.1.2. Cutting Tool Selection	80
2.1.3. Workpiece Preparation	81
2.2. Developed Models.....	83
2.2.1. Micro-mechanical Model	83
2.2.2. Macro Model	93
2.3. Strain Measurement Process	100
Results and Discussion	106
2.4. Strain Field Analysis.....	106
2.4.1. Experimental Results.....	106
2.4.2. Comparison of Numerical and Experimental Findings	110
2.5. Chip Formation Mechanism in Orthogonal Cutting of CFRP	113
2.5.1. The Course of Chip Formation.....	114
2.6. Conclusion	124

2.1. Experimental Process

2.1.1 Machine Setup

The experimental work has been carried out with a single axis, quasi-static to 2 m/sec cutting speed setup supported by a conventional milling machine, Fig. 2.1.1. This setup was first developed by [Blanchet, 2015] at Institut Clement Ader. In our research work, we modified the configuration according to our objectives. The modifications have been mentioned in each relevant chapter. However, in the present configuration, the cutting tool is fixed and the workpiece is clamped in a movable device. The cutting speed is transmitted from a motor to the device containing the specimen via a ball screw module. The motor speed is computer controlled via a COMPAX 3 C3 S150 V4 F11 I12 T11 M00 case. An angular sensor is integrated in the motor which allows recording the position and speed of the motor.

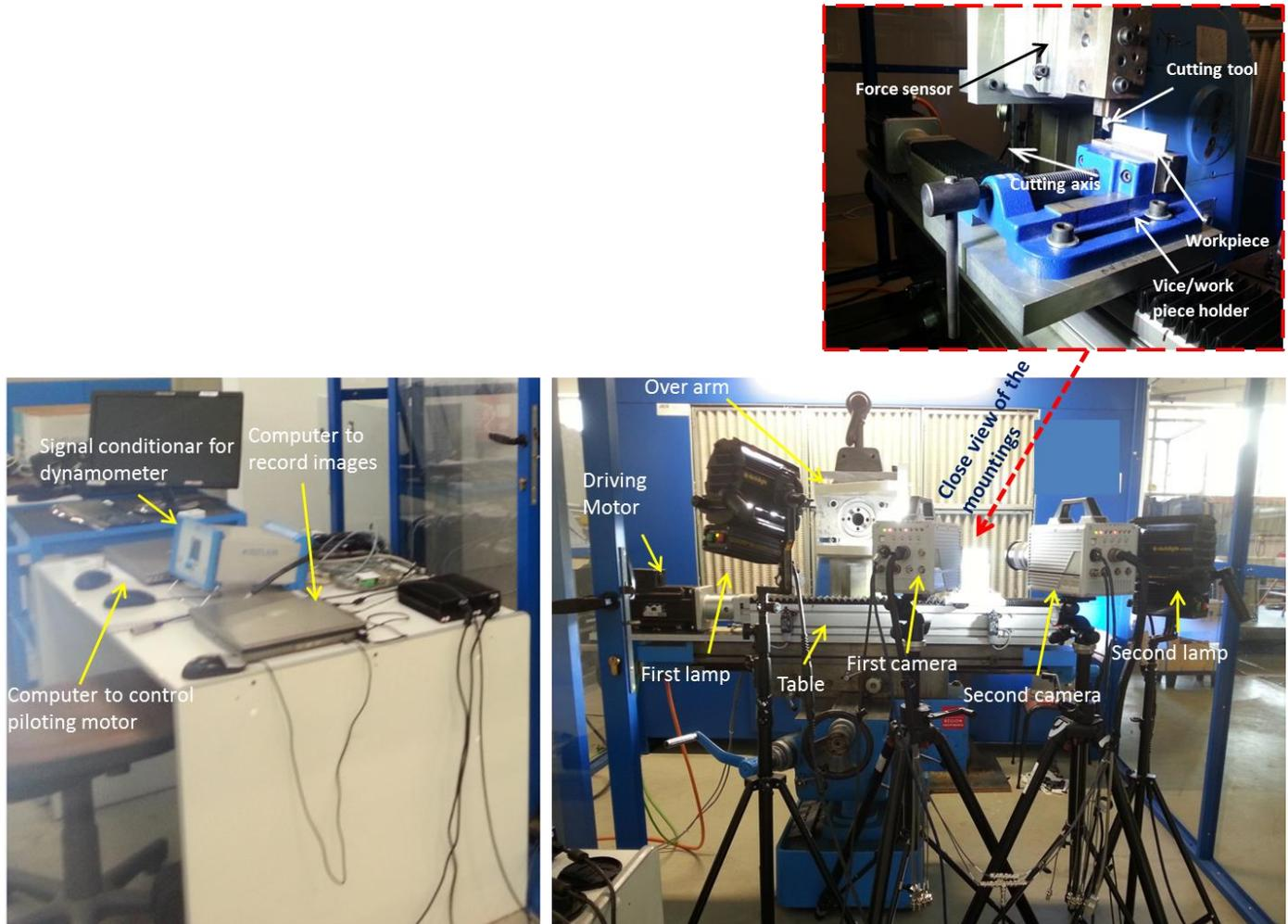


Fig. 2.1.1: Experimental setup

The motor and the module for converting the rotational movement into translation movement are fixed on the table of the milling machine frame. The cutting tool is mounted on a holder, and a KISLER 9257B triaxial force sensor placed in between the machine and the tool holder. The force sensor is tied to the fixed part of the milling machine by a chamber. The force sensor is designed to measure the forces in X, Y and Z directions where X represents the horizontal force (cutting force), Y represents the vertical force (thrust force) and Z represents the transverse force (e.g., reaction of vibration). Transverse force is not taken into account as it is considered near zero in orthogonal cutting.

2.1.1.1. Machine Operation and Its connections

The pilot motor and its speed are controlled via a COMPAX 3 C3 S150 V4 F11 I12 T11 M00 case which is already mentioned in the previous section. The holder (tied to the machine) does not move and the motor permits to move the workpiece/cutting tool right and left which allows the workpiece to be cut. The COMPAX case is a special operating software installed in a laptop computer, and this computer is connected to a switchgear which controls power supply to the pilot motor. A schematic diagram of the operating system and its connections is shown in Fig. 2.1.2. The whole operating system of the motor from the beginning to the end is described in Appendix B.

Parameter	Values
Rake angle	30°
Clearance angle	7° and 15° (7° on the first 4 mm clearance surface from the tool tip, and the rest is 15°)
Depth of cut	0.05 mm, 0.1 mm, 0.25 mm, 0.50 mm, 0.75 mm and 1.0 mm (depends on research objective)
Cutting speed	12 m/min for chip formation analysis and 3 m/min for strain filed analysis
Fiber and matrix volumetric ratio	60 % : 40 %
Fiber orientation	0°, 45°, 90°, and 135°
Used material	T800S/M21 carbon epoxy
Frequency of force fluctuation	7000 Hz/sec

Table. 2.1.1: Parameters of cutting configuration

Rake and clearance angles were kept fixed over all tests. The workpiece has been changed at every cut. So no workpiece came into use twice but each cutting depth got four tests at four different fiber orientations (0°, 45°, 90° and 135°).

2.1.2. Cutting Tool Selection

For the cutting tool, K20 micro grain tungsten carbide has been used. This material works well for cutting tools indeed fibers are known as abrasive material. The angles (rake angle and clearance angle) have been chosen according to the common uses in industries. The rake angle provides direction to the flow of the chips. For drill bits, this angle is chosen up to 45° with 30° being the most common [Roopak R, quora.com] [smithy.com] [mecholic.com]. If the rake angle is too high, the lips may be too thin and break under the cutting strain. Again, too small a rake angle increases the support behind the cutting edge but makes the tool chatter and vibrate excessively. Here in this research the rake angle is chosen 30°.

A range of clearance angle from 4° to 20° is used in drill bits depending on the application [Newman Tools Inc., newmantools.com]. However, [smithy.com] mentioned that general purpose drills have a clearance angle from 8° to 12°. The clearance angle needs to be selected according to material degree of hardness and machinability. Generally, a small clearance angle is preferred for hard materials and a higher one for softer materials. Similar to rake angle, too much clearance angle causes tool tip failure because of insufficient support of the lip; however, too little clearance results in little or not cutting edges, in which case the tool will need an increased force to penetrate the material which may cause the tool to break. On the other hand, to carry away the generated heat at the tool tip the lip thickness should be enough.

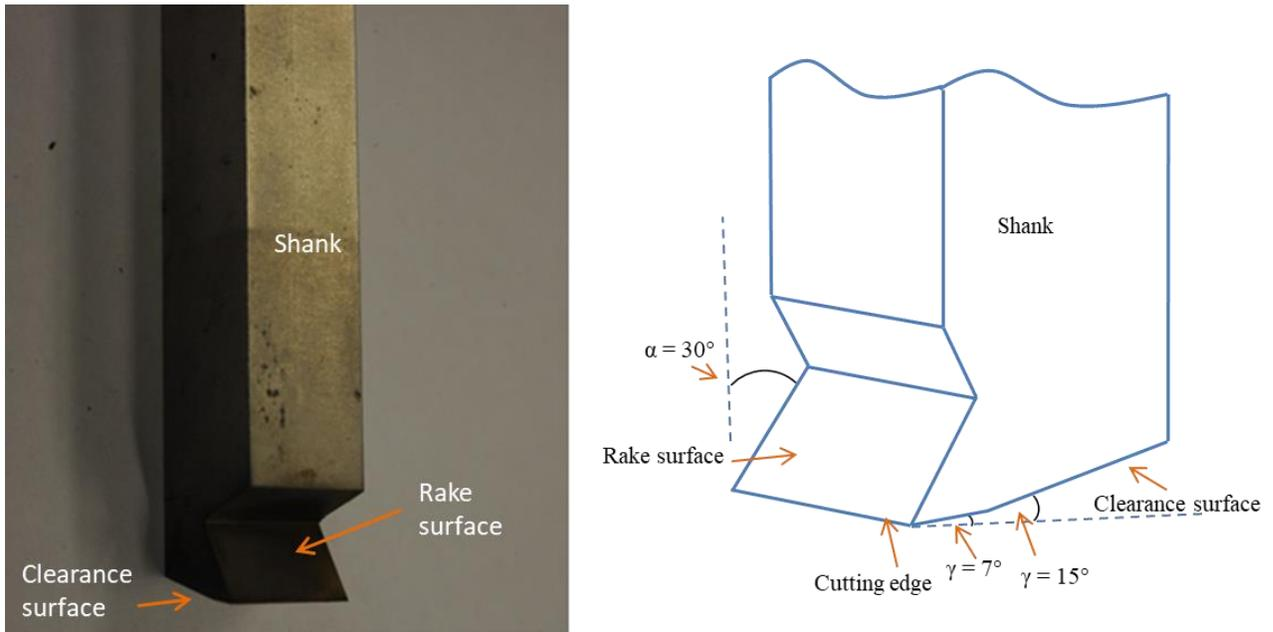


Fig. 2.1.3: Cutting tool and its angles

All these points have been considered in this present research, and that is why the clearance angle is kept 7° from the tool tip until 4 mm distance towards the clearance surface, and after this distance the angle is 15° . Near the tool tip, 7° angle permits more material near the tool tip which gives high stiffness to prevent the tip breaking. A schematic representation of the angles and a real tool are shown in Fig. 2.1.3. The tools have been manufactured by Wire Electrical Discharge Machining (WEDM) process.

2.1.3. Workpiece Preparation

An intermediate modulus unidirectional Carbon/Epoxy (T800S/M21) material has been used as a test specimen. Each specimen contains only one specific fiber orientation (unidirectional) and 16 prepreg layers. The fiber orientations are 0° , 45° , 90° and 135° , shown in Fig. 2.1.4. One single fiber angle permits to better understand the generated defects during machining as well as the cutting phenomenon of fiber at a given orientation. The dimensions of the workpiece are 80 mm \times 4 mm \times 45 mm (length \times width \times height accordingly).

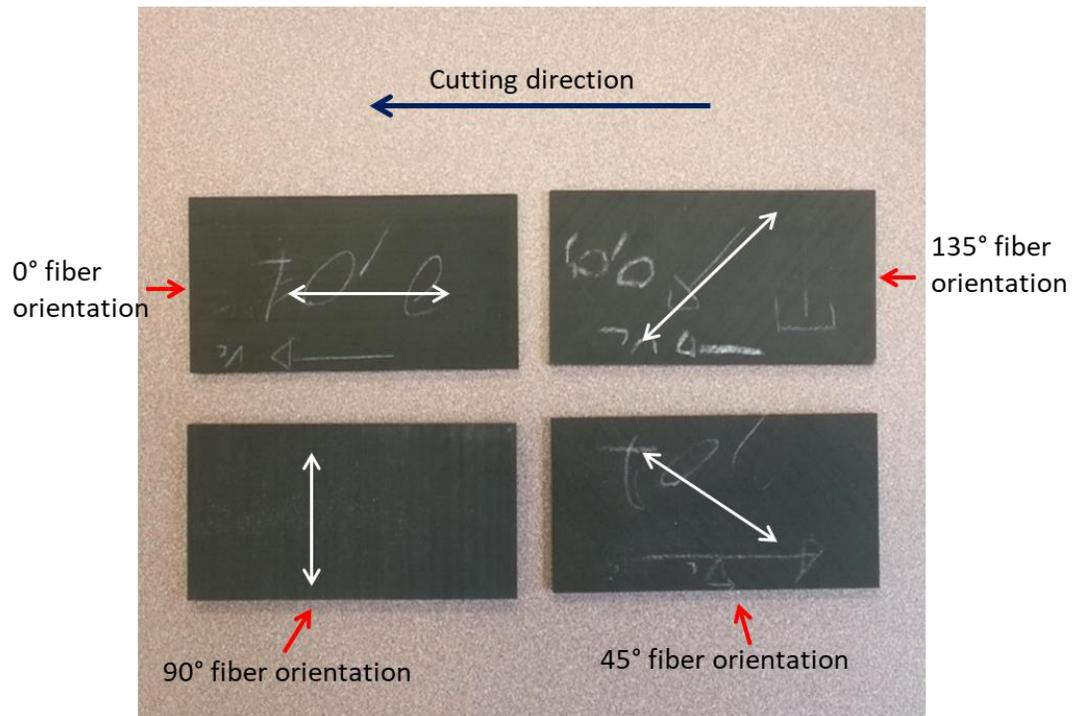


Fig. 2.1.4: Test specimens of different fiber orientations

The test specimens were initially manufactured by a previous PhD student, [Blanchet, 2015]. Many specimens were untouched which permitted us to utilize those specimens in this present research. The process used to manufacture these specimens is mentioned in Appendix A.

2.2. Developed Models

Research in engineering and science costs a lot of money and time, remarkably it is high if it is experimental research. In machining processes, experimental research cost money not only for manpower but also for the test specimens, test machines and related analyzing appliances. However, numerical simulation and modeling technologies can reduce the cost together with time hugely. Today in some cases numerical models can permit analyzing very complex processes which can be very difficult to understand experimentally.

Since composites are “designed material”, in the sense that the resulting desired properties are planned on the basis of the material constituents behaviors and performances, the development of accurate and reliable predicting methodologies in terms of constitutive behavior has been an active area of research for several decades [Nicola B. and Andrew R., 2006].

For this purpose, micro and macro-mechanical models have been developed to analyze the orthogonal cutting procedure which is discussed in this section 2.2. The first model is a micro-mechanical model and the second one is a macro-mechanical model. The micro-mechanical model permits to model the material with different phases (fiber or matrix) and allows giving different properties according to the phases. In this consideration, the micro-mechanical model is much representative to analyze the physical phenomenon. On the other hand, a macro-mechanical model has been developed using an anisotropic homogenized material which permits analyzing the machining loads measured during experimental tests.

2.2.1. Micro-mechanical Model

Generally, most of the micro-mechanical models in composite machining are constituted of three phases: the matrix phase, the fiber phase and interface phases (fiber-matrix interface). Here in this model different phases have been modeled differently. The fiber, Fig. 2.2.1-a, has been designed in round cylindrical shape like real fiber. The diameter is 7 μm and the length is kept 50 μm . The matrix is designed in rectangular shape in which some holes have been made in order to contain the fibers, Fig. 2.2.1-b. The dimension of the matrix is 92.32 μm long, 50 μm high and 30 μm wide and the diameter of the holes is 7 μm . The holes are created in random positions which can perfectly represent the real CFRP parts. The cutting tool is a rigid tool of which the rake and clearance angles are chosen according to the real tool geometry. The rake angle is 30° and the clearance angle is 7° near the tool tip and later 15° far from the tool tip, Fig 2.2.1-c. The cutting radius is 7 μm . Here there is no loss of material in the tool as it is a rigid part; as a result the angles and tool tip radius remain the same over the whole cutting distance.

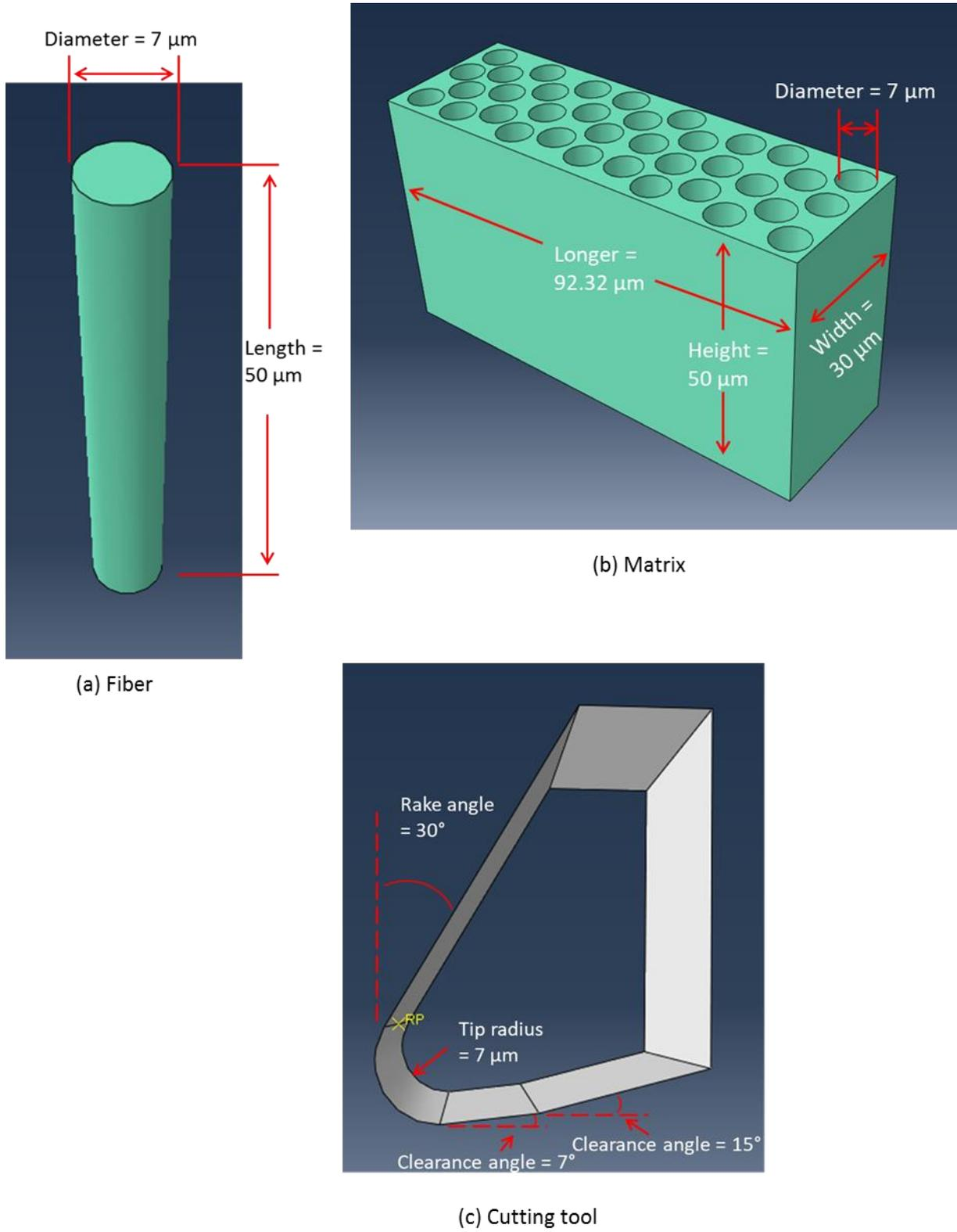


Fig. 2.2.1: Parts of the model, (a) fiber, (b) matrix, (c) cutting tool

2.2.1.1. Boundary Conditions and Meshes

In this configuration, the workpiece (fiber and matrix) is fixed and the cutting tool moves in one direction. The under edge of the workpiece ($y = Y_{\min}$) is clamped; all translations and rotations are constrained ($U_1=U_2=U_3=0, UR_1=UR_2=UR_3=0$). The displacement (at $x = X_{\min}$) is set with symmetry constrains according to the Y, Z plane ($U_1=0, UR_2=UR_3=0$). The two sides of the workpiece at $z = Z_{\min}$ and $z = Z_{\max}$ are set with symmetry constrains on the displacement according to X, Y planes ($U_3=0, UR_1=UR_2=0$) in order to introduce conditions close to plane strain, Fig. 2.2.2. The cutting tool is modeled as a rigid body with a geometry defined by the rake and clearance angles and the tool tip radius. A reference point was defined to control the movement of cutting tool with respect to the workpiece; the velocity of the tool was set to $0.2 \mu\text{m}/\mu\text{s}$. The other translations and rotations of the cutting tool are constrained ($U_2=U_3=0, UR_1=UR_2=UR_3=0$).

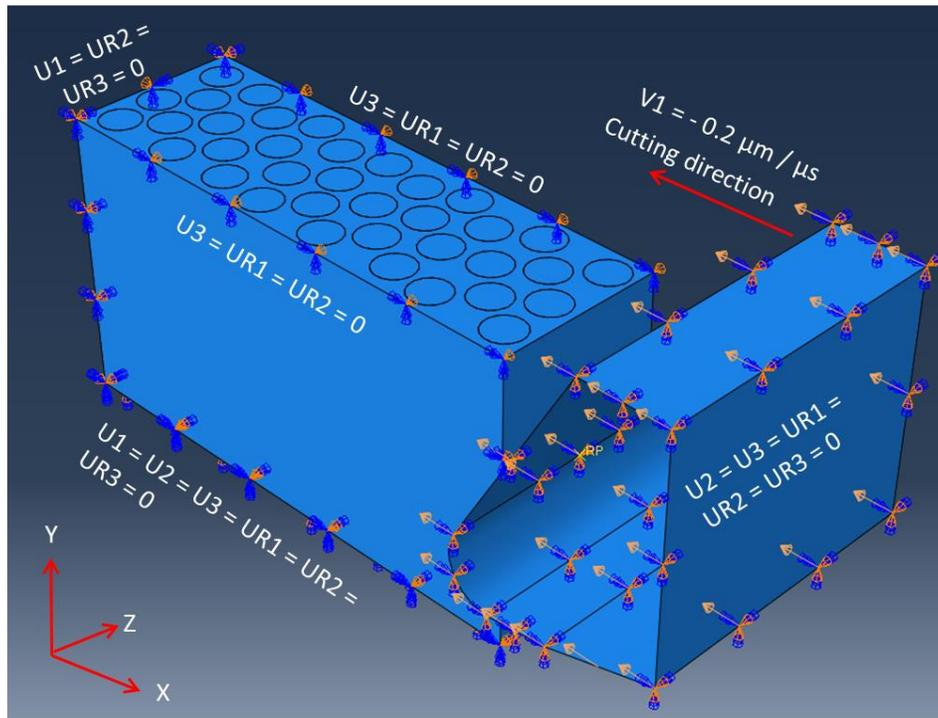


Fig. 2.2.2: Parts of the model, (a) fiber, (b) matrix, (c) cutting tool

The elements used are eight-node brick elements (C3D8R) for both the fibers and the matrix in 3D stress family. The element size is $0.8 \mu\text{m}$. For the cutting tool Discrete Rigid Element, R3D4 (4-node 3-D bilinear rigid quadrilateral) elements are used with $1.2 \mu\text{m}$ element size.

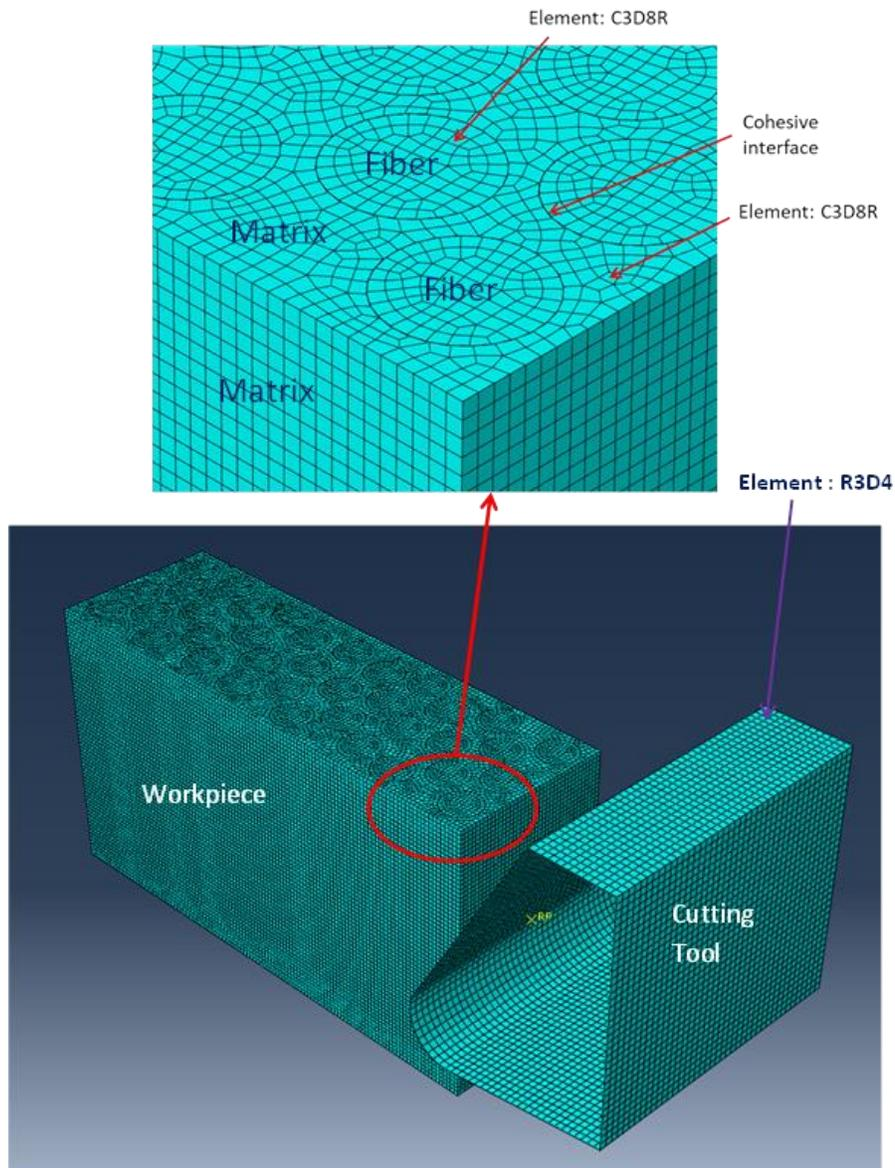


Fig. 2.2.3: Parts of the model, (a) fiber, (b) matrix, (c) cutting tool

2.2.1.2. Interaction Properties

General contact with Dynamic Explicit procedure is used. Global contact property is assigned between the cutting tool and the workpiece and individual properties are assigned to the fiber-matrix interface which behaves as a cohesive interface.

Tool-Workpiece Interaction

Tangential behavior with penalty friction formulation and hard contact (normal behavior) are used together. The friction coefficient is 0.3 and elastic slip stiffness is infinite. Two surface pairs of cutting tool and workpiece are used. In the first pair the first surface is the tool's outer surface and the second surface is the outer surface of all of the elements in the workpiece. In the second pair, all exterior faces of both workpiece and tool are used acting as self-interaction.

Fiber-matrix Interface (cohesive interaction)

Cohesive interaction is used in fiber-matrix interface. Quadratic traction criteria for damage initiation and energy type evolution are applied. Here the damage in interface is the interaction property. For cohesive surface, contact separation is δ . And traction (contact stress) is calculated as the ratio of Eq. 2.2.1.

$$t = \frac{\text{contact force } (F)}{\text{current area } (A) \text{ at each contact point}} \quad [2.2.1]$$

The linear elastic traction-separation behavior relates normal and shear stresses to the normal and shear separations across the interface before the initiation of damage. The used Stiffness Components for Cohesive Damage are as in Tab. 2.2.1.

K_n (normal)	K_s (first shear)	K_t (second shear)
10^5 MPa/mm	10^5 MPa/mm	10^5 MPa/mm

Table. 2.2.1: Stiffness values for cohesive damage

Here, K_n is Normal Stiffness Component, K_s and K_t are Shear Stiffness Components in first and second shear directions respectively.

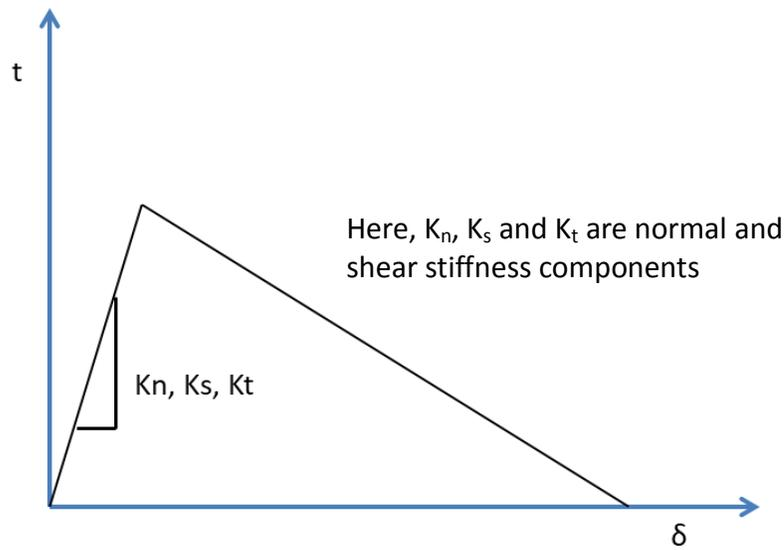


Fig. 2.2.4: Representation of shear stiffness components

Damage modeling of cohesive surfaces

In damage modeling, the failure mechanism consists of damage initiation criteria and a damage evolution law. Once a damage initiation criterion is met, damage can develop according to the damage evolution law. Fig. 2.2.5. shows the typical traction-separation response with failure mechanism.

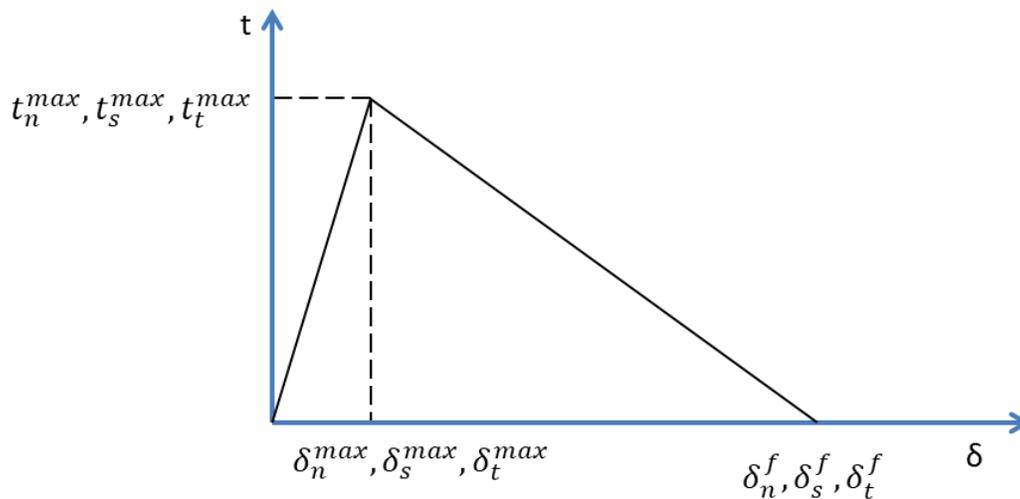


Fig. 2.2.5: Traction-separation response

Here,

$t_n^{max}, t_s^{max}, t_t^{max}$ are the peak values of the contact stress,

$\delta_n^{max}, \delta_s^{max}, \delta_t^{max}$ are the peak values of the contact separation and

$\delta_n^f, \delta_s^f, \delta_t^f$ are separations at failure

Damage initiation criteria

Damage initiation refers to the beginning of degradation of the cohesive response at the contact point. The degradation begins when the contact stress satisfy the damage initiation criterion. A value of 1 or higher indicates that the initiation criterion has been met.

Here in this model, a quadratic traction criterion has been used. Damage is assumed to initiate when this quadratic interaction function involving the contact stress ratios, Equ. 2.2.2, reaches 1.

$$\left[\frac{t_n}{t_n^{max}}\right]^2 + \left[\frac{t_s}{t_s^{max}}\right]^2 + \left[\frac{t_t}{t_t^{max}}\right]^2 = 1 \quad [2.2.2]$$

Here,

t_n is the normal contact stress in normal mode (X-X)

t_s is the shear contact stress in first shear direction (X-Z)

t_t is the shear contact stress in the second shear direction (X-Y)

In this model the values for Failure Stresses are as in Tab. 2.2.2.

$t_{n(max)}$	$t_{s(max)}$	$t_{t(max)}$
50 MPa	70 MPa	70 MPa

Table. 2.2.2: Failure stress in normal and shear modes

Damage evolution

The damage evolution law describes the rate at which the cohesive stiffness is degraded once the corresponding initiation criterion is reached. A scalar damage variable, D , represents the

overall damage at the contact point which evolves from 0 to 1 after the initiation of damage. The contact stress components are affected by the damage according to the equations below.

$$t_n = \begin{cases} (1 - D)\bar{t}_n \\ \bar{t}_n \end{cases} \quad [2.2.3]$$

$$t_s = (1 - D) \bar{t}_s \quad [2.2.4]$$

$$t_t = (1 - D)\bar{t}_t \quad [2.2.5]$$

Here, \bar{t}_n , \bar{t}_s and \bar{t}_t are the contact stress components predicted by the elastic traction-separation behavior for the current separations without damage. The evolution of damage under a combination of normal and shear separations across the interface as equation below [Abaqus user's Guide 6.14].

$$\delta_m = \sqrt{(\delta_n)^2 + \delta_s^2 + \delta_t^2} \quad [2.2.6]$$

Energy-based damage evolution method is used in damage evolution process. Here the damage evolution describes the degradation of the cohesive stiffness based on the energy that is dissipated as a result of the damage process (it is also called fracture energy). The values for Critical Energy Release Rate are chosen in this model following some previous research work at the laboratory, which are:

- Normal fracture energy, $G_n^C = 750 \text{ J/m}^2$
- Shear fracture energies, $G_s^C = G_t^C = 1250 \text{ J/m}^2$

The energy-based damage evolution criterion has been defined as a function of mix mode using Benzeggagn-Kenane form which is:

$$G_n^C + (G_s^C - G_n^C) \left[\frac{G_s}{G_T} \right]^\eta = G^C \quad [2.2.7]$$

Here

$$G_S = G_s + G_t \quad [2.2.8]$$

$$G_T = G_n + G_S \quad [2.2.9]$$

And η is a cohesive property parameter.

The damage variable D is linear and evolves from 0 to 1; it is defined Eq. 2.2.10.

$$D = \frac{\delta_m^f (\delta_m^{max} - \delta_m^0)}{\delta_m^{max} (\delta_m^f - \delta_m^0)} \quad [2.2.10]$$

Here $\delta_m^f = 2G^c / T_{eff}^0$ [2.2.11]

T_{eff}^0 is the effective traction at damage initiation and δ_m^{max} refers to the maximum value of the effective separation attained during the loading history.

2.2.1.3. Material Properties and Failure Criteria

The material properties are used following the properties of experimental workpiece. T800S/M21 carbon/epoxy is used for the experimentation which has intermediate modulus and high tensile strength. In this micro-mechanical model, the properties for fiber and epoxy matrix are used distinctly. The density of fiber is 1850 kg/m^3 and the elastic properties are given Tab. 2.2.3.

E11	E22	E33	Nu12	Nu13	Nu23	G12	G13	G23
250 GPa	50 GPa	50 GPa	0.27	0.27	0.45	10 GPa	10 GPa	3.75 GPa

Table. 2.2.3: Elastic properties of fiber

The failure parameters of fiber are used according to orthotropic material. The parameters are given in Tab. 2.2.4.

X1ft (tensile strength in fiber direction)	X1fc (compressive strength in fiber direction)	X2ft (tensile strength in transverse direction)	X2fc (compressive strength in transverse direction)	X3ft (tensile strength in transverse direction)	X3fc (compressive strength in transverse direction)	Sfc (ply shear strength)
2.5 GPa	1.7 GPa	0.5 GPa	0.8 GPa	0.5 GPa	0.8 GPa	1.5 GPa

Table. 2.2.4: Failure properties of fiber

Micro-mechanical model generates stress fields in the specimen, when the stress in an element reach the defined stress limit, then the element is considered deleted and the effort statement is considered equal to cutting effort. Here no damage criterion is used. The elements deletion criteria for fiber are:

Deletion or rupture in compression Eq. 2.2.12.

$$\left(\frac{\langle\sigma_{11}\rangle}{x_{1fc}}\right)^2 + \left(\frac{\langle\sigma_{22}\rangle}{x_{2fc}}\right)^2 + \left(\frac{\langle\sigma_{33}\rangle}{x_{3fc}}\right)^2 + \left(\frac{\langle\sigma_{12}\rangle}{s_{fc}}\right)^2 + \left(\frac{\langle\sigma_{13}\rangle}{s_{fc}}\right)^2 + \left(\frac{\langle\sigma_{23}\rangle}{s_{fc}}\right)^2 \geq 1 \quad [2.2.12]$$

Deletion or rupture in traction Eq. 2.2.13.

$$\left(\frac{\langle\sigma_{11}\rangle}{x_{1ft}}\right)^2 + \left(\frac{\langle\sigma_{22}\rangle}{x_{2ft}}\right)^2 + \left(\frac{\langle\sigma_{33}\rangle}{x_{3ft}}\right)^2 + \left(\frac{\langle\sigma_{13}\rangle}{s_{fc}}\right)^2 + \left(\frac{\langle\sigma_{23}\rangle}{s_{fc}}\right)^2 \geq 1 \quad [2.2.13]$$

M21 epoxy resin is used with fibers. It is a high performance and tough epoxy matrix which has excellent damage tolerance and high residual compression strength after impact [HexPly M21 Global DataSheet]. The density and modulus which are used in this model are shown in the Tab. 2.2.5.

Density	Young's Modulus	Poisson's Ratio
1200 kg/m ³	3.5 GPa	0.42

Table. 2.2.5: Elastic properties of matrix

For matrix rupture, von Mises failure criterion is used which states that if the von Mises stress is equal or greater than the stress limit of the same material, then the material will fracture (here in this model, the element will be deleted). The stress limit for failure is considered 50 MPa (0.05 GPa) and the von Mises definition is as Eq. 2.2.14. [Engineer's edge, 2018].

$$\sigma_v = \sqrt{\frac{1}{2}[(\sigma_{11} - \sigma_{22})^2 + (\sigma_{22} - \sigma_{33})^2 + (\sigma_{33} - \sigma_{11})^2 + 6(\sigma_{12}^2 + \sigma_{23}^2 + \sigma_{13}^2)]} \quad [2.2.14]$$

2.2.2. Macro Model

Macro-mechanical model does not require complex meshing which permits creating big model with fewer elements compare to micro-mechanical model. In CFRP machining, macro-mechanical models are familiar for analyzing cutting efforts.

2.2.2.1. Geometry and Boundary Conditions

The dimensions of the workpiece and the cutting tool have been modeled following the dimensions of the experimental workpiece and tool. A three-dimensional (3D) finite element (FE) model has been developed to analyze the machining forces and cutting induced damages on the machined surface. The workpiece has been modeled as a 3D deformable solid part. The bottom of the rectangular workpiece has been fixed by considering $U_x=U_y=U_z=0$, $UR_x=UR_y=UR_z=0$; the displacement and rotation in X direction (cutting direction) has been blocked by ($U_x=UR_y=UR_z=0$) and in Z direction (transverse direction) by ($U_z=UR_x=UR_y=0$) as in Fig. 2.2.6. In this model it is not essential to block in X direction (the workpiece in the experimentation remains blocked in Z direction by the holder).

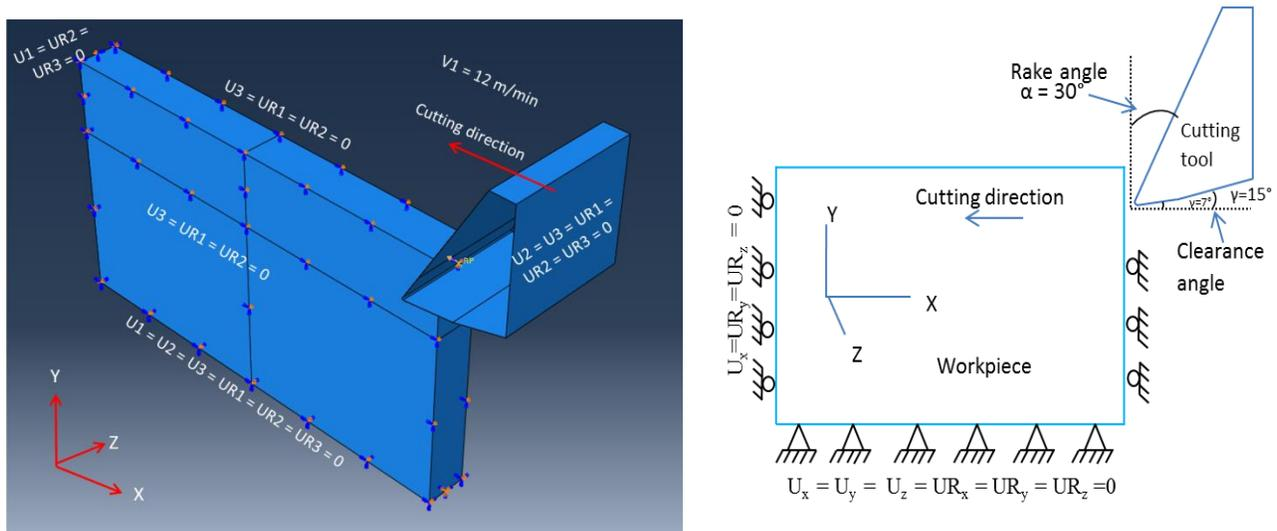


Fig. 2.2.6: Boundary conditions of macro-mechanical model

The cutting tool has been modeled as a discrete rigid shell part. The rake and clearance angles, $\alpha = 30^\circ$, $\gamma = 7^\circ$ and 15° have been used in all simulations. Two different clearance angles have been used at the same time (7° near the tool tip and 15° at the end) following the real geometry of the cutting tool. The displacement freedom of cutting tool has remained in X direction ($U_y=U_z=0$, $UR_x=UR_y=UR_z=0$) whereas a reference point is used to control the movement.

2.2.2.2. Contact Modeling

It should be noted that in numerical models it is very difficult to simulate ideal friction behavior. In this model a penalty friction formulation with friction coefficient 0.3 has been used following Coulomb friction model, Eq. 2.2.15, to define the interaction between the cutting tool and the workpiece. Coulomb friction hypothesis states a linear relationship between the shear stress and the normal stress when sliding occurs [Victor N., 2017]. It permits some relative motion; i.e., elastic slip, of the actual surface when they should remain sticking.

$$\tau_{lim} = \mu P + b \quad [2.2.15]$$

$$|\tau| \leq \tau_{lim} \quad [2.2.16]$$

Here τ_{lim} is the limiting shear stress, τ is the equivalent shear stress, μ , P and b are the friction coefficient, contact pressure and cohesion sliding resistance with zero normal pressure respectively.

2.2.2.3. Meshing, Adaptive Meshing and Distortion Control

For meshing, C3D8R elements in 3D stress family (8-node linear brick hexagonal) with reduced integration has been used for the workpiece throughout the simulations. The kinematic split of elements has been controlled by the average strain. 4 node 3D bilinear rigid quadrilateral elements, R3D4 (discrete rigid), has been used for cutting tool. In the cutting area, the mesh size has been kept small and, far below the cutting tool, the size of the mesh is comparably bigger (in order to reduce the number of elements), Fig. 2.2.7.

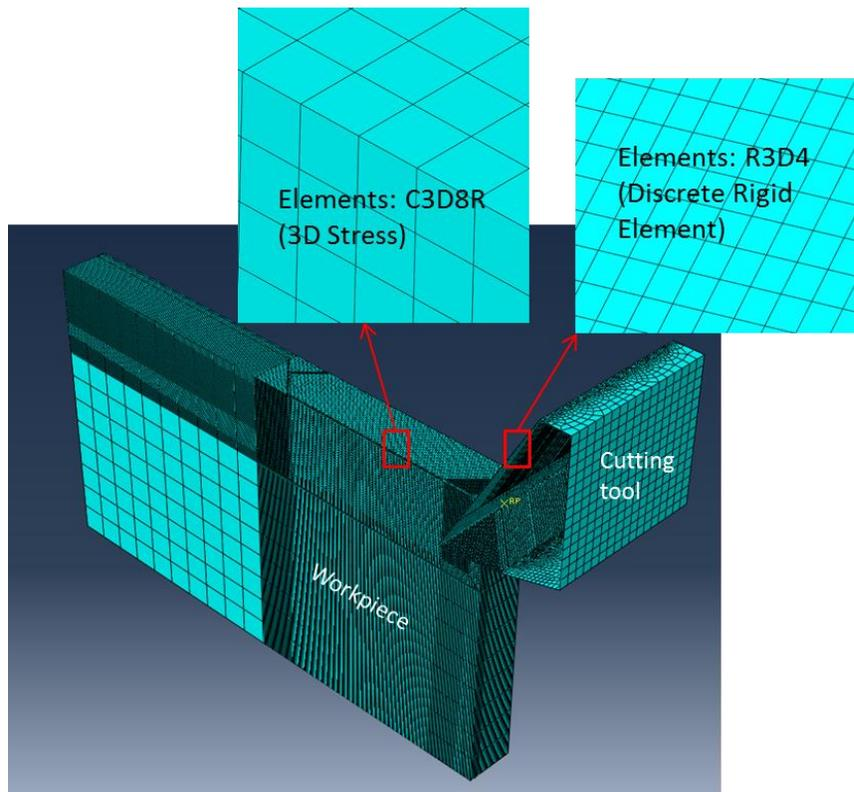


Fig. 2.2.7: Finite element mesh of macro model

Arbitrary Lagrangian-Eulerian (ALE) adaptive meshing has been used to retain high-quality mesh which permits the meshes to move independently of the material throughout the analysis. ALE combines the features of pure Lagrangian analysis and pure Eulerian analysis [Abaqus User Manuel, 2016] Fig. 2.2.8. It allows the material to flow through the mesh in order to keep good aspect ratio elements according to the Eq. 2.2.17.

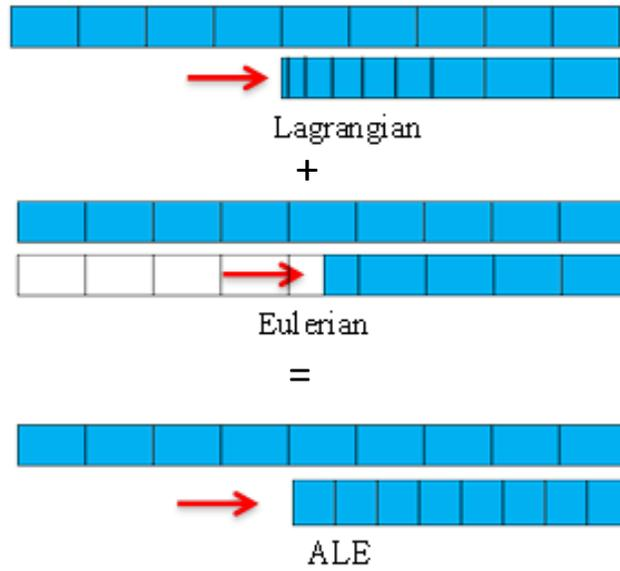


Fig. 2.2.8: Arbitrary Lagrangian-Eulerian (ALE) method

Here, X is the original position and X_{i+1} is the new position of a node, u_{i+1} its nodal displacement, is neighboring nodal positions and N^N are weighting functions.

The frequency used was 10 with remeshing sweep per increment 6 and the boundary region smoothing has been used as default values which are 30 for initial feature angle, 30 for transition feature angle and 60 for mesh constraint angle.

$$X_{i+1} = X + u_{i+1} = N^N X_i^N \quad [2.2.17]$$

2.2.2.4. Failure Criteria

An equivalent homogeneous anisotropic material has been used. Both the fiber and matrix materials are assumed to be locally isotropic. By using the homogenization procedure and the FEM, the global constitutive behavior of the corresponding orthotropic material has been framed by the symmetric stiffness matrix, as shown by Eq. 2.2.18.

$$\mathbf{S} = \begin{bmatrix} \frac{1}{E_{11}(1-d_1)} & \frac{-\nu_{21}}{E_{11}} & \frac{-\nu_{31}}{E_{11}} & - & - & - \\ \frac{-\nu_{12}}{E_{11}} & \frac{1}{E_{22}(1-d_2)} & \frac{-\nu_{32}}{E_{33}} & - & - & - \\ \frac{-\nu_{13}}{E_{11}} & \frac{-\nu_{23}}{E_{22}} & \frac{1}{E_{33}(1-d_3)} & - & - & - \\ - & - & - & \frac{1}{2G_{12}(1-d_4)} & - & - \\ - & - & - & - & \frac{1}{2G_{23}(1-d_5)} & - \\ - & - & - & - & - & \frac{1}{2G_{13}(1-d_6)} \end{bmatrix} \quad [2.2.18]$$

The failure modes have been managed by a Continuum Damage Mechanics (CDM) type constitutive law, which was first developed by [Matzenmiller, 1995] and later modified by [Ilyas, 2010] and [Blanchet, 2015]. From the different modes of rupture 5 damage criteria have been defined as $r_i, i = 1 \dots 5$.

- Tensile failure criterion in fiber direction,
- Compressive failure criterion in fiber direction,
- Crushing of matrix,
- Failure due to compression in transverse direction and,
- Delamination damage criteria.

This constitutive law was integrated in ABAQUS using a VUMAT sub-routine.

Tensile failure criterion in fiber direction:

$$\left(\frac{\langle \sigma_{11} \rangle}{X_{ft}} \right)^2 + \left(\frac{\sigma_{12}^2 + \sigma_{13}^2}{S_f^2} \right) = r_1 \quad [2.2.19]$$

X_{ft} is the tensile failure stress in fiber direction and S_f is the shear failure stress in shear direction.

Compressive failure criterion in fiber direction:

$$\left(\frac{\langle -\sigma_{11} \rangle}{X_{fc}} \right)^2 + \left(\frac{\sigma_{12}^2 + \sigma_{13}^2}{S_f^2} \right) = r_2 \quad [2.2.20]$$

X_{fc} is the compressive failure stress in fiber direction

Crushing of matrix:

$$\left(\frac{\langle -\sigma_{11} \rangle \langle -\sigma_{22} \rangle \langle -\sigma_{33} \rangle}{3Z_{fc}} \right)^2 = r_3 \quad [2.2.21]$$

Z_{fc} is compressive failure stress in Z direction

Failure due to compression in transverse direction:

$$\left(\frac{\langle \sigma_{22} \rangle}{Y_{ft}} \right)^2 + \left(\frac{\langle -\sigma_{22} \rangle}{Y_{fc}} \right)^2 + \left(\frac{\langle \sigma_{12} \rangle}{S_{12} + (-\sigma_{22}) \tan \beta} \right)^2 + \left(\frac{\langle \sigma_{23} \rangle}{S_{23} + (-\sigma_{22}) \tan \beta} \right)^2 = r_4 \quad [2.2.22]$$

Y_{ft} and Y_{fc} are the tensile and compressive failure stress in transverse direction and S_{12} and S_{23} are the shear failure stress. The coefficient of friction for material is $\tan \beta$ (in compression); thus, this parameter has an effect of material shear strength enhancement proportional to the compressive load.

Delamination failure criterion

$$\left(\frac{\langle \sigma_{33} \rangle}{Z_{ft}} \right)^2 + \left(\frac{\langle \sigma_{13} \rangle}{S_{13} + (-\sigma_{33}) \tan \beta} \right)^2 + \left(\frac{\langle \sigma_{23} \rangle}{S_{23} + (-\sigma_{33}) \tan \beta} \right)^2 = r_5 \quad [2.2.23]$$

Z_{ft} is tensile failure stress in Z direction

These 5 damage criteria, r_i , have been combined in a damage evolution variable \emptyset_i . If $\emptyset_i \leq 1$ then the damage evolution $\emptyset_i = 0$; otherwise, \emptyset_i evolves according to the damage criteria r_i and a damage evolution parameter m_i which is formed by the Eq. 2.2.24.

$$\emptyset_i = 1 - e^{-\frac{r_i}{m_i}} \quad [2.2.24]$$

Here, bigger m_i means rapid damage evolution (less energy will be needed for rupture once the criterion is reached) and smaller m_i means slow damage evolution (and more energy will be needed for rupture once the damage is started). This parameter represents the dissipated energy by rupture once the elastic limit r_i has been reached.

The damage evolution variables \emptyset_i is used to define the damage variables d_i by a coupling matrix, Eq. 2.2.25. The value of damage variables can vary from 0 to 1 which degrades Young modulus.

$$\begin{pmatrix} d_1 \\ d_2 \\ d_3 \\ d_4 \\ d_5 \\ d_6 \end{pmatrix} = \begin{pmatrix} 1 & 1 & 1 & 0 & 0 \\ 0 & 0 & 1 & 1 & 0 \\ 0 & 0 & 1 & 1 & 1 \\ 1 & 1 & 1 & 1 & 1 \\ 0 & 0 & 1 & 1 & 1 \\ 1 & 1 & 1 & 1 & 1 \end{pmatrix} \begin{pmatrix} \emptyset_1 \\ \emptyset_2 \\ \emptyset_3 \\ \emptyset_4 \\ \emptyset_5 \end{pmatrix} \quad [2.2.25]$$

$$d_1 = \emptyset_1 + \emptyset_2 + \emptyset_3 \quad [2.2.26]$$

The value of d_1 is defined by the Eq. 2.2.26, whereas the other values of d_i are defined by the Eq. 2.2.25. To limit the damage speed, two delay effect parameters, τ and α , have been introduced in the damage increment calculation Δd_n (Eq. 2.2.27).

$$\Delta d_n = \frac{\Delta t}{\tau} (1 - e^{-\langle d_n - d_{n-1} \rangle^+}) \quad [2.2.27]$$

The damage d_n increases from the previous damage time step (Δd_n) according to the Eq. 2.2.28.

$$d_n = d_{n-1} + \Delta d_n \quad [2.2.28]$$

2.3. Strain Measurement Process

2.3.1. Experimental Strain Measurement Process

The experimental setup has been instrumented with a Stereo Digital Image Correlation (S-DIC) device for strain measurement. The specimens were cut with the orthogonal cutting bench described in “section 2.1.1”. The main setup is Fig. 2.1.1, but in that setup a small modification was done regarding the mountings of cutting tool and the workpiece. A new mounting has been used which holds the workpiece up, Fig. 2.3.1. So the cutting tool has been hold down. In the new mountings the workpiece remains fixed and the cutting tool moves. The modification was done because in strain measurement process the workpiece needs to be fixed for better analysis. If the workpiece moves during image acquisition process, the Stereo Image Correlation does not give good result.

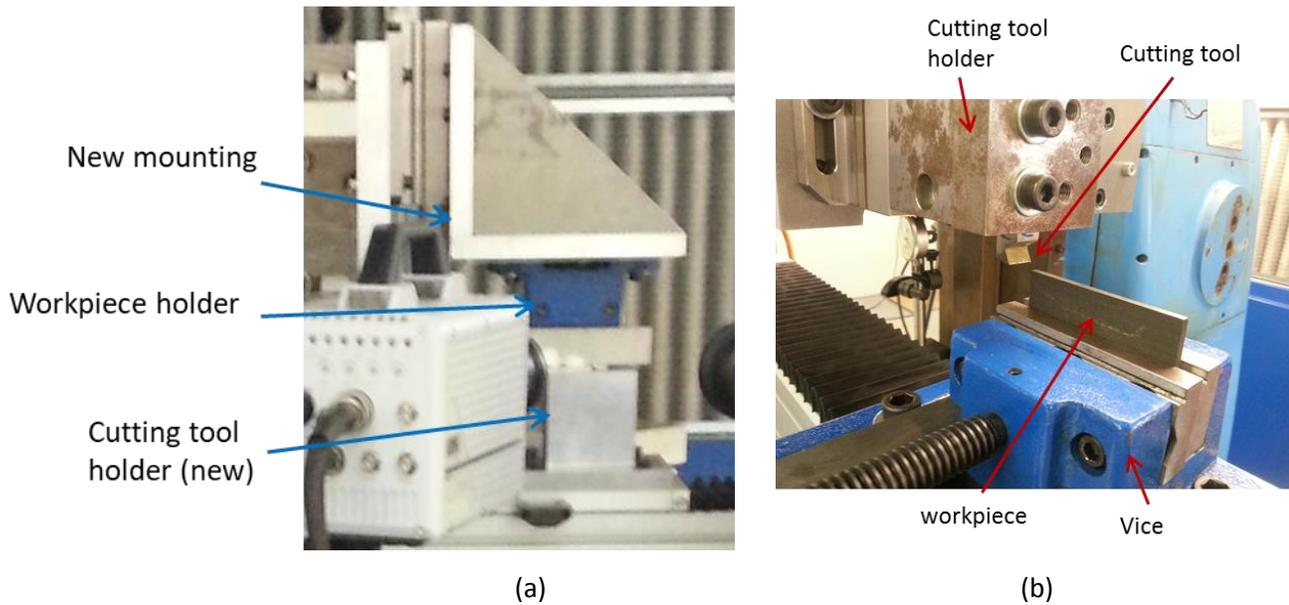


Fig. 2.3.1: (a) New mounting and (b) the old mounting to hold workpiece and cutting tool

For strain measurement, realistic cutting parameters have been chosen. The values are shown in Tab. 2.3.1. The same cutting tool and workpiece have been used as in “sections 2.1.3” and “section 2.1.4”.

Cutting speed	Cutting depths	Fiber orientation
3 m/min	50 μm , 100 μm , 200 μm and 300 μm	0°, 45°, 90°, 135°

Table. 2.3.1: Cutting parameters for strain analysis

Calibration

A 9 x 9 (9 points horizontally and 9 points vertically) laser etched glass calibration grids (combination of glass target and backlit) system has been used for the S-DIC system calibration. The distance between each two points is 1.78 mm, shown in Fig. 2.3.2.

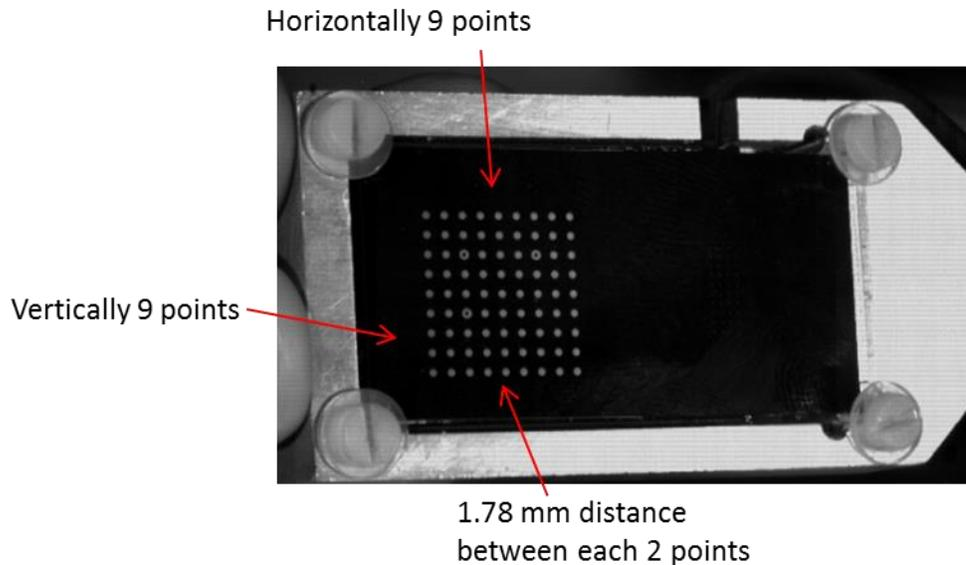


Fig. 2.3.2: 9 x 9 backlit glass calibration grid for stereo calibration

For analysis VIC-3D has been used. A user interface of VIC-3D is shown in Fig. 2.3.3. It presents a wide range of output data. In this present analysis the principal variables are mainly strain variables ϵ_{xx} , ϵ_{yy} and ϵ_{xy} where the strain is defined by the change in length, divided by initial length.

Here,

- ϵ_{xx} is the normal strain in the X-direction
- ϵ_{yy} is the normal strain in the Y-direction and
- ϵ_{xy} is the shear strain in the XY directions.

A positive strain indicates that the material has expanded, a negative one indicates that the material has contracted. Positive normal strains are referred to as tensile, while negative strains are compressive (not applicable in shear strain).

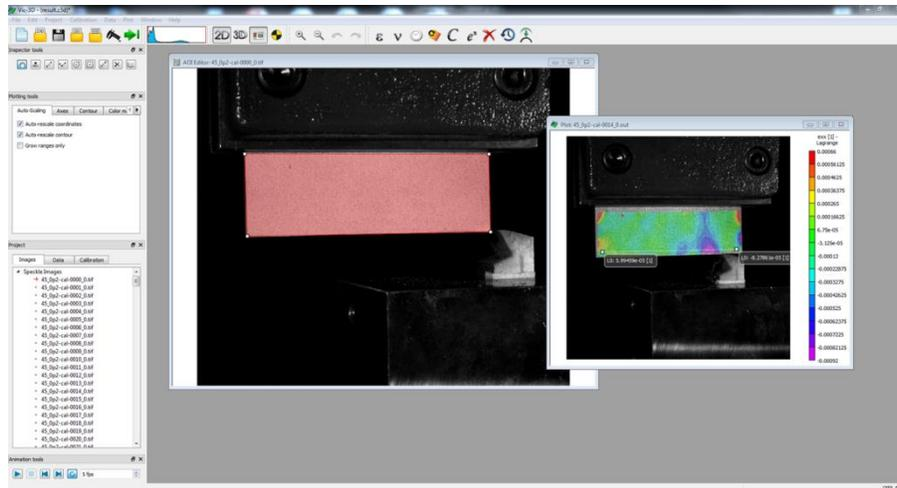


Fig. 2.3.3: User interface of VIC-3D

Two different ways have been used to extract the strain values.

- The first way is to show the strain in five places at 3 mm distance along the cutting line. This way shows the strain values as well as the maximum strain concentration area visually.
- In a second way, the strain values have been taken along a line at 3 mm distance from the cutting path. This way is to make a comparison with the numerical strain.

First Way of Strain Measurement

This measurement has been done at five places on each workpiece. The first one is at the beginning of the cut, the third one is at the middle of the cut, the fifth one is near the end of the cut and second and fourth are in between first and third, and third and fifth respectively (a schematic representation of the process is shown in Fig. 2.3.4). Each measurement has been done on a 10 mm × 5 mm area keeping the middle part of the measuring area at a 3 mm distance from the tool tip position (cutting line). On each measuring area, the maximum and minimum values of E_{xx} , E_{yy} and E_{xy} are recorded and plot, Fig. 2.3.4.

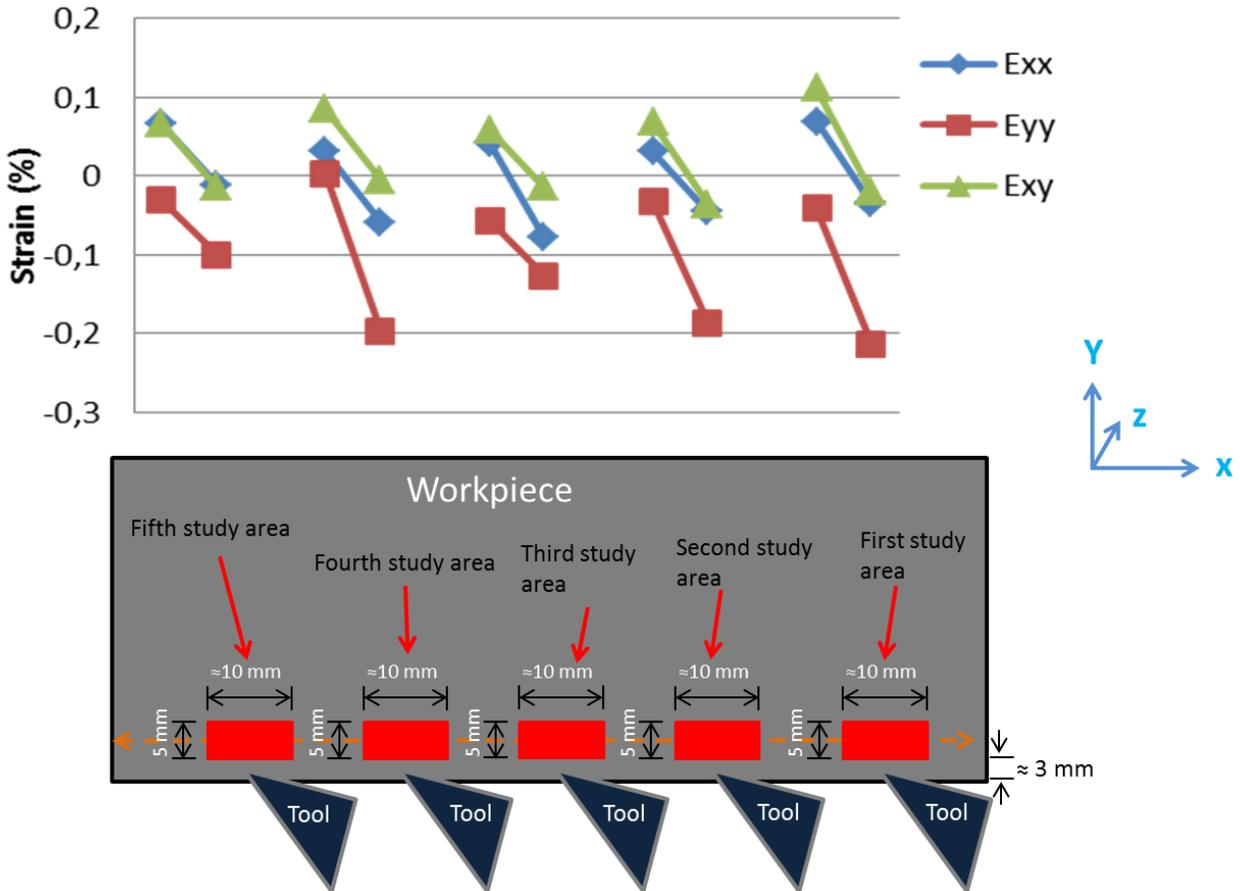


Fig. 2.3.4: Schematic view of the study areas in experimental strain analysis.

Second Way of Strain Measurement (to compare with numerical strain)

In the second measurement, the strains have been measured along a line at 3 mm distance from the cutting path. Around 80 values have been taken from the beginning to the end of cut, as shown in the Fig. 2.3.5. The strain values for E_{xx} and E_{yy} are the maximum tensile and compressive strains. This second measuring process has been chosen for comparison between numerical and experimental responses. As like in experimentation, the strains in numerical models have been measured at 3 mm distance along the cutting line, and there each element gives a discrete strain values.

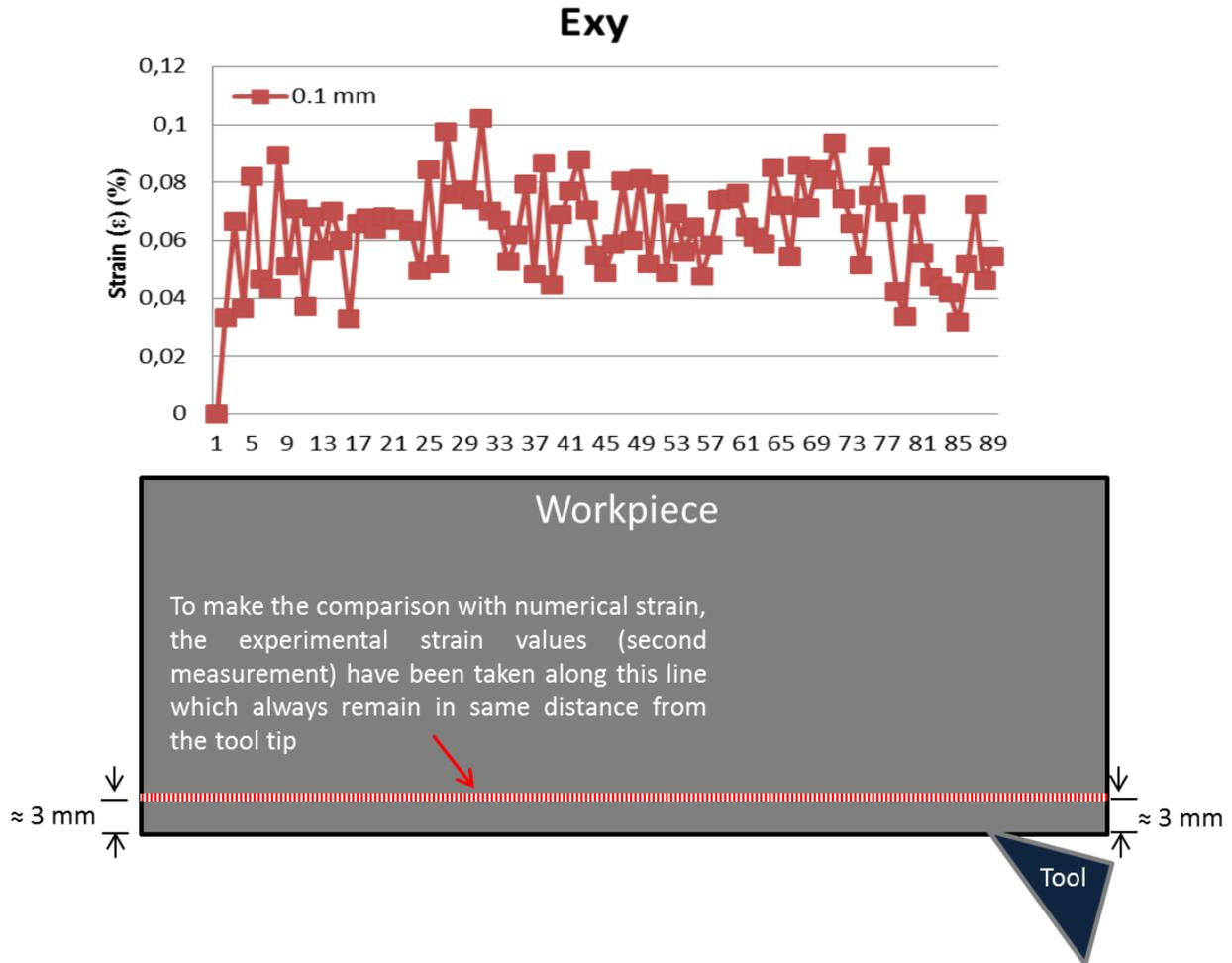


Fig. 2.3.5: Schematic view of the second experimental study path to compare with numerical strain.

2.3.2. Numerical Strain Measurement Process

For numerical strain measurement, the macro-model presented “section 2.2.2” has been used. As the maximum stress-strain area remains near the vicinity of the cutting tool, a set of elements below the cutting tool has been chosen, Fig. 2.3.6.

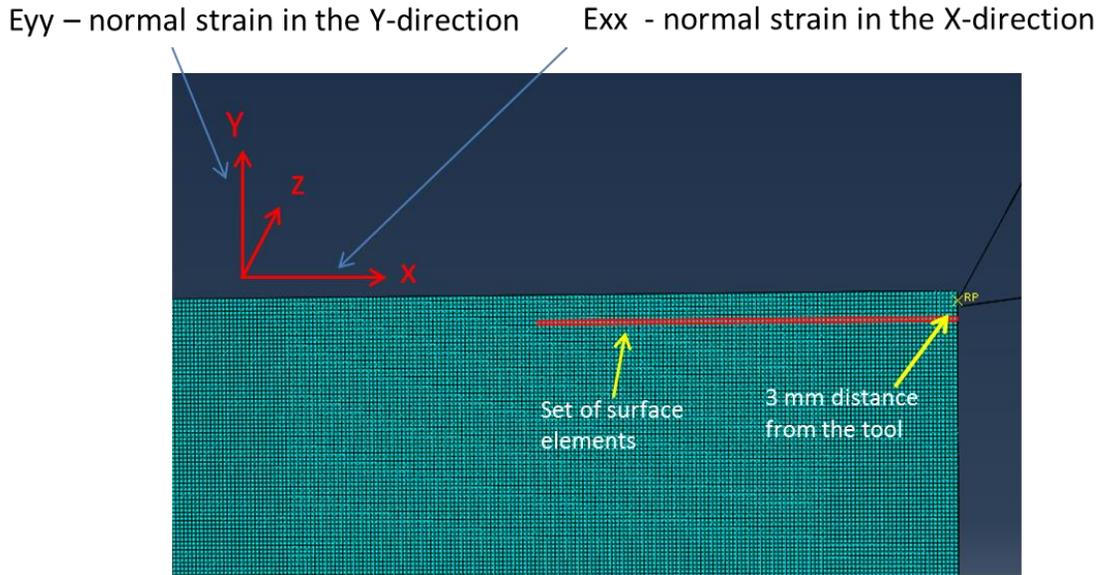


Fig. 2.3.6: Set of chosen elements below the cutting tool

Here logarithmic strain components are analyzed and the strain is the maximum strain which an element faces during the cutting course. Logarithmic strain provides the correct measure of the final strain when deformation takes place in a series of increments, taking into account the influence of the strain path [David Rees, 2006]. The logarithmic strain (ϵ) which is also called true strain [Hencky H., 1928] considers an incremental strain Eq. 2.3.1.

$$\delta\epsilon = \frac{\delta l}{l} \quad [2.3.1]$$

The logarithmic strain is found by integrating this incremental strain

$$\int \delta\epsilon = \int_{L_0}^L \frac{\delta l}{l} \quad [2.3.2]$$

$$\epsilon = \ln\left(\frac{L}{L_0}\right) = \ln(\lambda) = \ln(1 + e) \quad [2.3.3]$$

Here,

$$e = \frac{L - L_0}{L_0} \quad (e \text{ is the engineering strain}) \quad [2.3.4]$$

$$\lambda = \frac{L}{L_0} \quad [2.3.4]$$

Results and Discussion

2.4. Strain Field Analysis

2.4.1. Experimental Results

It is clear, Fig.2.4.1, that the distribution of the strain over the workpiece is not constant. The value changes from place to place and the maximum strain is located near the vicinity of the tool tip and this strain field moves forward with the movement of the cutting tool. Five values of both the tensile and compressive strains for 0.05 mm cutting depth of 45° fiber orientation are clearly visible on the surface of the workpiece in Fig. 2.4.1. It is seen that the tensile strain of E_{xx} remains in between 0% and 0.1% and the compressive strain remains in between 0 and -0.1%.

Fig.2.4.1 (E_{xx}), a compressive X-X strain occurs at forward position of the tool tip and a tensile strain at the backward position of the tool tip. The forwarding movement of the tool compresses the materials in front of the tool tip in X-X direction while the immediate backward area of the tool which just got cut remains in tension. So it is obvious that the forward area of the tool will face compressive strain and the immediate backward area face tensile strain. On the other hand, the normal strain in Y direction (E_{yy}) is always negative which means that in this direction, the strain is always compressive and the value reaches a maximum of -0.2%. Y direction is the vertical direction in which the tool tip generates a compressive stress zone on the material which is later responsible for the spring back effect. This phenomenon is visible in the Fig. 2.4.1.

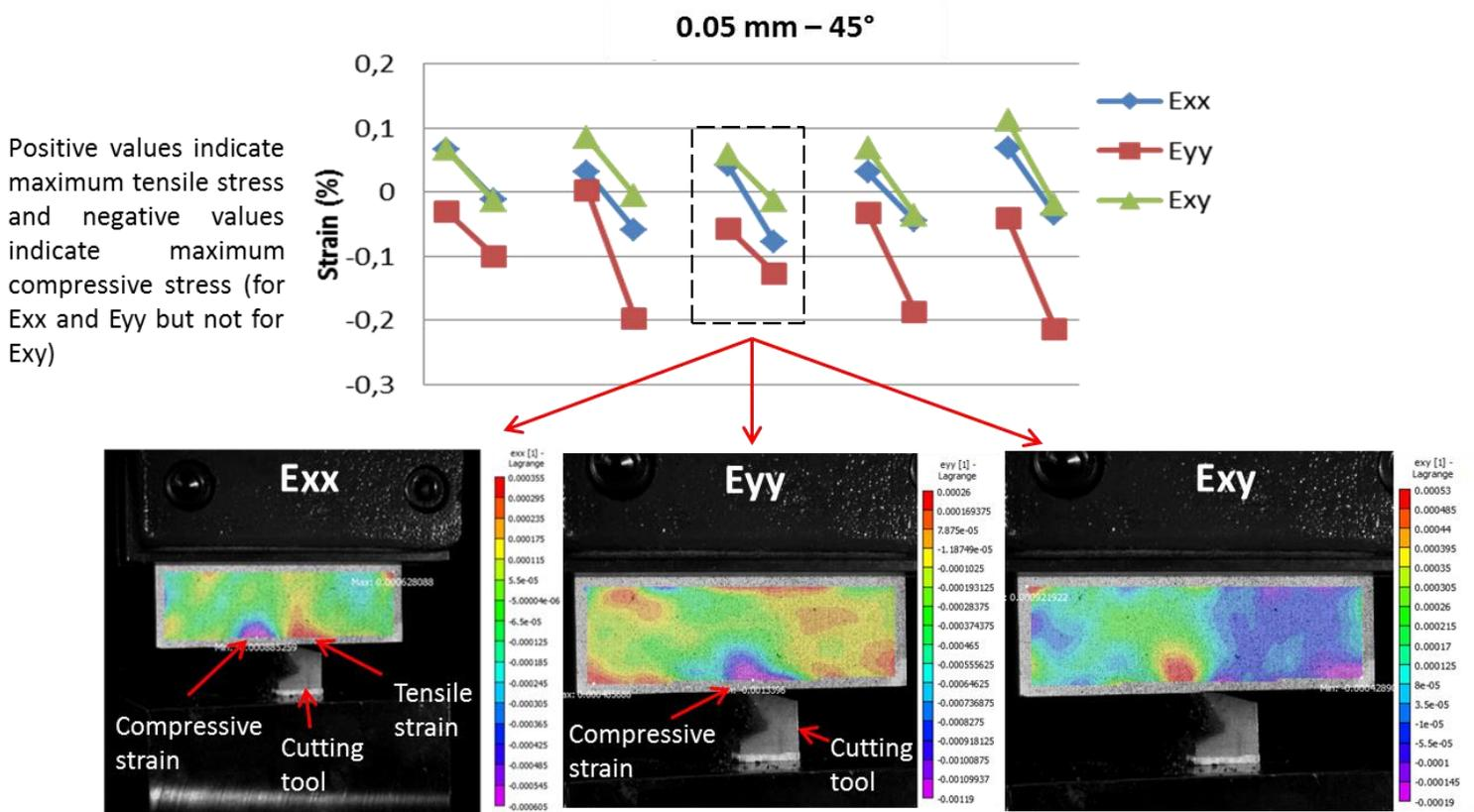


Fig. 2.4.1: Strain fields and maximum and minimum strain values at 5 particular locations as the tool moves for 0.05 mm depth cut of 45° fiber orientation (the measuring system is shown in Fig. 2.3.4)

Fig. 2.4.2, for the same cutting depth (0.05 mm) at 90° fiber orientation the maximum strain concentration area remains almost the same for Exx and Exy but in Y direction (Eyy) it is different. The compressive strain in X direction in the workpiece remains at the forward direction of the tool while the tensile strain at the immediate backward direction, (the same found in 45° fibers orientation) except for the levels of traction and compression which are significantly higher in the 90° case; this is clearly due to the fibers that transfer the cutting load in the sample directly in the X direction.

However, for Eyy it is seen that the value of generated compressive strain varies along the length of the workpiece and the strain concentration zone does not remain immediately upward of the tool position. The main reason behind this behavior is that at 90° fiber orientation the fibers are positioned vertically (transversely from the cutting direction), so the vertical compressive action of the tool tip is sheared very locally on the top of the fibers. Another reason behind this action is that during cutting at 90° fiber position the newly generated fiber head (on newly generated surface) remain debonded from the matrix (which decreases the stiffness of the newly generated surface); as a result the stress is locally absorbed instead of

shearing in the surrounding area. Also at 45°, the interaction between the tool and the fibers as the tool moves forward tends to press the sample upward; this phenomenon is not present at 90° fibers orientation leading to smaller compressive strain in the Y direction.

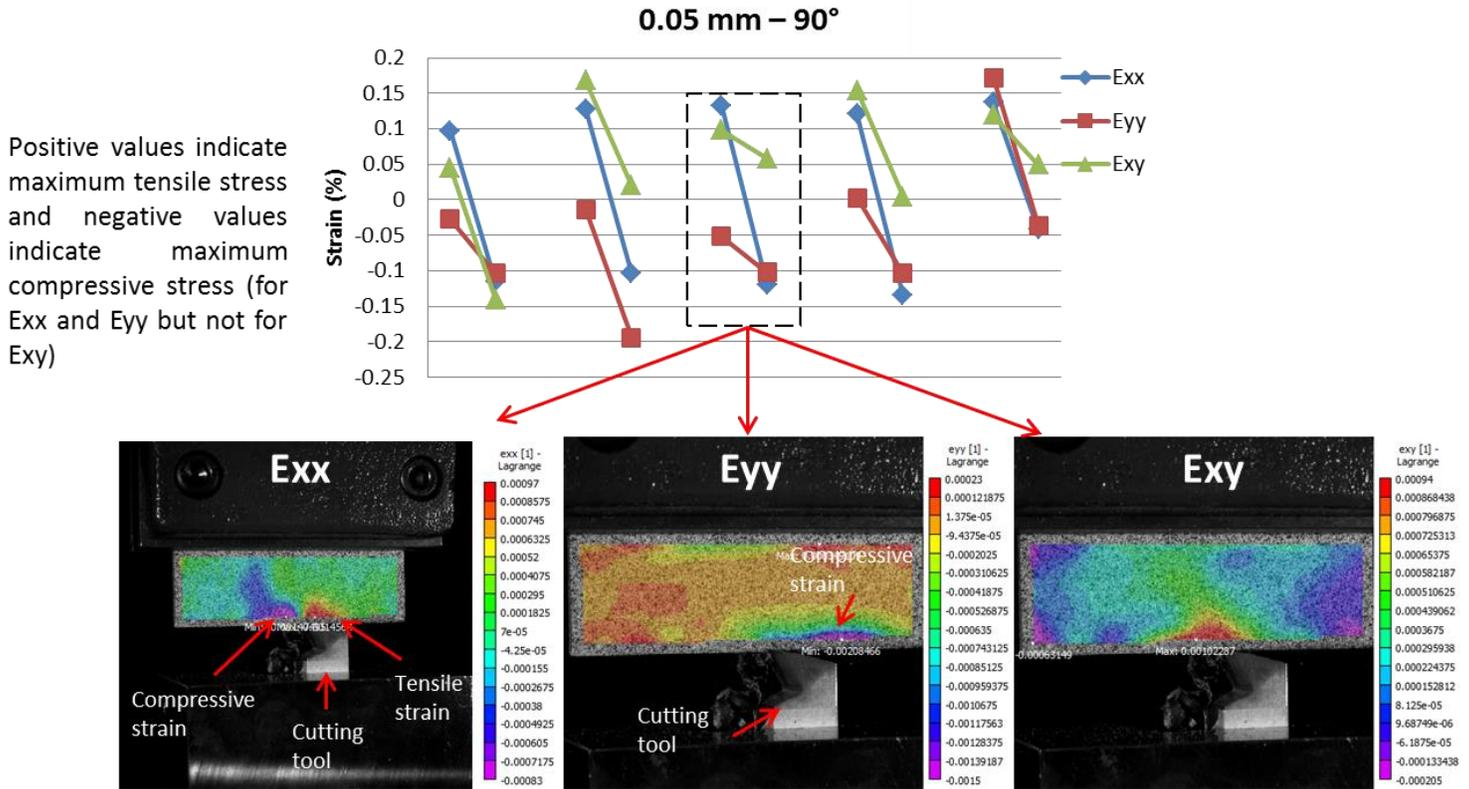


Fig. 2.4.2: Strain fields and maximum and minimum strain values at 5 particular locations as the tool moves at 0.05 mm cut of 90° fiber orientation

The strain values at 135° fiber orientation are higher than any other fiber orientation. Among Exx, Eyy and Exy the values of Exx is lower (compare to Eyy and Exy as can be seen in Fig. 2.4.3). At this particular material orientation, the fibers are inclined at -45° to the cutting direction presenting a strong obstacle to the tool tip, so in front of the tool tip, the material gets strongly compressed before getting cut while the newly generated surface (behind the tool tip) remains in tension (once the material get cut and the tool pass over, the newly generated surface gets rid from high compressive stress). In this particular phenomenon, the compressive strain in Exx is generated in front of the tool tip while the tensile strain is generated to the upward as well as behind the tool tip. It should be noted that at the beginning of the cut the shear strain (Exy) remains at around 0.5% and increases along the cutting distance making around 1 % towards the end of the cut.

In case of Eyy, it is found that the maximum compressive strain reaches to -1.3% while the tensile strain does not rise more than 0.5 %. Unlikely any other fiber orientation, the location of the compressive strain does not lie immediately upward of the tool tip but behind the tool tip and the tensile strain is in front of the tool tip. In 135° fiber orientation, the domination strain is shear strain (Exy), and for compression is vertical strain (Eyy).

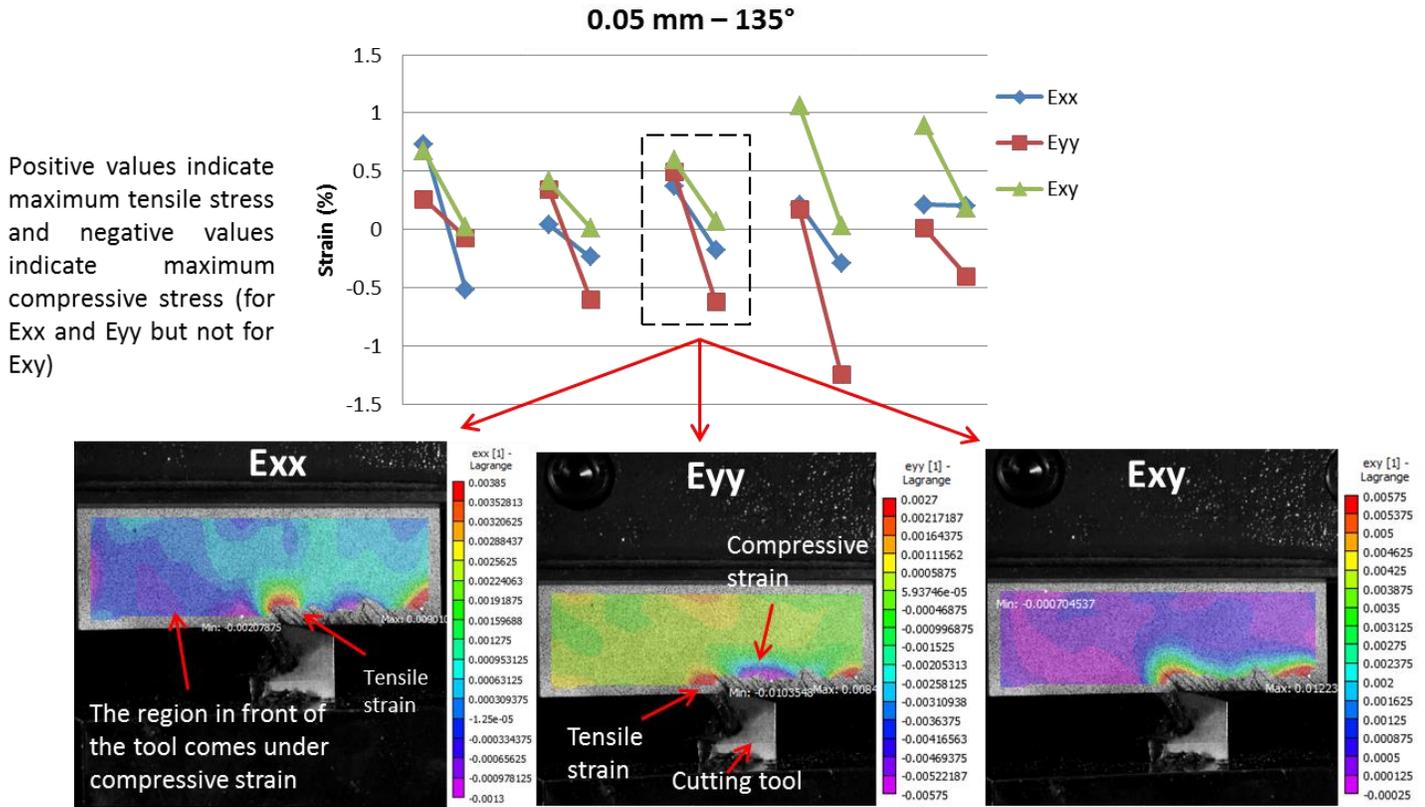


Fig. 2.4.3: Strain fields and maximum and minimum strain values at 5 particular locations as the tool moves at 0.05 mm cut of 135° fiber orientation

It is found that the strain Exx, both tensile and compressive, at 0° fiber orientation is generated randomly over the whole workpiece and the values fluctuate with the movement of the cutting tool. This particular behavior is seen because in the workpiece the fiber orientation was not exactly horizontal (not perfectly 0°) in this present research. The tool tip took more material along its forward movement which changes the depth of cut and the stress distribution became inhomogeneous over the cutting course. This behavior is seriously problematic if the cutting depth is comparably small; which is the case in this research (the cutting depth is 0.05 mm).

However, from the results it is seen that Exx strain is around 0.02% which is very low, Fig. 2.4.4. A similar scenario is found for the shear strain which reaches to maximum 0.04%. In case of Eyy both the tensile and compressive strain increase along the advancement of the cutting tool. The maximum value for tensile strain reaches 0.08 % and the compressive stress reaches 0.2%. This increase is nothing but because of the cutting depth's increment (as discussed earlier). Near the end of the cut, a sudden increase of the compressive Eyy strain is seen (the last value of Fig. 2.4.4). This particular increment is generated because the tool faced a sudden edge of material right after breaking of a chip (the edge is generated as the chip got broken, and this whole phenomenon arrives as the depth increase because of non-horizontal fiber). The new edge gets compressed resulting in high compressive strain.

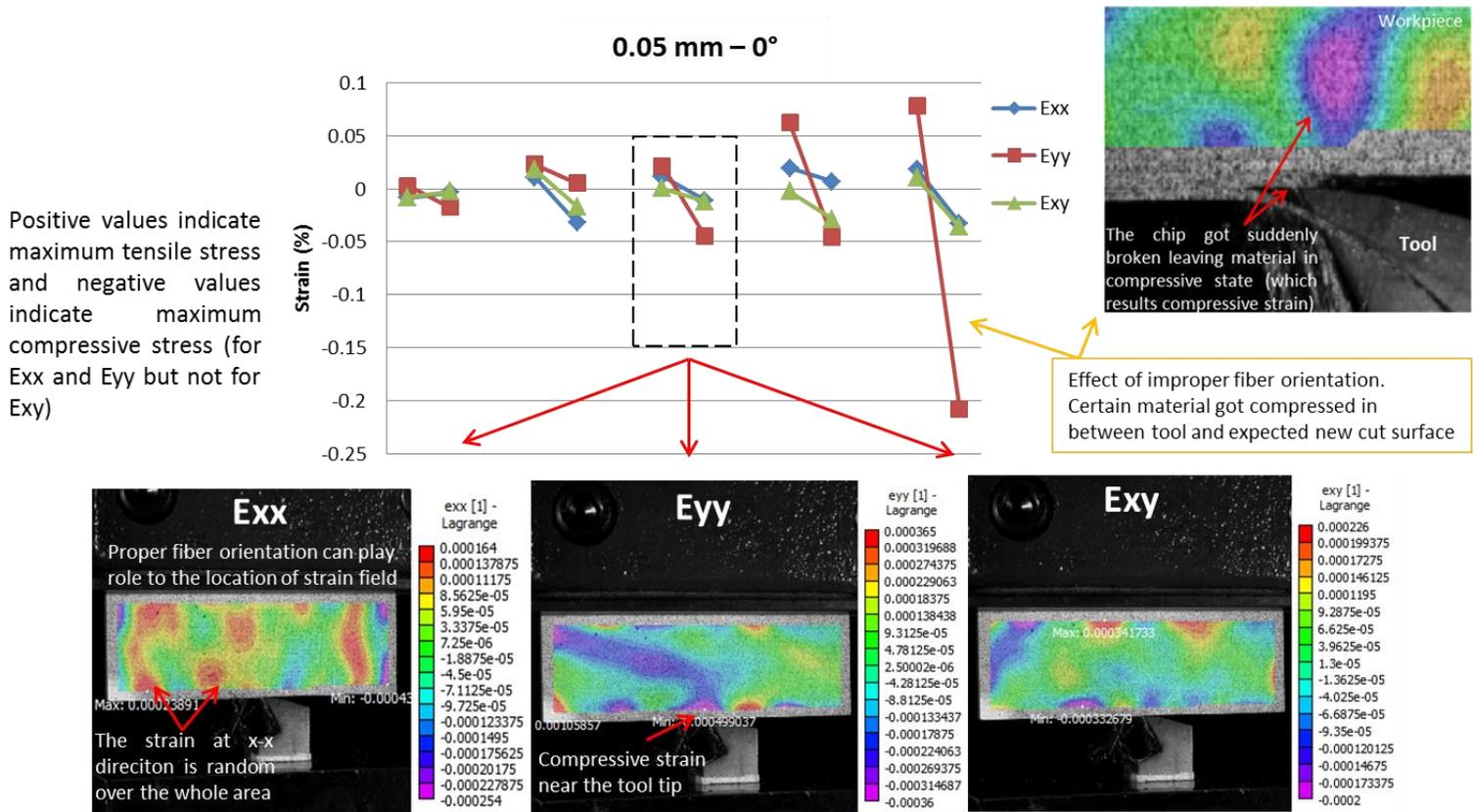


Fig. 2.4.4: Strain fields and maximum and minimum strain values at 5 particular locations as the tool moves at 0.05 mm cut of 0° fiber orientation

2.4.2. Comparison of Numerical and Experimental Results

A comparison of numerical and experimental strain is made here. If the comparison of Exx, Eyy and Exy is made for all cutting depths and fiber orientations it will be huge. So in order to

minimize the length of explanation the Exx strain is shown for 0° fiber orientation, Eyy for 90° fiber orientation and Exy for 135° fiber orientation. The cutting depths are 0.05 mm and 0.3 mm.

It is found that at 0° fiber orientation the strain values are very low both in numerical and experimental results. At 0.05 mm cut, the experimental strains lie in between 0.02% and 0.03% along most of the cutting length while in numerical model it fluctuates between 0.04% and 0.09%, Fig.2.4.5-(0.05 mm depth). The experimental average strain always remains lower than the numerical values. Nevertheless, these values are quite low in composite machining. However, near the end of cut, the maximum strain goes near 0.2% which occurred because of a sudden compressive zone in the workpiece (shown in Fig. 2.4.4.). It is related to proper fiber orientation.

At 0.3 mm cut, both the numerical and experimental values fluctuate along the cutting distance ranging the strain values from 0.03% to 0.1% in experimentation and 0.05% to 0.13% in numerical model. In the model, the strain is a bit higher than the experimental strain.

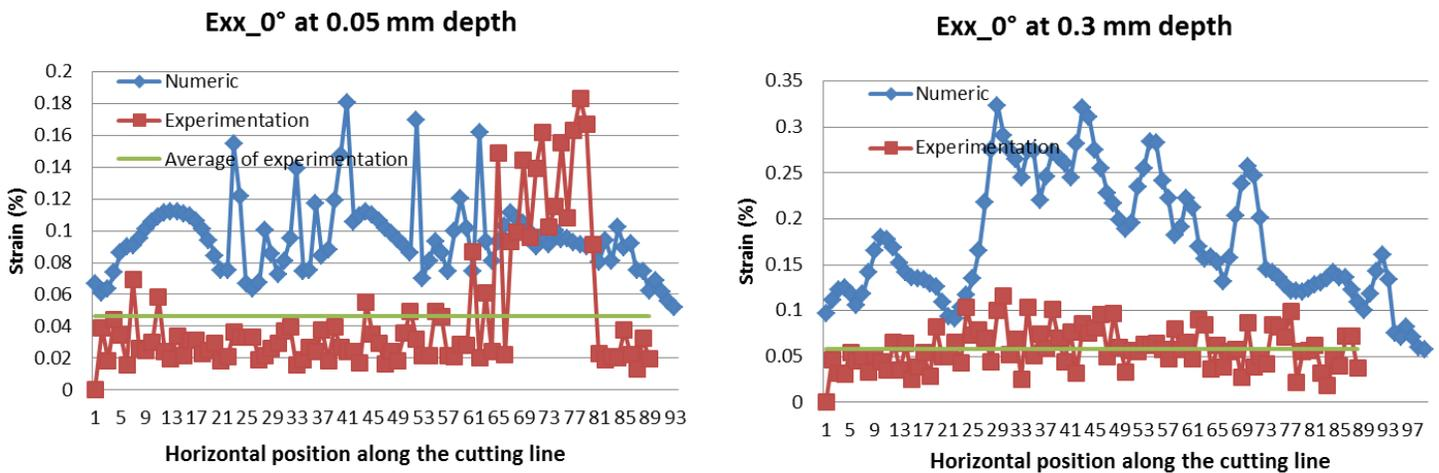


Fig. 2.4.5: Comparison of numerical and experimental normal strain in X direction at 0.05 mm and 0.3 mm cut for 0° fiber orientation.

The Eyy strain is found much higher than Exx. The comparison is made for 0.05 and 0.3 mm cut of 90° fiber orientation. The experimental strain looks stable compare to numerical strain. The experimental Eyy strain at 0.05 mm cut lies from 0.01% to 0.1% whereas the numerical values fluctuate from 0.1% to 0.7% which is much higher than experimental values. As the orientation of fiber is considered 90° , the stress distribution in the workpiece (in front of the tool tip) is not homogeneous. The strain at each element in the elements' set at the measured distance (3 mm downward from the cutting line, explained in Fig. 2.3.6) is not equal.

The same tendency is seen at 0.3 mm cut but remarkably the experimental strains are a bit higher which lie around 0.1% over the cutting length. However, the numerical strains are higher than experimental strain.

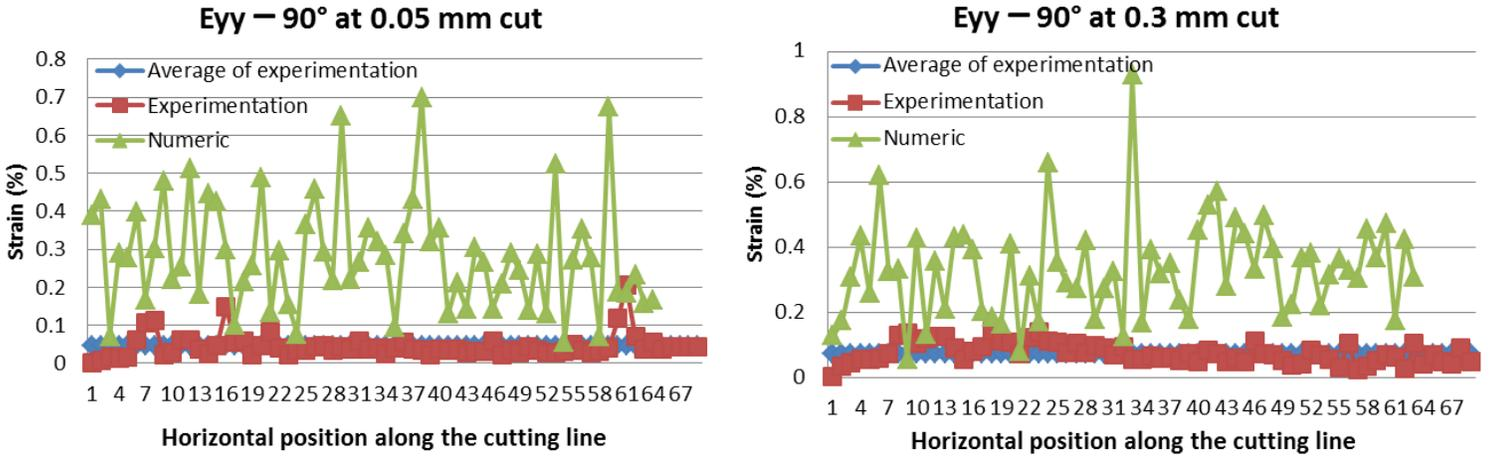


Fig. 2.4.6: Comparison of numerical and experimental normal strain in Y direction at 0.05 mm and 0.3 mm cut for 90° fiber orientation.

So here two remarks can be made. The first one is, even though the cutting depth increases, the strain does not increase hugely. And the second one is, the strain in numerical model remains higher than experimental strain which is because the macro model does not represent exactly the real phenomenon. So there is a deviation between the values.

At last, the shear strain is compared to the same cutting depths but at 135° fiber orientation. At 0.05 mm cut it is found that both the numerical and experimental strains have almost the same values which are at around 1.2%, as can be seen in Fig. 2.4.7. 1.2% strain is considered as a high value but as at 135° fiber orientation the fibers are inclined at -45° opposite to the cutting direction, the fibers get bend towards the cutting direction before being cut. This bending phenomenon increases the shear strain in material.

The same tendency is found at 0.3 mm cutting depth, Fig. 2.4.7, but here it is seen that both numerical and experimental strain increases with the forward motion of the cutting tool. At 0.3 mm depth, the generation of deformation, crack in the newly generated surface is much more than those at 0.05 mm cut. The more the tool moves forward, the longer the cracks are generated and the newly generated surface faces more deformation. As a result, the strain also increases accordingly. That is why it is seen that both the numerical and experimental strain increase along with cutting length. However, here the numerical and experimental strains have the same tendency of increment.

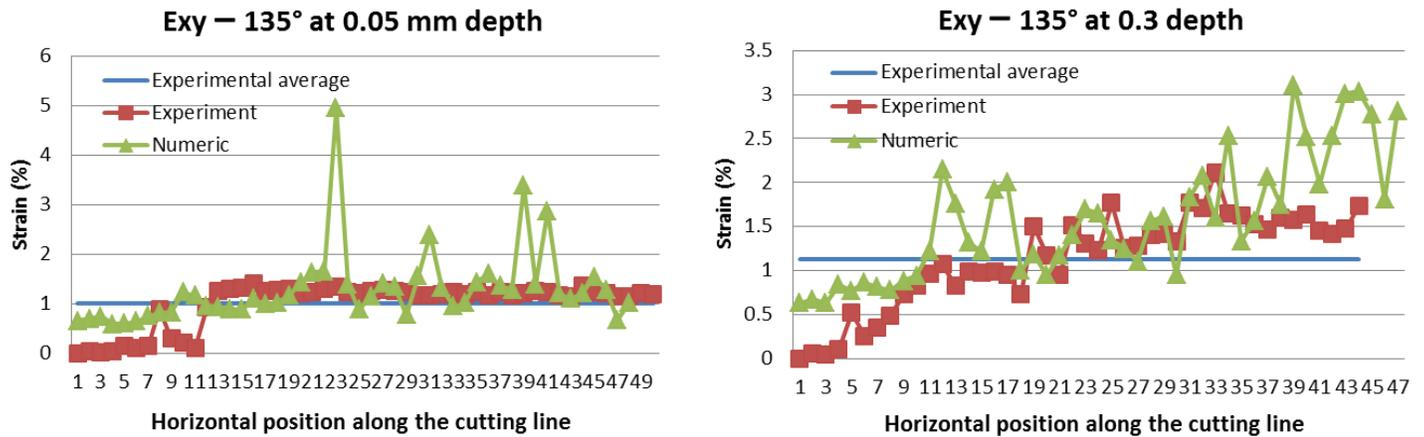


Fig. 2.4.7: Comparison of numerical and experimental shear strain in X-Y direction at 0.05 mm and 0.3 mm cut of 135° fiber orientation.

2.5. Chip Formation Mechanism in Orthogonal Cutting of CFRP

A good understanding of the chip formation mechanism of Carbon Fiber Reinforced Polymer (CFRP) in orthogonal cutting can reveal the reason for many machining induced defects in manufactured parts. To understand the mechanics of chip formation of metal machining much work has been done over the past century and the same technique has been used to study composite machining but not much success was found [Ahmad, 2009]. [Koplev, 1980] was the first in 1980 to conduct a series of experiments under orthogonal cutting of carbon fiber-reinforced polymer composites (CFRP).

Many explanations on chip formation mechanisms have been found in literature including distinguishing fiber orientation but a fundamental explanation is missing. Composite materials are not homogeneous and the chip formation process in machining fiber-reinforced polymers (FRP) is significantly different from that in machining of metals. The general idea of chip formation analysis is primarily based on the concept that a shear plane extends from the tip of the cutting edge and runs upward to the free surface of the workpiece. [Koplev et al., 1983] and [Lopresto et al., 2017] mentioned that chip formation process in machining FRPs is critically controlled by the fiber orientation and the cutting edge and rake angle but they did not explain what will be the effect if the fiber orientation and rake angle are changed. [Alaiji et al., 2015] supported the theory of Koplev and added that it is a series of fractures observed in the fibers. Similar observations were later made by several authors [Rao et al., 2008] [Zitoune et al., 2005] but a fundamental explanation of how fibers get cut locally is missing.

According to [Liu et al., 2012], bending-induced fracture occurs ahead of the cutting edge and perpendicular to the fiber direction. A small distinct chip segment is thus formed and the process repeats itself. Their theory seems a general concept which will not be the case for all fiber orientations. [Pramanik et al., 2007] said that chip separation occurs when the strain value of the leading node is greater than or equal to a limiting value at MMC. [Youliang et al., 2016] investigated the effect of depth of cut on chip formation mechanism in machining of CFRP by using 10 μm , 30 μm , 50 μm depth of cut. These cutting depths are too low for industrial use.

In this present research, an all-inclusive fundamental explanation of the course of chip formation has been done based on both experimental observations as well as micro-mechanical numerical modeling. It has been found that the course of the chip generation is divided into four steps. The steps are sequential and do not depend on the cutting depth.

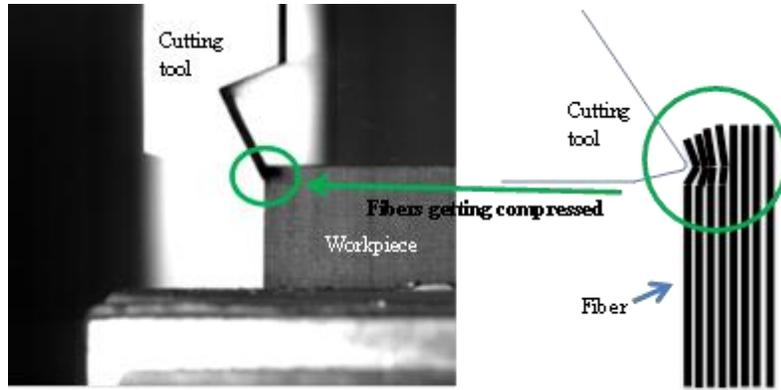
2.5.1. The Course of Chip Formation

The common concept of chip formation mechanism in metal is based on the theory that a shear plane extends from the tip of the cutting edge and runs upward to the free surface of the workpiece. However, in this analysis it was found that the chip formation of CFRP is critically controlled by the fiber orientation and the rake angle; and the same phenomenon was mentioned by [Koplev et al., 1983] and [Alaiji et al., 2015]. However, the findings of this present research say that the chip formation phenomenon of CFRP cutting must be explained distinguishing the fiber orientation in favor of an inclusive explanation of this process.

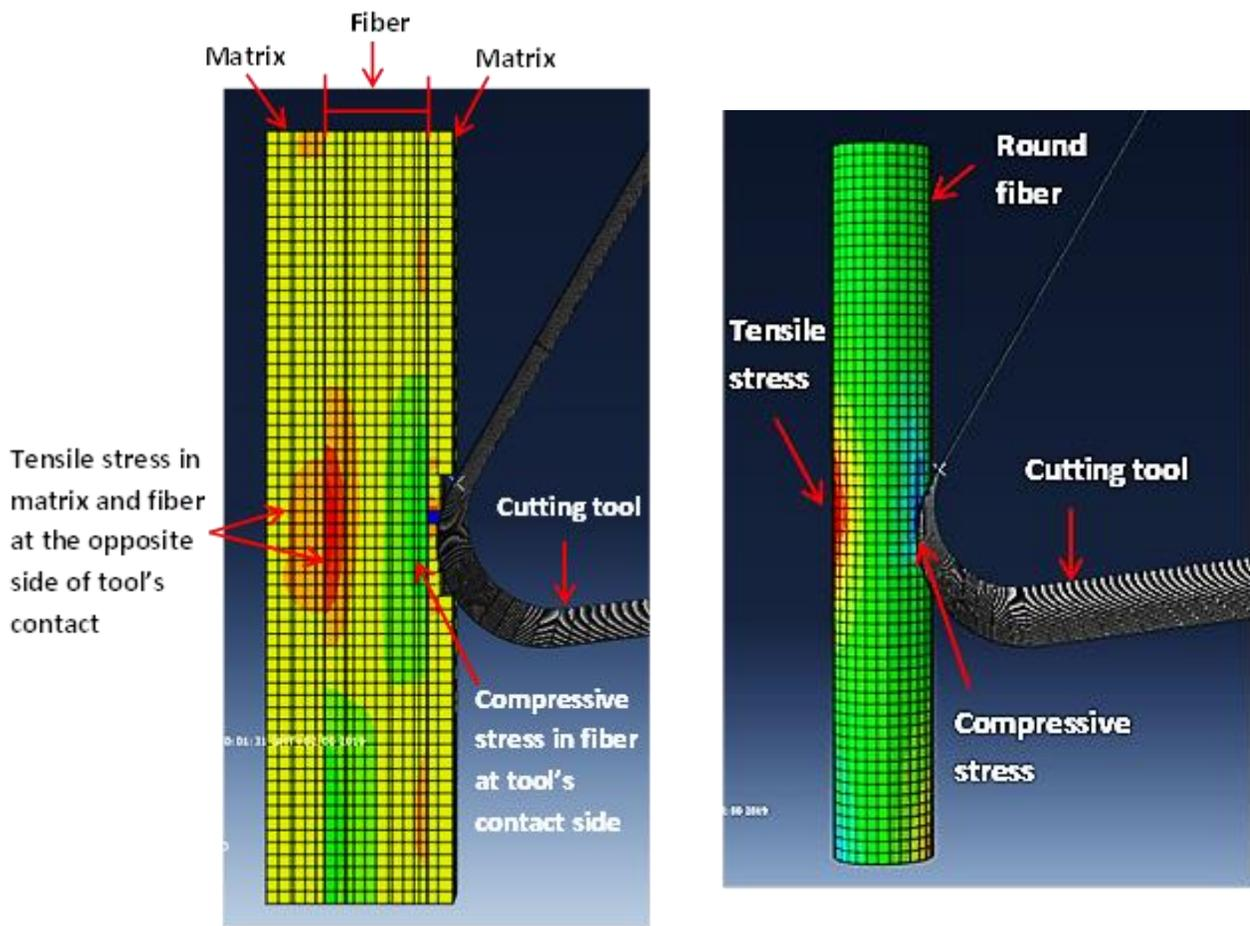
It has been found that there are four steps in chip formation process while the fibers are oriented separately at 0° , 45° , 90° and 135° angles. The course of every step varies according to the fiber orientation but the steps exist at every orientation.

First Step

At the first step, the tool tip presses the fibers. This phase is the very beginning step of a chip formation cycle. This pressing phenomenon creates a stress zone at the tip-workpiece contact area in the workpiece and tensile stress on the opposite side of the fiber. Here it should be noted that this stress field is obligatory for any machining process and this is the initial action of chip generation at every cutting angle and cutting depth in orthogonal machining. This stress zone size and shape vary due to the direction of fiber. The sharpness of the cutting tool also plays a role to the stress field size.



(a)



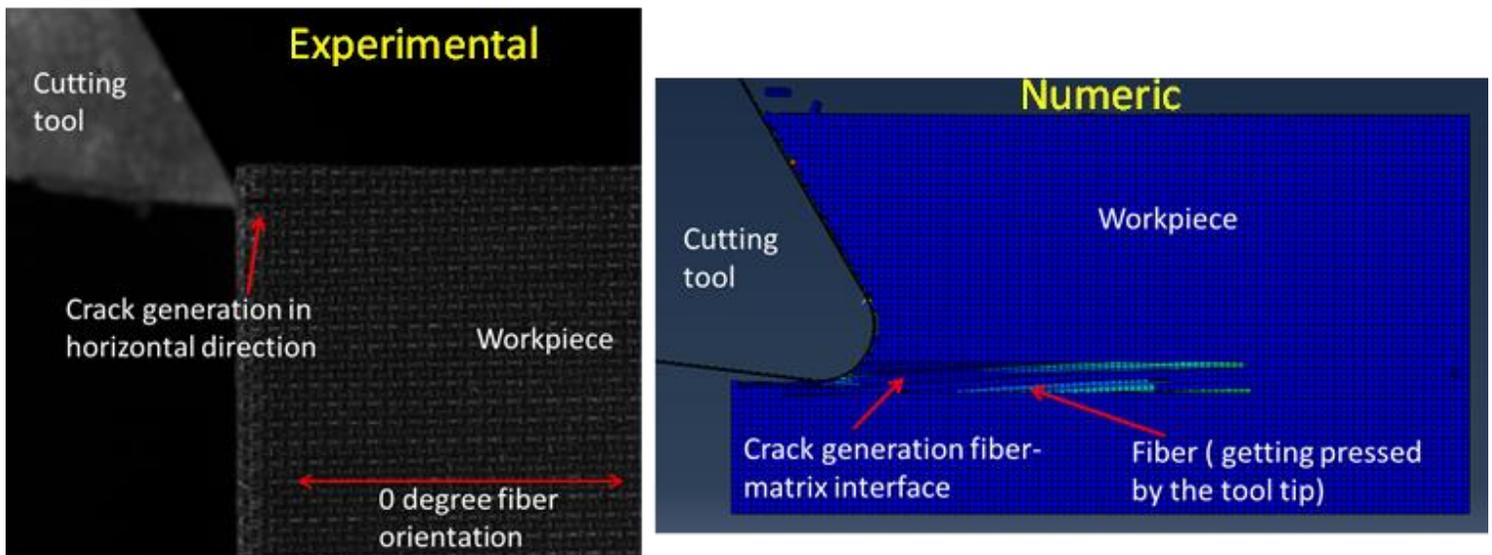
(b)

Fig. 2.5.1: Stress generation by tool (first step) at 90° fiber orientation, (a) experimental observation, (b) numerical observation at single fiber

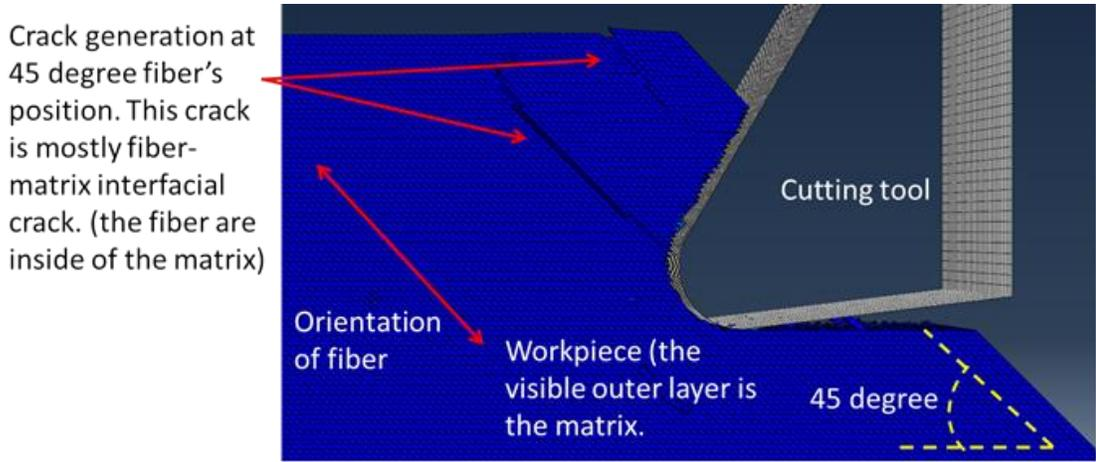
This stress field mostly propagates along the cutting direction at 0° fiber orientation. At 45° it propagates more likely upward along the fiber direction. At this fiber angle, the lower part of the tool lip faces maximum upward pressure from the fiber. At 90° fiber orientation, this stress field is placed around the tool tip contact area cross-sectionally of the fibers. This phenomenon is shown in Fig. 2.5.1 (a) experimentally and (b) numerically. At 135° fiber orientation, it is more likely propagated cross-sectionally of fibers which are -45° upward from the cutting direction.

Second Step

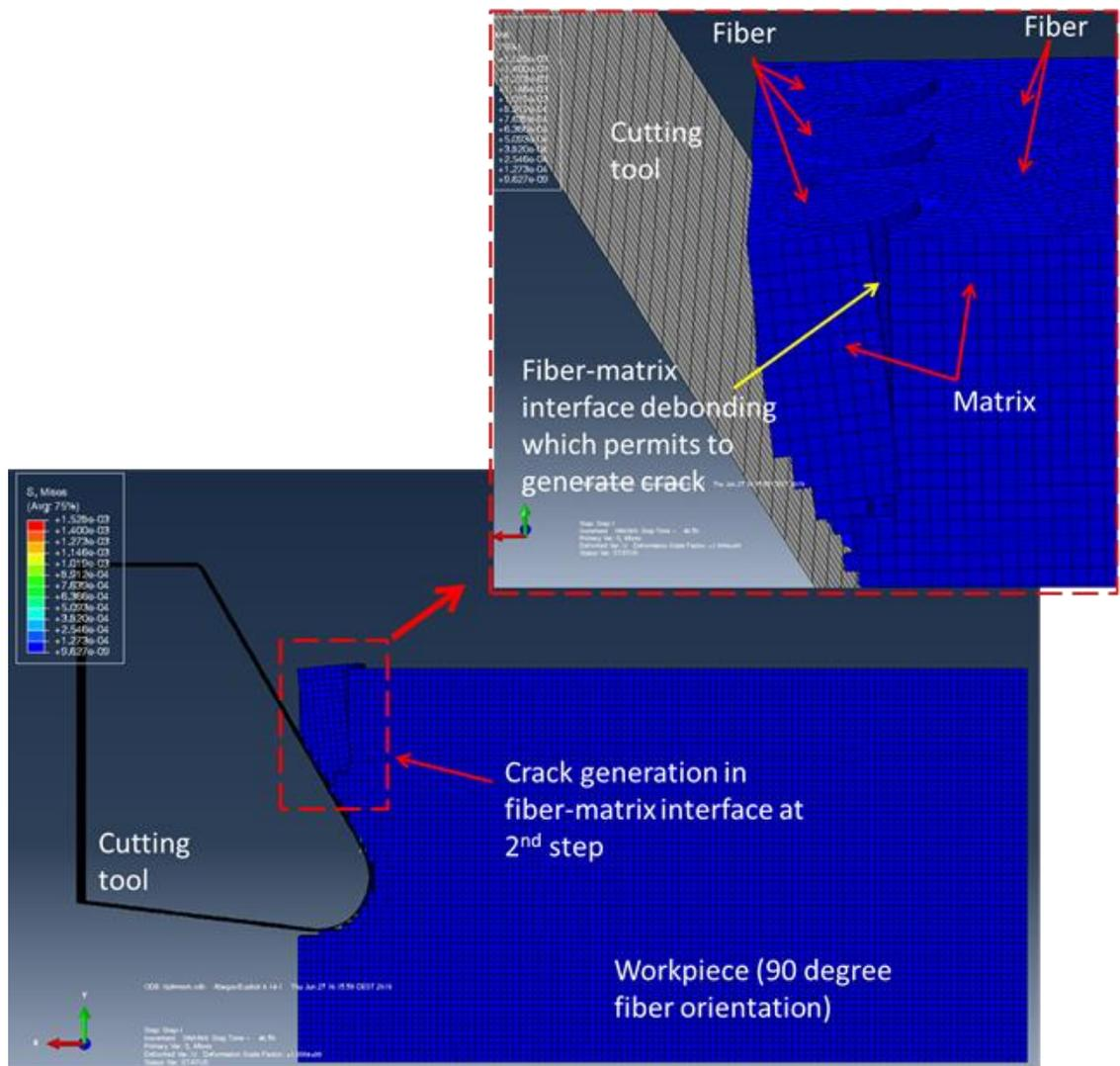
At the second step at 0° fiber orientation, a crack is generated horizontally in between fiber and matrix which permits the tool to advance more forward. It should be pointed out that at this angle if the fibers are horizontally well oriented they will not get cut cross-sectionally. At 45° and 90° orientation, the initiation of cut of fibers is started cross-sectionally at the tool-workpiece contact point. The phenomenon is shown in Fig. 2.5.2 (a) for 0° (b) for 45° and (c) for 90° fiber position. At 135° the real take-up of cutting depth is more than the set depth as the fibers are inclined negatively (-45°) to the cutting line. Because of this negative orientation the tool's forwarding motion impels the fibers to get debonded at the opposite direction of the cut surface which keeps the cutting depth region comparably less fractured.



(a)



(b)



(c)

Fig. 2.5.2: Crack generation (second step), (a) 0°, (b) 45° and (c) 90° fiber orientation

In the second step, the cohesive interface degrades. Numerically it is considered that the degradation starts from 0 and increases gradually to 1. When it is 0, the stiffness of the cohesive interface between the fiber and the matrix is maximum (the originally defined value) and when it is 1 the cohesive force vanishes (no cohesive force); and subsequently the fiber and matrix get debonded.

Here the scalar degradation of the cohesive interface has been shown for 90° fiber orientation in Fig. 2.5.3. Only the fiber surface is shown here and the matrix is kept in hide so that the damage on the fiber surface is clearly visible. On the images it can be seen that the surface gets damaged gradually and once the value reaches 1, the cohesive interface is totally broken. Subsequently if the tool continues to move forward, the fiber starts to be separated from the matrix or get debonded from the matrix.

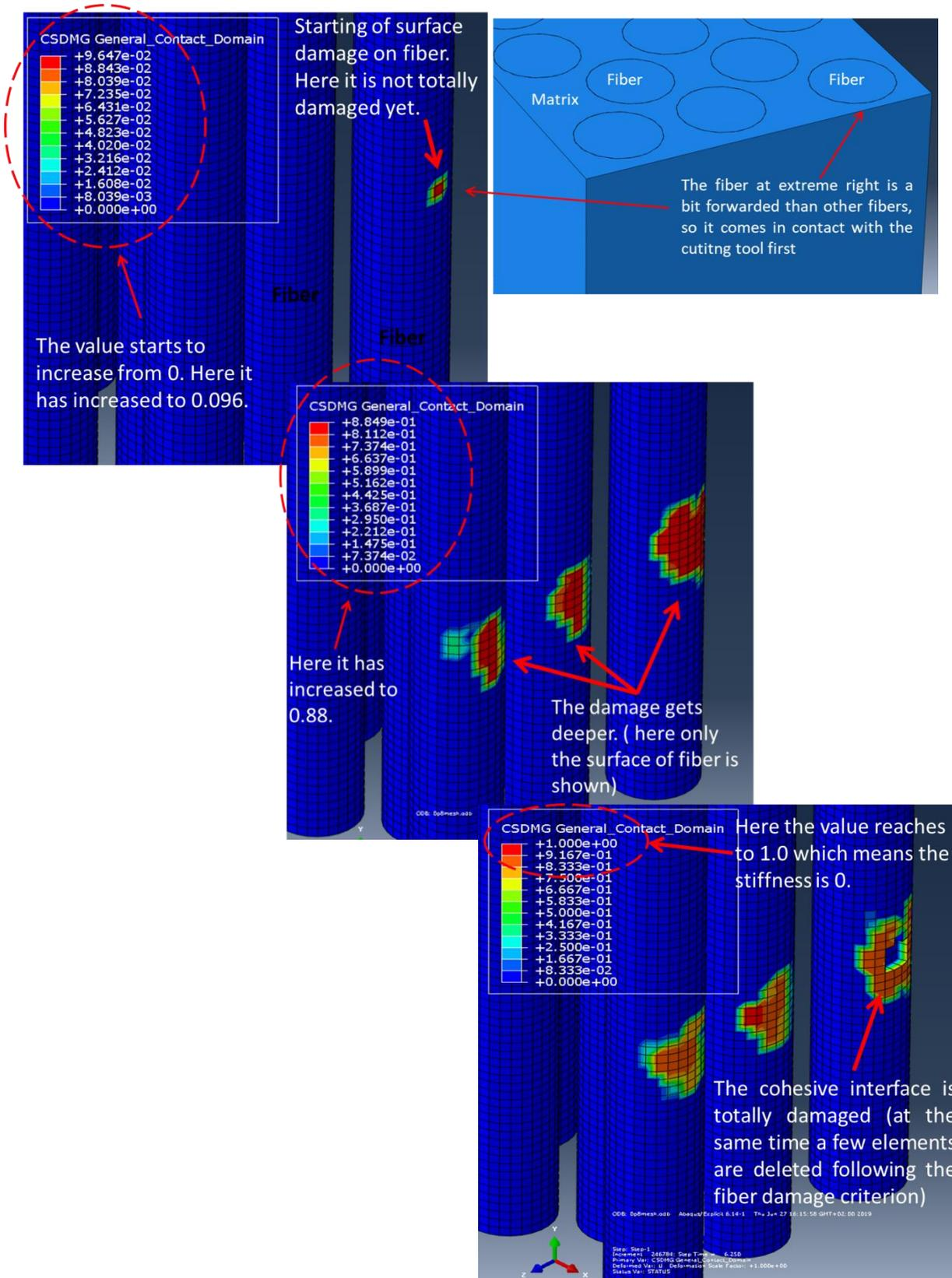
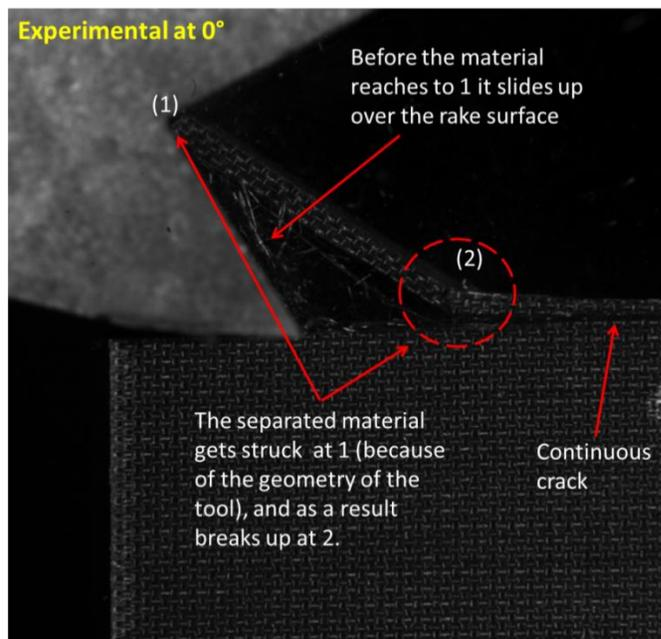


Fig. 2.5.3: Cohesive stiffness degradation in fiber-matrix interface.

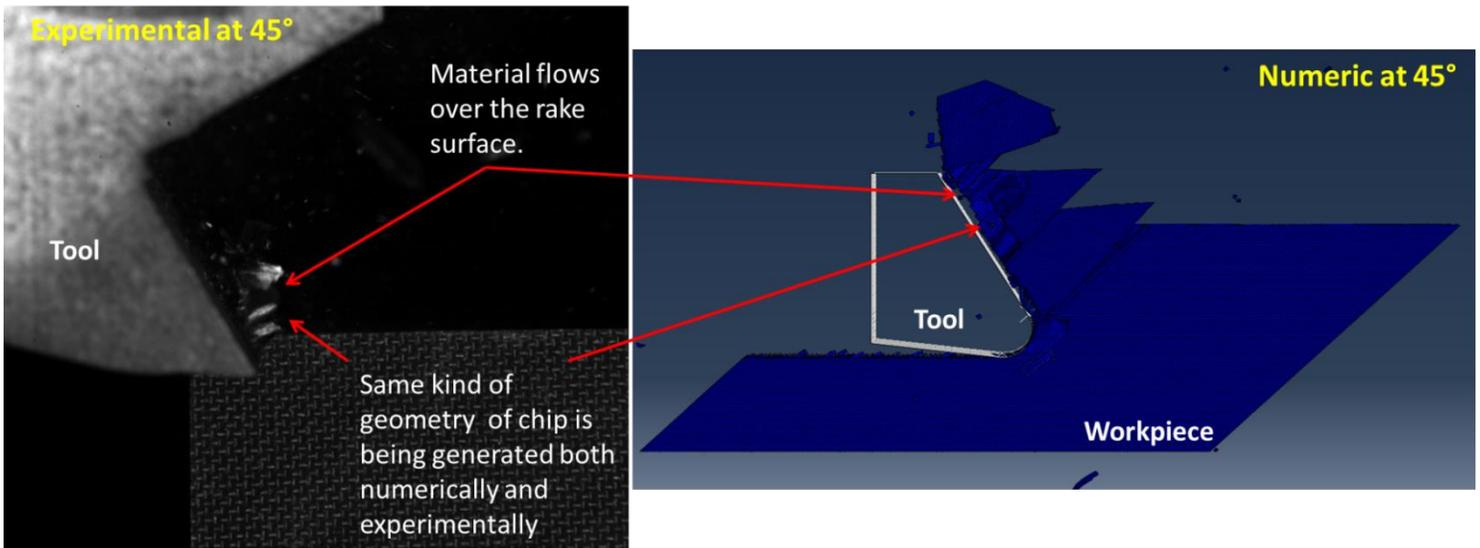
Third Step

In the course of chip formation, the third step deals with the sliding of cut material on the rake surface of the tool simultaneously with the tool forward motion. At 0° fiber orientation, the generated horizontal crack in fiber-matrix interface propagates with the forwarding movement of the cutting tool which permits to generate a long chip. At 45° and 90° , a shear deformation along the fiber-matrix is generated which allows generating a slice of material, and this slice of material slides upward touching the rake surface of the tool. In Fig. 2.5.4 the phenomenon is shown for 0° and 45° fiber orientation (in Fig. 2.5.4-a, “1” indicates the corner at the end of the rake surface, and “2” indicates chip breaking area).

The fundamental difference between 45° and 90° is that at 45° , the amount of material is more than 90° which confirms longer chip length (the volume of chip at 45° is more than 90° as at 90° the chips get separated at short distance from the tool rake surface). Additionally, at 45° fiber orientation, the tool tip faces highly abrasive behavior from the inclined fibers. At 135° fiber orientation, the cut material completely lies on the rake surface of the tool by generating a downward fiber-matrix interfacial crack. At this angle, comparably longer area of rake surface gets into contact with the material.



(a) Phenomenon of step 3 at 0° fiber orientation (experimental)



(b) Phenomenon of step 3 at 45° fiber orientation (experimental and numeric)

Fig. 2.5.4: The material slides over the rake surface, (a) at 0° fiber orientation and (b) at 45° fiber orientation

It can be worthy to hint at the possible defects development in the workpiece at this step. [Piquet, 1999] and [Surcin, 2005] found small holes generation on the newly generated surface while the fiber orientation is 135° (in drilling). In drilling, even if the fibers are unidirectional, the drill bit will face multiple fiber orientations during a revolution of the tool, Fig. 2.5.5.

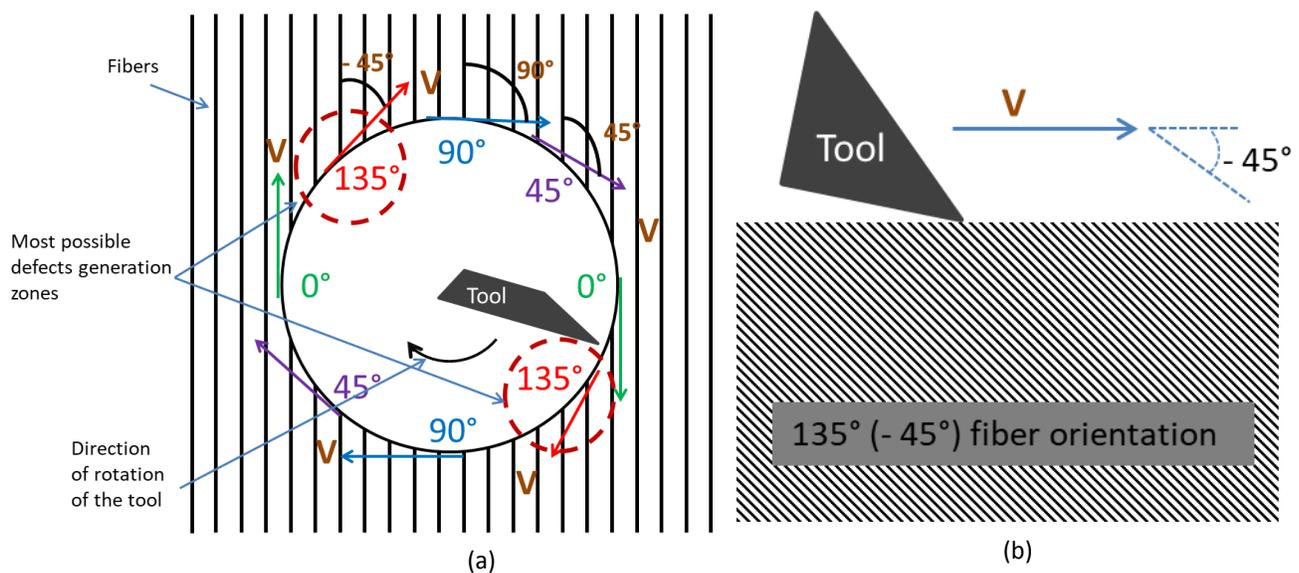


Fig. 2.5.5: Schematic representation of movement of the tool; (a) in drilling and (b) in orthogonal cutting.

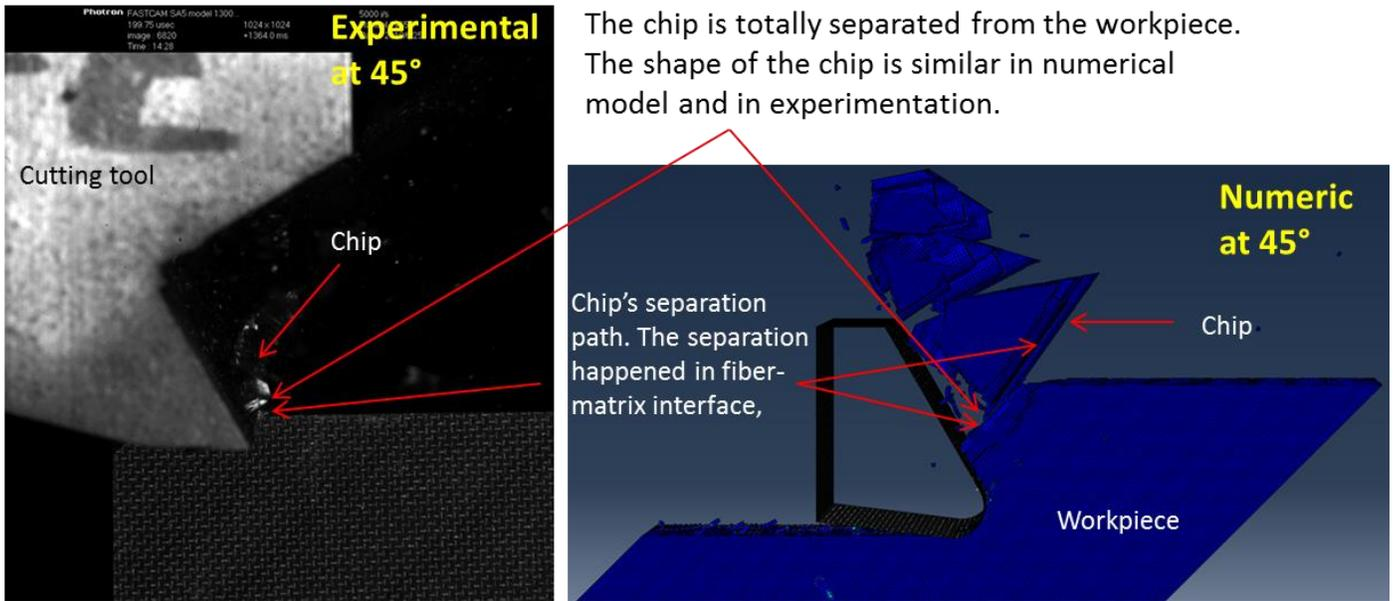
In the Fig. 2.5.5-a, it can be seen that even though the fibers are unidirectional, the cutting tool faces different fibers angle according to its position. The potential defects are generated while the tool cuts over the position of 135° orientation. In the third step of chip formation, the possible defects are structured.

Forth Step

Forth step is the last phase in chip formation course. In this step the chip gets its full shape and size and become separated from the main part. At 0° fiber orientation for the fourth step, as the fibers do not get cut cross-sectionally, the chip separation is mainly happening once the cutting tool reaches the opposite edge of the workpiece if the tool shape does not create obstacles. But in our experimentation the chip gets broken during formation because of the particular geometry of the tool which creates obstacles at a certain length of chip which is visible in the Fig. 2.5.4. (a).

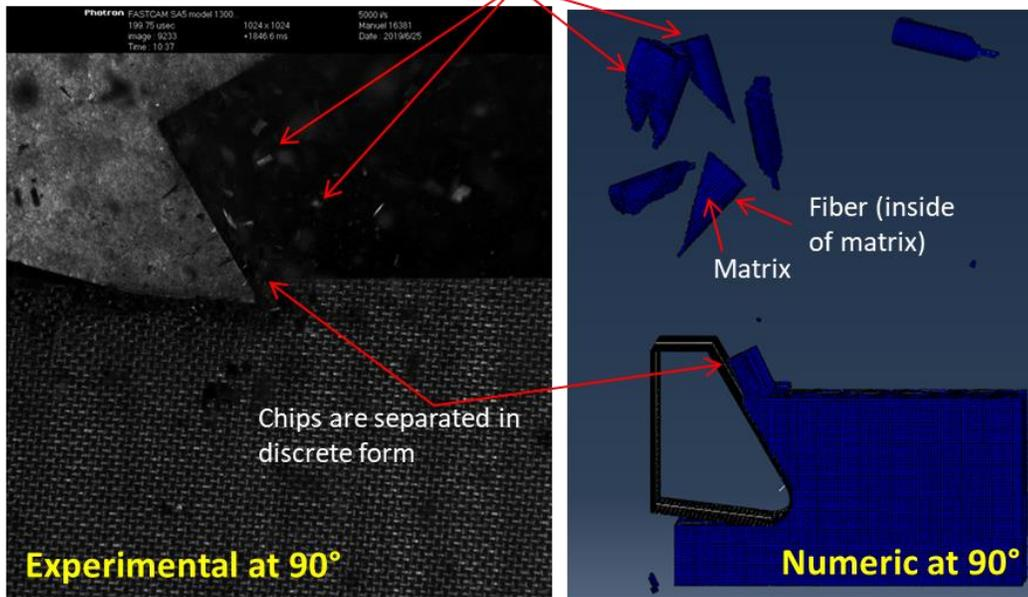
Contrary, at 45° and 90° with the advancement of the cutting tool the materials get separated along the shear deformation zone and slides upward as a chip, Fig. 2.5.6. The point angle of the tool plays an important role at this step, especially to define the direction of flow of chip. Low point angle permits the chip to flow on the rake, and more this angle increase, less it permits the chip to flow on the rake surface but presses the front chip rather than pushing it upward.

At 135° a bundle of fibers is separated along the fiber matrix interface at the shear deformation zone which is a bit foremost from the tool edge. Once the tool edge reaches to this zone line, this part of material gets separated from the workpiece as a chip. It was seen that the chip formation mechanism does not get remarkably influenced by the cutting depth.



(a) Chip separation in fourth step at 45° fiber orientation

Some chips have a bundle of fibers matrix and some chips have only single fiber (fiber-matrix get severely debonded which results dust form of discrete chips)



(b) Chip separation in fourth step at 90° fiber orientation

Fig. 2.5.6: The last step of chip formation, (a) at 45° fiber orientation and (b) at 90° fiber orientation

2.6. Conclusion

Along with experimental analysis of strain field and chip formation mechanism, two models have been developed which are described in detail in this chapter. The first model is a macro-mechanical model constituted with anisotropic material and the second model is a micro-mechanical model consists of distinguishing individual material's properties of fiber and matrix. The numerical model represents the practical scenario of chip formation mechanisms as well as strain values.

It is found that under newly generated surface, the material gets strained more than the rest of the area. This behavior is common at every fiber orientation and cutting depth. The strain field does not vary depending on cutting depths but on fiber orientation. Minimum strain (0.02%) is observed when fiber orientation is 0° and maximum strain ($\approx 2\%$) is observed when fiber orientation is 135° , while in all fiber orientation, compressive strain is found to be the dominating strain specially in Y direction.

Depending on fiber orientation, the stress propagation path in cutting zone varies; and this stress field defines how the fiber will be cut. So originally, the fiber angle plays the role here. Every chip is formed with four steps during cut. At first step the tool tip presses the material which creates a stress zone in the workpiece. Then a crack is generated or fiber-matrix get debonded at the second step (this is the initiation of chip generation). At third step the chip slides on the rake surface of the tool and at the fourth step the chip get separated from the workpiece having a complete shape. These steps are common at every fiber orientation, and remain the same even when the cutting depth is changed (which means the cutting depth does not play a role on chip formation mechanism). The numerical model provides a good agreement with the experimental observation of chip formation process.

Chapter 3: Effects of Cutting Depths

In this chapter the influences of cutting depths to the quality of machining and to chip generation have been discussed. In the study, a range of five different cutting depths from 0.1 mm to 1.0 mm has been used at four different fiber orientations in experimentation. The influences of the depths to the cutting and thrust forces have been analyzed, and a comparison between an equivalent homogeneous material (EHM) macro-model and experimental results have been made. The generated chips at every depth were measured and a comparison was made to analyze the change of size and shape because of cutting depth's change. Later a post analysis of the machined parts has been done to analyze the generated surface roughness and fiber-matrix interface crack generation for every cutting depth. Additionally, the parts were brought to Tomography X-ray which permitted to observe the subsurface damage and delamination inside the parts.

Content

3.1. Configurations of Analysis	127
3.1.1 Machine Setup.....	127
3.1.2. Materials and Cutting Conditions.....	127
3.1.3. Measurement Techniques.....	128
3.2. Effects to Machining Forces	132
3.2.1. Results and Discussion	133
3.2.1.1 Cutting Force	133
3.2.1.2. Thrust Force.....	135
3.2.2. Force When the Tool Touches the Workpiece.....	137
3.3. Effects to Surface Roughness	139
3.3.1. Results and Discussions	139
3.4. Effect to Subsurface Damage	144
3.4.1. Crack Generation and Propagation	144
3.4.2. Subsurface Damage Analysis by X-ray Tomography	149
3.5. Effects to Chip's Shape and Size	156
3.5.1. Chip's Length	157
3.5.2. Chip's Height and Width.....	159
3.6. Conclusion	161

3.1. Configurations of Analysis

3.1.1 Machine Setup

The experimental work has been carried out by the same machine setup as in Fig. 2.1.2 of chapter 2. But to measure the cutting efforts, the cutting tool is placed by a holder putting a KISLER 9257B triaxial force sensor in between the machine and the tool holder. The force sensor is tied to the fixed part of the milling machine by a chamber. The force sensor is designed to measure the forces in X, Y and Z directions. More details about forces measuring process has been explained in section 3.1.3.1.

3.1.2. Materials and Cutting Conditions

An intermediate modulus unidirectional Carbon/Epoxy (T800S/M21) material has been used as a test specimen. Each specimen contains only one specific fiber orientation (unidirectional) and 16 fiber layers. The Representative Elementary Volume (REV) of the workpiece is 80 mm x 4 mm x 45 mm. For the cutting tool, K20 micro grain tungsten carbide has been used. The cutting parameters have been shown in Tab. 3.1.1. From the tool to 4 mm distance to the clearance surface 7° clearance angle was kept in order to maintain high stiffness to resist the tip breaking. After this distance the angle is 15°.

Parameter	Values
Rake angle	30°
Clearance angle	7° and 15°
Depth of cut	0.1 mm, 0.25 mm, 0.50 mm, 0.75 mm and 1.0 mm
Cutting speed	200 mm/sec (12 m/min)
Fiber and matrix volumetric ratio	60 % : 40 %
Fiber orientation	0°, 45°, 90°, and 135°
Used material	T800S/M21
Frequency of force fluctuation	7000 Hz/sec

Table. 3.1.1: Cutting parameters

The workpiece was changed at every cut. So not any workpiece came into use twice but each cutting depth got four tests at four workpieces at four different fiber orientations (0°, 45°, 90° and 135°).

3.1.3. Measurement Techniques

3.1.3.1. Force Measuring Procedure

The forces were measured using a setup of KISTLER 9257B triaxial force sensor in the experimentation process. The sensor was placed in between the cutting tool holder and the mounting holder of the cutting machine as in the Fig. 3.1.1. The resistances the cutting tool faces during cut is taken by the sensor and transmits as signal to the signal amplifier through the transmission cable. The sensor takes signals in three directions, as in X direction the transverse force, in Y direction the thrust force and Z direction the cutting force.

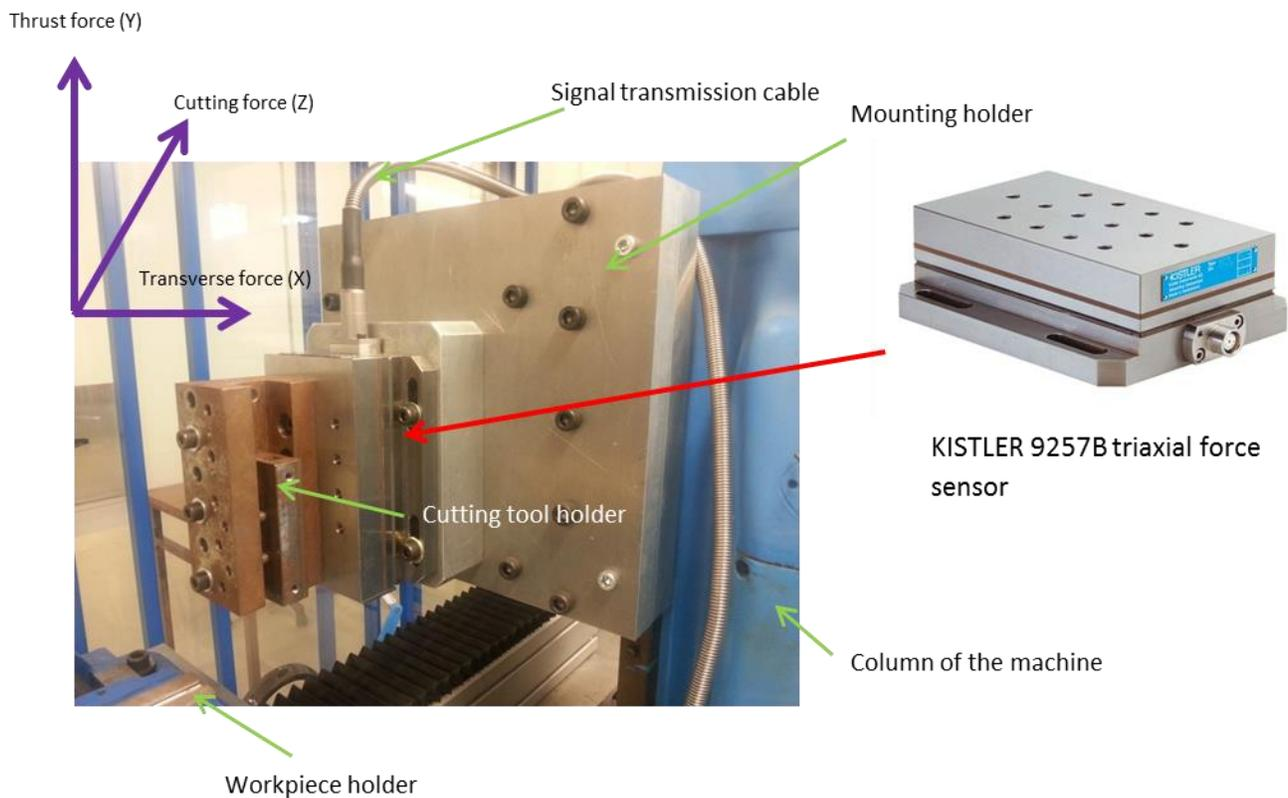


Fig. 3.1.1: Force measuring configuration

The signal amplifier, Fig. 3.1.2., amplifies the received signals from the sensor and transmits to the KISTLER software in the computer. In the computer the magnitudes of the signals are visualized as a function of recording time. Here in the present experimentation the force measuring frequency was set 7000 Hz/sec.



Fig. 3.1.2: KISTLER signal amplifier

At the beginning of the cut (once the cutting tool touches the workpiece), the force may fluctuate rapidly but later it becomes stabilized in a smaller range as in the Fig. 3.1.3. Here in this research the forces, F_x , F_y and F_z , were measured at the stabilized zone. In all measurements the average value was taken into account.

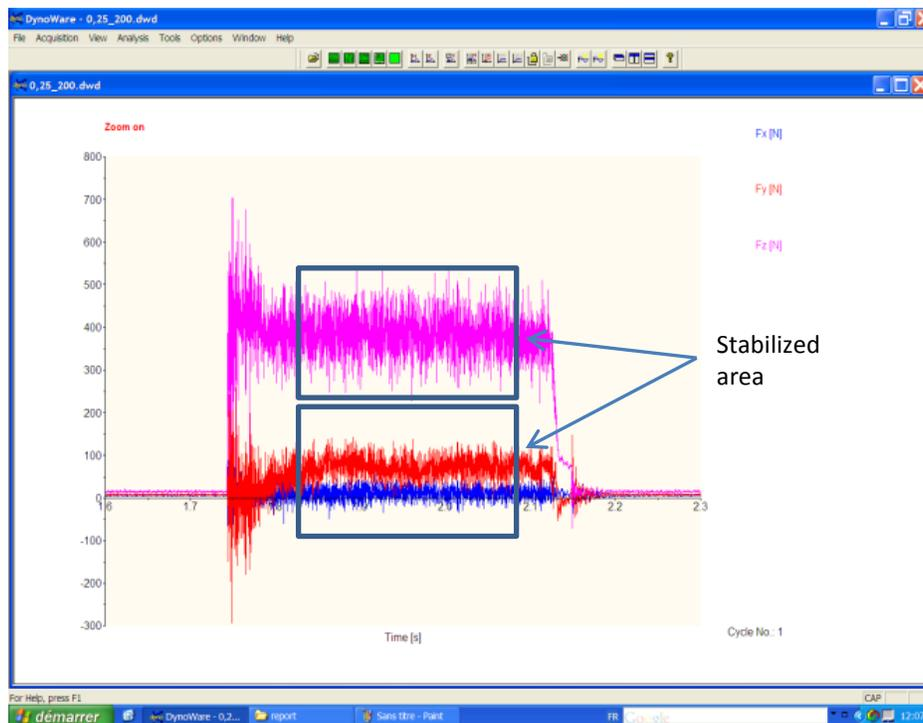


Fig. 3.1.3: Representation of the force

3.1.3.2. Roughness Measuring Technique

In order to evaluate the surface roughness after machining, Alicona INFINITEFocus SL with standard straight edge 10x has been used. A cross-sectional measurement of the machined surface on the workpiece has been done taking three profiles of 100 micrometer width at three different places, Fig. 3.1.4. And the average of these three values has been taken into consideration as the roughness value. Typical surface profiles recorded for all cutting conditions. The parameter discussed here is mainly the average roughness of the profile, R_a , which is formulated according to the Eq. 3.1.1.

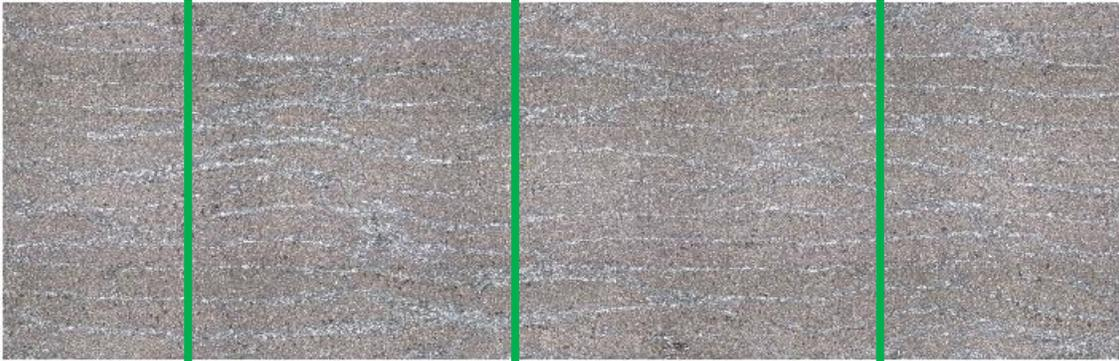


Fig. 3.1.4: Roughness measuring profiles on the surface.

$$R_a = \frac{1}{l} \int_0^l |y(x)| dx \quad (3.0.1)$$

It is defined as the average absolute deviation of the roughness irregularities from the mean line over one sampling length as shown in Fig. 3.1.5.

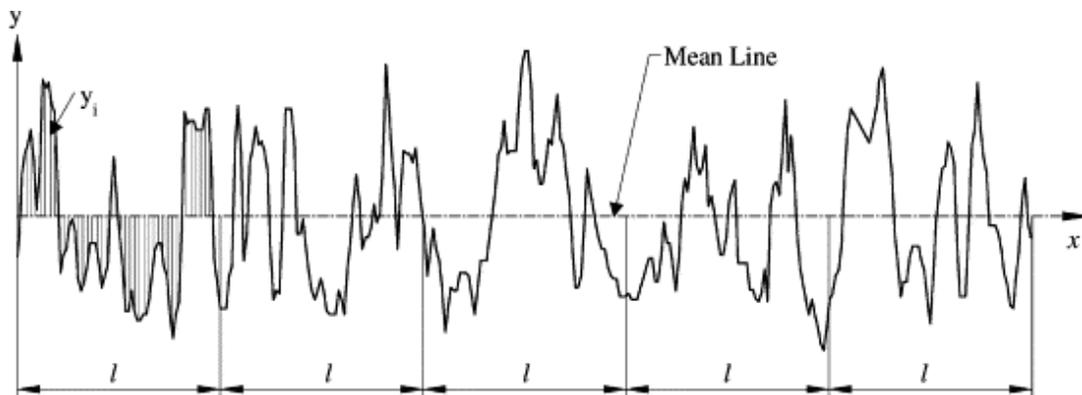


Fig. 3.1.5: Arithmetic average height, R_a [Gadelmawla et al., 2002].

3.1.3.3. Chip's Dimensions Measuring Technique

The cut chips have been collected by putting a temporary paper bed around the workpiece and later measured separately for every cutting depth and fiber orientation. Scanning Electron Microscope (SEM) has been used to measure the sizes of the chips. Different lengths of chips have been marked at each cut but the particular values, presented here in the result analysis section, were taken from the major sizes of the generated chips.

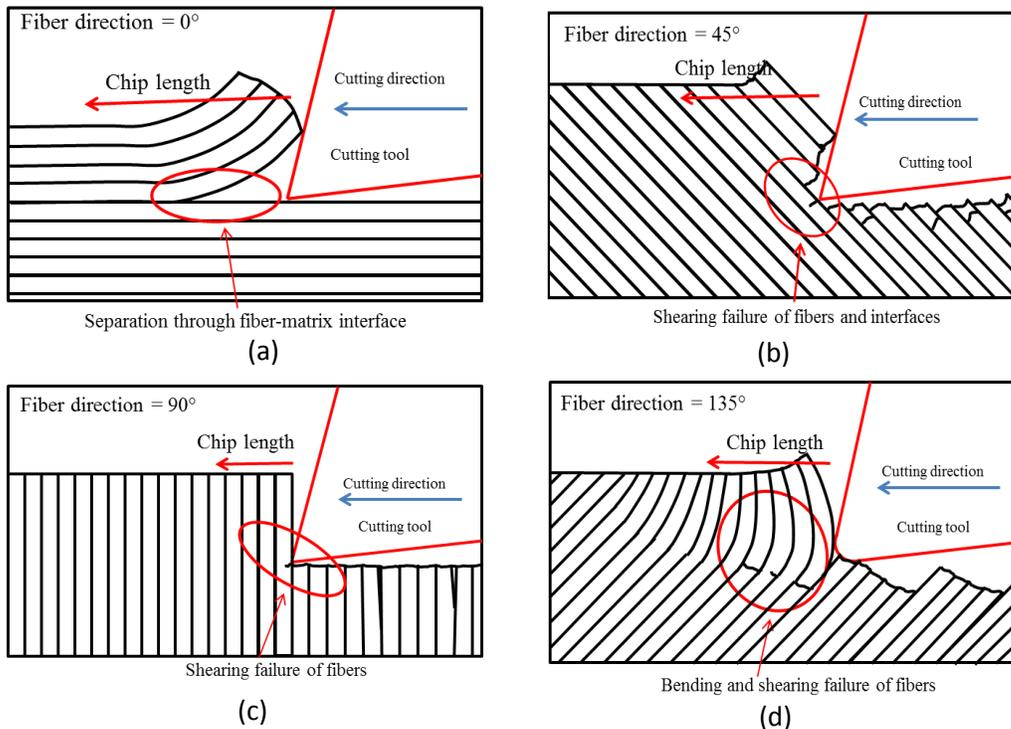


Fig. 3.1.6: Chip length's direction; (a) at 0° , (b) at 45° , (c) at 90° and (d) at 135°

Regardless of the fiber orientation, the chip length is the horizontal length of the chip which lies to the cutting direction as in Fig. 3.1.6. The height lies vertically 90° from cutting direction and the width is the cross-sectional width of the workpiece, shown in Fig. 3.1.7. Three different chips from each cut were measured and the most approximate value was chosen.

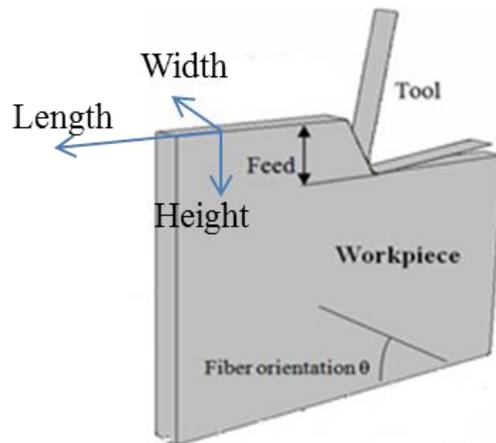


Fig. 3.1.7: Length, width and height of a chip according to the cutting direction

3.2. Effects to Machining Forces

Regarding the orthogonal cutting of Carbon Fiber Reinforced Polymer (CFRP) many answers in literature are limited, especially concerning how different cutting depths affect the cutting and thrust forces. On the subject of cutting depth influence [Zitoune et al. 2005] analyzed the cutting forces using 0.05 to 0.25 mm cutting depth at 0° , 45° , 90° and 135° fiber orientation of unidirectional T2H/EH25 materials. In their numerical model only 0° fiber orientation has been used. [Blanchet, 2015] analyzed the resultant force F_c (cutting force) and F_t (thrust force) and the machined surface quality with respect to the cutting speed from quasi-static to 120 m/min. He used four different fiber orientations keeping the cutting depth constant throughout the whole research. [Wang and Zhang, 2003] focused to the machining forces with respect to the rake angle and fiber orientation. Several analytical models [Bhatnagar et al., 1995] [Zhang et al., 2001] [Jahromi and Bahr, 2010] have been found to predict the cutting forces but the concern of cutting depth effect is missing. The numerical models mentioned here to predict the cutting and thrust forces mainly used an equivalent homogeneous material (EHM) which, basically, deviate the numerical results from experimentation. [Nayak et al., 2005] tried to amend it by modeling the fiber and matrix separately without taking matrix damage in calculating the cutting forces. It was found that both the cutting and thrust forces matched quite well with the experimental results.

Here in this present research a comparison between numerical (Finite Element Analysis) and experimental research has been carried out on the influences of different cutting depth to the cutting and thrust forces (the numerical model which is used here is the macro model of chapter

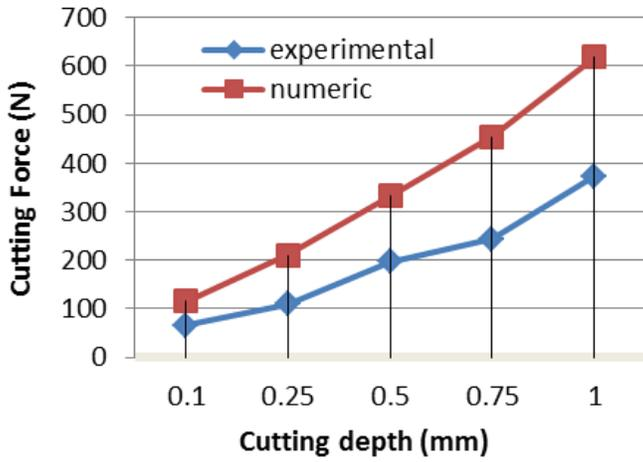
2). The cutting and thrust force have been analyzed at every cutting depth and fiber orientations. It was found that, initially, once the tool touches the workpiece the cutting and thrust force get higher and become unstable which later decreases and stabilized. Any analytical description of this phenomenon has not been found in the literature. In this research work, the reason for this initial high force has been analyzed and explained.

3.2.1. Results and Discussion

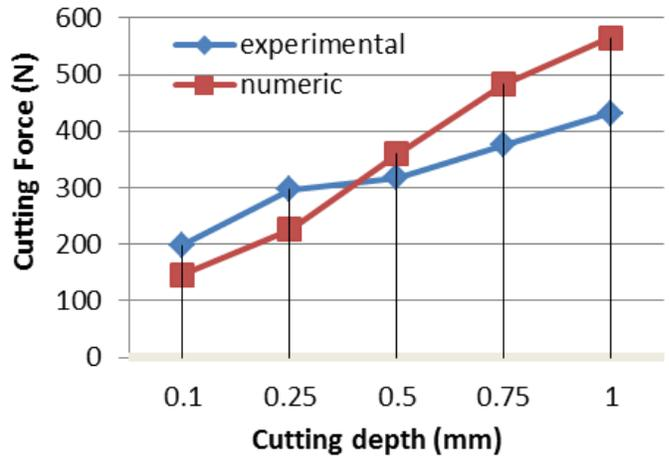
3.2.1.1 Cutting Force

In Fig. 3.2.1, the cutting forces are separated according to fiber orientation and compared with respect to the cutting depths. It is clearly seen that there is a strong influence of cutting depths to the cutting forces. Regardless of fiber orientation, it is found that if the cutting depth increases, the cutting force increases as well both numerically and experimentally. It is because the cutting force is not just the force needed to cut the adjacent fibers near the tool tip but it is a function of the forces needed to cut fibers by the tool tip, bend the cut fibers by the rake surface of the tool to give a chip's form and remove it from the workpiece as a chip. Here in this process if the cutting depth increases the thickness of the chip will increase. As a result the rake surface will need more force to bend the cut fibers and to remove it as a complete chip. Therefore, more the cutting depth, more the cutting force and this is what found not only in the experimental results but also in the numerical simulation.

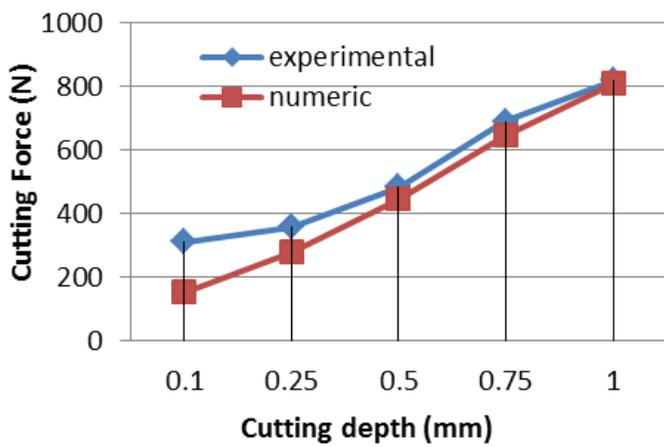
Similar tendency has been found by [Youliang et al., 2016] where their cutting depths were comparably too low (10 μm , 30 μm and 50 μm), Fig 3.2.1-e. At those cutting depths their forces increased almost linearly at 90° and 135° fiber orientation while the cutting depth increase, but at 0° and 45° this increment is less gradual. In our opinion, 10 μm is theoretically a cuttable depth, but experimentally it does not make a clear cut of the material. We have discussed this issue in minimum cutting depth section in chapter 4. So we emphasis that if their depths are more to a great extent, e.g.: 100 μm or more, then the scale of increment of cutting forces along with cutting depth increment at 0° and 45° will be like 90° and 120° fiber position. Here in this analysis no matter what the fiber orientation is, at 0.1 mm depth the force is always minimum and at 1.0 mm depth the force is maximum.



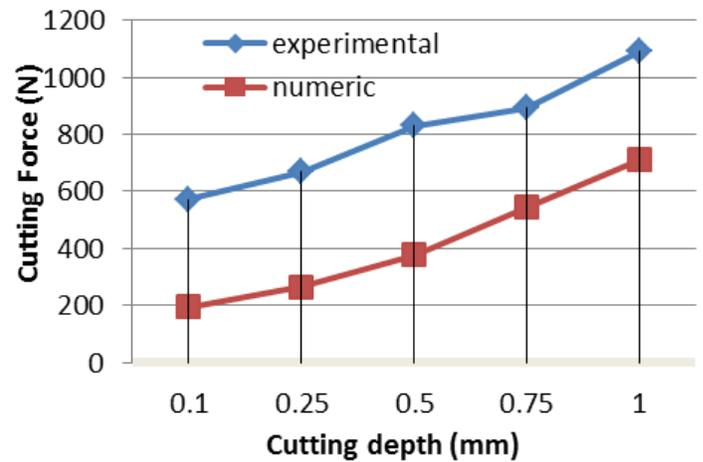
(a) 0° fiber orientation



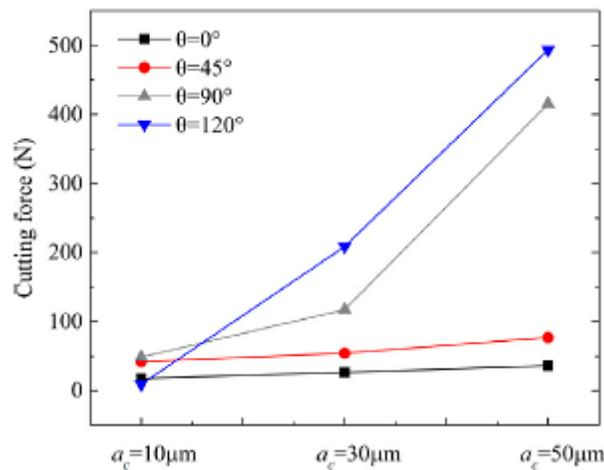
(b) 45° fiber orientation



(c) 90° fiber orientation



(d) 135° fiber orientation



(e) Cutting force increment respect to cutting depths [Youliang et al., 2016]

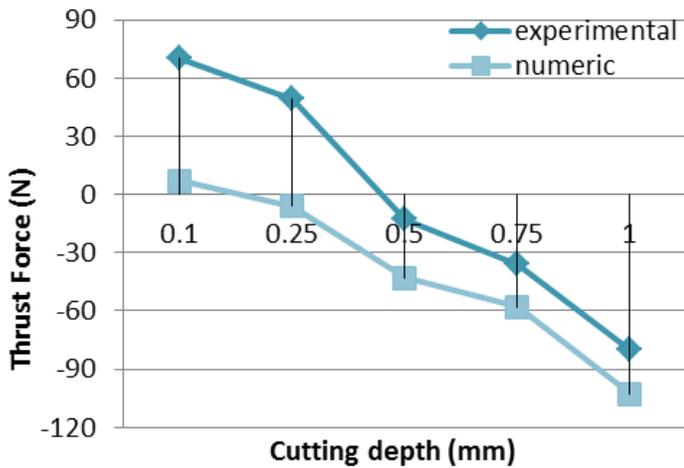
Fig. 3.2.1: Comparison of numerical and experimental cutting forces: (a) 0° fiber orientation (b) 45° fiber orientation (c) 90° fiber orientation and (d) at 135° fiber orientation (e) cutting force increment with respect to cutting depths and fiber orientation by [Youliang et al., 2016].

At 0° fiber orientation, Fig. 3.2.1-a, the simulated forces at every cutting depth is greater than the experimental forces whereas it is the contrary at 90° , Fig. 3.2.1-c, and 135° , Fig. 3.2.1-d, fiber angles. At 45° fiber orientation, Fig. 3.2.1-b, the experimental force remains higher until 0.5 mm cutting depth. These results are comparable with [Alaiji et al., 2015] which found that if the fiber orientation is less than 40° , the experimental cutting force remains less than numerical value and if the orientation is more than 40° the experimental value gets higher than the numerical value. The reason for this phenomenon is because at 0° fiber orientation the tool needs comparably less force to complete the course of formation as the fibers are parallel to the cutting direction. Moreover, at this angle the fibers are not more likely cut cross-sectionally and the elastic return effect from fiber is minimum.

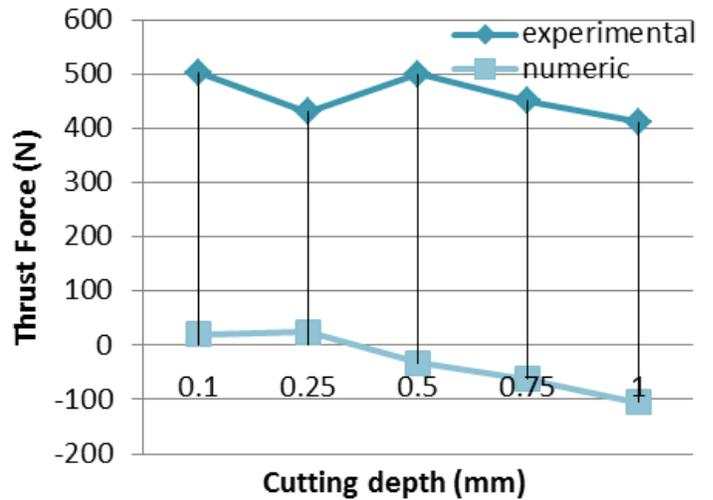
By the same token, at 135° fiber orientation, Fig. 3.2.1-d, a large deviation between the numerical cutting force and experimental values is found indeed both forces have the same rising tendency with respect to the cutting depth. It is because at 135° fiber orientation the fibers are cut in big bunches rather than smooth cutting, causing an increase in the average cutting force. This phenomenon is less realistic in EHM model which is the cause of this difference. Nevertheless, the trend of cutting forces predicted by FE simulations matched well with the experimental results.

3.2.1.2. Thrust Force

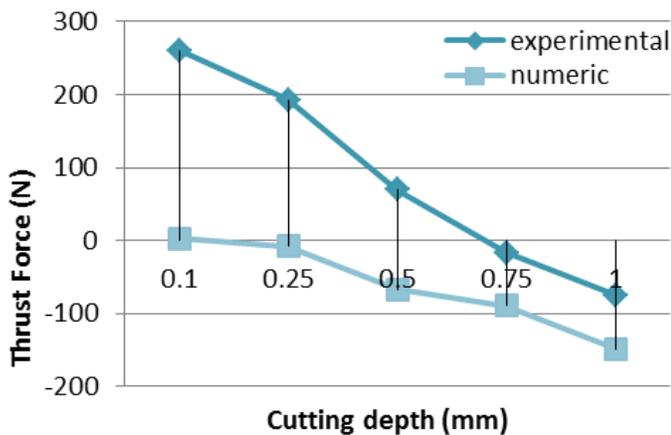
It was found that whether the thrust force will be positive or negative it depends together on both cutting depth and fiber orientation. Fundamentally the main contribution to thrust force comes from the elastic return phenomenon of fibers. Same findings were mentioned by [Lasri et al., 2009] and [Ghidossi et al., 2003]. Due to this phenomenon, the real and nominal depths of cut vary. Besides, it was found that it is not always the elastic return property which causes the thrust force; it can be the downsloping pressure exerted by the fibers on the rake surface of the tool during cut which is mostly the case at 135° fiber orientation. Thrust force causes deflection of the tool and reduces the depth of cut which affects tolerances. But it fluctuates rapidly if the cutting depth is changed, and a small variation in experimental setup can change the result dramatically.



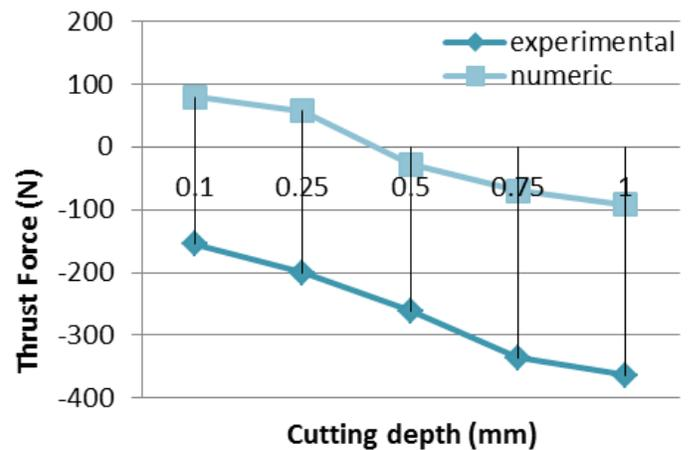
(a) 0° fiber orientation



(b) 45° fiber orientation



(c) 90° fiber orientation



(d) 135° fiber orientation

Fig. 3.2.2: Comparison of numerical and experimental thrust forces: (a) 0° fiber orientation (b) 45° fiber orientation (c) 90° fiber orientation and (d) at 135° fiber orientation.

The thrust force drops if the cutting depth increases regardless of fiber orientation, which means it has inverse relationship with cutting depth. At 0.1 mm cutting depth of 0° and 90° fiber orientation the thrust force is maximum and the minimum at 1 mm depth, Fig. 3.2.2-a and (c). For all cutting depths at 45° fiber orientation, Fig. 3.2.2-b, the experimental values remain always positive and at 135° orientation, Fig. 3.2.2-d, it is always negative. Additionally, a significant deviation between the numerical and experimental forces is found. It is because at 45° fiber orientation the fibers are inclined to the cutting direction which is totally inverse at 135° fiber orientation. So at 45° fiber orientation while the tool moves forward the fibers experience high downward pressing from the tool tip during cutting. It generates highly concentrated stress in the pressing zone. Once the fiber is cut, due to elastic return

characteristics it pushes upward on the clearance surface of the cutting tool which is stronger than any other fiber orientation. Additionally, the clearance surface of the tool faces comparably more surface contact from the cross-sectional cut surface of fiber at this particular fiber orientation. More contact means more friction and high vertical force.

On the other hand, at 135° fiber orientation the fibers are inclined at the opposite orientation than cutting direction. Fibers do not face the downward pressing action from the tool tip and the elastic return phenomenon is the minimum or zero. But as on the rake surface the tool faces downward vertical force from the ongoing cutting chip the total vertical force (thrust force) gets negative for all cutting depths. Here it should be remarked that according to the cutting mechanics, no matter how much the cutting depth is, at 45° fiber orientation the thrust force will always be positive and at 135° fiber orientation it will always be negative.

This particular thrust force phenomenon cannot be found by any HEM FEM model which is the fact in present research work too. The same cause was mentioned by [Gopala et al. 2007]. The HEM models found on literature are not realistic to represent the thrust force. To predict this phenomenon numerically the only way is to develop micro mechanical models with individual fiber and matrix properties. But it will not be easy because to calculate a stable cutting force the relevant model needs to be long enough. But as a fiber has around 7 μm diameter, the model will create a huge number of elements which may deserve very large computer memory and longer simulation time.

Eventually, it can be said that the trends of the predicted cutting and thrust forces at all cutting depths matched to the experimental results in spite of the fact that there are some deviations.

3.2.2. Force When the Tool Touches the Workpiece

It has been found that initially once the tool tip touches the workpiece the cutting force increases rapidly and thrust force remains lower than the average value while both of the forces become unstable and fluctuate inordinately, Fig. 3.2.3. The transverse force also shows the same tendency but in this research the transverse force has not been taken into consideration to analyze. These initial high contact forces are a function of the tool tip radius, cutting speed, contact pressure, friction parameter and the type of generated stress field in the workpiece. While the tool touches the workpiece it faces a strong reaction force which lasts from initial tool-workpiece contact point to the initiation of fiber cut. This incident generates a momentary high vibration in both cutting tool and workpiece that influence the initial unstable contact forces. Just before the point of fiber separation (fiber cut), the force reaches its peak values; once the front fibers start to be cut the force reduces until the total separation of the first chip (the first peak zones of the zoomed area of cutting and thrust forces of Fig. 3.2.3). The duration

of this phenomenon was measured 0.0165 second (at 3.3 mm cutting length and 200 mm/sec cutting velocity) which is interestingly equal to the length of the first chip.

Concurrently, the thrust force fluctuates both in positive and negative direction unstably; as in this very initial cutting zone, the fibers experience both pressing and cutting phenomenon. The same phenomenon is repeated during the course of the second chip generation (the second peak zones of the zoomed area of cutting and thrust forces of Fig. 3.2.3.) though the second chip's length has been found around 4 mm, which is longer than the first one. By the end of second chip separation (7.3 mm total cut in this particular test) the generated initial high vibration and instability in the tool and workpiece are reduced considerably as both of them are held tightly in the holders. The cut becomes smoother and the forces get more stabilized in a short range and continue throughout the rest of cut.

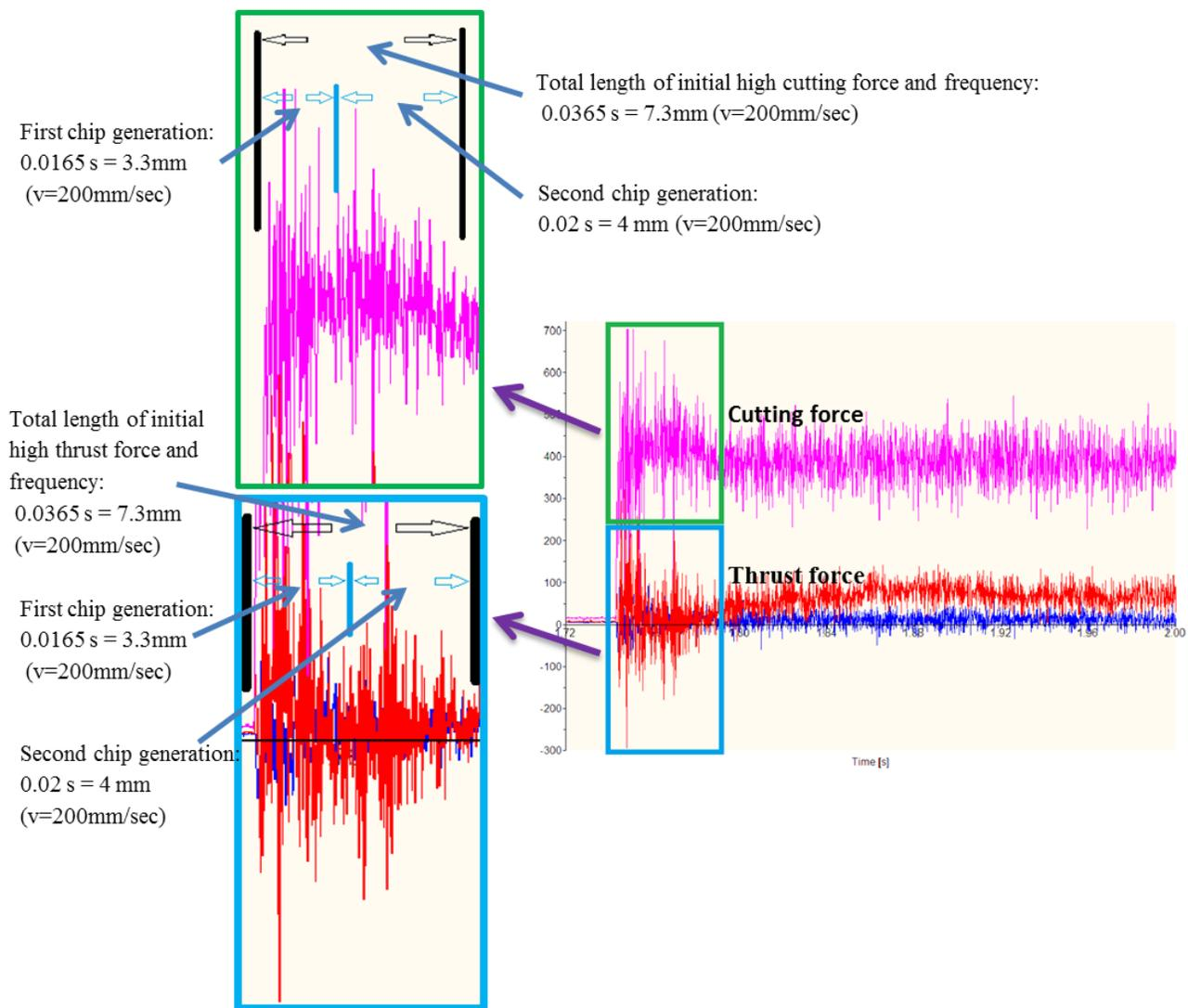


Fig. 3.2.3: Initial contact forces (experimental) at 0.25 mm cutting depth and 90° fiber orientation

3.3. Effects to Surface Roughness

The quality of machined surface relies on many surface parameters. [Pramanik et al., 2007] mentioned that newly generated surface remains under residual compressive stress and these surfaces are damaged due to cavities left by the pull-out of fibers; whereas [Shchurov et al., 2016] said it is the interfacial debonding between fibers and matrix in the area under machined surface which is responsible. Since the surface quality and subsurface damage have been known to be highly dependent on many process parameters, there have been many previous studies focused separately on the effect of fiber position, cutting speed, rake angle on the surface quality, e.g.: [Blanchet, 2015] [Iliescu, 2008][Shchurov et al., 2016] [Arola et al., 1996] [Arola et al., 2002] [Alaiji et al., 2015] [Wang and Zhang, 2003]. Different failure models, Hashin, Maximum stress and Hoffman criterion have been used by [Lasri et al., 2009] focusing on progressive failure of unidirectional glass fiber-reinforced polymer composite (FRP).

The outputs answered many questions regarding the surface quality of machined parts; nevertheless, the effect of different cutting depth is not answered yet. The present research carried out a post analysis of newly generated machined surfaces to analyze the surface roughness and crack generation and propagation in the fiber-matrix interface as function of cutting depth. A comparison has been made according to different cutting depths. Simultaneously, the work also shows in-depth findings regarding the influence of fiber orientation to the surface quality of machined part.

3.3.1. Results and Discussions

The surface roughness which is going to be discussed here are the experimentally found results. The explanation has been made as a function of cutting depths and the graphs have been separated as fiber orientation. It has been found that the cutting depth has influence to surface roughness but the proportion scale mainly depends on the fiber orientation. The experimental results, Fig. 3.3.1, show that at 0° and 45° fiber orientation the cutting depth influences much less to the surface roughness, which means the roughness does not vary hugely if the cutting depth is increased or decreased. However, at 90° and 135° fiber orientation if the cutting depth increases the roughness also increases.

It is seen that the main contribution to surface roughness comes from the fiber's elastic return phenomenon. The fibers get compressed near the vicinity of the cutting tool. Once the tool tip cuts and passes the fiber the compressed newly generated head of fiber returns making the surface rough.

At 0° fiber orientation, Fig. 3.3.1-a, the average roughness remained in between $0.3\ \mu\text{m}$ to $0.4\ \mu\text{m}$ while at 45° orientation, Fig. 3.3.1-b, it is around $0.8\ \mu\text{m}$ for all cutting depths. It should be noted that when the fibers are positioned at 0° they are parallel to the cutting direction; so

normally they are not supposed to get cut cross-sectionally (if well positioned at 0°) which gives a smooth surface. So even the cutting depth increase or decrease (whether 0.1 mm or 1.0 mm) it does not notably affect the roughness.

Comparably, at 45° fiber position the roughness is more likely generated by the elastic return of the fibers which previously got compressed by the tool tip during cut. This phenomenon gives the same type of profile all over the cut surface of the workpiece. The roughness profile remains almost the same whatever the cutting depth. At 90° fiber orientation, Fig. 3.3.1-c, there is little gradual increase of the roughness as the cutting depth increases; indeed, the maximum value does not pass over $2\ \mu\text{m}$. At this fiber orientation as the fibers are vertically positioned the newly generated fibers' head gets debonded from the matrix which generates more likely rugged surface and it increases if the cutting depth increases. These roughness values are similar to the values found by [Dhiraj K. and Kalyan S., 2014] in drilling, [Meenu G. and Surinder K., 2015] in turning and a bit lower to the results found by [Guangjun et al., 2017] in milling of CFRP where they used combinedly $0^\circ/45^\circ/90^\circ/135^\circ$ orientation in different milling speeds (from 50 m/min to 200 m/min).

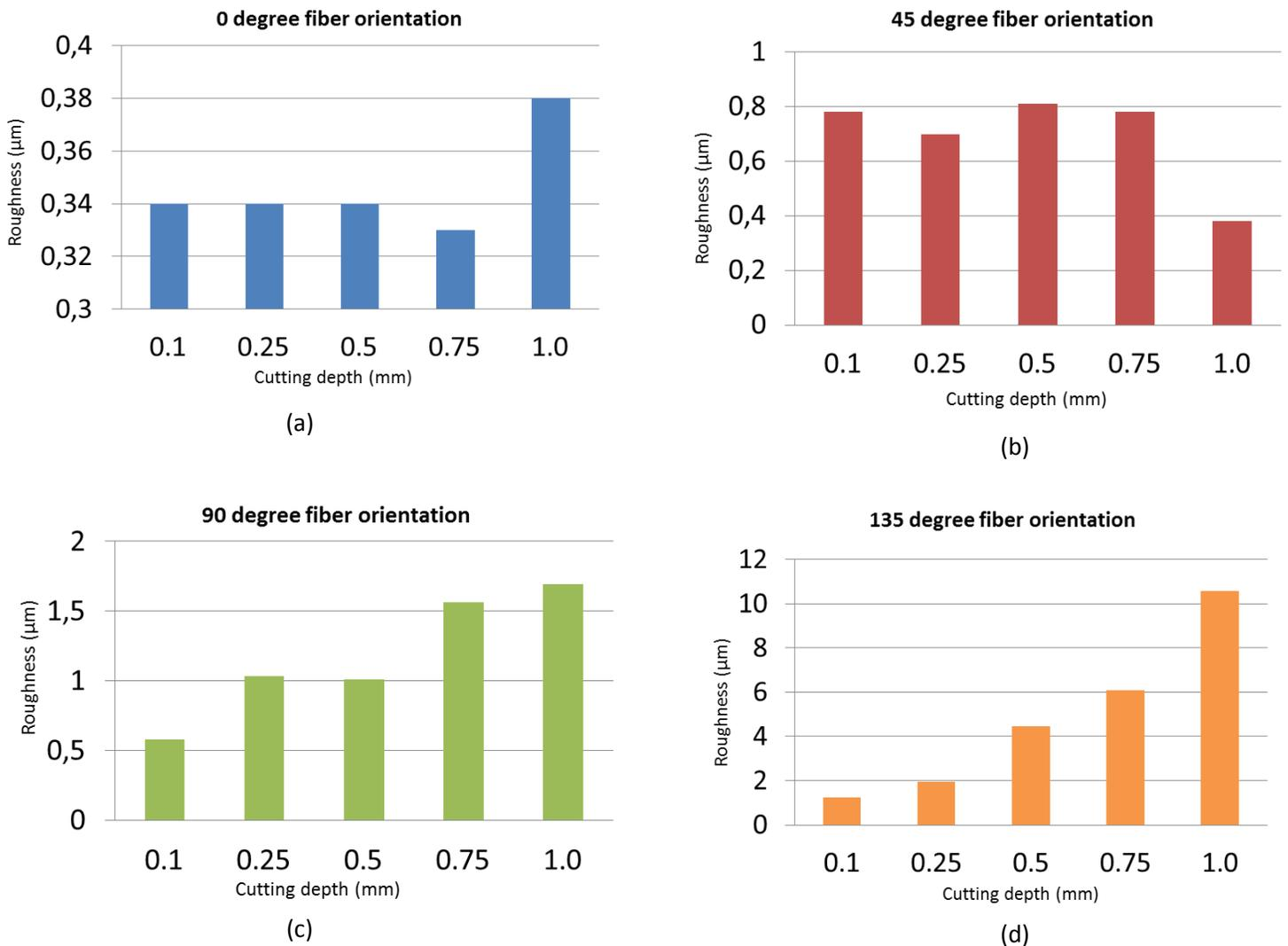
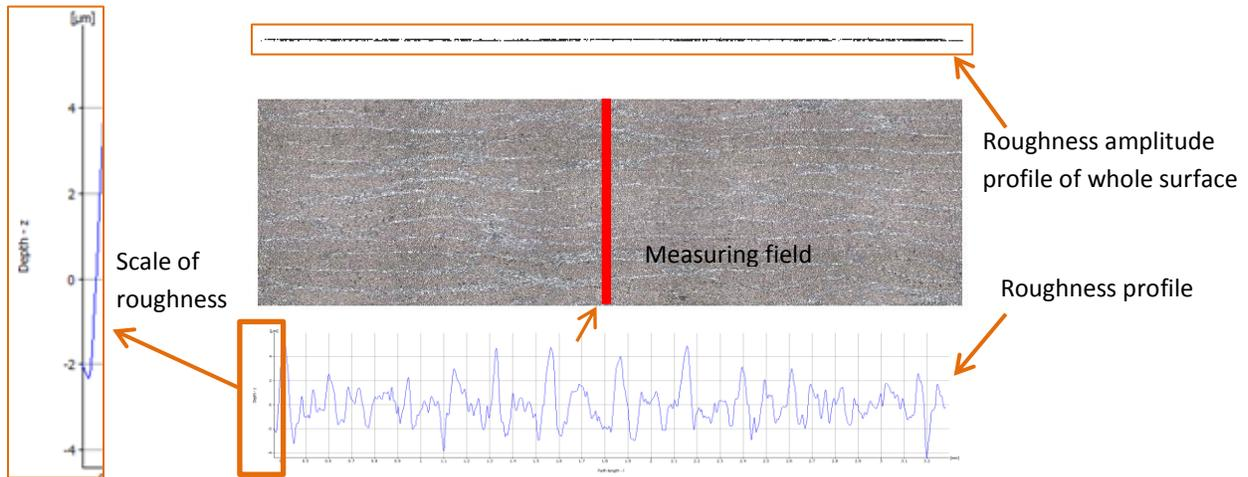


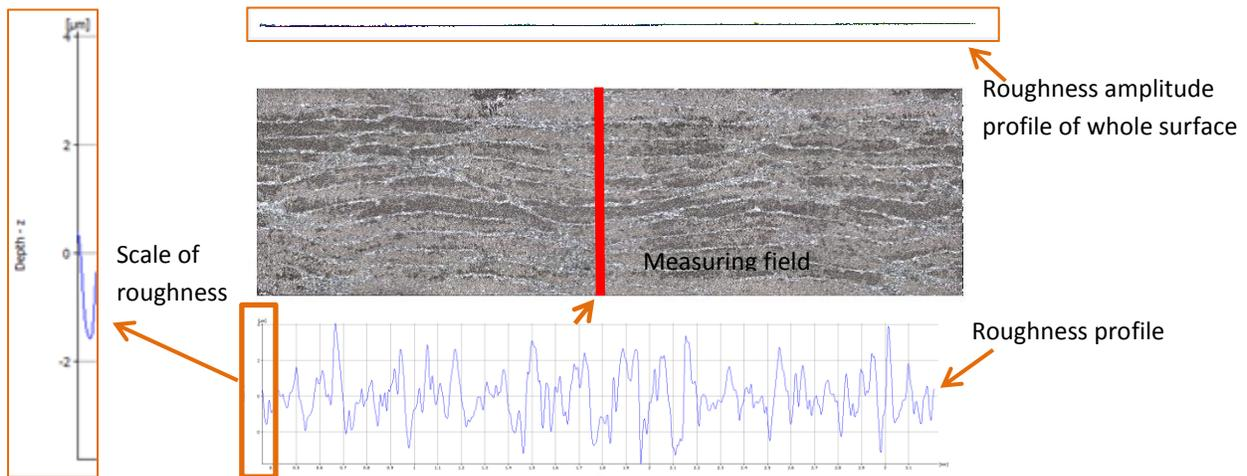
Fig. 3.3.1: Roughness (experimental): (a) 0° fiber orientation (b) 45° fiber orientation (c) 90° fiber orientation and (d) at 135° fiber orientation.

A strong influence of cutting depth is seen at 135° fiber position, Fig. 3.3.1-d. As the fibers are inclined toward the opposite way of cutting direction, not only the apex of the cut surface of fibers get debonded from the matrix by the tool tip but also micro-cracks are generated along the fiber-matrix interface which gets longer depending on cutting depth. It is because the cross-sectional stiffness of fiber is higher than the adhesive force of the fiber-matrix interface. So higher the cutting depth, longer the micro cracks. This argument well supports the findings of [Wang and Zhang, 2003] and [Koplev, 1983] which show that if the fiber orientation gets greater than 90°, the roughness increases rapidly, that means the fiber orientation plays a role here. Moreover, fibers are very abrasive which causes sharpness loss of cutting tool. The more the

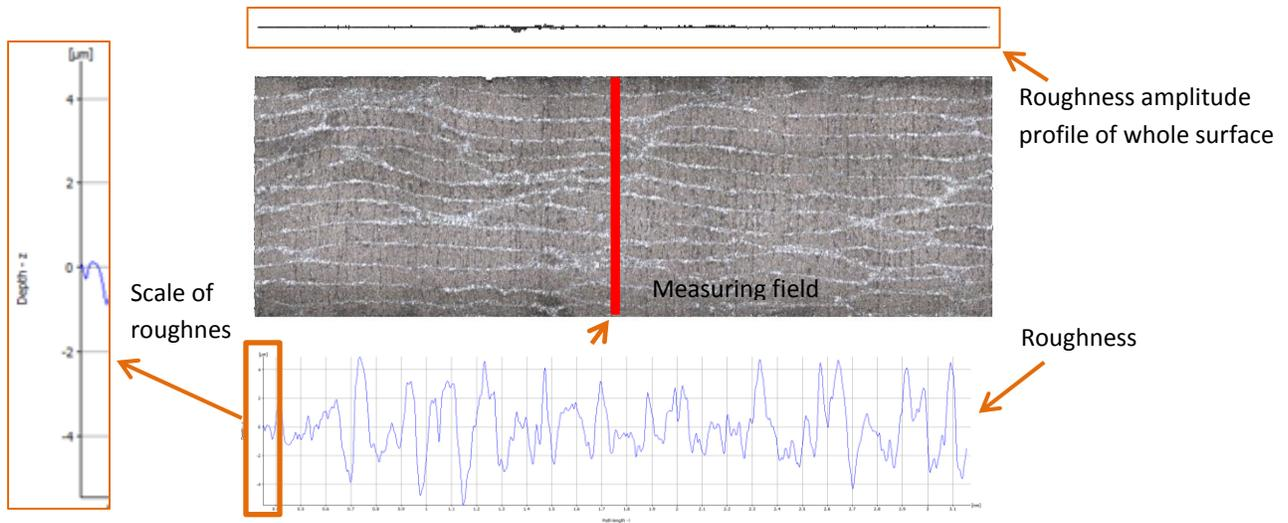
tool is used, the more it loses its sharpness, and, as a result, the radius of the tool tip increases, hence increased springback and surface roughness.



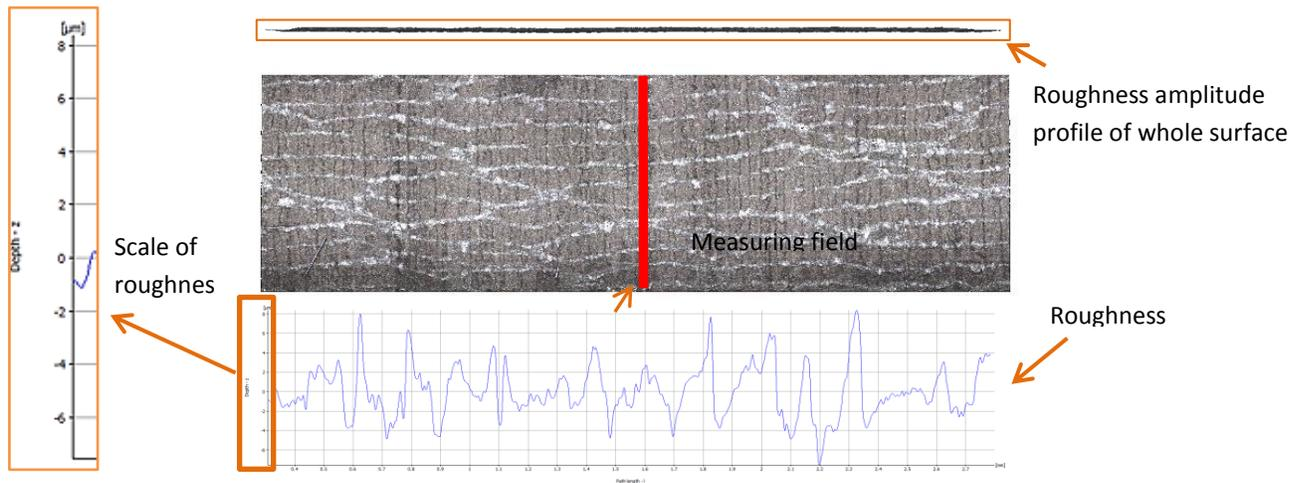
(a) 0.25 mm cutting depth. Comparably frequent oscillation of roughness but low magnitude of depth. Very few high peaks.



(b) 0.50 mm cutting depth. More frequent oscillation of roughness and large number of high peaks compared to 0.25 mm cutting depth.



(c) 0.75 mm cutting depth. Less frequent oscillations but each individual oscillation has comparably higher heights than at 0.25 and 0.5 mm cut.



(d) 1.0 mm cutting depth. Much less frequent oscillations of roughness but the amplitude of depth is much higher than any other cutting depth. Moreover, the roughness amplitude profile of the whole surface is much thicker than any other cutting depth.

Fig. 3.3.2: Typical roughness profiles at 0.25 mm, 0.50 mm, 0.75 mm, and 1.0 mm cutting depths at 90° fiber orientation.

The oscillations of cut surfaces at different cutting depths at 90° fiber orientation have been shown in Fig. 3.3.2. The profile here is the cut-off length transverse to the cutting direction at

the middle of the workpiece. What is clear on the profiles is that the frequency of oscillation is very frequent at low cutting depths (as here at 0.25 mm) and it decreases once the cutting depth increases (the lowest at 1.0 mm). But a close look on the magnitude (value of depth) shows that the magnitude of depth is lower at 0.25 mm cutting depth (4 μm maximum) and higher at 1.00 mm cutting depth (8 μm maximum). At the same time the roughness amplitude profile of whole cut surface is found increase if the cutting depth increase.

As the cutting sequence was from low cutting depth to high cutting depth tests the tool was sharper at 0.25 mm then 0.5 mm, 0.75 mm and 1.00 mm cut. More the tool gets used more it loses its sharpness and as a result the amplitude (depth) and wavelength of roughness becomes higher. Additionally, it was found that if the cutting depth increase the chips become longer which also affect the wavelength of the roughness profile too.

3.4. Effect to Subsurface Damage

3.4.1. Crack Generation and Propagation

Subsurface damage or crack generation can be of different types according to [Lasri et al., 2009] which are fiber-matrix interface debonding, inter-ply delamination, transverse matrix cracking and fiber rupture. The trend of rising crack and damage during cutting is found to be a function of cutting depth and fiber orientation. At 0° and 45° fiber position at all cutting depths no crack has been found, neither numerically nor experimentally, Fig. 3.4.1. Thus the remarkable point is that the cutting depth has no influence on the surface damage at these fibers' positions. It is because the majority of cracks in CFRP machining are generated by the tensile stress (normally the one at cross-sectional direction to fibers) or shearing stress (at the fiber direction).

At 0° fiber orientation the transverse tensile stress in fiber is minimum, however, the shearing stress in fiber direction is significant but as the fibers are horizontally orientated the crack is not generated vertically. Likely at 45° the transverse compressive stress in fiber and also the shearing stress is significant but these stress fields do not go far below than the cut surface of the workpiece. So the subsurface area does not get affected by crack.

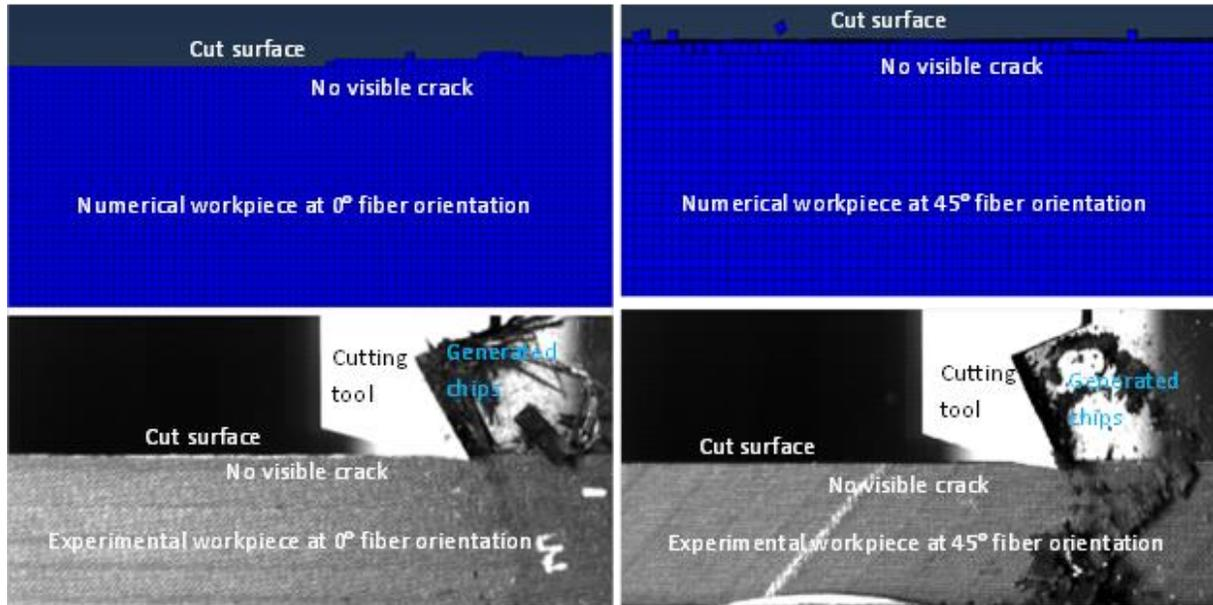


Fig. 3.4.1: Numerical and experimental surface state at (a) 0° and (b) 45° fiber orientation.

At 0.1 mm and 0.25 mm cutting depth of 90° fiber orientation no crack has been found experimentally indeed a number of cracks were seen numerically at 0.25 mm cutting depth. However, 0.50 mm, 0.75 mm and 1 mm depth generated several noticeable cracks having maximum 4 mm long in experimentation and 2.5 mm in numerical model as shown in Fig. 3.4.2. At this fiber position the cracks remain just on the workpiece's two sides and do not get cross-sectionally through the whole workpiece. So the cracks which are visible on the workpiece at this fiber orientation are nothing but just on the outer folders.

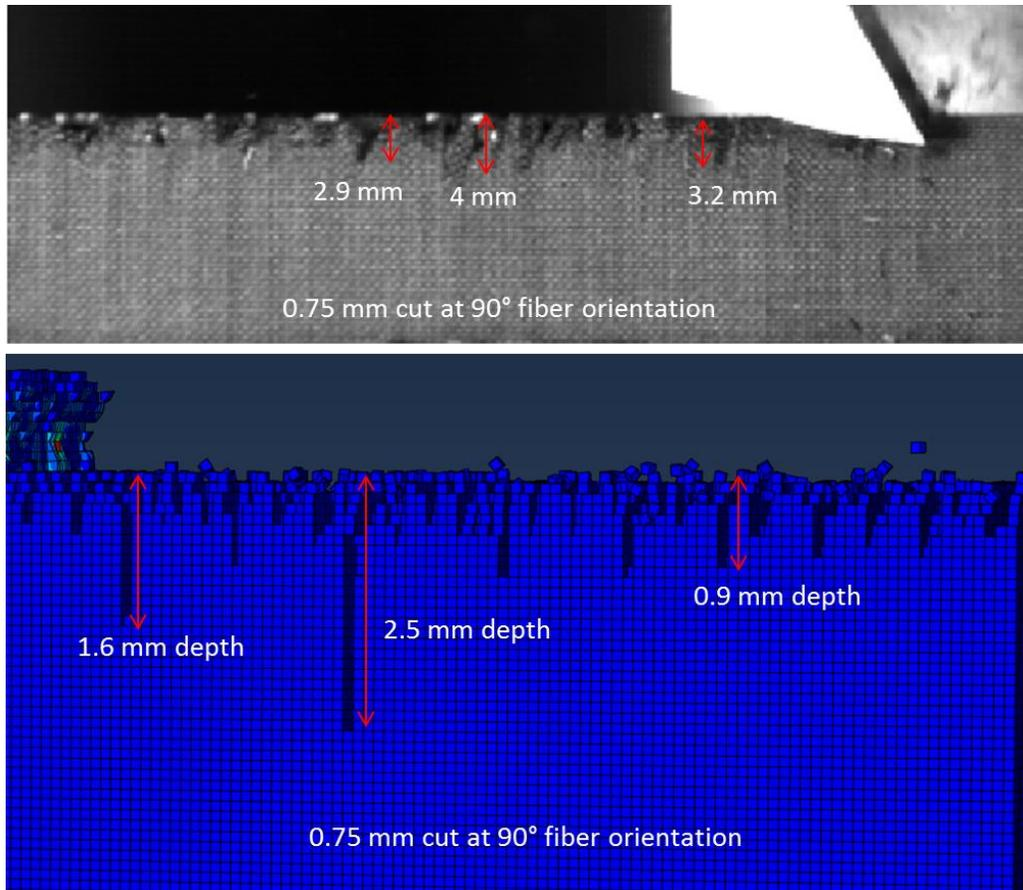


Fig. 3.4.2: Numerical and experimental surface state of 90° fiber orientation at 0.75 mm cutting depth.

The reason for these cracks is that the outer folders of the workpiece remain in contact with the inner materials of the workpiece but at outer side it is totally free (no support). So by the forward movement of the cutting tool these outer folds get debonded and bend outward of the workpiece. The severe debonding of these folds shows visible crack on the side surface. Nevertheless, they remain just on the side surface. An image of numerical model with a close look has been shown in Fig. 3.4.3. The same remark was made by [Blanchet, 2015].

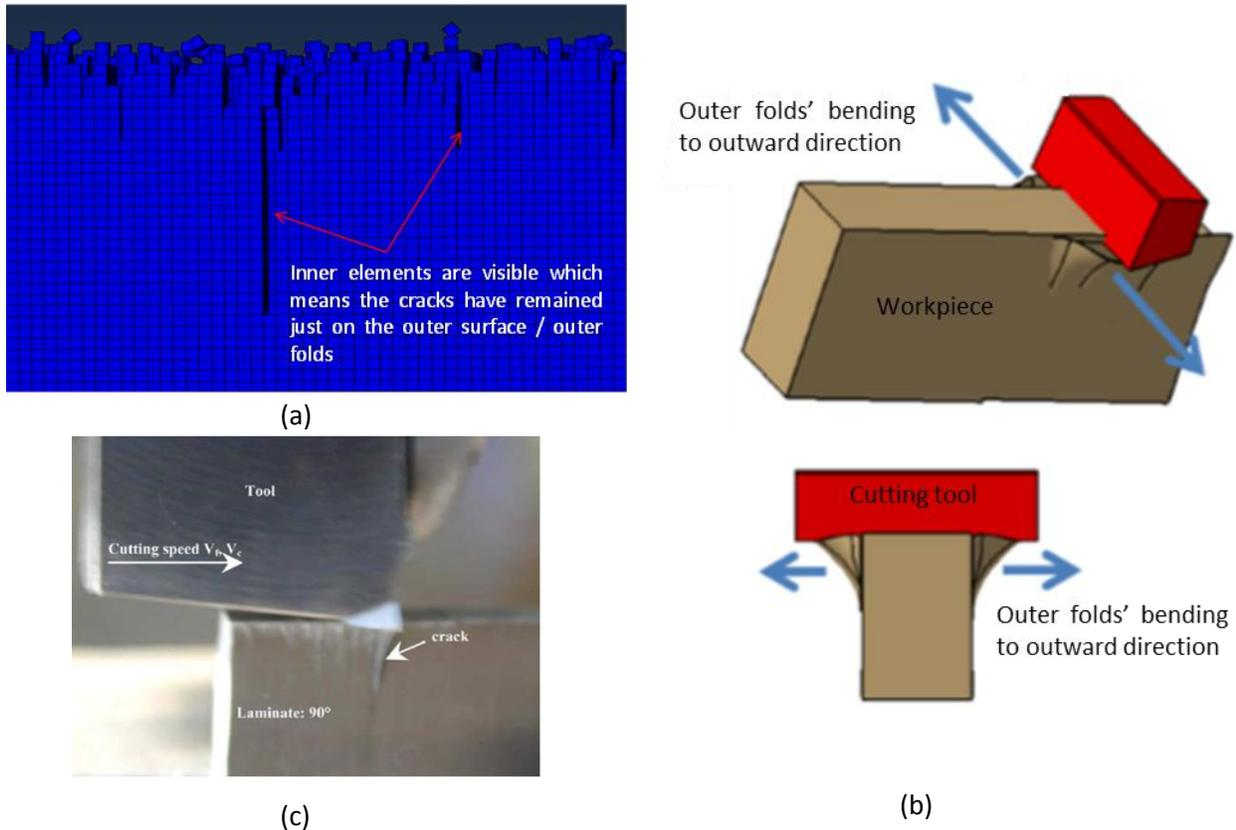


Fig. 3.4.3: Side surface cracks at (a) 90° fiber orientation's model, (b) drawn image by [Blanchet, 2015] (c) crack on surface found by [Zitoune et al. 2005].

Significant crack generation and propagation have been found at 135° fiber orientation. A numerical and experimental comparison of generated cracks for different cutting depths is shown in Fig. 3.4.4. On the figure it can be clearly seen that if the cutting depth increases, the crack extends. At 0.1 mm depth the fiber matrix interface crack is 0.85 mm in simulation and 4.5 mm in experimentation, whereas, at 1 mm cutting depth the simulated crack is 10.2 mm and the experimental one is 14 mm. The simulated cracks are shorter than the experimental ones. The reason behind it is that in CFRP there are three different phases; fiber, matrix and fiber-matrix interface. Each of the phases contains distinct characteristics. As the cross-sectional stiffness of fiber is higher than the adhesive force between fiber and matrix, the fibers get debonded from the matrix which generates crack and permits propagating depending on the amount of force exerted by the forwarding tool; similar note was found from [Shchurova et al., 2016]. Unlikely, the EHM model does not hold quietly those discrete characteristics which are the causes of varying result from experimentation.

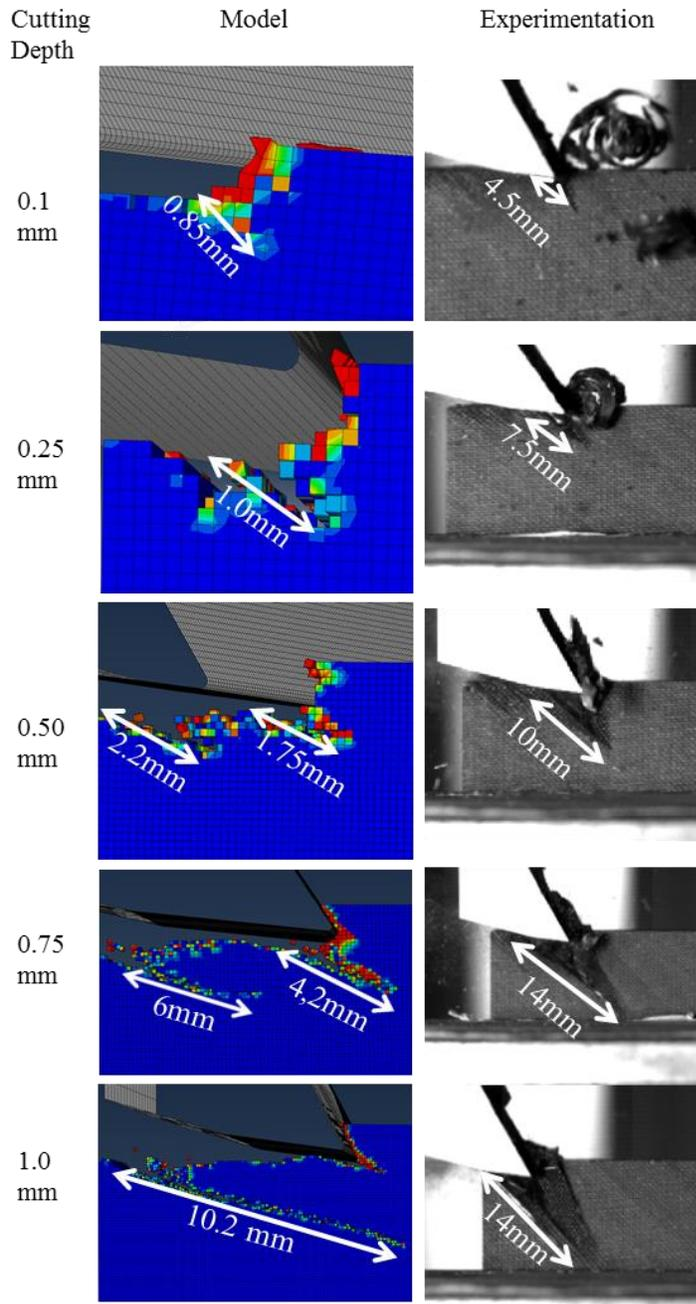


Fig. 3.4.4: Numerical and experimental fiber-matrix interface crack as a function of cutting depth at 135° fiber position.

3.4.2. Subsurface Damage Analysis by X-ray Tomography

X-ray Tomography collects radiographs through 360° rotation of the object that is reconstructed into a 3D model and this reconstruction data includes the inner structure of the scanned part as well as the outer surface. It allows imaging of the interior microstructure of materials non-destructively and with spatial resolution which can approach that of optical microscopy [Stock S.R., 1999] and it is capable of assessing entrance and exit delamination of machining holes [Tsao CC and Hocheng H, 2004].

No remarkable X-ray Tomography analysis has been found in literature in orthogonally machined parts but a lot of research work has been found when it comes to CFRP drilling. [Nadia K. et al. 2015] demonstrated that in drilling the complete whole inner surface and near surface region can be inspected by X-ray Tomography and it can also provide information on all the laminates throughout the hole that may have been affected by the drilling with a focus on the quality of finished parts, particularly relevant in aerospace industry.

Here in this present research it has been found that the X-ray Tomography shows the surface state of newly generated surface as well as the inner state of the whole workpiece. The crack generation and propagation, inner voids of the workpiece, delamination, folds' splitting, etc. are clearly visible. In Tomography only one cutting depth (250 μm) at 0°, 45°, 90° and 135° fiber orientation has been used. So the result mainly shows the difference of generated defects if the fiber orientation is changed.

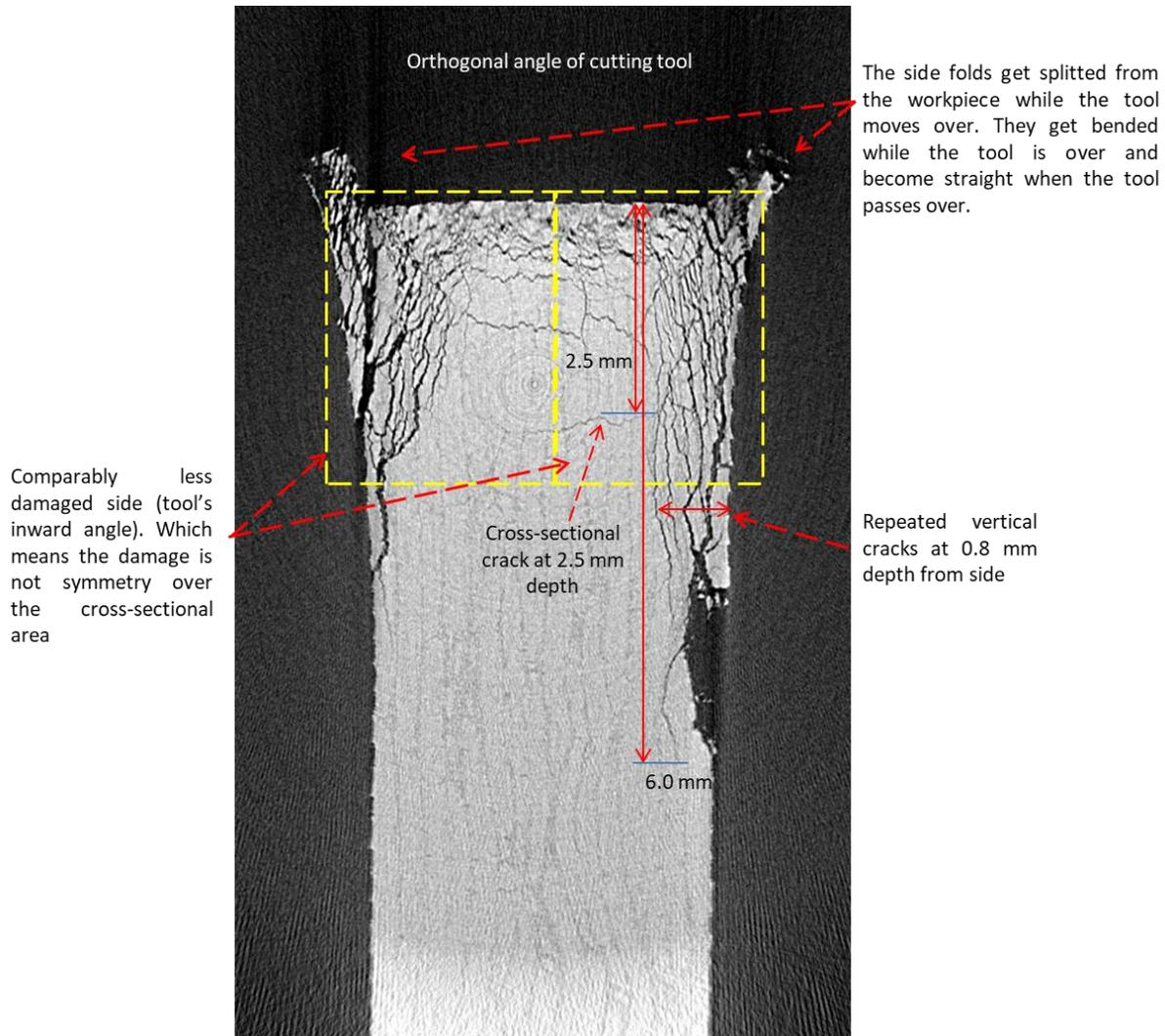


Fig. 3.4.5: Machining induced defects at 135° fiber orientation and $250\ \mu\text{m}$ cutting depth.

It has been found that the workpiece gets severely damaged both inside the workpiece and on the surface if the fibers are oriented at 135° . The dominating defect is crack generation and propagation both vertically and horizontally in the workpiece. As visible in Fig. 3.4.5, the two sides near the cut surface of the workpiece get severely damaged by crack. The source of the crack is the newly generated surface. They propagate toward the side surfaces keeping vertically downward trend. The subsurface up to around 3.5 mm depth from the newly generated surface is seriously damaged. The maximum vertical crack has been measured 6 mm long from the surface. However, the damage looks almost symmetry to two side surfaces.

The most remarkable point is some horizon cracks have been generated. The noting point is that these horizontal cracks are not interfacial debonding or interfacial crack but here the fibers get cross-sectionally broken which substantially reduces the stiffness of the material. The deepest

horizontal crack is seen at 2.5 mm depth from the new surface. These phenomena arise because of this particular fiber orientation. The tool needs maximum efforts at this position which generates compressive stress field in the workpiece in front of the tool nose but at the same time the area which gets cut and released from the tool lip becomes stress free; such potential crack is generated at the area below the tool lip.

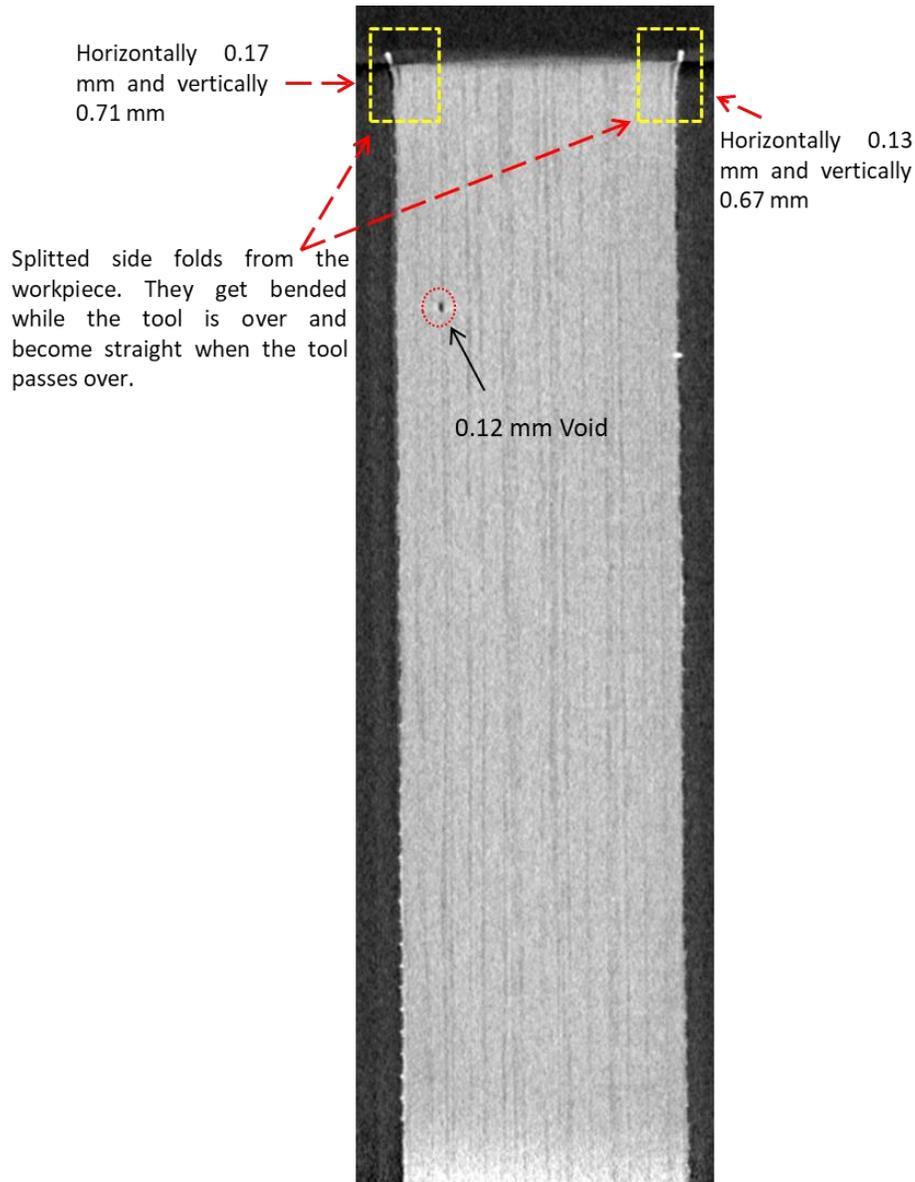


Fig. 3.4.6: Machining induced defects at 90° fiber orientation and 250 μm cutting depth.

Unlikely to 135° at 90° fiber orientation for the same cutting depth (250 μm) no remarkable crack is seen, neither vertical crack or horizontal crack. But it is found that the side folds near the cutting zone get split from the main workpiece which causes a short split ranging 0.71 mm vertically and 0.17 mm horizontally at left side and 0.67 mm vertically and 0.13 mm horizontally

at the right side, Fig. 3.4.6. These side folds get bent outward while the cutting tool over them and returns once the tool passes over causing a permanent split with the main workpiece. On the other hand, a few voids have been found in the workpiece. The influence of voids to the material has been discussed in the next paragraphs (paragraphs of 45° and 0° fiber orientation).

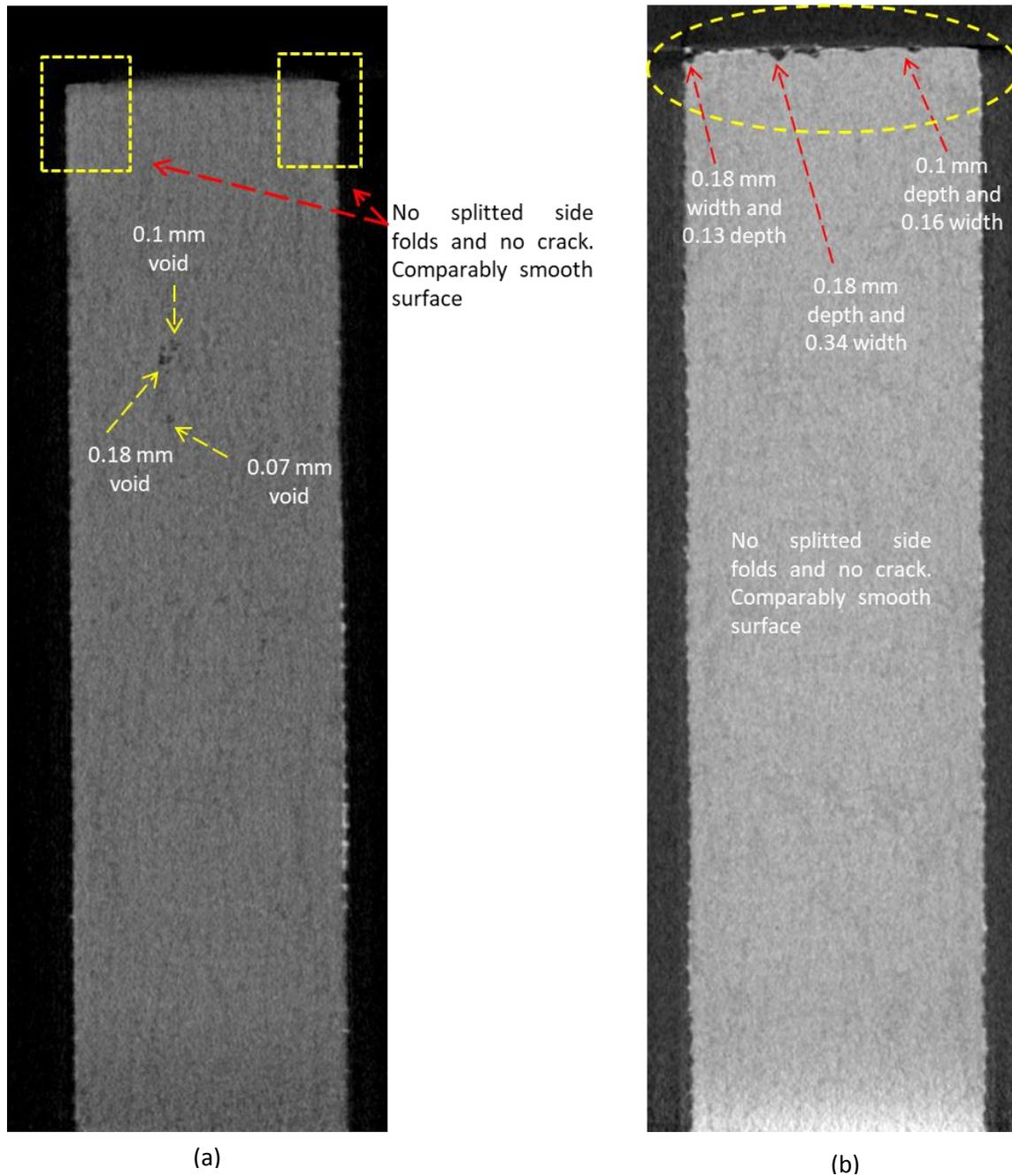


Fig. 3.4.7: Machining induced defects at 250 μm cutting depth (a) at 45° and (b) at 0° fiber

Fig. 3.4.7-a shows the cross-sectional area of 45° fiber orientation and (b) shows of 0° fiber orientation in tomography. At both of these fiber orientations no vertical or horizontal crack is seen. Additionally, there is no side fold's splitting in these fiber angles indeed at 135° and 90° side folds' splitting was seen on both sides. In Fig. 3.4.7-a several voids are visible. In the tomography test many voids were found in along the longer of the workpiece at 45° fiber angle but at 0°, this occurrence is negligible.

Voids in the material is a concerning issue. They are one of the most common manufacturing induced defects which indicate the presence of air in the matrix [Strong A.B., 1989]. They influence the mechanical property of materials. [Xueshu LIU and Fei CHEN, 2016] said that voids are always the potential locations of failure and cause discontinuities in the material properties of CFRP, which degrade the mechanical performance of CFRP, notably to inter-laminar shear strength, compressive strength, flexural strength, fatigue strength etc. The influence of voids to compressive strength is analyzed by [Zhang A. et al. 2016], Fig. 3.4.8. However, it has not been found in the literature whether the cutting angle or cutting depth has influence to void.

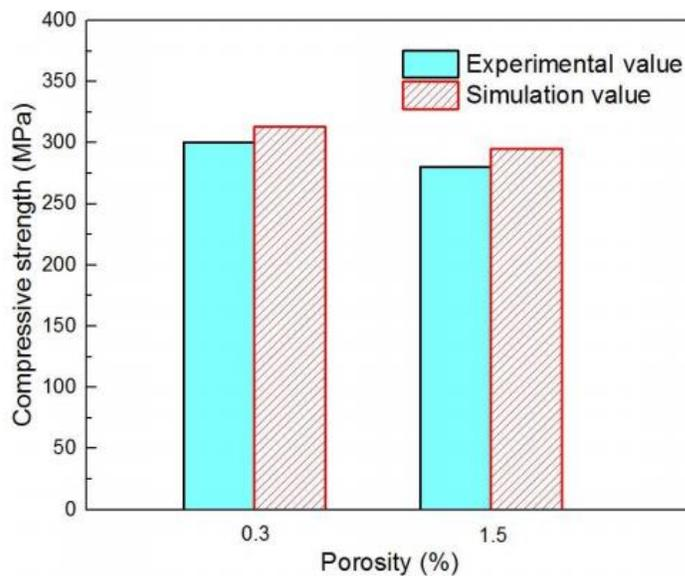


Fig. 3.4.8: Finite element simulation and experimental value of the effect of void on compressive stress, found by [Zhang A. et al. 2016].

In case of 0° fiber orientation, Fig. 3.4.7-b, indeed no crack or side folds' splitting are seen but a few cavities are generated on the newly generated cut surface. The biggest cavity has 0.18 mm depth and 0.34 mm width. These cavities substantially affect the surface quality and increase

the surface roughness. In the assembly process, they minimize the contact surface which results reduced the mechanical strength in joining.

If the fibers are not well oriented at 0° angle, they get cut/broken in bunches during machining that results cavity on the newly generated surface. So during CFRP manufacturing process the fiber should be well oriented to avoid this kind of defects.

Subsurface Damage in Oblique Cut

During the experimentation process, a few tests were carried out putting the oblique configuration of the cutting tool. Here the oblique angle of the tool is 12° . The main intention of the tests was to see the differences between the generated damages in orthogonal cutting and oblique cutting. Here as seen in the Fig. 3.4.9, the configuration of the tool is oblique, the cutting depth is $250\ \mu\text{m}$, and the fiber orientation is 135° . The tool was horizontally 12° positive at the right side, so 12° horizontally negative at left side (it means the tool's right edge will more likely push the fibers inward to the workpiece and at left side it will push the fibers outward of the workpiece). In case of orthogonal cutting, all the parameters are the same as oblique but just the tool is in orthogonal angle.

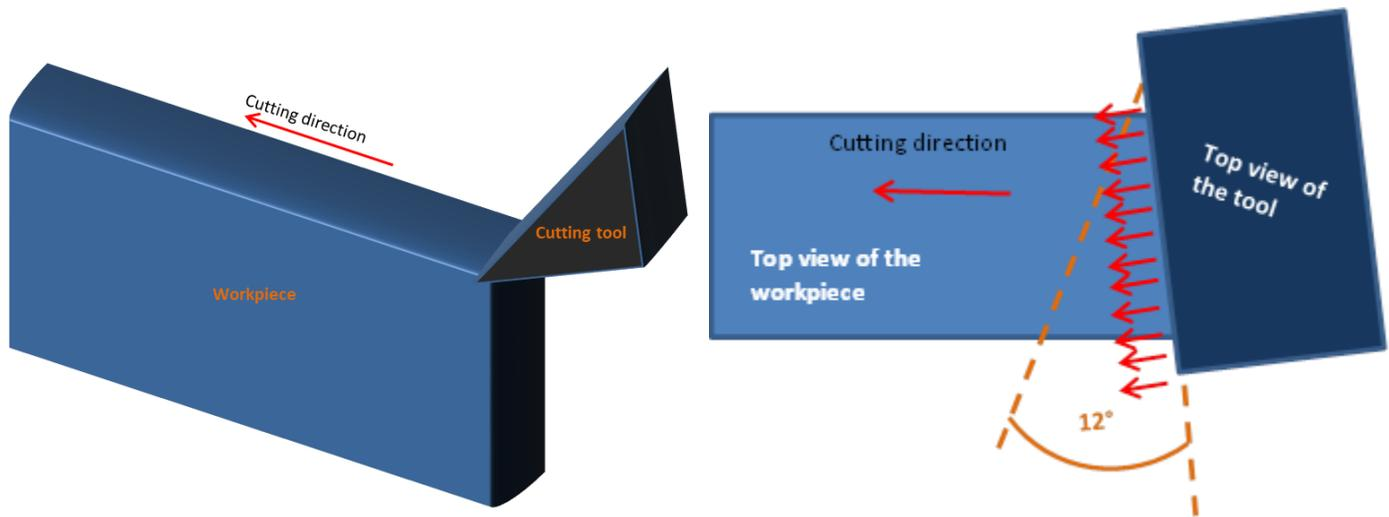


Fig. 3.4.9: Schematic view of oblique cutting configuration

It is found that there is a big difference in the area of generated defects between oblique cutting and orthogonal cutting. In oblique cutting the left side of the workpiece is severely damaged whereas at right side it is comparably low, Fig. 3.4.11-a. Many vertical cracks are generated at the left side which prolongs up to around 9 mm depth but at the right side the cracks are comparably less.

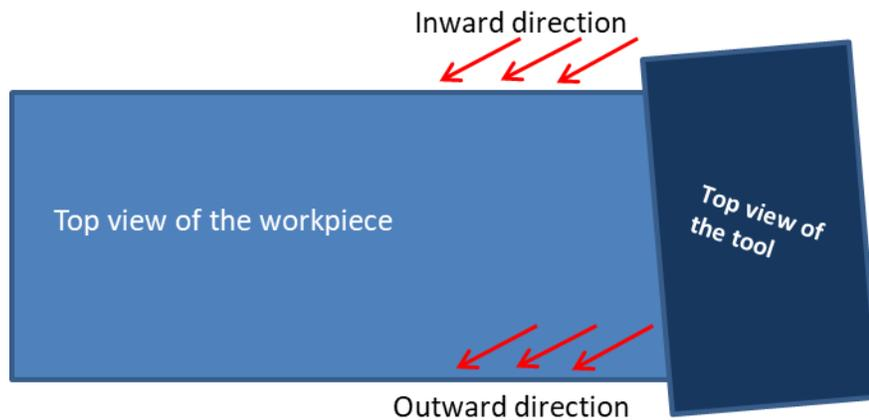


Fig. 3.4.10: Schematic view of oblique cutting configuration

However, at orthogonal cutting, Fig. 3.4.11-b, the generated defects are more likely symmetry at both sides of the workpiece. Many cracks are generated but they are shorter compared to the left side of the oblique test's workpiece. The main reason behind this difference is the orientation of the cutting tool. As said already, at oblique cutting one side of the tool edge shoves the fibers inward and other side outward of the workpiece. Fig. 3.4.10 illustrates this phenomenon. So at the outward direction's side the surface of the workpiece gets fatally damaged.

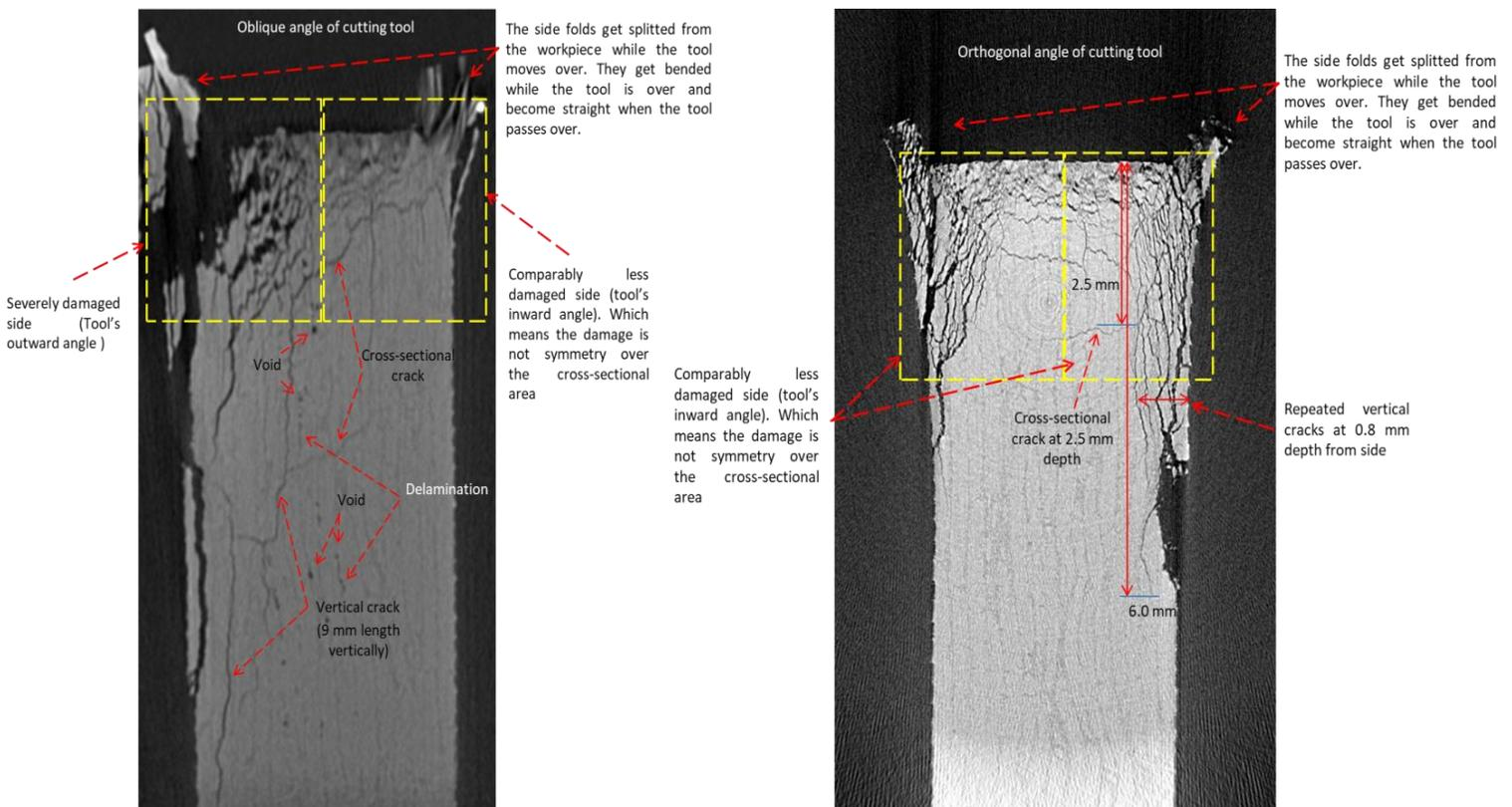


Fig. 3.4.11: Machining induced defects at 250 μm cutting depth (a) at oblique cutting (135° fiber orientation) and (b) at orthogonal cutting (135° fiber orientation).

3.5. Effects to Chip's Shape and Size

Many research works have been done to reveal the physics of orthogonal cutting of CFRP but the effect of cutting depth to the generated chip's size and shape is remained unrevealed. [Arola et al., 2002] did some research regarding the displacement of a tool needed to form a chip at different fiber angles from 15° to 90° without changing the cutting depths. [Vořa et al., 2014] worked on chip roots analysis for five different unidirectional fiber orientations using an orthogonal cutting test rig. [Hao et al., 2016] mentioned that two main factors, namely the depth of cut and fiber orientation angle, which influence the chip morphology. Their research was done assuming four ranges of fiber angles from 0° to 180° . Range based fiber orientation is not appropriate for the parts with particular unidirectional fiber orientation. [Lasri et al., 2009] analyzed the chip's thickness according to fiber orientation and then compared with the experimentally measured results of [Nayak et al. 2005]. They took into account the positive fiber orientation, 50° rake angle and single cutting depth in their work. It is believed that the chip size and shape can be different according to the fiber orientation but any comprehensive analysis

concerning the length of the chips has not been found. Moreover, in literature it was not found if the cutting depth is changed how it affects the generated chips size and shape. So an analysis of chip's size and shape at different fiber orientations and cutting depths would reveal the relevant phenomenon.

3.5.1. Chip's Length

Size and shape of chip depend on the input parameters of the process as well as the fiber orientation. In other ways, this is the input process parameter and the tool geometry along with the fiber orientation. In this present experimental research work, some process parameters were constant while the cutting depth was kept as a variable. The chip lengths were studied according to different cutting depths and fiber orientations. The features of a generated chip at 90° fiber orientation have been shown in Fig. 3.5.1.

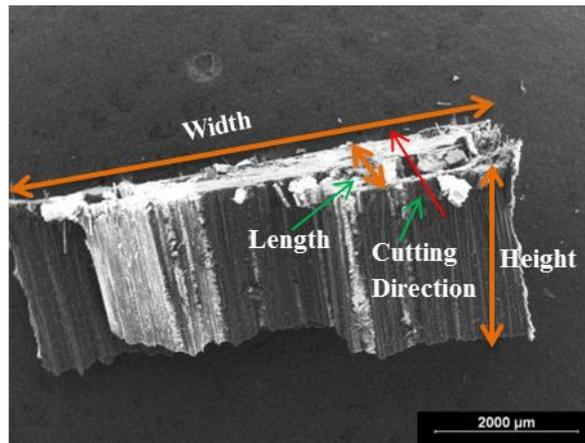


Fig. 3.5.1: Features of a chip at 90° fiber orientation.

It has been found that the cutting depth has remarkable influence to the chip lengths but this influence depends strongly on fiber orientation. Chip length increases if the cutting depth increases at 45° and 90° fiber orientation as shown in Fig. 3.5.2-b and (c). At 0° fiber orientation, the chip length fluctuates according to the depth of cut. On the other hand, at 135° fiber orientation the chip length decreases if the cutting depth increases. At 0° fiber orientation, the fibers normally do not get cut cross-sectionally as they are placed horizontally to the cutting direction. At shallow cutting depths (here at 0.1 mm and 0.25 mm) the generated chip is very thin, it does not hold enough strength to resist the tool's rake surface exerted forwarding drive force, so it gets broken at certain lengths during the forming course, Fig. 3.5.2-a. In our experimentation, for 0.1 mm cut the length of a particular chip was 6.45 mm whereas for 0.25 mm depth it was 23 mm. It was found that while the cutting depth is 0.5 mm, the chip gets

bended along the entire length but does not get separated from the main workpiece; as a result the chip length remains equal to the length of the workpiece (we also tested it for 0.3 mm cutting depth separately, and found the same scenario as 0.5 mm depth). However, at 0.7 mm and 1.0 mm cutting depths the chips get struck at the end corner of the rake surface (the context is shown in Fig. 2.5.4-a); because of that, the chips get broken at the middle. As a result, the length of chip becomes shorter, Fig. 3.5.2-a. It is deduced that if the tool rake surface permits the chip free flowing, then the chip length will be equal to the length of the workpiece.

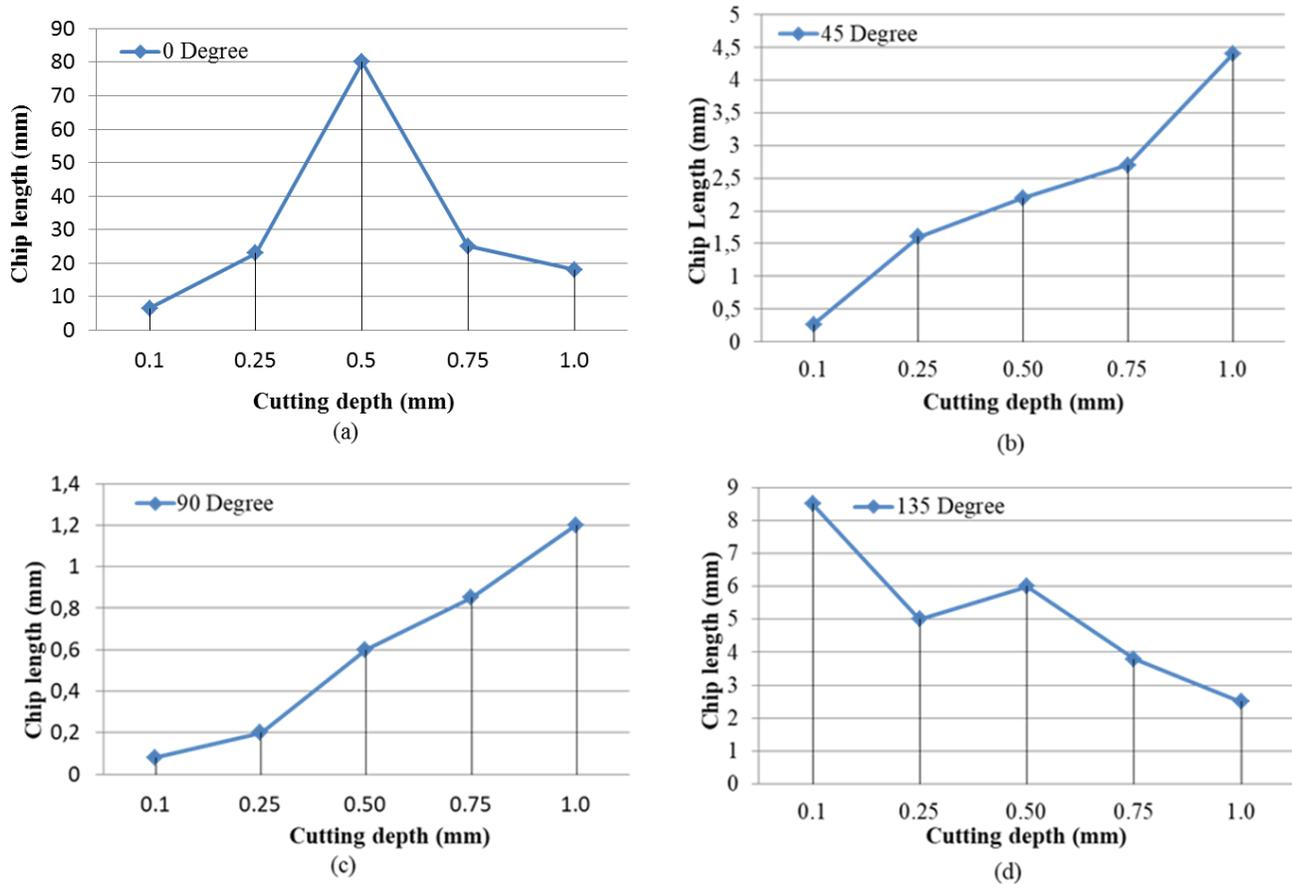


Fig. 3.5.2: Fiber lengths according to the cutting depths; (a) at 0°, (b) at 45°, (c) at 90° and (d) at 135°

At 45° fiber orientation the fibers are inclined to the cutting direction. The maximum stress zone remains around the tool tip, so more the tool gets down from the cut surface less the cut surface field gets stressed which permits the tool to penetrate further before the chip split from the part. As a result, more the cutting depth, longer the chip. The same scenario can be seen for 90° fiber orientation but a notable difference is that at 90° as the fibers are straight vertical from cutting direction the fiber matrix interface debonding starts at the proximate region which is responsible for shorter chip length compared to the one at 45°. On the contrary, at 135° fiber

orientation the tool's rake surface gets more material contact if the cutting depth increases (as the fibers are placed at negative direction to cutting path). More tool-material surface contact means bigger stress field. Consequently, more the cutting depth increases more the stress field is generated in the load region, and chips get separated from the workpiece at short length. That is why, in Fig. 3.5.2-d, at low cutting depth the chip length is longer and at high depth the chips are comparably shorter.

3.5.2. Chip's Height and Width

Theoretically it is considered that the chip height is equal to the initial cutting depth. In this research it was found that the height and the normal shape largely depend on the chip separation phenomenon which is linked to the tool geometry, e.g.: rake angle, fiber orientation, cutting depth etc. Notably, fiber orientation and cutting depth plays an important role to the chip shape. In current work the length of the workpiece was 80 mm and the width was 4 mm; so a 3 dimensional shape analysis can reveal the appropriate geometry of the chip.

As mentioned earlier, it was found that at 0° fiber orientation the longer of the chip is equal to the longer of the workpiece for all tested cutting depths except the one of 0.1 mm (the reason is explained in chip length section) but the height becomes more than the cutting depth. It is because the material in the chip becomes deleted and fiber matrix interface becomes mostly debonded, and as a result the chip height gets higher than the initial cutting depth. In the case where the chip remains unbroken the width gets a bit higher than the original width. It should be noted that in chip shape analysis it will not be logical to study chip shape with quantitative value as a wide range of chips with different shapes are generated during CFRP cutting. In Fig. 3.5.3, some typical chips at every cutting depth and fiber orientation have been shown, except at 0.5 mm, 0.75 mm and 1.0 mm cutting depths of 0° fiber orientation (the fibers were too long to capture in the SEM).

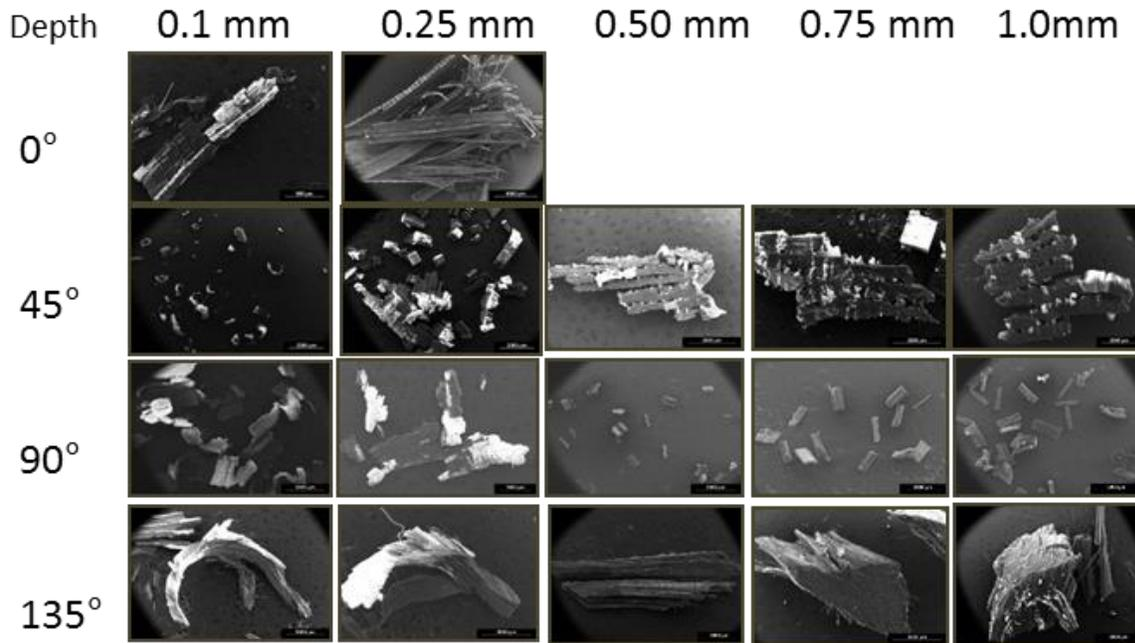


Fig. 3.5.3: Generated chips in experimentation

At 45° fiber orientation it was found that the height of chips varies with cutting depth. At 0.1 mm cutting depth most of the chips' height lie in between 50 μm to 60 μm which is around half of the initial depth. It is because at this fiber angle the fibers are inclined to the cutting direction. At this low cutting depth the fibers become highly pressed at downward direction and the tool tip faces comparably high reaction and abrasive frictions from the inclined pressed fibers. As a result the real depth of cut becomes less than the set depth of cut. So the generated chip height becomes less than the cutting depth.

At 0.25 mm, 0.5 mm, 0.75 mm and 1.0 mm the chip heights were found almost the same as the original set depth. In these depths the load region gets enough volume of material to share the tool exerted stress which resists the fibers from being highly pressed before cut. As a result the real cutting depth remains almost the same as original set depth. Regarding the width of the chips, it was found that at 0.1 mm and 0.25 mm cutting depth the chips get broken vertically along the fiber direction. This phenomenon is practical as the chip height is comparably short but, contrary, at 0.5 mm, 0.75 mm and 1.0 mm depth the width of the chip was around 4 mm as the width of the workpiece.

Regarding the chip height the same scenario, those of 45°, was found at 90° fiber orientation but the width of the chip was much smaller at every cutting depth. Some of the chips got around 500 μm widths but all other got much lower. As the fibers are oriented perpendicularly to the cutting direction the fibers experience cross-sectional penetration from the cutting tool. Consequently the fibers and matrix get fatally debonded all-around in all directions. That is the

reason why the chips are broken vertically along the width and get much smaller at this cutting angle no matter how much the cutting depth is.

For all cutting depths from 0.1 mm to 1.0 mm the height of the chip was almost double than the initial cutting depths at 135° fiber position. This increment reveals that the real depth take-up at 135° fiber orientation is much higher than the initial set depth. Here this particular fiber position angle causes the difference. Regarding the width it was found that majority of chips' width remain from 0.5 mm to 1.0 mm at 0.1 mm and 0.25 mm cutting depth though at 0.5 mm, 0.75 mm and 1.0 mm depth the width lies from 1.0 mm to 2.0 mm. This difference comes because of differ stress distribution at lower cutting depth as like other fiber angles.

Remarks

The cutting depths have less effect to chip size and shape compared to the fiber orientation. For a same cutting depth, the chip length is higher at 0° fiber orientation than any other fiber position. The final depth of cut or chip height is more than the original set depth at 135° fiber orientation.

3.6. Conclusion

In orthogonal cutting depending on the type of material, the part quality and generated defects can vary. It is not just because of the mechanics of cut but also because of individual characteristics of materials. Understanding the relationship of cutting variables with cutting quality and required cutting efforts are crucial to secure the best cutting parameters and to understand their influences well. A range of cutting depths has been used to analyze their influences to the machining efforts, surface and subsurface damages and to formation of chips.

It is found that the numerical results of cutting forces provide a good agreement with the experimental cutting forces, which reveals that the cutting force increases if the cutting depth increases; the thrust force is mainly dominated by fibers' orientation rather than cutting depths. For any cutting depth at 135° fiber orientation, the thrust force will always be negative (vertically downward) and at 45° fiber orientation always positive (vertically upward). On the other hand, the initial unstable high force is found as functions of initial compression of fibers by the tool and generated vibration and instability in the cutting tool and the workpiece.

Cutting depths have significant influence on surface roughness and crack generation principally at 135° fiber orientation. The visual study and X-ray Tomography results show that at this fiber orientation the newly generated surface and subsurface get severely damaged but at all other fiber positions it is unlikely. No crack has been found at 0° and 45° fiber angle. Besides, it is seen that cutting depth has marginal influence to the chip length compared to fiber orientation. At

45° and 90° fiber orientation, the chip length increases if the cutting depth increase but it is totally contrary at 135° fiber direction.

Chapter 4: Tool Wear and Minimum Cutting Depth for Continuous Cut

This chapter is the last chapter which talks about minimum cutting depth (cd_{min}) in orthogonal cutting of CFRP and the tool wear while cutting CFRP. Both of the subject matters have been analyzed experimentally. In CFRP machining, not any particular cd_{min} has been found throughout the literature. Thus, this study has been carried out to realize the minimum depth, below which, the tool does not cut the material smoothly and continuously over the thickness as well as longer of the workpiece. The study has been done by distinguishing the fiber orientations (for each fiber orientation, a distinct cd_{min} has been investigated).

Another research focused to tool wear mechanism (principally the sharpness loss) while cutting CFRP. It is more likely a preliminary study which mostly focuses on the behavior of tool wear during cutting. The tool was used several times at a certain cutting length at distinct fiber orientations. Later the amount of sharpness loss in the tool and their locations were examined. This study gives a preliminary understanding of the mechanism of cutting tool sharpness loss. Moreover, it gives a framework for further research on tool wear mechanism at different configurations of cutting in future.

Content

Chapter. 4. Tool Wear and Minimum Cutting Depth for Continuous Cut.....	163
4.1. Minimum Cutting Depth for Continuous Cut	165
4.1.1. Experimental Procedure	165
4.1.2. Result Analysis	168
4.1.3. Conclusion, Difficulties and Perspectives	175
4.2. Tool Wear Mechanism	176
4.2.1. The Tool and the Wear Measuring Procedure	177
4.2.2. Results Analysis	181
4.2.3. Conclusion and Perspectives	186

4.1. Minimum Cutting Depth for Continuous Cut

The determination of minimum cutting depth (cd_{min}) is essential in micromachining in order to avoid or minimize the plowing effect and achieve desired material removal and surface quality [Aramcharoen A and Mativenga PT, 2009]. The definition of cd_{min} in CFRP cutting is complex. Generally it is referred to the minimum depth at which the cutting tool cuts the material continuously over the whole surface of the workpiece. [Zhanging Liu et al., 2013] said that when depth of cut keeps decreasing till a critical value, there will be no chip formation. Material will be plowed under the cutting edge without forming a chip. The tool may cut material even if the depth of cut is less than cd_{min} but in that case the cutting will not be continuous and smooth over the whole surface of the workpiece. There is no any particular value of cd_{min} in CFRP cutting. This complexity arises mainly because composite materials are made of several components and each component has distinct behavior during the cut. In CFRP cutting this depth also varies due to the fibers orientations. Moreover, there are some process parameters which can play a role too; for example, the tool tip radius (r_{tt}), the rake angle, the cutting speed etc. The tool tip diameter should not exceed the diameter of the fiber in order to cut the fibers effectively and avoid overlarge cracks in the matrix [Teti R., 2002].

[Youliang Su et al., 2016] analyzed the chip formation phenomenon for 10 μm , 30 μm and 50 μm cutting depths. They used cemented carbide cutting tool with 5 μm r_{tt} . They found continuous cut at these cutting depths while for 0° fiber orientation. For 45° and 120° fiber orientation, the chip formation phenomenon was the same at 10 μm while at 90° the chipping process was found unstable and discontinuous even for a larger depth of cut.

In orthogonal cutting of CFRP one suitable way to analyze the cd_{min} is by distinguishing the fiber orientations. At the same time, the r_{tt} and the rake angle should be measured before carrying out the experimentations. Normally, if the rake angle is fixed and the tip radius is measured before cut, then at any particular fiber orientation the cd_{min} can be found. Here in this current work the analysis has been done at each fiber orientation separately keeping the cutting speed constant. This particular method has simplified the analyzing process as well as made the result much comprehensible.

4.1.1. Experimental Procedure

Setup of Cutting Bench

In this study the same orthogonal cutting bench, Fig.2.1.1, was used. But for image recording, only one camera was used which is a high speed camera with maximum capacity 110,000 photos per second. It was placed in one side of the cutting tool, transverse to the workpiece. Two lights were placed on both sides of the camera keeping focused on the opposite side of the workpiece as in the Fig.4.1.1. A white blank paper was placed at the opposite side of the

workpiece so that the light can get reflected to the camera. It makes transparent under the workpiece. As a result, while the cutting tool moves forward if any portion of the workpiece is cut it becomes clearly visible to the camera.

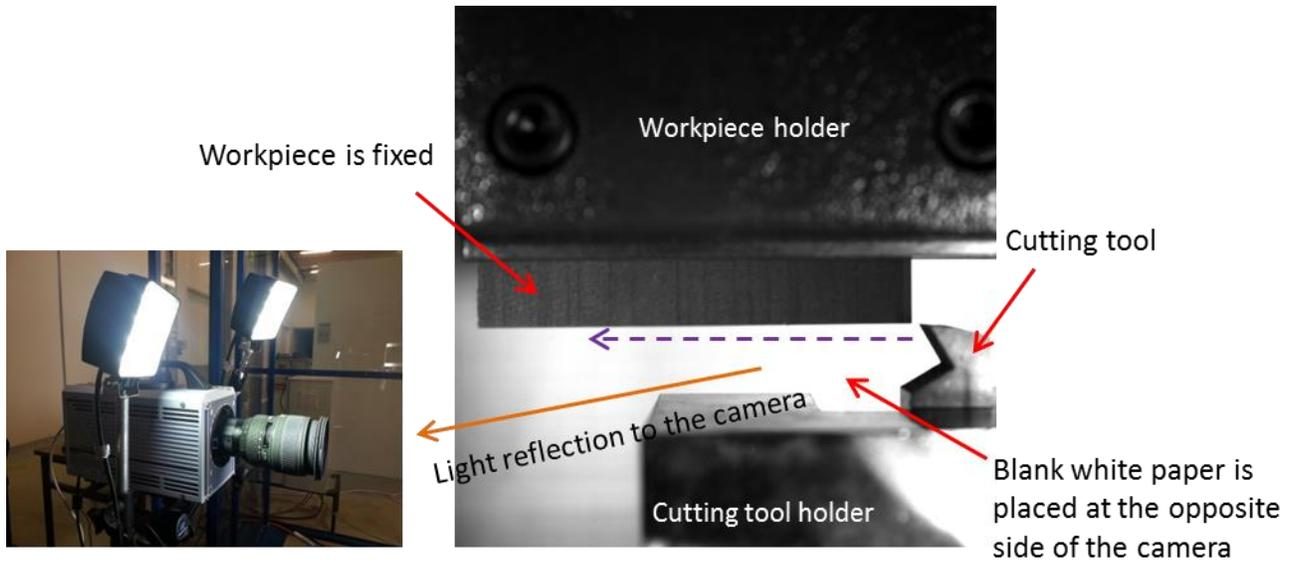


Fig. 4.1.1 : Setup of the experimentation

To set the cutting depth a Mechanical Dial Indicator Gauge was used as in Fig.4.1.2. The magnetic tool holder was placed on the table of the orthogonal bench keeping the gauge head in touched with a portion of the column of the machine. So if the height of the table is changed (which can be done by the vertical movement crank of the machine) the gauge shows the amount of change. As the cutting tool mounting is bolted on the table if the table moves up the tool also moves up. So looking on the scale mark plate of the gauge it is possible to fix the desire height which refers to the cutting depth. The other relevant parameters are as in Table 4.1.1.

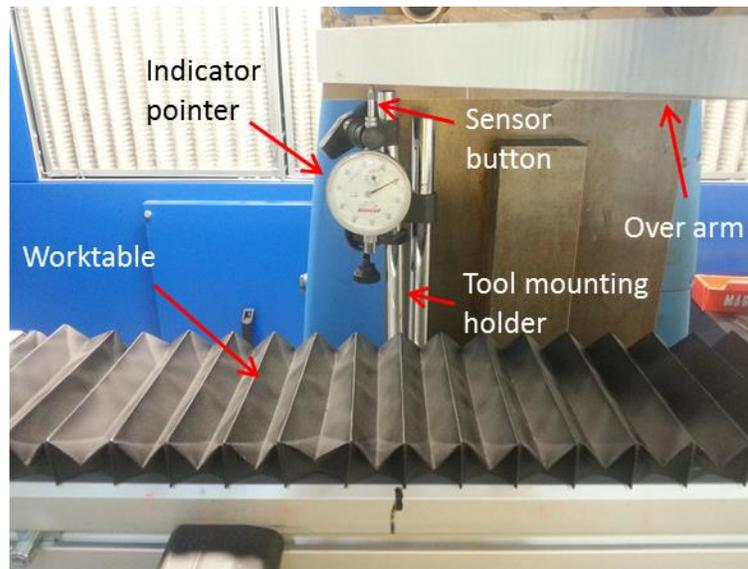


Fig.4.1.2 Mechanical Dial Indicator

Measuring Technique

While the cutting tool moves forward, the tool tip cuts the workpiece surface. As the lower surface of the workpiece is cut, the cut material falls below immediately after separation from the main part. Any material which falls below is clearly visible and the scenario is captured by the camera. During experimentations, the cutting depth was increased gradually from very low depth, which does not generate any chip, until the formation of a continuous chip. The camera took images while the cutting tool moves to the cutting direction from the beginning to the end of cut.

At any cutting depth, if the tool cuts material from the whole cross-sectional area of the workpiece and remains continuous over the whole surface, this depth is considered to be the minimum cutting depth (cd_{min}). And as the area under the cut is transparent and illuminated by external lights, it becomes clearly visible and comprehensible whether the whole surface over the thickness of the workpiece is getting cut or not. On the other hand, at any depth below this cd_{min} , the tool will generate high friction on the surface of the workpiece; the material will not get cut smoothly and continuously over the whole surface.

Parameter	Value
Camera Type	High speed (capacity: 110000 images/sec)
Image recording rate	10000 images/sec
Resolution	1024*1024
Fiber angles	0°, 45°, 90° and 135°
Depth sequence	Low depth to high depth
Tool tip radius	6 μm to 16 μm but varies at each cut
Cutting speed	12 m/min

Table. 4.1.1: Process parameters

4.1.2. Result Analysis

At 0° Fiber Orientation

At 0° fiber angle, the first cut was done at 25 μm cutting depth. The r_{tt} was measured 10.51 μm before being used. At this cutting depth, the tool clearance surface makes strong friction with the workpiece. A small portion of material gets cut and comes out in dust form, Fig. 4.1.3-a. Notably, the tool tip bites a very small margin of fibers; hence, the cut is not smooth over the thickness of the workpiece. Therefore, the 25 μm cutting depth (at 10.51 μm r_{tt} and 30° rake angle) cannot be considered as cd_{min} .

Generally, the diameter of fiber is around 7 μm . And in this case at 25 μm set cutting depth the practical depth on the nose of the tool tip will be the set depth minus the lower radius of the tool tip (under the lip of the tip). At this depth the tool tip nose gets just around 2 fibers on it to push forward as a chip; and these fibers get drawn, torn by the tool tip. As a result no chip is generated.

In minimum cutting depth analysis the tool tip radius should be taken into consideration too. Generally the diameter of fiber is around 7 μm . At 25 μm set cutting depth the practical depth on the nose of the tool tip will be the set depth minus the lower radius of the tool tip (under the lip of the tip). So if the set cutting depth is 21 μm , the tool tip nose will get just around 2 fibers on it to push forward as a chip; and these fibers get drawn, torn by the tool tip. As a result no chip is generated.

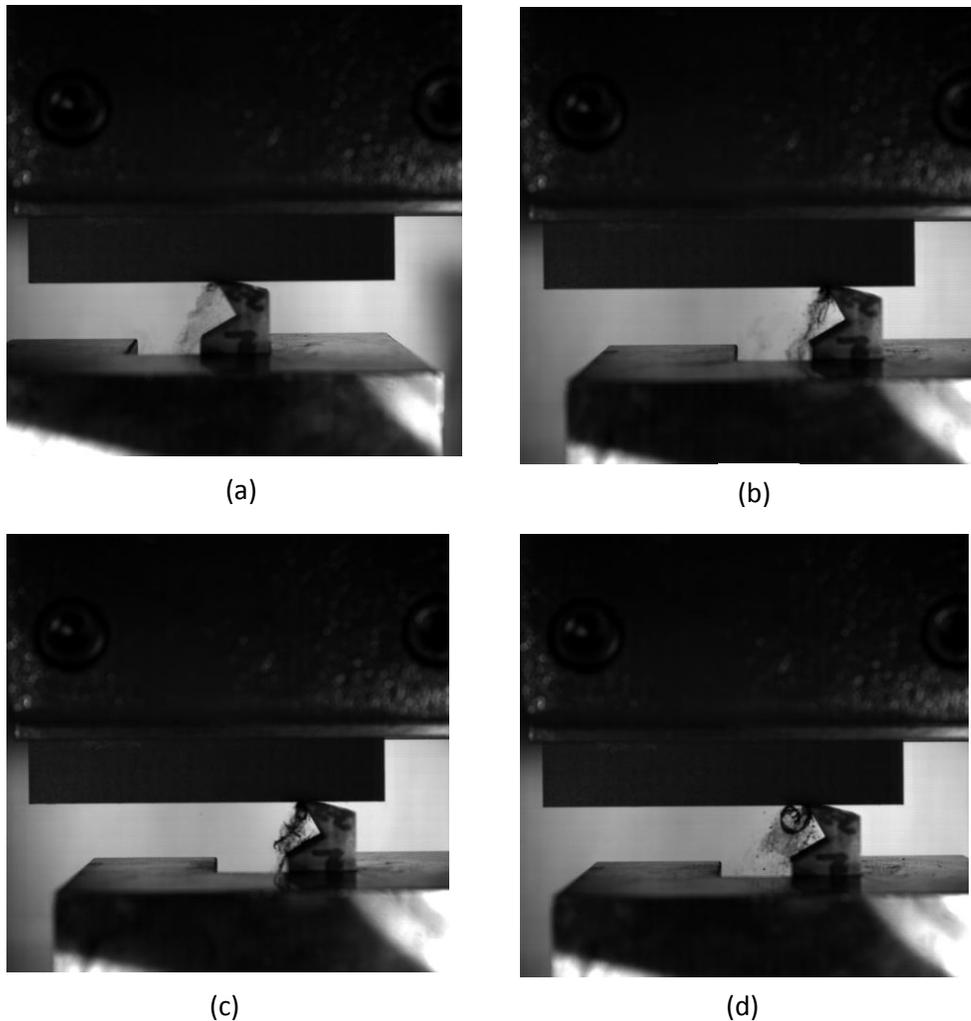


Fig. 4.1.3: Minimum cutting depth at 0° fiber orientation (a) $25\ \mu\text{m}$ and tool tip radius: $10.51\ \mu\text{m}$, (b) $35\ \mu\text{m}$ and tool radius: $8.95\ \mu\text{m}$, (c) $40\ \mu\text{m}$ and tool tip radius $7.49\ \mu\text{m}$, (d) $45\ \mu\text{m}$ and tool tip radius: $9.10\ \mu\text{m}$

In the second test, the cutting depth was increased to $35\ \mu\text{m}$ and the r_{tt} was $8.95\ \mu\text{m}$. At this depth the tool tip nose gets a bit more fibers. The tool takes out some fibers from the workpiece in discrete form as in Fig.4.1.3-b. On the figure it can be seen that the tool seems to take up fibers in a continuous form from the workpiece but it is unsure if the real take up is over the whole surface or not. The cut fibers do not have any form of chip as the density of fibers is very low. Moreover, during the cutting course a bunch of cut fibers get accumulated at the nose of the tool tip which keeps pressure on the newly separated fibers from the cut surface and resist them from forming a chip. From this phenomenon it is not clear if the workpiece surface get cut in a regular form smoothly over the whole area or not. To get a clearer cut, the cutting depth was then increased to $40\ \mu\text{m}$ during the next test. At $40\ \mu\text{m}$ the whole surface of the workpiece come under cut. The fibers get separated in small bunches and get cut in very short length. The fibers and matrix cannot make any chip's form as most of the separated fibers get cut shortly and are debonded. This cut fiber can be seen in the Fig.4.1.3-c-. Here we can say that

as the workpiece comes under cut continuously over the whole surface so this is the cd_{min} at this particular cutting configuration. At this test the r_{tt} was $7.49 \mu\text{m}$ which is comparably less than previous tests' radiuses, that means the tool is sharper.

At the end, an additional cutting test was carried out by increasing the cutting depth to $45 \mu\text{m}$ in order to see if the fibers make any particular form of chip at that depth. The r_{tt} was measured $9.10 \mu\text{m}$ before the test. It was found that, as in Fig.4.1.3-d, at $45 \mu\text{m}$ cutting depth, most of the cut fibers form a curvature shape of chips in front of the rake surface to the tool. A small portion of the matrix gets out in dust form along with the generated chip. It is quite obvious that the tool cut materials over the whole surface of the workpiece and this depth is above the cd_{min} .

At 45° Fiber Orientation

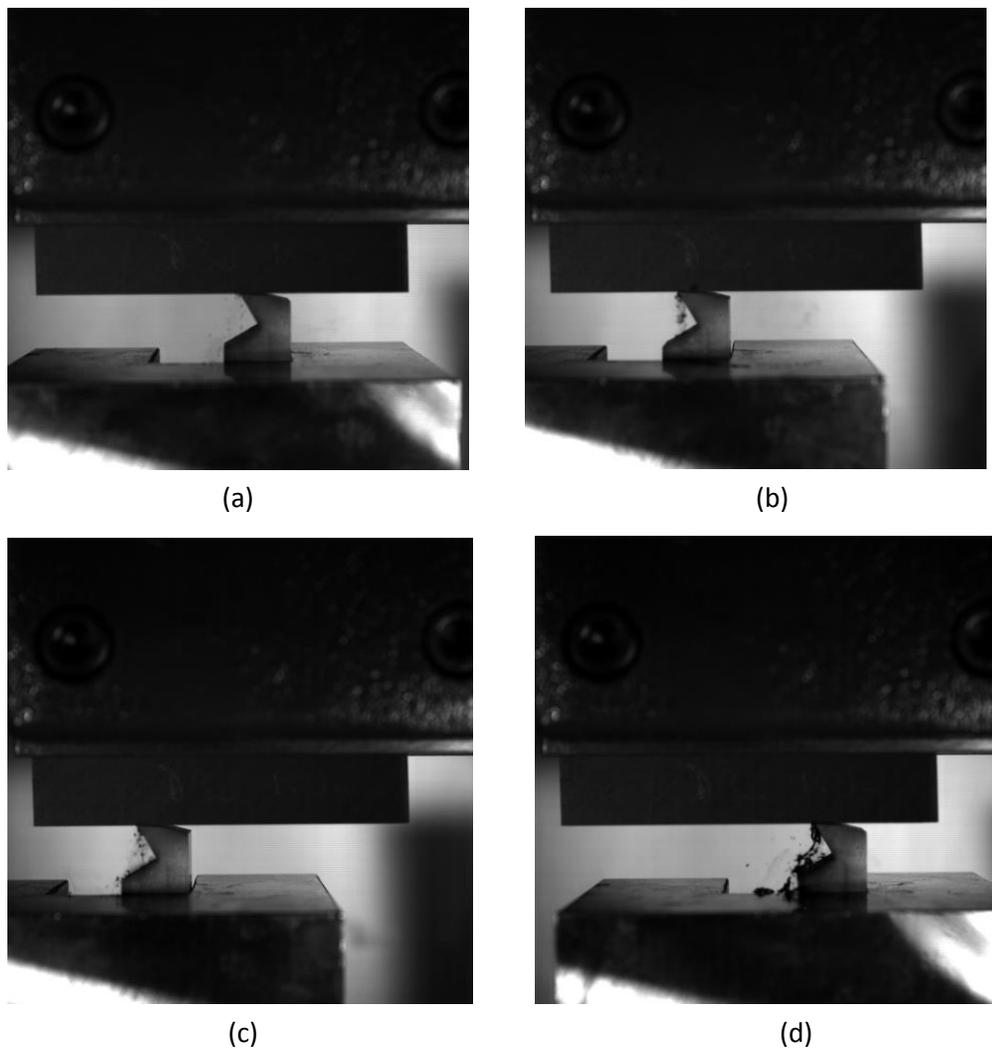


Fig. 4.1.4: Minimum cutting depth at 45° fiber orientation (a) $30 \mu\text{m}$ and tool tip radius: $15.85 \mu\text{m}$, (b) $35 \mu\text{m}$ and tool tip radius: $10.61 \mu\text{m}$, (c) $40 \mu\text{m}$ and tool tip radius: $11.31 \mu\text{m}$, (d) $50 \mu\text{m}$ and tool tip radius: $9.12 \mu\text{m}$

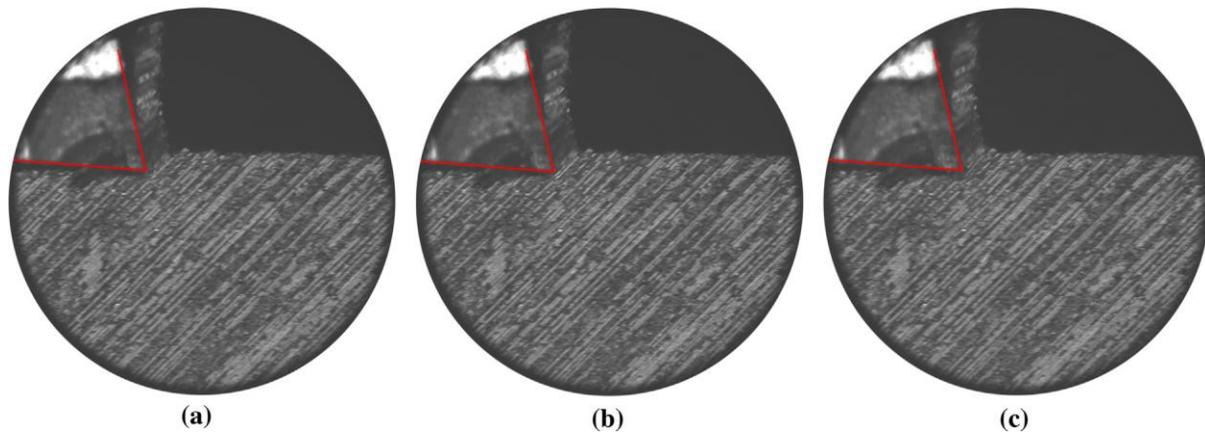


Fig. 4.1.5: Chip formation at 50 μm depth of 45° fiber orientation [Youliang Su et al., 2016]

At 45° fiber orientation the first test was carried out at 30 μm cutting depth while the r_{tt} was 15.85 μm . It was found that the tool makes strong friction with the workpiece but no material is cut. At 45° fiber orientation the fibers are inclined towards the cutting direction. So if the cutting depth is comparably low, the tool tip pushes the fibers which generates high compressive action on the workpiece surface. As a result, the fibers get highly pressed and pass under the cutting tool making high friction on the clearance surface.

In the next test the cutting depth was increased to 35 μm . The r_{tt} was 10.61 μm . The result shows that a very small portion of material comes out from the surface, Fig. 4.1.4-b. Here we do not say that the material is cut all the way. The small portion of material which comes out from the surface is a very thin and plane surface overlay of the main matrix of the workpiece. The reason is that the matrix has much less strength compared to fiber is also responsible behind this overlay's come up. It is assumed that if the cut happens below this surface overlay then the fiber will get cut. According to the findings 35 μm cutting depth cannot be the minimum cutting depth. So the cutting depth was increased to 40 μm in the next cut while the r_{tt} was 11.31 μm . The result found in the test shows that indeed the tool does not create continuous cut but very small portion of fibers get cut along with matrix overlay. In the Fig. 4.1.4-c it is clearly seen that the cut materials do not have any specific shape of chips as the number of cut materials is much less and the cut is sporadic.

To get a more continuous cut over the workpiece surface the cutting depth needs to be increased. So during the next cutting test the depth was increased to 50 μm and the r_{tt} was measured 9.12 μm before being used in the test. A continuous and smooth cut over the surface was seen at the test. The cut materials made some flat and very thin chips, Fig. 4.1.4-d. Similar findings were mentioned by [Youliang Su et al., 2016] as in the Fig. 4.1.5. They had continuous

chip at 50 μm . In their setup the workpiece was below of the cutting tool. So it can be said that at 45° fiber orientation, the cd_{min} is 50 μm while the cutting speed is 12 m/sec and r_{tt} is 9.12 μm .

At 90° Fiber Orientation

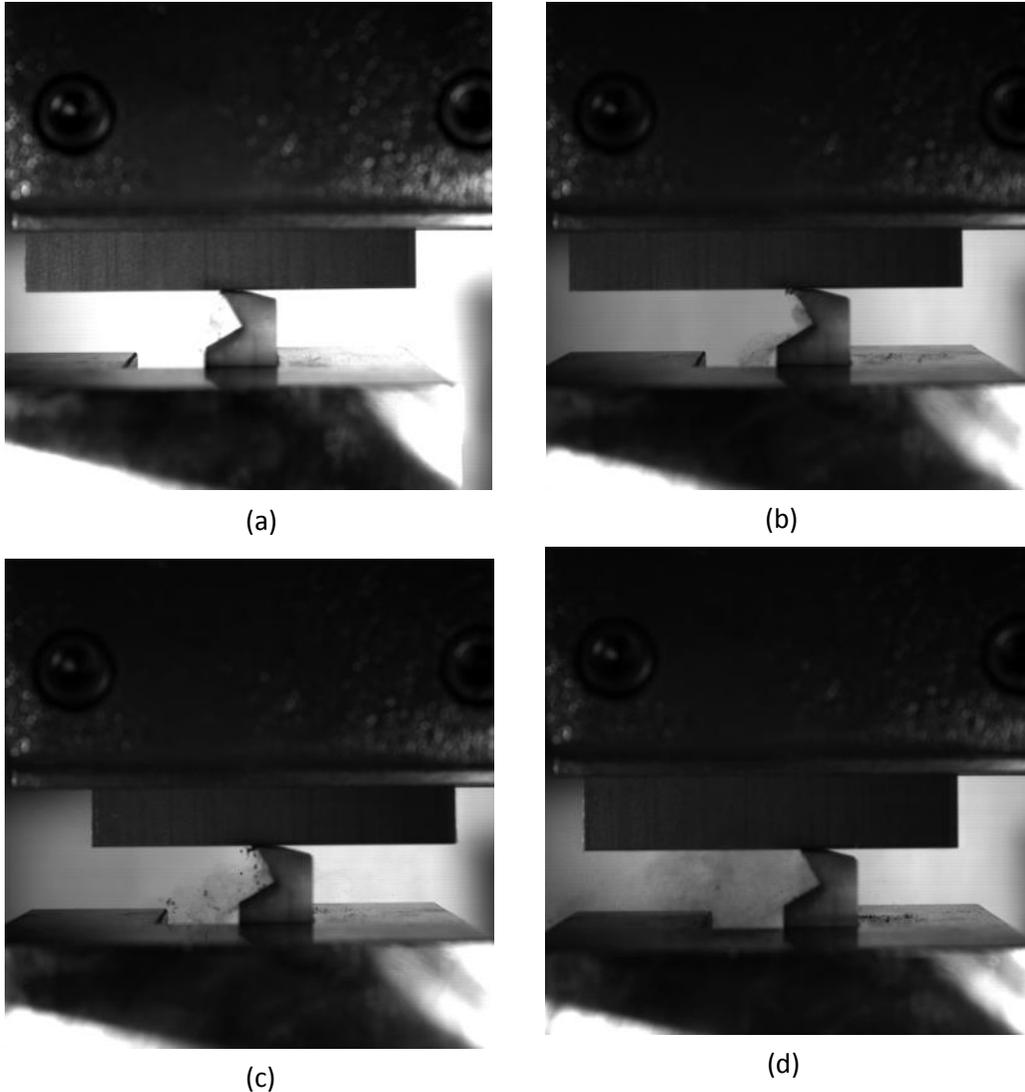


Fig. 4.1.6: Minimum cutting depth at 90° fiber orientation; (a) 25 μm and tool tip radius: 14.92 μm , (b) 35 μm and tool radius 12.23, (c) 45 μm and tool tip radius: 12.97 μm , (d) 50 μm and tool tip radius: 13.19 μm .

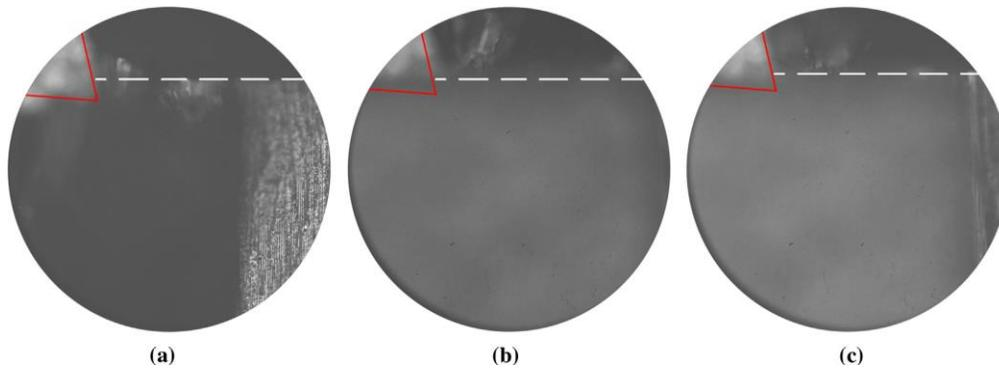


Fig. 4.1.7: Chip formation at 50 μm depth of 90° fiber orientation [Youliang Su et al., 2016]

The first test at 90° fiber orientation was carried out putting 25 μm cutting depth. The r_{tt} was 14.92 μm . It was found that the 25 μm cutting depth is not enough to make the fibers cut, Fig. 4.1.6-a. It should be noted that at this particular fiber angle, the fibers get cut cross-sectionally by the tool. The head of the fibers get pressed by the lips of the tool, as a result no much amount of fibers remain on the nose of the tool. So the tool passes without cutting material but making strong friction. In the next test the cutting depth was increased to 35 μm . The r_{tt} was measured 12.23 μm . Like for the previous test, 35 μm is not enough to generate a smooth cut over the workpiece surface as in Fig. 4.1.6-b. At this depth, as the tool presses the top of the workpiece, a small film of dust is generated which is mainly by the matrix particles from the surface of the workpiece.

The results of the first two tests showed that the cutting depth needs to be increased. To keep the incremental coherence the depth was increased to 45 μm in the next test. It was seen that the surface of the matrix get cut but the fibers are cut partially at very small portion, Fig. 4.1.6-c. The material removal is not smooth and homogeneous but the lip of the tool starts to take materials. According to this phenomenon it is easily understandable that if the tool tip lip gets a bit more material, the cutting will be continuous and homogeneous. So the depth was increased to 50 μm in the next test.

At 50 μm cutting depth while the r_{tt} was 13.19 μm a smooth and continuous cut was seen over the whole course of the cut. The chips were in dust form, Fig. 4.1.6-d. This particular form is generated because of the cutting modes. In the first mode the fibers get bent, in the second mode fiber-matrix interface becomes fractured and in the last mode the matrix get fractured which permits the chip to be generated. As the depth is very low most of the fibers get totally separated from the matrix after debonding in the chip region. [Youliang Su et al., 2016] did a cut at 50 μm for 90° fiber orientation as in the Fig. 4.1.7. They found unstable and discontinuous cutting process at this depth.

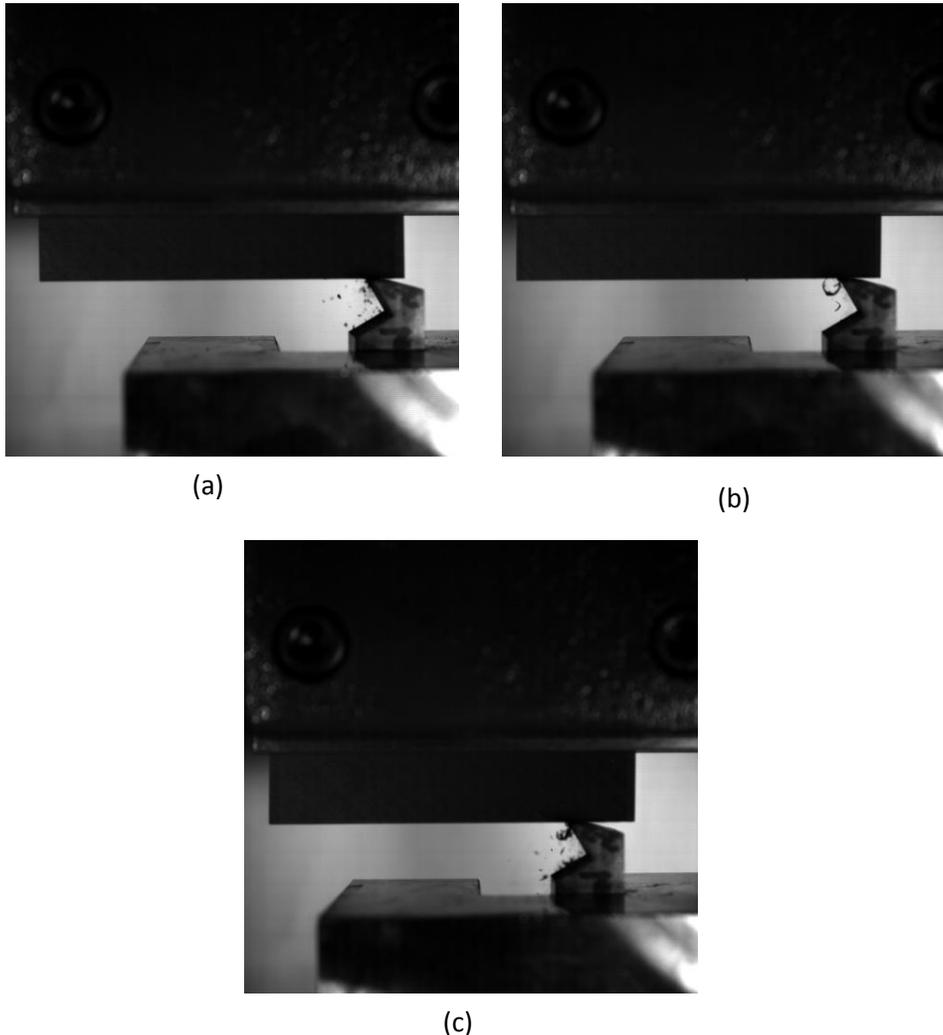
At 135° Fiber Orientation

Fig. 4.1.8: Minimum cutting depth at 135° fiber orientation (a) 25 μm and tool tip radius: 11.18 μm , (b) 30 μm and tool tip radius 10.87 μm , (c) 35 μm and tool tip radius: 10.03 μm

At this fiber orientation the fibers are inclined at opposite to the cutting direction. The first cutting depth at this angle was 25 μm and the r_{tt} was 11.18 μm . It was seen that the tool starts to cut the surface of the workpiece at very small portion and the cut is not homogeneous over the whole course, Fig. 4.1.8-a. Indeed this cutting depth is much less comparing to the minimum cutting depths of those at 0°, 45° and 90° fiber orientations but as the fibers are inclined at -45° to the cutting direction the tool tip nose pushes the fibers forward which trend the fibers to more vertical position that increases the real take-up of fibers. However, this cutting depth cannot be considered to be the cd_{min} .

In the next test, the depth was increased to 30 μm while the tool tip radius was 10.87 μm . The tool was found cutting the material homogeneously and continuously over the whole surface of the workpiece. Here it should be noted that the real take-up will be more than the original set depth because of this particular fiber orientation angle. So at 135° fiber orientation, the cd_{min} is 30 μm while the cutting speed is 12 m/min and the r_{tt} is 10.87 μm .

4.1.3. Conclusion, Difficulties and Perspectives

It is not possible to generalize the cd_{min} by any single value for all fiber orientations in CFRP machining as this material is constructed from different phases. The minimum value changes according to fiber orientations. At the same time, the tool sharpness also plays a role to this definition. More tool tip radius means less sharpness and the tool needs more cutting depth to make a regular cut over the whole surface of the workpiece.

In this research four minimum cutting depths have been found for four different fiber orientations. These values are accountable only at those particular tool sharpness and cutting speed. A summary of the cd_{min} values has been shown in the Table. 4.1.2.

Fiber orientation (°)	Minimum cutting depth (μm)	Tool tip radius (μm)	Cutting speed (m/min)
0°	40	7.49	12
45°	50	9.12	
90°	50	13.19	
135°	30	10.87	

Table. 4.1.2: Summary of the minimum cutting

It has been found that at 135° fiber orientation, the cutting depth is minimum while at 45° and 90° fiber orientation it is maximum. The values found, Table. 4.1.2, are valid only if the r_{tt} and the cutting speed are accordingly as in the table. It should be noted that if the tool tip radius is different or the cutting speed is changed the cd_{min} values might be different but it is a question of research.

Mechanical Dial Indicator Gauge was used in the tests to set the cutting depths, and the depths were set manually in the tests. There is a tolerance in the measurement accuracy which can be upto maximum 10 μm . This tolerance should be taken into consideration in the results.

However, for the future researchers it might be interesting to analyze the minimum cutting depths:

- Keeping the same sharpness of the tool for all fiber orientations (in our research we wanted to keep the same sharpness in all the tests, but it was not possible as different sharpness were automatically generated for different tools during machining the tool edges).
- Changing the cutting speed.

4.2. Tool Wear Mechanism

In machining the performance of cutting tool is a concerning issue. Cutting tools are expensive and if the tool gets broken or loses its sharpness it needs to be changed which is time consuming as well as costly. It is well known that the anisotropic and heterogeneous structure of the laminates and the highly abrasive nature of the carbon fibers make it prone to critical damages in the workpiece as well as extensive tool wear [Gaugel et al., 2016]. A lot of research work identified abrasive wear as dominant tool wear mechanisms in both conventional machining and high speed machining of composite laminates due to the highly abrasive nature of fibers [Liu et al., 2012].

In spite the fact that existing models can provide estimation for the principal cutting forces resulting from orthogonal cutting, tool wear is often overlooked [Arola et al., 2002]. [Liu et al., 2012] and [Iliescu et al., 2010] compared flank wear of the tool in drilling according to the number of holes the tool made in which Iliescu suggested 10° to 25° clearance angle for the tool to avoid delamination. [Wang et al., 2013] found that the edge rounding wear is the main wear type in drilling. They used several cutting tools and compared the results in drilling. [Hamednianpoura and Chatelainb, 2013] used a 3/8 inch diameter CVD diamond coated carbide tools with six straight flutes to trim 24-ply carbon fiber laminates. They found that tool wear increases if cutting length increases and the rated of defects increases if tool wear increases but they used too high cutting speed, from 200 m/min to 400 m/min, which is not realistic.

In this research the tool sharpness loss has been analyzed experimentally. Different fiber orientations and cutting depths have been used during the tests. The wear analysis has been done mainly considering the amount of use of the tool.

4.2.1. The Tool and the Wear Measuring Procedure

Goal of the Tests

Two different types of analyses were done. The main aim of these studies is to investigate the amount of sharpness loss of the tool at certain cutting length of material (taking into account the amount of use of the tool). First one is the sharpness loss after the tool comes into a number of uses in experimentations at comparably high cutting depths and the second one is the sharpness change at low cutting depths. The first one permit us to understand the change of the tool tip radius (which refers to sharpness), rake surface, clearance surface, rake angle and clearance angle at high cutting depths. And the second one permits us to understand those phenomenons at comparably low cutting depths.

First Test

Tool Arrangement and Cutting Configuration of First Test

A micro grain tungsten carbide orthogonal cutting tool sharpness was measured before it has been used. During cutting the tool was used by considering three different sections on the tip edge as in the Fig. 4.2.1. Totally 40 times the tool came under use at 80 mm long and 4 mm width workpiece. The first two sections, left and middle (Fig. 4.2.1), came under 13 times uses each and the right section came under 14 times. This three different sections technique was used so that the tool tip and rake surface get equally used almost everywhere.

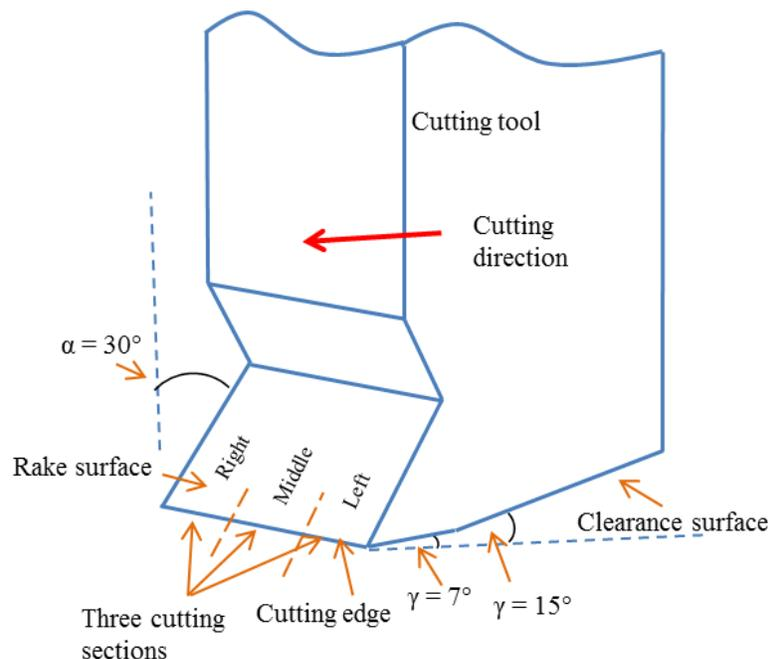


Fig.4.2.1: Schematic diagram of the cutting tool

For the first 20 tests the cutting depth was 0.1 mm, 0.25 mm, 0.5 mm, 0.75 mm and 1.0 mm at 0°, 45°, 90° and 130° fiber orientation. So every cutting depth got four times experimentation with four fiber orientations separately. The rest 20 experimentations were at the same fiber orientations but the cutting depths were 100 μm , 50 μm , 40 μm , 30 μm and 20 μm . So again each cutting depth got four experimentations at four different fiber positions. The cutting velocity and other parameters are as on the Tab. 4.2.1.

Parameter	Values
Fiber and matrix volumetric ratio	60 % : 40 %
Fiber orientation	0°, 45°, 90°, and 135° separately
Used material	T800S/M21
Frequency of force fluctuation	7000Hz/sec
Rake angle	30°
Clearance angle	7° and 15°
Depth of cut	0.1 mm, 0.25 mm, 0.50 mm, 0.75 mm and 1.0 mm
Cutting speed	12 m/min

Table. 4.2.1: Cutting parameters

Wear Measuring Procedure

Alicona INFINITFocus SL with standard straight edge 10x has been used for tool wear and sharpness measurements, Fig. 4.2.2. Before using the tool, its sharpness was measured in three different locations as in the Fig. 4.2.1. At each measurement, Alicona takes 10 different profiles on the measuring area, Fig. 4.2.3, and then the average value of these 10 profiles is considered as the actual value. The profiles are taken from 500 μm distance at each location whereas the distance from the clearance edge to the rake surface edge is 400 μm .

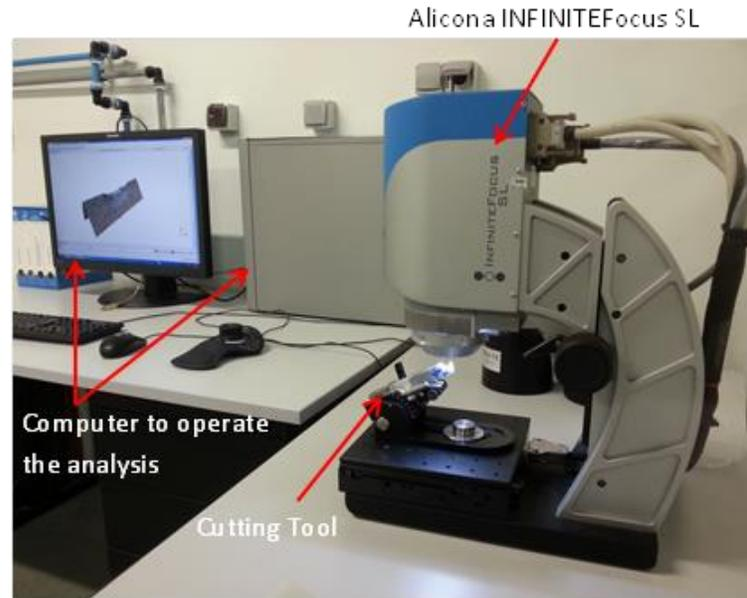


Fig. 4.2.2: Alicona INFINITEFocus SL to measure tool sharpness

After having finished all the cutting tests the tool sharpness was measured again to analyze the differences. The measurement was done at the same places as before. The new radius of the tool tip, new rake angle, clearance angle, rake surface and clearance surface were measured. At the same time, the surface state of rake surface and clearance surface were observed. At the end a comparison with the initial measurements was done to find out the differences.

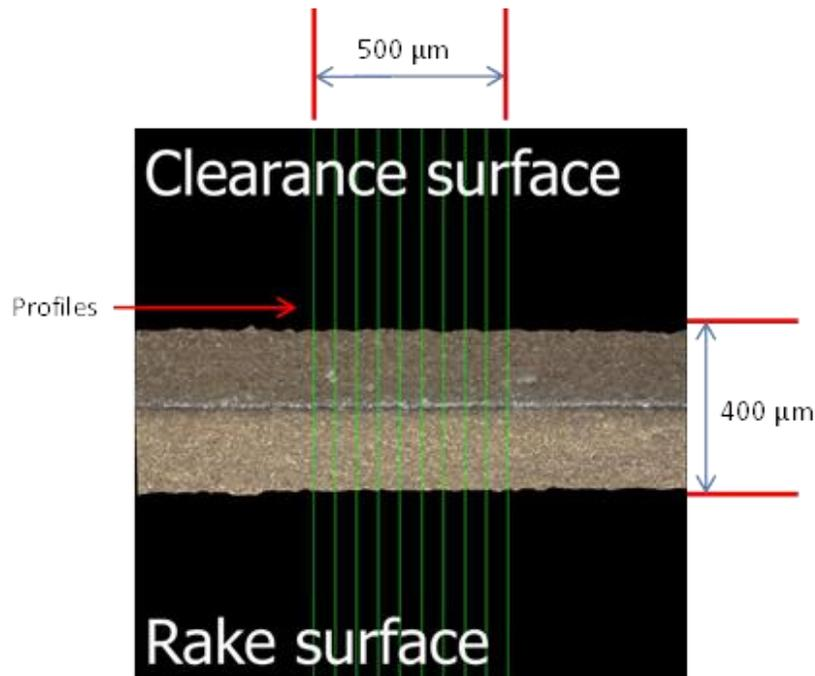


Fig. 4.2.3: Profiles on the measurement area

Second Test

The Tool and Cutting Configuration of the Second Test

The second test of the sharpness change was done using the same orthogonal cutting tool but the tool was machined again so that the tool gets new sharpness. Same types of workpieces as in the first test were used but in this analysis the cutting depths were more realistic. At each fiber orientation, 4 cutting tests were done specifically at 50 μm , 100 μm , 200 μm and 300 μm cutting depth. So every fiber orientation got the same set of cutting depths. The cutting places of the tool tip which come into contact with the workpiece are as in the Fig. 4.2.4.

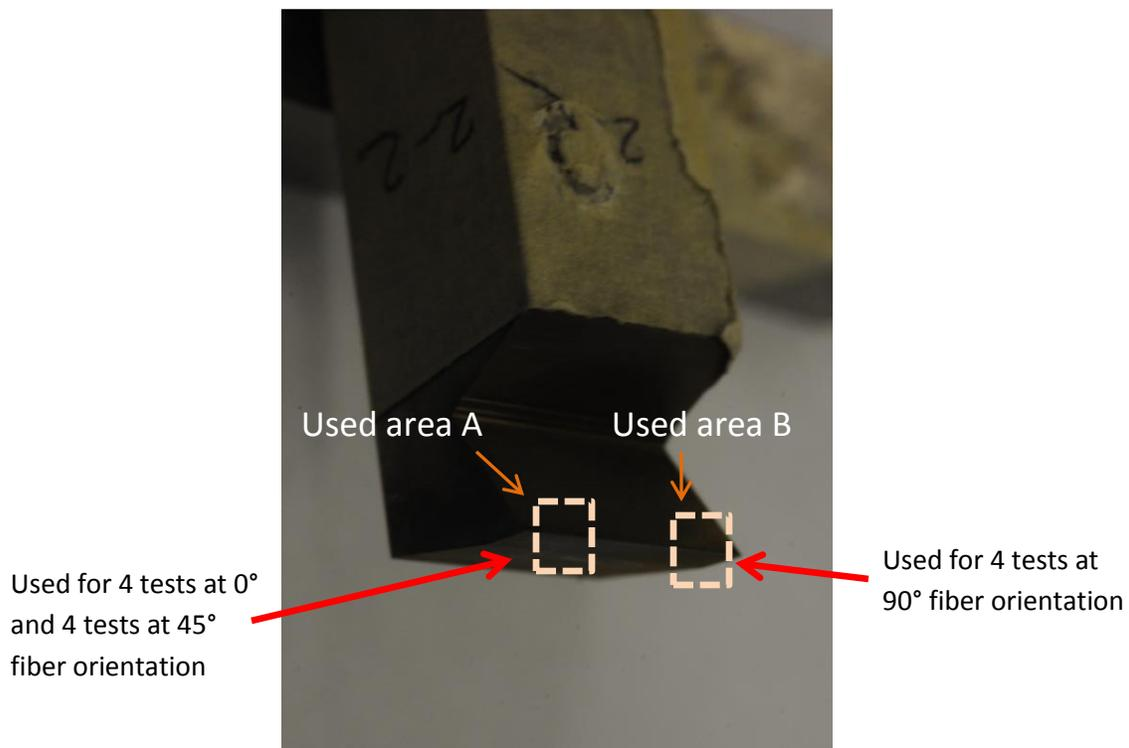


Fig. 4.2.4: The areas which came into contact with the workpiece

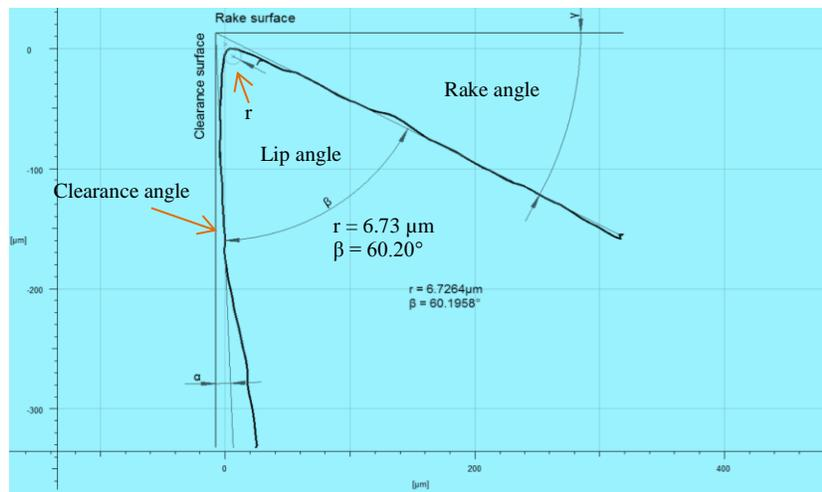
0°, 45° and 90° fiber orientations were used separately at the tests where each workpiece contains a single type of fiber orientation.

Before each cutting test, the sharpness of the tool was measured along with the rake and clearance angles. At the end of the cut the sharpness, rake angle and clearance angle were measured again and then the difference between before cutting and after cutting was measured. At the same time the damage on the tool tip was observed and analyzed. For all measurements Alicona INFINITEFocus SL with standard straight edge 10x was used.

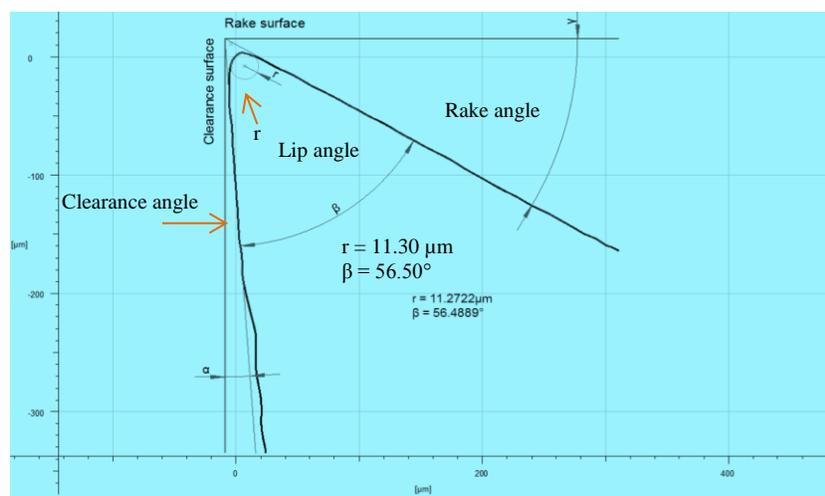
4.2.2. Results Analysis

4.2.2.1. First Test

It is well known that carbon fibers are more abrasive than any other material which is the reason why the cutting tools get highly worn during cut. In this experimental analysis it has been found that during CFRP cutting not only the tool loses its sharpness but also the clearance surface and rake surface get worn. As a result, the lip angle gets reduced. In Fig. 4.2.5, two 2D diagram of the cutting tool tip have been shown where (a) is the tool tip before use and (b) is the tool tip after use. The rake angle, clearance angle, lip angle, tool tip before and after use are visible on the figures.



(a)



(b)

Fig. 4.2.5: Tool cutting edge, (a) before use (b) after use

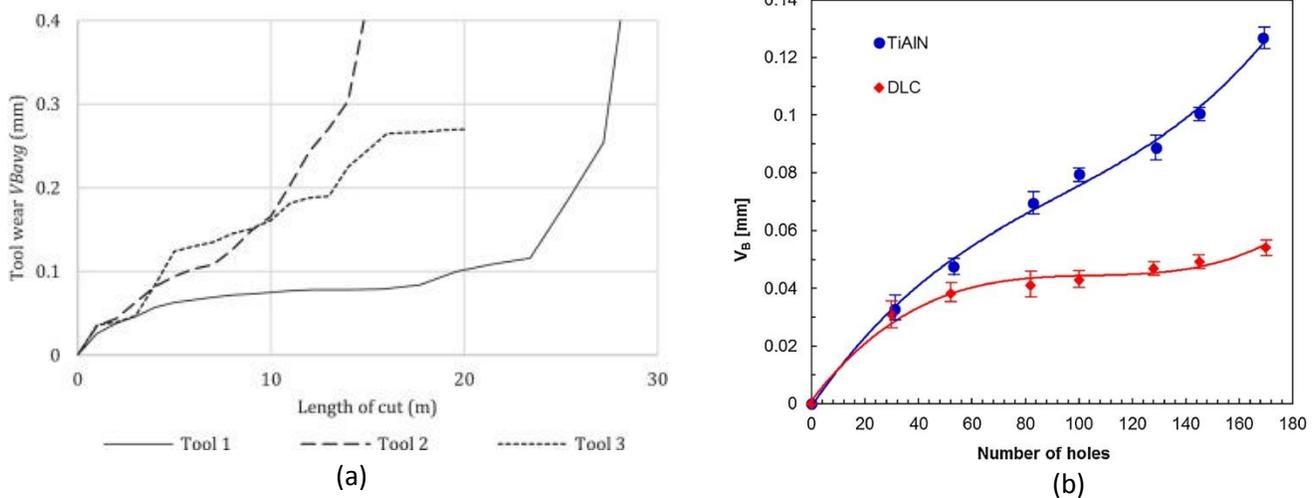
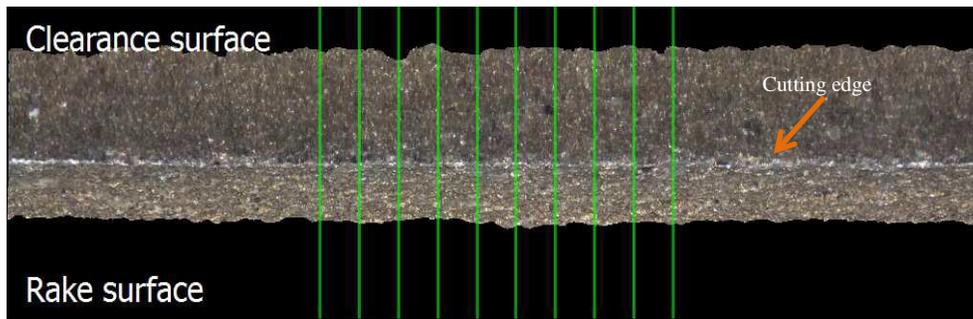


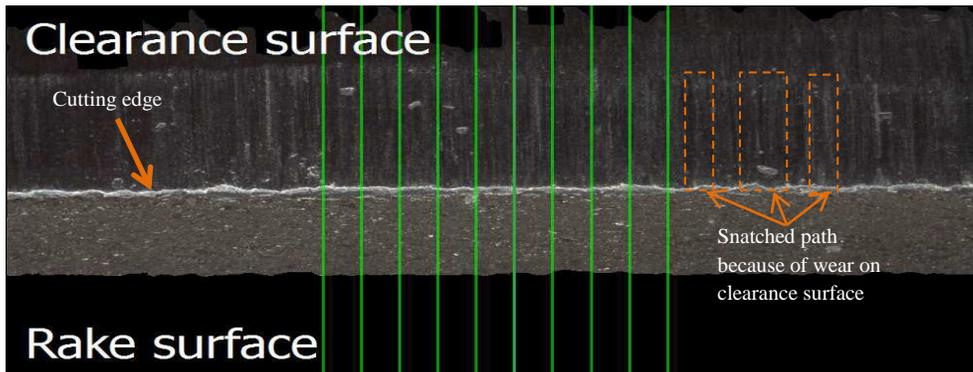
Fig. 4.2.6: Tool wear found by (a) [Rimpault X. et al, 2017] in trimming at the speed of 400 m/min for tool 1, 300 m/min for tool 2 and 200 m/min tool 3 with rake angle 8° and clearance angle 10° and (b) [D’Orazio A. et al., 2017] in drilling for the tool with DLC coating: 170.8 m/min cutting speed, 0.2 mm/rev feed rate; and for the tool with TiAlN coating: 128 m/min cutting speed and 0.163 mm/rev feed rate

The tool cutting edge radius before being used was $6.73 \mu\text{m}$ which becomes $11.30 \mu\text{m}$ making $4.57 \mu\text{m}$ sharpness losses after being used. This value is much less compared to the results found by [Rimpault X. et al, 2017] which is around $150 \mu\text{m}$ and [D’Orazio A. et al., 2017], around $30 \mu\text{m}$, Fig. 4.2.6. Their values are much higher as their length of cut is longer as well as the cutting speed is higher. The sharpness reduction happens because of material loss from the cutting edge; as a result the sharp edge gradually becomes smoother.

By this research it is not possible to show which fiber orientation causes maximum sharpness loss as the measurements were done after all cuts. The clearance angle of the cutting tool was kept 7° from the tool tip until 4 mm backward distance and after the angle was 15° . Less clearance angle near the tool tip gives more material under the cutting edge; which gives comparably higher stiffness to the tool tip to resist it from getting broken. However, it has been found that some very small portion of material were come out from different places of the cutting edge, Fig. 4.2.7-b. It happens not only because of the high friction between the tool and the workpiece but also nonequilibrium resistive stiffness at the cutting edge.



(a)



(b)

Fig. 4.2.7: Wear on clearance surface, (a) before use, (b) after use

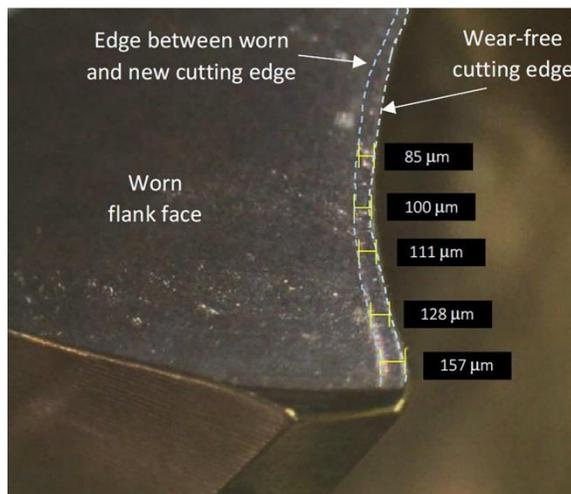


Fig. 4.2.8: Wear on the clearance face [D’Orazio A. et al., 2017]

The clearance surface gets highly worn during cutting. It is because this surface comes into high sliding friction with the newly generated cut surface which, at the same time, generates heat (the generated heat in the tool tip reduces stiffness of tool material). Moreover, the elastic

return of fibers causes friction on the clearance surface of the tool that also results wear. In Fig. 4.2.7-a and (b) the difference of non-used and used tool is shown. Similar findings were noted by [D’Orazio A. et al., 2017] (Fig. 4.2.8) in drilling which shows that the tool lip is splitted towards clearance surface by flank face wear. However, in our research at the clearance surface along the tool edge many wear path from tool tip to flank direction have been generated, Fig. 4.2.7-b. Because of this high material wear the clearance angle increases causing the tool tip much weaker. This scenario on clearance surface is much different than those on the rake surface.

The wear on the rake surface is more homogeneous. The rake surface encounters less frictional contact compared to clearance surface. The main friction zone on the rake surface is located immediately upward of the tool tip. The formed chips in CFRP cutting are shorter and lighter compare to those in metallic cutting; therefore, the chips get displaced from the rake surface quickly. That is why most part of the clearance surface which is not adjacent to the tool tip does not come under frictional contact. Because of rake and clearance surface wear the lip angle, which was 60.2° before experimentation, has become 56.5° losing 3.7° .

4.2.2.2. Second Test

Realistic cutting depths refer to the depths which are used in the industries and which are applicable in machining that do not generate damage at the cutting tool as well as workpiece. The cutting depths which were used here in this analysis are used by industries.

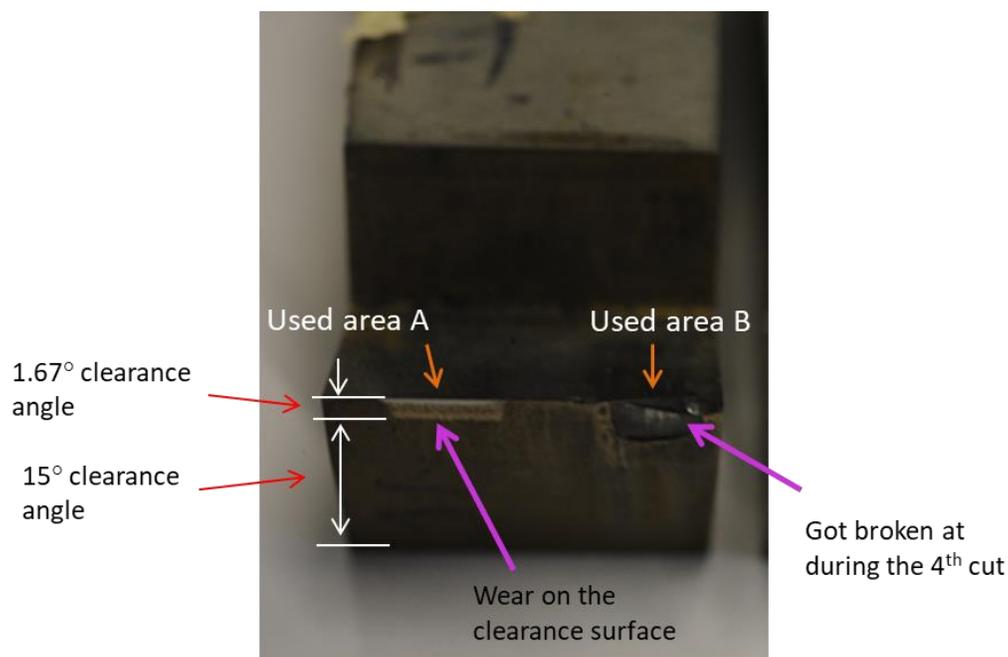


Fig. 4.2.9: Wear and damage at the tool tip

As in the previous analysis' results, it has been found that the clearance surface gets highly worn compared to the rake surface which is clearly visible on the Fig. 4.2.9-(used area A). It should be noted that the visible wear area on the Fig. 4.2.9 had the clearance angle of 7° which afterward became 15° . At 7° angle the clearance surface is much closer than at 15° angle to the cut surface of the workpiece. However, no remarkable wear was found on the clearance surface at 15° angle.

On the other hand, at "used area B" on the Fig. 4.2.9, there were in total 4 cuts at 90° fiber orientation at the cutting depths $50\ \mu\text{m}$, $100\ \mu\text{m}$, $200\ \mu\text{m}$ and $300\ \mu\text{m}$. It was found that during the last cut (4^{th} test at $300\ \mu\text{m}$) the tool tip got broken, the Fig. 4.2.9-(used area B). The breaking part took place from the tool tip towards to the clearance surface which shows most of the broken part was from the clearance surface. This type of failure direction is produced because the tool tip gets strong shearing support from the clearance area, so tip failure results propagation towards the clearance surface.

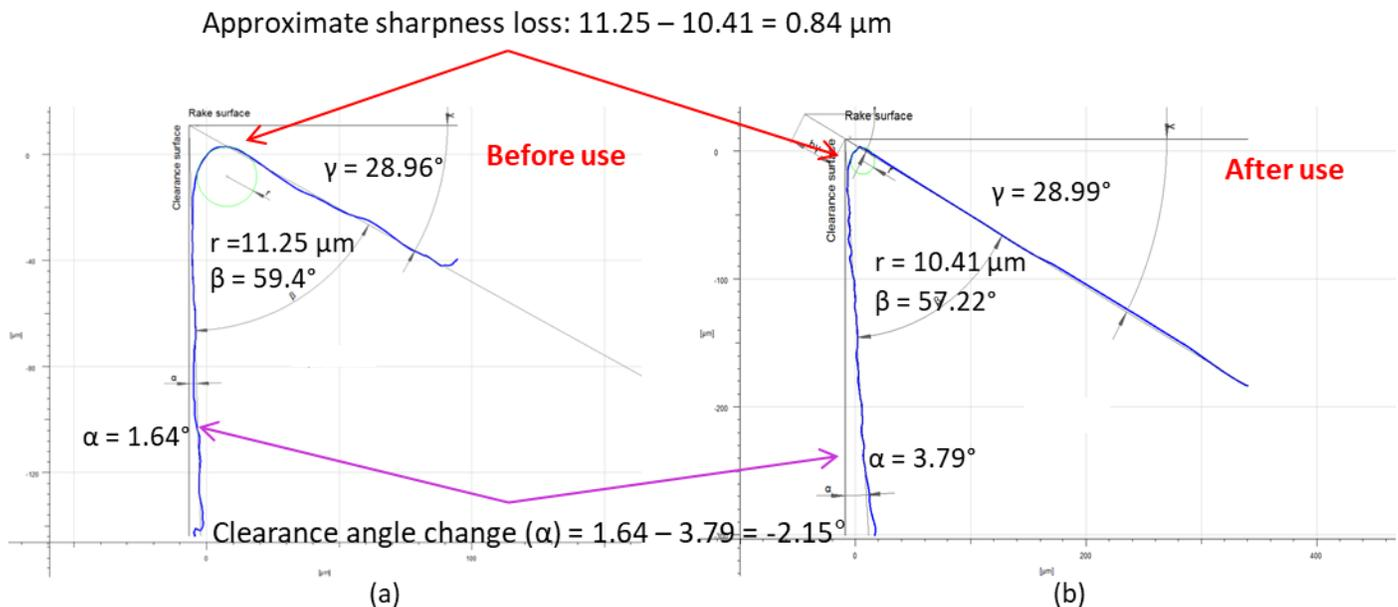


Fig. 4.2.10: Tool tip radius, rake angle, clearance angle and wedge angle, (a) before use (b) after use

The sharpness loss and the rake and clearance angle change at the "used area A" of Fig. 4.2.9, were measured by Alicona INFINITEFocus SL. It was found that the tool lost material from the tip which reduced the tip radius from $11.25\ \mu\text{m}$ (Fig. 4.2.10-a) to $10.41\ \mu\text{m}$ (Fig. 4.2.10-b). Here clearance angle played an important role. This angle which was 1.64° is too less that makes the clearance surface almost flat. As a result the material loss over the surface made the tool tip

thinner. It means the tip can get thinner by being used but depends on the clearance angle. However, even the tip gets thinner it becomes less stiff as the tool loses material from the clearance surface. This is what makes the tool tip more fragile because the tip lip does not remain smoother anymore.

The clearance surface of the tool got highly worn losing material from the surface (as said before) which changes the clearance angle from 1.64° to 3.79° . This remarkable wear appeared because 1.64° clearance angle brings the clearance surface too close to the newly generated cut surface of the workpiece. As a result the elastic return of fibers causes abrasive wear on the clearance surface.

On the other hand, the rake surface got barely worn compared to the clearance surface. The rake angle before use was 28.96° which became 28.99° after the cuts. Here the rake surface was mostly not worn because the cutting depths were low which did not generate large amount of chips to make high friction on the rake surface. The wear on rake and clearance surface causes the change of wedge angle. The difference of wedge angle is nothing but the summation of rake and clearance angle change.

4.2.3. Conclusion and Perspectives

Tool wear is an important issue as changing tool because of wear or break is expensive and time consuming. In this analysis, the measurements of the sharpness were done at the vicinity of the tool tip ranging from $100\ \mu\text{m}$ to maximum $300\ \mu\text{m}$ from the tip lip as the notable wear occurred in this zone.

Clearance angle plays an important role to both clearance surface wear as well as to the tool tip breaking phenomenon. Less clearance angle means thicker tool tip which increases the stiffness to resist tip from getting broken but high clearance surface wear is seen as this surface comes too close to the newly generated cut surface. Additionally, the r_{tt} decreases if the clearance surface gets highly worn. Here in both analyses it is found that the clearance surface gets highly worn compared to the rake surface.

It is known that the cutting depth and fiber orientation have distinct effect to tool wear mechanism but in this research a mixture of different cutting depths and fiber angles have been used. By this research it is not possible to understand the effect of distinct fiber orientations to tool wear. So it is proposed to the future researchers to analyze the wear and damage by distinguishing the fiber orientation. Moreover, it can be revealing to analyze the wear mechanism distinguishing different cutting speed and cutting depths.

Global Conclusion and Perspectives

These days, lots of CFRP materials are used in the high performance engineering parts in aeronautic, automotive, wind energy, sports equipment, pressure vessel and construction domains. As the parts are manufactured in near-net-shape, the last machining process (like drilling, milling, turning etc.) should be highly accurate. But poor machining quality in CFRP is remained a principal concerning issue which demands distinguished research in order to ameliorate the quality. The global objective of this present research is to better understand the CFRP cutting phenomenon through orthogonal technique which will facilitate to improve the conventional machining processes, e.g. drilling, milling, turning etc. For this purpose this research has been carried out by distinguishing the process parameters and the cutting quality in machined part. Apart from that, the chip formation mechanism has also been investigated to a large extent.

The study was started by experimental investigation of strain field generation in the workpiece during cut at four different fiber orientations. Subsequently, the fundamental analysis of chip formation mechanism at those fiber orientations have been done. Separate study was carried out at each fiber orientation (of 0° , 45° , 90° and 135°) as it is known that the cutting mechanism of CFRP varies according to fiber position. Having observed the experimental cutting procedure, a micro-mechanical model has been developed with discrete CFRP characteristics. The model has generated the identical cutting and chip formation scenario as found in experimentations. The results show that, the maximum strain fields in the workpiece lie near the vicinity of the cutting tool tip. Besides, distinct chip formation process was found for each fiber orientation, in fact, each course of formation is formed with four steps.

As this model is able to generate distinct physical phenomenon of the process, it can be utilized in future for further research, for example, elastic return behavior, cutting load analysis etc.

The previous research work, [Blanchet, 2015], at the present laboratory focused extensively to the cutting speed's effect to machining quality, whereas, the cutting depth was constant. In this present research, the effect of five different cutting depths to cutting efforts, surface quality and chip size have been studied. Along with experimental observation of all these subject matters, a macro-mechanical model with homogeneous equivalent material was developed. The model showed good agreement with the experimental results, which showed that, if the cutting depth increases the cutting force also increases but the thrust force decreases. A significant difference between experimental and numerical thrust forces has been found for 45° and 135° fiber orientation. This difference appears because the material in macro-model was considered homogeneous which does not show the actual physical behavior of a real fiber. In that case, a micro-mechanical model can be useful to analyze those forces. The cutting depth is found

influential to chip shape and size too. The chip length increases if the cutting depth increases at all fiber orientation except 135° at which the trend is totally inverse.

On another note, the minimum cuttable depth for CFRP machining is found dependent on the fiber orientation. The lowest depth which can be cut experimentally is found $30\ \mu\text{m}$ while fiber orientation is 135° , and for the other fiber orientations it is a bit higher.

The surface quality largely refers to the surface roughness and subsurface damages. Experimentally found results showed that the surface roughness is governed remarkably by fiber orientation compared to cutting depths. At 0° fiber orientation the roughness scale is minimum and at 135° it is maximum. At 90° and 135° fiber orientations if the cutting depth increases then the roughness also increases although at 0° and 45° the effect is almost neglectable. Likewise, at 0° and 45° , no subsurface damage in the workpiece has been found. However, at 90° and 135° fiber orientation, lots of cracks have been identified. The macro model revealed the identical behavior as in experimentation in terms of crack generation and propagation. Besides, the inner subsurface damages and delaminations which are nor visible from outside have been investigated by X-ray tomography. Interply delamination as well as sever crack propagation have been found while fibers are oriented at 135° . However, those types of defects have not been appeared at the other fiber orientations. So in CFRP machining, the most risk of poor quality is more likely to appear at 135° fiber orientation.

Throughout the cutting operations, cutting tool wear was a concerning issue. It was found that the clearance surface gets highly worn compare to rake surface. The elastic return phenomenon of fiber plays a vital role to generate this wear. High clearance angle will make the tool tip thinner, which causes tool tip breaking. So it is recommended to keep enough material at the tool tip in order to maintain high stiffness to prevent from tool tip breaking.

Even though this research work touched some of the most important subject matters in CFRP machining but a few issues still remained undiscovered or needed to be further studied. In literature it was found that elastic return behavior of fiber affects the tolerance and surface roughness of newly generated surface. A future research on elastic return behavior will disclose those concerns as well as its effect to clearance surface wear of cutting tool. The cutting tool wear mechanism was studied briefly in this present research; nevertheless, a further research to discover which fiber orientation causes maximum wear on the cutting tool can be worthwhile. Additionally, different types of materials can be sued for cutting tool in order to confirm the best tool material in defiance of tool wear.

References

Abaqus user's Guide 6.14, available from: <http://abaqus.software.polimi.it/v6.14/books/usb/default.htm?startat=pt09ch37s01aus165.html>

Abena A, Sein Leung Soo, and Khamis Essa. 2017. "Modelling the Orthogonal Cutting of UD-CFRP Composites: Development of a Novel Cohesive Zone Model." *Composite Structures* 168: 65–83.

Abrão A. M., J. C. Campos Rubio, P. E. Faria, and J. P. Davim. 2008. "The Effect of Cutting Tool Geometry on Thrust Force and Delamination When Drilling Glass Fibre Reinforced Plastic Composite." *Materials & Design* 29 (2): 508–13.

Ahmad Jamal. 2009. *Machining of Polymer Composites*. Springer Science & Business Media. P-321

Alaiji R. El., L. Lasri, and A. Bouayad. 2015. "3D Finite Element Modeling of Chip Formation and Induced Damage in Machining Fiber Reinforced Composites." *American Journal of Engineering Research (AJER)* 4 (7): pp-123-132.

Altair Engineering Inc., 2012, *The A350 XWB Prepares For Static Testing*; available from: <http://altairenlighten.com/2012/12/the-a350-xwb-prepares-for-static-testing>

Altintas, Yusuf. 2012. *Manufacturing Automation: Metal Cutting Mechanics, Machine Tool Vibrations, and CNC Design*. Cambridge University Press. P -381

Aramcharoen, Ampara, and Paul Mativenga. 2009. "Size Effect and Tool Geometry in Micromilling of Tool Steel." *Precision Engineering-Journal of The International Societies for Precision Engineering and Nanotechnology - PRECIS ENG* 33 (October): 402–7.

Arola D., M. Ramulu, and D.H. Wang. 1996. "Chip Formation in Orthogonal Trimming of Graphite / epoxy Composite" 27 (2): 121–33.

Arola D, and M Ramulu. 1997. "Orthogonal Cutting of Fiber-Reinforced Composites: A Finite Element Analysis." *International Journal of Mechanical Sciences - INT J MECH SCI* 39: 597–613.

Arola D., M. B. Sultan, and M. Ramulu. 2000. "Finite Element Modeling of Edge Trimming Fiber Reinforced Plastics." *Journal of Manufacturing Science and Engineering* 124 (1): 32–41.

Arola D., M. B. Sultan, and M. Ramulu. 2002. "Finite Element Modeling of Edge Trimming Fiber Reinforced Plastics." *Journal of Manufacturing Science and Engineering*, 124 (1): 32–41.

Attahu, Cephas Yaw, and L. An. 2017. "Influence of Assembly Gap and Shims on the Strain and Stress of Bolted Composite-Aluminum Structures" 12 (January): 1593–1619.

Bhatnagar, N., N. Ramakrishnan, Nk Naik, and R. Komanduri. 1995. "ON THE MACHINING OF FIBER-REINFORCED PLASTIC (FRP) COMPOSITE LAMINATES." *International Journal of Machine Tools & Manufacture*, 35(5), 701-716

Blanchet Florent. 2015. "Etude de la coupe en perçage par le biais d'essais élémentaires en coupe orthogonale : application aux composites carbone-époxy". PhD Thesis, Université Toulouse 3 – Paul Sabatier.

Boeing AERO, Boeing 787 from the Ground Up; available from: https://www.boeing.com/commercial/aeromagazine/articles/qtr_4_06/AERO_Q406_article4.pdf

Bonnet, C., F. Valiorgue, J. Rech, and H. Hamdi. 2008. "Improvement of the Numerical Modeling in Orthogonal Dry Cutting of an AISI 316L Stainless Steel by the Introduction of a New Friction Model." *CIRP Journal of Manufacturing Science and Technology, High Performance Cutting*, 1 (2): 114–18.

Bonora, Nicola, and Andrew Ruggiero. 2006. "Micromechanical Modeling of Composites with Mechanical Interface – Part 1: Unit Cell Model Development and Manufacturing Process Effects." *Composites Science and Technology* 66 (February): 314–22.

BUET Khuzdar. 2013. "Mechanics of Chips Formation." [cited Sep 19, 2016], Available from: www.slideshare.net/hashimhasnainhadi/mechanics-of-chips-formation.

Calzada Kevin A., Shiv G. Kapoor, Richard E. DeVor, Johnson Samuel, and Anil K. Srivastava. 2012. "Modeling and Interpretation of Fiber Orientation-Based Failure Mechanisms in Machining of Carbon Fiber-Reinforced Polymer Composites." *Journal of Manufacturing Processes, Micro and Nano Manufacturing*, 14 (2): 141–49.

Campilho, R. D. S. G., M. F. S. F. de Moura, and J. J. M. S. Domingues. 2008. "Using a Cohesive Damage Model to Predict the Tensile Behaviour of CFRP Single-Strap Repairs." *International Journal of Solids and Structures* 45 (5): 1497–1512.

Canadian Metalworking, Controlling Cutting Forces, [cited on April 8, 2019] Available from: <https://www.canadianmetalworking.com/canadianmetalworking/article/cuttingtools/controlling-cutting-forces>

Cantero J. L., C. Santiuste, N. Marín, X. Soldani, H. Miguélez, Mariano Marcos, and Jorge Salguero. 2012. "2D and 3D Approaches to Simulation of Metal and Composite Cutting." *AIP Conference Proceedings* 1431 (1): 651–59.

- Caprino G., A. Langella. 2012. "Analysing cutting forces in machining processes for polymer-based composites"; *Machining Technology for Composite Materials*, Pages 75-115
- Caprino G., L. Santo, and L. Nele. 1998. "Interpretation of Size Effect in Orthogonal Machining of Composite Materials. Part I: Unidirectional Glass-Fibre-Reinforced Plastics" 29 (8): 887–92.
- Caprino G. and L Santo. 1998. "Interpretation of Size Effect in Orthogonal Machining of Composite Materials. Part II. Sheet Moulding Compound" 29 (8): 893–97.
- Caprino G. 2019. "Cutting Force - an Overview" [Accessed April 8, 2019] <https://www.sciencedirect.com/topics/engineering/cutting-force>
- Cédric BONNET. 2010. "Compréhension Des Mécanismes de Coupe Lors Du Perçage À Sec de L'empilage Ti6Al4V/Composite Fibre de Carbone." ENSAM.
- Dandekar, Chinmaya R., and Yung C. Shin. 2009. "Multi-Step 3-D Finite Element Modeling of Subsurface Damage in Machining Particulate Reinforced Metal Matrix Composites." *Composites Part A: Applied Science and Manufacturing*, Special Issue: 15th French National Conference on Composites - JNC15, 40 (8): 1231–39.
- D’Orazio, A., M. El Mehtedi, A. Forcellese, A. Nardinocchi, and M. Simoncini. 2017. "Tool Wear and Hole Quality in Drilling of CFRP/AA7075 Stacks with DLC and Nanocomposite TiAlN Coated Tools." *Journal of Manufacturing Processes* 30 (December): 582–92.
- Dref Le, John. 2014. "Contribution À La Modélisation Du Perçage Assisté Par Vibration et À L'étude de Son Impact Sur La Qualité D'alésage : Application Aux Empilages Multi-Matériaux." PhD Thesis, Université de Toulouse.
- David Rees. 2006. *Basic Engineering Plasticity: An Introduction with Engineering and Manufacturing Applications*. Butterworth-Heinemann. Pages 528
- Engineer’s edge, 2018, "Von Mises Criterion (Maximum Distortion Energy Criterion)". [Retrieved 8 February 2018]; available from: https://www.engineersedge.com/material_science/von_mises.htm
- Everstine G. C., and T. G. Rogers. 1971. "A Theory of Machining of Fiber-Reinforced Materials." *Journal of Composite Materials* 5 (1): 94-106
- Fay Baylis. 2012; Boeing 787 Advancements; available from: <http://aviationknowledge.wikidot.com/aviation:boeing-787-advancements>
- Gadelmawla, E. S., M. M. Koura, T. M. A. Maksoud, I. M. Elewa, and H. H. Soliman. 2002. "Roughness Parameters." *Journal of Materials Processing Technology* 123 (1): 133–45.

- Gaitonde V. N., S. R. Karnik, J. Campos Rubio, A. Esteves Correia, A. M. Abrão, and J. Paulo Davim. 2008. "Analysis of Parametric Influence on Delamination in High-Speed Drilling of Carbon Fiber Reinforced Plastic Composites." *Journal of Materials Processing Technology* 203 (1–3): 431–38.
- Garekani, Amir Hossein Afrasiabi. 2016. "Numerical Modeling of Orthogonal Cutting of Carbon Fibre Reinforced Polymer Composites." University of British Columbia; Available from: <https://open.library.ubc.ca/cIRcle/collections/ubctheses/24/items/1.0305793>.
- Ghidossi Patrick. 2003. *Contribution à L'étude de L'effet des Conditions D'usinage D'éprouvettes en Composites à Matrice Polymère sur Leur Réponse Mécanique*. PhD Thesis, ENSAM Paris.
- Gibson, Ronald F. 2010. "A Review of Recent Research on Mechanics of Multifunctional Composite Materials and Structures." *Composite Structures* 92 (12): 2793–2810.
- Gopala Rao, G. Venu, P. Mahajan, and N. Bhatnagar. 2007. "Micro-Mechanical Modeling of Machining of FRP Composites – Cutting Force Analysis" 67 (3–4): 579–93.
- Guegan, Pierrick. 1994. *Contribution a La Qualification de L'usinage de Materiaux Composites a Matrice Organique*. PhD Thesis, ECN Nantes.
- Guo, Yang, W. Dale Compton, and Srinivasan Chandrasekar. 2015. "In Situ Analysis of Flow Dynamics and Deformation Fields in Cutting and Sliding of Metals." *Proc. R. Soc. A* 471 (2178): 20150194.
- Gupta, Meenu, and Surinder Kumar. 2015. "Investigation of Surface Roughness and MRR for Turning of UD-GFRP Using PCA and Taguchi Method." *Engineering Science and Technology, an International Journal* 18 (1): 70–81.
- Hamedanianpoura, H., and J-f Chatelainb. 2013. "Effect of Tool Wear on Quality of Carbon Fiber Reinforced Polymer Laminate during Edge Trimming" 325–236: 34–39.
- Hao, Li, Qin Xuda, He Gaiyun, Jin Yan, Sun Dan, and Mark Price. 2016. "Investigation of Chip Formation and Fracture Toughness in Orthogonal Cutting of UD-CFRP" 89: 1079–88.
- Hencky, H. 1928. "Über die Form des Elastizitätsgesetzes bei ideal elastischen Stoffen". *Zeitschrift für technische Physik*. 9: 215–220
- Hernandez, Dany Arnaldo, Carlos Alberto Soufen, Marcelo Ornaghi Orlandi, Dany Arnaldo Hernandez, Carlos Alberto Soufen, and Marcelo Ornaghi Orlandi. 2017. "Carbon Fiber Reinforced Polymer and Epoxy Adhesive Tensile Test Failure Analysis Using Scanning Electron Microscopy." *Materials Research* 20 (4): 951–61.

Harshit Agarwal, Akshay Amaranath, Yogesh Jamthe & Suhasini Gururaja, 2015 “An Investigation of Cutting Mechanisms and Strain Fields during Orthogonal Cutting in CFRPs” *Machining Science and Technology*; Vol 19, Issue 3Pages 416-439

HexPly M21 Global DataSheet; [cited 30.09.2019]; available from: <https://fr.scribd.com/document/358159244/HexPly-M21-Global-DataSheet>

Hocheng H., and C. C. Tsao. 2005. “The Path towards Delamination-Free Drilling of Composite Materials.” *Journal of Materials Processing Technology*, 2005 International Forum on the Advances in Materials Processing Technology, 167 (2–3): 251–64.

Holmes, Mark. 2014. “Global Carbon Fibre Market Remains on Upward Trend.” *Reinforced Plastics* 58 (6): 38–45.

Iliescu D., D. Gehin, I. Iordanoff, F. Girot, and M. E. Gutiérrez. 2010. “A Discrete Element Method for the Simulation of CFRP Cutting.” *Composites Science and Technology* 70 (1): 73–80.

Iliescu, D., D. Gehin, M. E. Gutiérrez, and F. Girot. 2010. “Modeling and Tool Wear in Drilling of CFRP.” *International Journal of Machine Tools & Manufacture*, 50 (2): 204–13.

Iliescu, Daniel. 2008. “Approches experimentale et numerique de l’usinage a sec des composites carbone /epoxy.” PhD Thesis, ENSAM PARIS.

Ilyas Muhammad. 2010. “Damage Modeling of Carbon Epoxy Laminated Composites Submitted to Impact Loading.” PhD Thesis, Universite de Toulouse .

Jamal Y., Sheikh-Ahmad. 2009. "Machining of Polymer Composites." Springer US; DOI:10.1007/978-0-387-68619-6

J. Broderick, E. Archer, A. McMillan, AT. McIlhagger, 2012. “Internal Strain Measurement and Impact Response of 3D Woven Carbon Fibre Composites.” *ECCM15 - 15TH EUROPEAN CONFERENCE ON COMPOSITE MATERIALS*, Venice, Italy

Klinkova Olga, Joël Rech, Sylvain Drapier, and Jean-Michel Bergheau. 2011. “Characterization of Friction Properties at the Workmaterial/cutting Tool Interface during the Machining of Randomly Structured Carbon Fibers Reinforced Polymer with Carbide Tools under Dry Conditions.” *Tribology International* 44 (12): 2050–58.

Konig W., and P. Grab. 1989. “Quality Definition and Assessment in Drilling of Fibre Reinforced Thermosets”. *CIRP Annals* 38 (1): 119–24.

- Koplev, A., Bunsell, A. R. 1980. "Cutting of CFRP with Single Edge Tools," *Advances in Composite Materials: Proceedings of the 3. International Conference*. Vol. 2 Oxford : Pergamon Press, 1980. p. 1597-1605.
- Koplev A., Lystrup Aa., and Vorm T. 1983. "The Cutting Process, Chips, and Cutting Forces in Machining CFRP." *Composites* 14 (4):371-76
- Kourra, Nadia, Jason M. Warnett, Alex Attridge, Ercihan Kiraci, Aniruddha Gupta, Stuart Barnes, and Mark A. Williams. 2015. "Metrological Study of CFRP Drilled Holes with X-Ray Computed Tomography." *The International Journal of Advanced Manufacturing Technology* 78 (9–12): 2025–35.
- Kumar, Dhiraj, and K. K. Singh. 2015. "An Approach towards Damage Free Machining of CFRP and GFRP Composite Material: A Review." *Advanced Composite Materials* 24 (sup1): 49–63.
- Lachaud L, Piquet R, Collombet F, and Surcin L. 2001. "Drilling of Composite Structures." *Composite Structures* 52: 511-516
- Lasri L., M. Nouari, and M. El Mansori. 2009. "Modelling of Chip Separation in Machining Unidirectional FRP Composites by Stiffness Degradation Concept." *Composites Science and Technology* 69 (5): 684–692.
- Lasri Larbi. 2009. "Modélisation macromécanique et micromécanique de l'usinage des composites à matrice polymère et fibres longues." PhD Thesis, ENSAM PARIS.
- Lazar Mihai-Bogdan, and Paul Xirouchakis. 2011. "Experimental Analysis of Drilling Fiber Reinforced Composites." *International Journal of Machine Tools and Manufacture* 51 (12): 937–46.
- Le Dref, John. 2014. "Contribution À La Modélisation Du Perçage Assisté Par Vibration et À L'étude de Son Impact Sur La Qualité D'alésage : Application Aux Empilages Multi-Matériaux." PhD Thesis. December 11, 2014.
- Limido J., C. Espinosa, M. Salaun, C. Mabru, R. Chieragatti, and J.I. Lacombe. 2011. "Metal Cutting Modelling SPH Approach." *International Journal of Machining and Machinability of Materials* 9 (3–4): 177–96.
- Liu, DeFu, YongJun Tang, and W. L. Cong. 2012. "A Review of Mechanical Drilling for Composite Laminates." *Composite Structures* 94 (4): 1265–79.
- Liu, Guangjun, Hongyuan Chen, Zhen Huang, Fei Gao, and Tao Chen. 2017. "Surface Quality of Staggered PCD End Mill in Milling of Carbon Fiber Reinforced Plastics." *Applied Sciences* 7 (2): 199.

- Liu, Haitao, Jie Lin, Yazhou Sun, and Jinyang Zhang. 2019. "Micro Model of Carbon Fiber/Cyanate Ester Composites and Analysis of Machining Damage Mechanism." *Chinese Journal of Mechanical Engineering* 32 (1): 52.
- Liu, Xueshu, and Fei Chen. 2016. "A Review of Void Formation and Its Effects on the Mechanical Performance of Carbon fiber Reinforced Plastic." *Engineering Transactions* 64 (1): 33–51.
- Lopresto, V., A. Langella, G. Caprino, M. Durante, and L. Santo. 2017. "Conventional Orthogonal Cutting Machining on Unidirectional Fibre Reinforced Plastics." *Procedia CIRP*; Volume 62: Pages 9–14.
- Mahadevan D. 2005. "Experimental Determination of Velocity and Strain Rate Fields in Metal Cutting of OFHC Copper." Master's Thesis, Anna University.
- Mahdi Mofid, and Liangchi Zhang. 2001. "A Finite Element Model for the Orthogonal Cutting of Fiber-Reinforced Composite Materials." *Journal of Materials Processing Technology*, 5th Asia Pacific conference on Materials processing, 113 (1–3): 373–77.
- Markopoulos Angelos P., J. Paulo Davim. 2017. *Advanced Machining Processes: Innovative Modeling Techniques*. Manufacturing Design and Technology, pages: 327
- Martin Madaj, and Miroslav Piška. 2013. "On the SPH Orthogonal Cutting Simulation of A2024-T351 Alloy." 14th CIRP Conference on Modeling of Machining Operations (CIRP CMMO).
- Matzenmiller A., Lubliner J., Taylor R.L. 1995. "A Constitutive Model for Anisotropic Damage in Fiber-Composites." *Mechanics of Materials*; Volume 20, Issue 2, Pages 125-152
- Maurin Romain, Peter Davies, Nicolas Baral, and Christophe Baley. 2008. "Transverse Properties of Carbon Fibres by Nano-Indentation and Micro-Mechanics." *Applied Composite Materials* 15 (2): 61.
- Mecholic magazine; Mecholic for mechanical engineering; available from: <https://www.mecholic.com/2017/05/twist-drill-angles.html>
- Merchant M. Eugene. 1945a. "Mechanics of the Metal Cutting Process. I. Orthogonal Cutting and a Type 2 Chip." *Journal of Applied Physics* 16 (5): 267–75.
- Merchant M. Eugene. 1945b. "Mechanics of the Metal Cutting Process. II. Plasticity Conditions in Orthogonal Cutting." *Journal of Applied Physics* 16 (6): 318–24.
- Mkaddem Ali, Ibrahim Demirci, and Mohamed El Mansori. 2008. "A Micro–macro Combined Approach Using FEM for Modelling of Machining of FRP Composites: Cutting Forces Analysis." *Composites Science and Technology* 68 (15): 3123–27.

-
- Moore Mckenzie, William. 1960. "Fundamental Aspects of the Wood Cutting Process." *Forest Prod. J.* 10.
- Nayak D., Singh I., Bhatnagar N. and Mahajan P. 2004. "An Analysis of Machining Induced Damages in FRP Composites - A Micromechanics Finite Element Approach." *American Institute of Physics* 712. 327-31
- Nayak D., Singh I., Bhatnagar N., Mahajan P. 2004. "An Analysis of Machining Induced Damages in FRP Composites - A Micromechanics Finite Element Approach." *AIP Conference Proceedings* 712, 327
- Nayak D., Bhatnagar N. and Mahajan P. 2005. "Machining Studies of Ud-Frp Composites Part 2: Finite Element Analysis." *Machining Science and Technology* 9 (4): 503-28
- Nayak D., N. Bhatnagar & P. Mahajan, 2007. "Machining Studies of Ud-Frp Composites Part 2: Finite Element Analysis." *Machining Science and Technology*; Volume 9, Issue 4 Pages 503-528
- Newman Tools Inc., Machine tool manufacturer; available from: <https://www.newmantools.com/machines/drillpoint.html>
- Ozaki, Motoyoshi. 2000. "Supervisory Control of Drilling of Composite Materials." Ph.D. Thesis. University of California, Berkeley
- Paiva Jane Maria Faulstich de, Sergio Mayer, and Mirabel Cerqueira Rezende. 2005. "Evaluation of Mechanical Properties of Four Different Carbon/epoxy Composites Used in Aeronautical Field." *Materials Research* 8 (1): 91–97.
- Pan Bing, Kemao Qian, Huimin Xie, and Anand Asundi. 2009. "Two-Dimensional Digital Image Correlation for in-Plane Displacement and Strain Measurement: A Review." *Measurement Science and Technology* 20 (6): 62001.
- Paul K. Wright E M Trent, 2000. "Metal Cutting - 4th Edition". [access on 30.09.2019]; available from: <https://www.elsevier.com/books/metal-cutting/wright/978-0-7506-7069-2>
- Peters, W. H., and W. F. Ranson. 1982. "Digital Imaging Techniques In Experimental Stress Analysis." *Optical Engineering* 21 (3): 213427.
- Piquet R, Ferret B, Lachaud F, Swider P. 2000 "Experimental Analysis of Drilling Damage in Thin Carbon/epoxy Plate Using Special Drills." *Composites Part A* 31: 1107-1115
- Piquet Robert. 1999. Contribution a L'étude Des Reparations Provisoires Structurales Aeronautiques ; Etude Du Percage de Plaques Minces Carbone/epoxy. Université de Toulouse III - Paul Sabatier.

-
- P.P. Camanho, and Carlos G. Davila. 2002. "Mixed-Mode Decohesion Finite Elements for the Simulation of Delamination in Composite Materials." Available from: <https://ntrs.nasa.gov/archive/nasa/casi.ntrs.nasa.gov/20020053651.pdf>
- Pramanik A., L. C. Zhang, and J. A. Arsecularatne. 2007. "An FEM Investigation into the Behavior of Metal Matrix Composites: Tool–particle Interaction during Orthogonal Cutting." *International Journal of Machine Tools and Manufacture* 47 (10): 1497–1506.
- Pwu H. Y., and H. Hocheng. 1998. "Chip Formation Model of Cutting Fiber-Reinforced Plastics Perpendicular to Fiber Axis." *Journal of Manufacturing Science and Engineering* 120 (1): 192–96.
- Rahman M, S Ramakrishna, J. R. S Prakash, and D. C. G Tan. 1999. "Machinability Study of Carbon Fiber Reinforced Composite." *Journal of Materials Processing Technology* 89–90 (May): 292–97.
- Rahme Pierre. 2008. Contribution À L'étude de L'effet Des Procédés de Perçage-Alésage Sur L'apparition Du Délaminage Dans Les Structures Composites Épaisses. PhD Thesis, Université de Toulouse.
- Ramesha M.V., K.N. Seetharamub, N. Ganesanc, and M.S. Sivakumarc. 1998. "Analysis of Machining of FRPs Using FEM" 38 (12): 1531–49.
- Rao, G. Venu Gopala, P. Mahajan, and N. Bhatnagar. 2007. "Micro-Mechanical Modeling of Machining of FRP Composites – Cutting Force Analysis." *Composites Science and Technology* 67 (3): 579–93.
- Rao G. Venu Gopala, Puneet Mahajan, and Naresh Bhatnagar. 2008. "Three-Dimensional Macro-Mechanical Finite Element Model for Machining of Unidirectional-Fiber Reinforced Polymer Composites." *Materials Science and Engineering: A, International Conference on Recent Advances in Composite Materials (ICRACM 2007)*, 498 (1–2): 142–49.
- Rimpault, X., J. -F. Chatelain, J. E. Klemberg-Sapieha, and M. Balazinski. 2017. "Tool Wear and Surface Quality Assessment of CFRP Trimming Using Fractal Analyses of the Cutting Force Signals." *CIRP Journal of Manufacturing Science and Technology* 16 (January): 72–80.
- Robert Voss, Lukas Seeholzer, Friedrich Kuster Konrad Wegener, 2019. "Analytical Force Model for Orthogonal Machining of Unidirectional Carbon Fibre Reinforced Polymers (CFRP) as a Function of the Fibre Orientation." *Journal of Materials Processing Technology*; Vol 263, Pages 440-469
- Roopak Rawat. 2018., Quora.com. available from: <https://www.quora.com/What-is-the-rake-angle-in-twist-drill>
-

- Sahraie Jahromi, A., and B. Bahr. 2010. "An Analytical Method for Predicting Cutting Forces in Orthogonal Machining of Unidirectional Composites." *Composites Science and Technology, Metal Matrix Composites Reinforced with Nano-sized Reinforcements*, 70 (16): 2290–97.
- S. Zenia, L. Ben Ayed, M. Nouari, and A. Delamézière. 2015. "An Elastoplastic Constitutive Damage Model to Simulate the Chip Formation Process and Workpiece Subsurface Defects When Machining CFRP Composites." 15th CIRP Conference on Modelling of Machining Operations.
- Sahraie Jahromi A., and B. Bahr. 2010. "An Analytical Method for Predicting Cutting Forces in Orthogonal Machining of Unidirectional Composites." *Composites Science and Technology, Metal Matrix Composites Reinforced with Nano-sized Reinforcements*, 70 (16): 2290–97.
- Schön, Joakim. 2004. "Coefficient of Friction and Wear of a Carbon Fiber Epoxy Matrix Composite." *Wear* 257 (3): 395–407.
- Shchurov I. A., A. V. Nikonov, and I. S. Boldyrev. 2016. "SPH-Simulation of the Fiber-Reinforced Composite Workpiece Cutting for the Surface Quality Improvement." *Procedia Engineering, 2nd International Conference on Industrial Engineering (ICIE-2016)*, 150: 860–65.
- Simon Gaugel, Prithvi Sripathy, Andreas Haeger, Dieter Meinhard, Timo Bernthaler, Fabian Lissek, Michael Kaufeld, Volker Knoblauch, Gerhard Schneider, 2016. "A comparative study on tool wear and laminate damage in drilling of carbon-fiber reinforced polymers (CFRP)" *Composite Structures; Volume 155, Pages 173-183*
- Singh, I., N. Bhatnagar, and P. Viswanath. 2008. "Drilling of Uni-Directional Glass Fiber Reinforced Plastics: Experimental and Finite Element Study." *Materials & Design* 29 (2): 546–53.
- Smith Faye, CEng, FIMMM. Avalon Consultancy Services Ltd.; available from: <https://avaloncsl.files.wordpress.com/2013/01/avalon-the-use-of-composites-in-aerospace-s.pdf>
- Smithy, Detroit Machine Tools, available from: <https://smithy.com/machining-handbook/chapter-6/page/4>
- Soussia Aymen Ben. 2014. "Modélisation tribo-physique de la coupe des composites FRP : Approches numérique et expérimentale." PhD Thesis, ENSAM.
- Stock, S. R. 1999. "X-Ray Microtomography of Materials." *International Materials Reviews* 44 (4): 141–64.
- Strong, A. Brent. 1989. *Fundamentals of Composites Manufacturing: Materials, Methods, and Applications*. Society of Manufacturing Engineers.

Surcin, Laurent. 2005. Contribution À L'étude Théorique et Expérimentale Du Perçage de Plaques Composites Mince. Université de Toulouse 3 - Paul Sabatier

Szekrényes, András, and József Uj. 2002. Finite Element Modelling of the Damage and Failure in Fiber Reinforced Composites," Research Group for Dynamics of Machines and Vehicles Hungarian Academy of Sciences. Vol. 46, No. 2, PP. 139–158

Takeyama H., and N. Iijima. 1998. "Machinability of Glassfiber Reinforced Plastics and Application of Ultrasonic Machining." CIRP Annals 37 (1): 93–96.

Teti, R. 2002. "Machining of Composite Materials." CIRP Annals 51 (2): 611–34.

Tsao, C. C., and Hong Hocheng. 2004. "Taguchi Analysis of Delamination Associated with Various Drill Bits in Drilling of Composite Material." International Journal of Machine Tools and Manufacture; Volume 44, Issue 10, Pages 1085-1090

Turki Y., M. Habak, R. Velasco, P. Vantomme, and Z. Aboura. 2011. "Evaluation Expérimentale Du Comportement d'un Composite Carbone/époxy En Usinage - Economy & Finance - We Share Success." DocumentSlide.Org. <https://documentslide.org/evaluation-experimentale-du-comportement-d-un-composite-carbone-epoxy-en-usinage>.

Valery Marinov. 2016. "Manufacturing Technology" Eastern Mediterranean University; Manufacturing Technology ME 364.

Vaziri R., M.D. Olson, and D.L. Anderson. 1992. "Finite Element Analysis of Fibrous Composite Structures: A Plasticity Approach." Computers & Structures 44 (1–2): 103–16.

Victor N. Kaliakin, 2017. "Soil Mechanics: Calculations, Principles, and Methods." Butterworth-Heinemann; ISBN: 978-0-12-804491-9

Vijayan, D., P. Abhishek, Y. G. Manoj Kumar, P. Balaji, and P. Siva kumar Reddy. 2018. "Optimization of Drilling Parameters of Carbon Fiber Composites Using RSM Based Desirability Function." IOP Conference Series: Materials Science and Engineering 390: 12076.

Voba, Robert, Marcel Henerichsa, Friedrich Kustera, and Konrad Wegenera. 2014. "Chip Root Analysis after Machining Carbon Fiber Reinforced Plastics (CFRP) at Different Fiber Orientations." Procedia CIRP, Vol 14, Pages 217-222

W. Yousfi, Ph. Darnis, O. Cahuc, R. Laheurte, M. Calamaz. 2015. "3D modeling of strain fields and strain rate in the cutting area: application to milling" The International Journal of Advanced Manufacturing Technology; Volume 84, Issue 9–12, pp 2207–2218

-
- Wang, Changying, Gongyu Liu, Qinglong An, and Ming Chen. 2017. "Occurrence and Formation Mechanism of Surface Cavity Defects during Orthogonal Milling of CFRP Laminates." *Composites Part B: Engineering* 109: 10–22.
- Wang, Dongyao, Xiaodong He, Zhonghai Xu, Weicheng Jiao, Fan Yang, Long Jiang, Linlin Li, Wenbo Liu, and Rongguo Wang. 2017. "Study on Damage Evaluation and Machinability of UD-CFRP for the Orthogonal Cutting Operation Using Scanning Acoustic Microscopy and the Finite Element Method." *Materials* 10 (2).
- Wang Duck, M Ramulu, and D Arola. 1995. "Orthogonal Cutting Mechanisms of Graphite/epoxy Composite. Part I: Unidirectional Laminate." *International Journal of Machine Tools and Manufacture* 35: 1623–38.
- Wang, Xin, Y. Kwon Parick, Caleb Sturtevant, Dave Kim, and Jeff Lantrip. 2013. "Tool Wear of Coated Drills in Drilling CFRP" 15 (1): 127–35.
- Wang X.M., and L Zhang. 2003. "An Experimental Investigation into the Orthogonal Cutting of Unidirectional Fibre Reinforced Plastics." *International Journal of Machine Tools and Manufacture* 43: 1015–22.
- William M., McKenzie, 1961, "Fundamental Analysis of the Wood-Cutting Process." The University of Michigan; PhD thesis
- Xu Jinyang, Mohamed EL Mansori, and Julien Voisin. 2016. "Numerical Modeling and FE Analysis of CFRP/Ti Stack Orthogonal Cutting." *Procedia CIRP* 46: 67–70.
- Youliang, Su, Jia Zhenyuan, Niu Bin, and Bi Guangjian. 2016. "Size Effect of Depth of Cut on Chip Formation Mechanism in Machining of CFRP." *Composite Structures* 164: 316–27.
- Zadshakoyan M, and vahid Pourmostaghimi. 2013. "Genetic Equation for the Prediction of Tool–chip Contact Length in Orthogonal Cutting." *Engineering Applications of Artificial Intelligence* 26: 1725-30.
- Zhang, Aying, Haibao Lu, and Dongxing Zhang. 2016. "Research on the Mechanical Properties Prediction of Carbon/epoxy Composite Laminates with Different Void Contents." *Polymer Composites* 37 (1): 14–20.
- Zhang L. C., H. J. Zhang, and X. M. Wang. 2001. "A Force Prediction Model for Cutting Unidirectional Fibre-Reinforced Plastics." *Machining Science and Technology* 5 (3):293-305
- Zhanqiang, Liu, Shi Zhenyu, and Wan Yi. 2013. "Definition and Determination of the Minimum Uncut Chip Thickness of Microcutting." *The International Journal of Advanced Manufacturing Technology* 69 (5–8): 1219–32.

Zitoune R., F. Collombet, F. Lachaud, R. Piquet, and P. Pasquet. 2005. "Experiment–calculation Comparison of the Cutting Conditions Representative of the Long Fiber Composite Drilling Phase." *Composites Science and Technology, JNC13-AMAC-Strasbourg*, 65 (3–4): 455–66.

Zitoune Redouane. 2004. "Analyse Des Conditions D'usage Lors Du Perçage de Structures Composites Fibres Longues En Carbone-Époxy". PhD Thesis, Université Toulouse 3 - Paul Sabatier.

Mitsubishi Materials, 2017, "Comparison of Hole-Drilling in CFRP Using High-Speed Camera (Video); Available from:
http://www.carbide.mht.co.th/solution/purpose/tech/test_library/video4

Appendixes

Appendix A

Manufacturing process of the CFRP workpiece

T800S/M21 unidirectional tape CFRP is used for the specimens. According to the stacking of specimen, laminate of 200 mm X 300 mm is prepared through hand lay-up by positioning one unidirectional ply over another along required ply angle. The laminate is conditioned under vacuum press to solidate the stacking, Fig. A1.

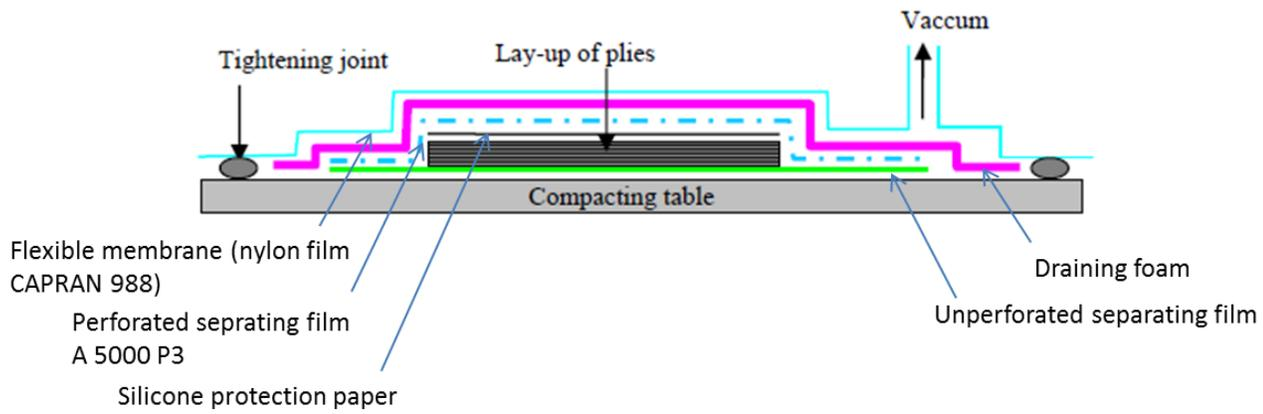
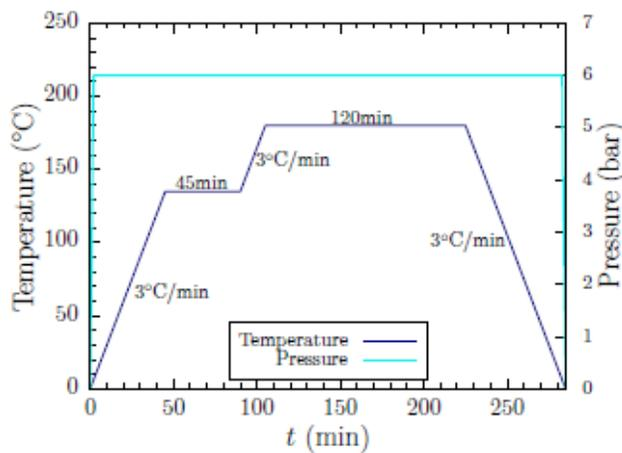


Fig. A1: Compacting lay-ups by vacuum

The curing of material is achieved in auto-clave available at Institut Clement Ader, Fig. A2-b. This curing process follows strictly the recommendation of supplier, Fig. A2-a.



(a)



(b)

Fig. A2: (a) Curing spectrum and, (b) autoclave for material curing

Appendix B

The developed orthogonal bench by [Blanchet, 2015] at Institut Clement Ader runs by a particular semi-automatic operating system. There are a number of steps to follow to make the machine run. Here in this section, the operating procedure is explained according to the sequences. This explanation will be useful to the future users of the machine.

1. General Checkup:

- Be sure that the electric connection is disconnected.
- First check if the vice and the tool are well fixed .
- Check if the vice can move freely without obstacle (e.g. enough space below the upper holder).

2. Connecting the Motor Operating Laptop:

- Connect the laptop to the drive motor.

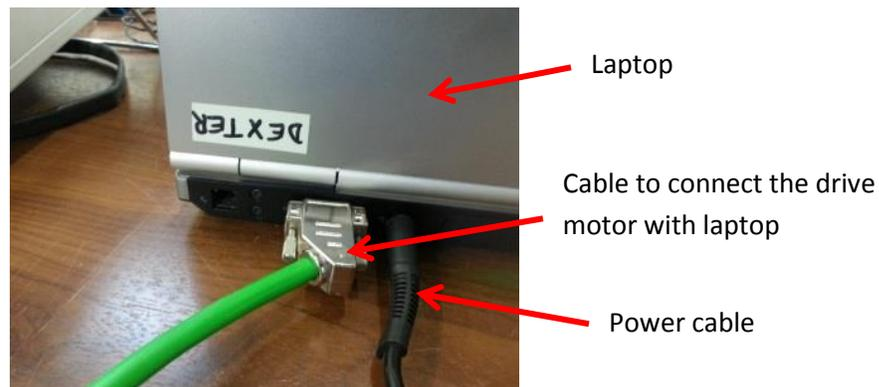


Fig. B1: Cables to connect to the drive motor operator

- Connect the laptop to electric line

3. Operating Software and Initial Parameters:

Starting the software

- Click on the file named: "*Config-1-2015-10-14.C3P*" (clicking on this file means we start the software C3MGR2_R09-40)
- Manually move the carriage/cart to the desired zero position
- Double click on '*Fonctions d'appareil en ligne > Mettre à zéro la position absolue*'

- Click on 'Oui'

Initial configuration

- Double click on 'Configurer C3S I12 T11'
- Follow the next steps by clicking next
- Before clicking on 'Chargement de la Configuration seule dans l'appareil', make sure that the homing has been done.
- Click on 'Mise régulateur hors tension et démarrage Chargement de la Configuration'
- Select 'puis ouvrir la fenêtre d'optimisation'
- Click on 'Exécuter'

4. Optimization Window

Oscilloscope settings

- Find the tab 'Réglages Oscilloscope' at left below
- Choose ROLL for continuous scrolling of the measure (if not: SINGLE,...)
- Define the quantities to be measured: choose them in the window at the bottom at right, tab 'Valeurs d'états', and drag and drop them onto the desired measurement channel.
- Click on 'Démarrer mesure'
- At the end of the movement click on 'Arrêter mesure'
- To export the measures, click on 'Fonctions spéciales (OSCILLO) and choose 'Export CSV'

Commissioning

- Commissioning (*Mise en Service*) is located below at right
- Click on 'ON'
- Click on the icon at right 'Mise sous/hors tension'
- Click on  or  to move the holder manually

- Click on  to redefine zero

5. General Use

To define other desired parameters (if needed)

- Click on 'Saisie des paramètres' or on 'Paramètres'

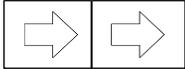
- In the green banner, select the desired page, adjust the settings and exit from this page by clicking on '*Prise en compte des entrées*'.

Automatic identification of moments of inertia

Choose load identification settings. To start load identification:

- Click on '*Identification de charge: Démarrer*' 
- Click on '*Start*'
- After the identification cycle, click on '*Affectation des valeurs*' and check that the lower and upper terminals defined previously frame well the value of the measured inertia, if not modify them.

6. Driving the Movement

- Choose '*mouvement manuel*' or '*en relatif*' or '*en absolu*'.
- Define the movement parameters (speed, position etc.)
- To start the movement:
 - Click on  if the mode '*absolu*'; or  for the mode '*relatif*'
 - Click on '*Arrêter le mouvement*' when it is finished (if not it will continue to move).

To refresh an error

- Click on  left at the bottom.

To Exit from the optimization window

- Turn everything off: '*Hors tension*'  right at the bottom of the window,  right at the top of the window
- Close the window

To Measure the Cutting Efforts:

To measure the forces you need to connect the laptop in which the KISTLER software is installed.

- Connect both signal and data cables in between the KISTLER installed laptop and the Multichannel Charge Amplifier as in Fig.B2.

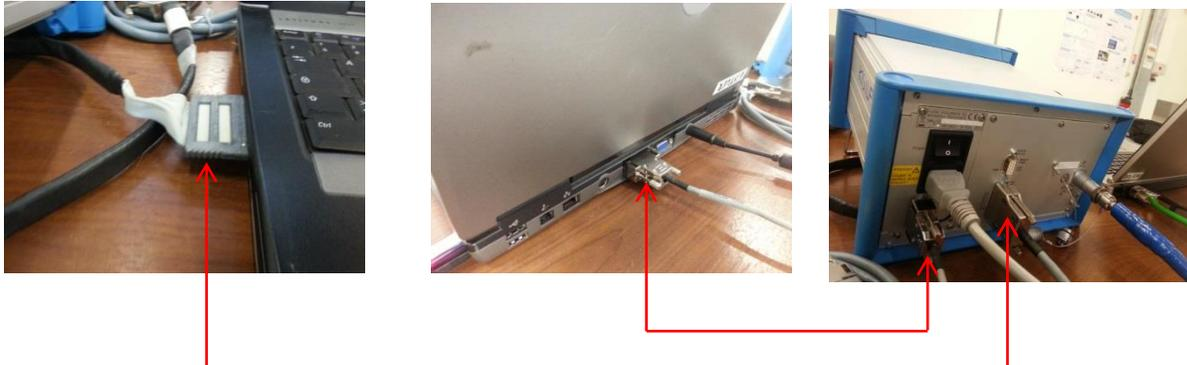


Fig. B2: Connections between KISTLER installed laptop and Multichannel Charge Amplifier

- Connect the dynamometer cable with the Multichannel Charge Amplifier



Fig. B3: Connection between dynamometer and Charge Amplifier

- Connect the power cable of Multichannel Charge Amplifier
- Connect the power cable of the KISTLER installed laptop
- Switch on the power of the Charge amplifier



Fig. B4: Power switch of Multichannel Charge Amplifier

Numerical and Experimental Analysis of CFRP Machining Process in Orthogonal Cutting

The composite materials, including CFRP (Carbon Fiber Reinforced Polymer), are increasingly used in aeronautics and automotives which is currently raising many complications in the machining processes. As those materials are made with multiple phases, they are accountable for poor machining quality and undesired defects. This thesis seeks to better understand the fundamental physical technique involved in chip formation mechanism in orthogonal cutting of CFRP machining by combined numerical and experimental studies. Then, the analysis focuses to how certain cutting parameters, e.g., cutting depth, affect to the cutting efforts, surface quality, interply delaminations, inner crack generation and to generated chip shape and size. Moreover, an experimental observation has been made to find out the minimum cuttable depth below which the material does not get cut smoothly over the whole surface. This research work has been finished by a preliminary study on cutting tool wear mechanism.

Analyse numérique et expérimentale du processus d'usinage CFRP en coupe orthogonale

Les matériaux composites, y compris le PRFC (polymère renforcé de fibre de carbone), sont de plus en plus utilisés en aéronautique et dans l'automobile, ce qui soulève actuellement de nombreuses complications dans les processus d'usinage. Comme ces matériaux sont fabriqués en plusieurs phases, ils sont responsables d'une mauvaise qualité d'usinage et de défauts indésirables. Cette thèse vise à mieux comprendre la technique physique fondamentale impliquée dans le mécanisme de formation de copeaux dans le découpage orthogonal d'usinage en PRFC par des études numériques et expérimentales combinées. Ensuite, l'analyse se concentre sur la manière dont certains paramètres de coupe, par exemple, la profondeur de coupe, affectent les efforts de coupe, la qualité de surface, les délaminations entre couches, la génération de fissures internes et la forme et la taille de copeaux générées. De plus, une observation expérimentale a été faite pour déterminer la profondeur de coupe minimale en dessous de laquelle le matériau ne peut pas être coupé en douceur sur toute la surface. Ce travail de recherche a été complété par une étude préliminaire sur le mécanisme d'usure des outils de coupe.